V. 122, NO. 3
MAY 2025

ACI MATERIALS JOURNAL

A JOURNAL OF THE AMERICAN CONCRETE INSTITUTE

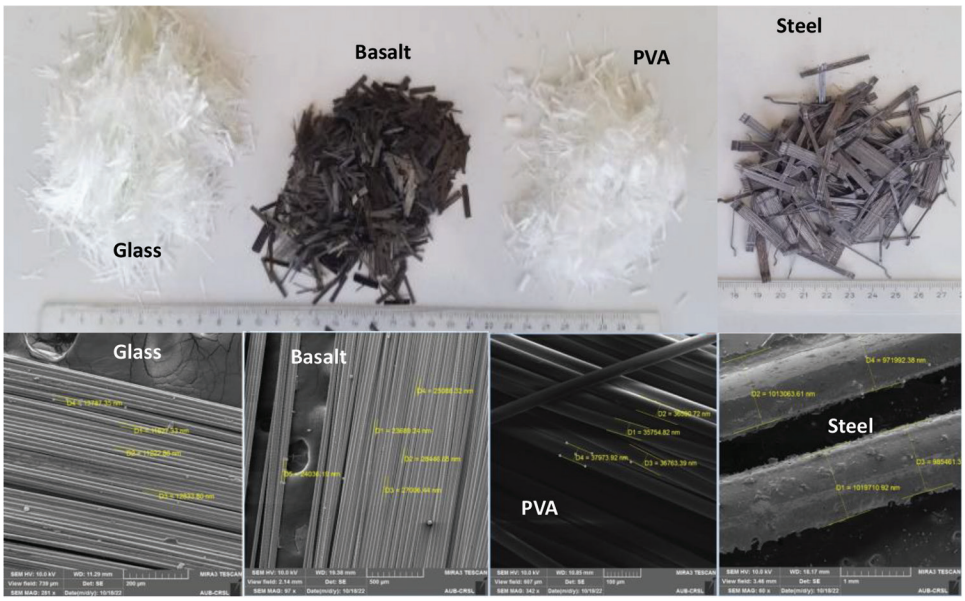

American Concrete Institute

CONTENTS

ACI Materials Journal

May 2025, V. 122, No. 3

A JOURNAL OF THE AMERICAN CONCRETE INSTITUTE
AN INTERNATIONAL TECHNICAL SOCIETY

The *ACI Materials Journal* (ISSN 0889-325x) is published bimonthly by the American Concrete Institute. Publication office: 38800 Country Club Drive, Farmington Hills, MI 48331. Periodicals postage paid at Farmington, MI, and at additional mailing offices. Subscription rates: $210 per year, payable in advance. POSTMASTER: Send address changes to: *ACI Materials Journal*, 38800 Country Club Drive, Farmington Hills, MI 48331.

Canadian GST: R 1226213149.

Direct correspondence to 38800 Country Club Drive, Farmington Hills, MI 48331. Telephone: +1.248.848.3700.
Website: http://www.concrete.org.

MEETINGS

JUNE 2025

16-18—Concrete Solutions 9th International Conference on Concrete Repair, Durability and Technology, Lisbon, Portugal, https://concrete-solutions.org

16-18—*fib* Symposium 2025 – Concrete Structures: Extend Lifespan, Limit Impacts, Antibes, France, https://fibsymposium2025.sciencesconf.org

23-25—3rd International Workshop on Calcium Sulfoaluminate Cements (CSA 2025), Leeds, UK, https://eps.leeds.ac.uk/events-39/doc/3rd-international-workshop-calcium-sulfoaluminate-cements

JUNE-JULY 2025

29-4—Shaping the Fate of Low-Carbon Cement Science, Ascona, Switzerland, https://lccs.epfl.ch

30-3—*fib*CACRCS 2025 – Capacity Assessment of Corroded Reinforced Concrete Structures: from Research to Daily Engineering Evaluation, Lecco, Italy, https://cacrcs.cte-eventi.com

JULY 2025

3-5—Third International Conference on Construction Materials and Structures (ICCMS-2025), Tirupati, India, https://theconcreteconference.com

7-9—Numerical Modelling Strategies for Sustainable Concrete Structures (SSCS2025), Rotterdam, the Netherlands, https://www.sscs2025.org

14-15—2025 ACPA Safety Summit, Dallas, TX, www.concretepumpers.com/content/2025-acpa-safety-summit

14-16—12th International Conference on Fiber-Reinforced Polymer (FRP) Composites in Civil Engineering (CICE 2025), Lisbon, Portugal, https://cice2025.org

17-19—Concrete Foundations Convention (CFACON25), Deadwood, SD, https://cfaconcretepros.org/events/details/?event=573fb936-0078-c4e8-8e96-0b4734b1f19b

21-24—BEI-2025 – Bridge Engineering Institute Conference, Paris, France, https://beibridge.org/BEI2025.html

24—The Fourth International Conference of Construction, Infrastructure, and Materials (ICCIM 2025), West Jakarta, Indonesia, https://iccim.untar.ac.id

25-27—ACF Workshop on Emerging Concrete Technologies – 20th Anniversary of Asian Concrete Federation, Changsha, China, www.concrete.org/newsandevents/eventscalendar.aspx?m=CalendarSearchDetails&CurrentID=210882

ACI CONCRETE CONVENTION: FUTURE DATES

2025—Oct. 26-29, Hilton Baltimore & Baltimore Marriott Inner Harbor, Baltimore, MD
2026—Mar. 29-Apr. 1, Hyatt Regency O'Hare Chicago, Rosemont/Chicago, IL
2026—Oct. 11-14, Hilton Atlanta, Atlanta, GA
2027—Mar. 21-24, Caesars Palace Las Vegas, Las Vegas, NV

For additional information, contact:
Event Services, ACI
38800 Country Club Drive
Farmington Hills, MI 48331
Telephone: +1.248.848.3795
email: conventions@concrete.org

ON FRONT COVER: 122-M14, p. 27, Fig. 2—Photos and scanning electron microscope (SEM) images for glass, basalt, polyvinyl alchohol (PVA), and steel fibers (Al Ghali et al. 2023).

Contributions to *ACI Materials Journal*

The *ACI Materials Journal* is an open forum on concrete technology and papers related to this field are always welcome. All material submitted for possible publication must meet the requirements of the "American Concrete Institute Publication Policy" and "Author Guidelines and Submission Procedures." Prospective authors should request a copy of the Policy and Guidelines from ACI or visit ACI's website at **www.concrete.org** prior to submitting contributions.

Papers reporting research must include a statement indicating the significance of the research.

The Institute reserves the right to return, without review, contributions not meeting the requirements of the Publication Policy.

All materials conforming to the Policy requirements will be reviewed for editorial quality and technical content, and every effort will be made to put all acceptable papers into the information channel. However, potentially good papers may be returned to authors when it is not possible to publish them in a reasonable time.

Discussion

All technical material appearing in the *ACI Materials Journal* may be discussed. If the discussion is received within four months of the paper's print publication, it will appear in the issue dated ten months from this journal's date. Discussion material received after specified dates will be considered individually for publication or private response. ACI Standards published in ACI Journals for public comment have discussion due dates printed with the Standard. Discussion should be complete and ready for publication, including finished, reproducible illustrations. Discussion must be confined to the scope of the paper and meet the ACI Publication Policy.

Follow the style of the current issue. Discussions should not exceed 1800-word equivalents (illustrations and tables count as 300 words each). References should be complete. Do not repeat references cited in original paper; cite them by original number. Numbering of additional references, figures, tables, and equations should follow sequentially from the original manuscript throughout the discussion. The discusser must indicate the month, year, volume number, issue number, authors' names, and manuscript number of the original manuscript. Closures responding to a single discussion should not exceed 1800-word equivalents in length, and to multiple discussions, approximately one half of the combined lengths of all discussions. Closures are published together with the discussions.

Discuss the paper, not some new or outside work on the same subject. Use references wherever possible instead of repeating available information.

Discussion offered for publication should offer some benefit to the general reader. Discussion which does not meet this requirement will be returned or referred to the author for private reply.

Send manuscripts to:
http://mc.manuscriptcentral.com/aci

Send discussions to:
Journals.manuscripts@concrete.org

ACI MATERIALS JOURNAL TECHNICAL PAPER

Title No. 122-M12

Multiscale Nanofiber-Reinforced Concrete for Enhancing Intrinsic Tensile Strength

by S. H. Chu

The weakness of concrete in tension can be mitigated by developing fiber-reinforced concrete (FRC) to induce pseudo-ductility. However, enhancing the intrinsic tensile strength of the matrix in FRC has received little attention. In this regard, nanofibers, which can improve the intrinsic tensile properties of the matrix, were used in conjunction with microfibers to enhance intrinsic tensile strength. Different volumes of nanofibers (0.0 to 0.6%) and microfibers (0.0 to 2.0%) were tested, and various fresh and hardened properties were analyzed. Test results show that the high-range water-reducing admixture dosage increased with both nanofiber and microfiber volume and that strength increased with microfiber volume, reaching an optimum point at a certain nanofiber dosage. Moreover, incorporating nanofibers and microfibers to develop multiscale FRC (MSFRC) significantly improved direct tensile strength and energy absorption. The synergy between nanofibers and microfibers was revealed both qualitatively and quantitatively, contributing to the advancement of FRC.

Keywords: fiber-reinforced concrete (FRC); intrinsic; microfiber (MF); nanofiber (NF); synergy; tensile.

INTRODUCTION

Fiber-reinforced concrete (FRC) can overcome intrinsic brittleness and improve the tensile performance of conventional plain concrete.[1] Fibers are indispensable for the development of FRC.[2] Boulekbache et al.[3] reported a 242% increase in flexural strength after adding hooked steel fibers with aspect ratios of 65 and 80 at fiber volumes of 0.5% and 1.0%. Enhancements were observed in compressive strength,[4] reinforcing bar bond strength,[5,6] and direct tensile strength[7] of plain and steel FRC (SFRC) at fiber volumes up to 2.0%. Despite the significant increase in tensile strength and ductility achieved by developing FRC, the matrix itself has undergone little alteration. The pseudo-ductility of FRC, attributed to the fiber-bridging effect at the post-cracking stage, enables the development of pseudo-ductile cementitious composites (PDCCs).[8]

However, such PDCCs are still far from perfect, not only because structural components at the serviceability limit state rarely approach their ultimate strength limit, let alone the post-cracking stage, but also because multiple cracks, though sometimes acceptable in terms of average crack width, tend to localize, allowing the penetration of water, air, and hazardous substances.[9] Therefore, it is imperative to develop advanced FRC that exhibits intrinsically high tensile performance in addition to pseudo-ductility. The novel FRC is expected to demonstrate exceptional tensile strength throughout both the elastic and post-cracking stages.[10]

Nanofibers (NFs), acting as nanoscale reinforcement, are considered to impart intrinsically high tensile strength to FRC. One innovative and promising solution is the incorporation of nanoclay (NC) as NFs into the mixture.[11-14] NC, sourced from mineral materials, is inorganic, sustainable, and contributes to fire and corrosion resistance in concrete more effectively than other types of fibers.[15-18] Most importantly, its cost-effectiveness and compatibility with concrete are among the highest of all NFs, suggesting a wide range of applications.[19,20] For instance, Hamed et al.[19] used NC at varying dosages of 5.0, 7.5, and 10.0% as partial cement replacements in concrete mixtures and reported that 7.5% NC resulted in the highest strength, as evidenced by the densified matrix observed through scanning electron microscopy. In addition, Morsy et al.[20] demonstrated that replacing 6% of cement with metakaolin-based NC increased the compressive strength of mortar by 18%. Overall, NC has been shown to slightly improve compressive strength by densifying the matrix and bridging cracks at the nanoscale. However, a systematic evaluation of the influence of NC on the direct tensile performance of FRC remains limited.

Microfibers (MFs), specifically steel in this study, have been widely used in the production of high- and ultra-high-performance FRC. These MFs can arrest microcracks and slightly increase the first-cracking strength of concrete under tension.[7,21] Beyond improving first-cracking strength, the addition of MFs can sometimes result in post-cracking strength exceeding first-cracking strength, thereby inducing strain-hardening behavior and significantly increasing energy dissipation.[7,22] For instance, Wille et al.[22] evaluated various elastic, strain-hardening, and softening tensile parameters—such as first-cracking strength and strain, elastic and strain-hardening modulus, composite strength, and energy dissipation capacity—and observed improved performance. Overall, incorporating MFs enables pseudo-ductile behavior through fiber bridging, primarily at the post-cracking stage. However, the material remains pseudo-ductile rather than fully ductile.

The co-use of NFs and MFs in developing multiscale FRC (MSFRC) represents a novel and promising approach to overcoming these challenges. While NFs and MFs have typically been used individually, as documented in the literature,

ACI Materials Journal, V. 122, No. 3, May 2025.

MS No. M-2022-189.R4, doi: 10.14359/51746710, received March 5, 2023, and reviewed under Institute publication policies.

their combined use remains uncommon, and limited attention has been given to the potential synergistic effects that may arise from their integration. First, NFs are hypothesized to reinforce the matrix at the nanoscale and extend the tensile stress-strain curve in the elastic stage. Second, MFs are expected to play a critical role in enhancing the tensile strength of concrete when used alongside NFs, attributable to the improved fiber bond and pronounced fiber-bridging effect at both the nanoscale and microscale. Based on these hypotheses, it is likely that the tensile behavior of both the matrix and the composite can be significantly enhanced in MSFRC. However, such investigations have been relatively scarce. Above all, research aimed at developing intrinsically high-strength MSFRC and exploring the synergy between NFs and MFs remains limited. To address this gap, an experimental program was designed to develop MSFRC with intrinsically high tensile strength and investigate the potential synergistic effects between NFs and MFs. In this study, a series of mortar mixtures were prepared with varying NF and MF volumes, and a range of tests was conducted to assess the workability and strength of the resulting MSFRC. Particular emphasis was placed on evaluating the direct tensile strength of MSFRC.

RESEARCH SIGNIFICANCE

The advantages and disadvantages of the individual and combined use of NFs and MFs were evaluated, quantifying their synergistic effects on compressive strength and direct tensile strength. The novelty and contributions of this study are as follows: a) the intrinsic tensile strength of the matrix (as opposed to pseudo-tensile properties) in MSFRC can be enhanced using mineral NFs; and b) the synergy between MFs and NFs in MSFRC was identified and quantified.

EXPERIMENTAL PROGRAM

Materials

Type CEM I ordinary portland cement (OPC) of Class 52.5N was used. Microsilica (MS) was incorporated as a supplementary cementitious material (SCM) to enhance strength. The specific gravities of OPC and MS were determined as 3.11 and 2.60, respectively, and their particle-size distributions are presented in Fig. 1(a).

For mortar production, quartz sand (QS) with a maximum size of 1.18 mm (0.046 in.) was used. To produce MSFRC, fibers of different scales were introduced into the plain matrix. Self-dispersing hydrated magnesium aluminosilicate with high purity was used as NF (Fig. 1(b)), and its chemical composition is provided in Table 1. Physically, the NF (in colloidal form for better dispersion) has an average diameter of 30 nm (1.18×10^{-6} in.), a length of 1.5 to 2.0 μm (5.90 to 7.87×10^{-5} in.), and a specific gravity of 2.29.

Steel MFs are shown in Fig. 1(c). Physically, they have a diameter of 0.2 mm (0.00787 in.) and a length of 13 mm (0.512 in.). Mechanically, the MFs have a minimum tensile strength of 2000 MPa (290 ksi), a Young's modulus of 210 GPa (30 Msi), and a specific gravity of 7.85.

A third-generation polycarboxylate ether (PCE) high-range water-reducing admixture (HRWRA), with a solid content of 20% and a specific gravity of 1.03, was used to adjust workability.

Mixture design

In this study, a total of 16 mortar mixtures were produced. The primary variables evaluated were the NF volume and the MF volume. The NF volume was varied at 0.0, 0.2, 0.4, and 0.6% of the total mixture volume, while the MF volume was adjusted to 0.0, 0.5, 1.0, and 2.0%. QS was fixed at 25% of the total volume to reduce variability in control experiments. Similarly, the water-cementitious materials ratio (*w*/*cm*) was fixed at 0.20. To ensure that workability did not influence the mechanical properties of the mortar mixtures, the slump and flow diameter of all mixtures were maintained within a narrow range by adjusting the HRWRA dosage. The HRWRA dosage for each mixture was recorded accordingly.

Table 2 presents the volume-based concrete mixture design (VCD) for 1 m^3 (1.3 yd^3) of material.[23] For clarity, each mixture is labeled in the form of A-B, where A represents the

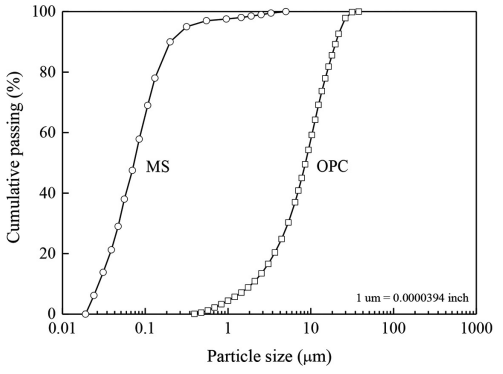

(a)

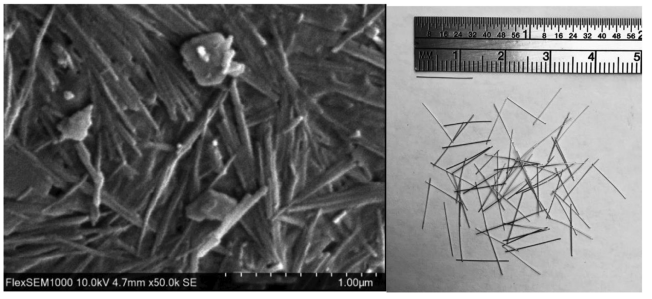

(b) (c)

Fig. 1—Raw materials: (a) particle-size distributions of OPC and MS; (b) image of nanofibers; and (c) image of microfibers.

Table 1—Chemical composition of NF

Chemical composition	SiO_2	Al_2O_3	MgO	Fe_2O_3	CaO	K_2O	P_2O_5	Na_2O	LOI
Mass, %	55.2	12.2	8.6	4.1	2.0	0.68	0.65	0.53	15.66

Note: LOI is loss on ignition.

Table 2—Volume-based concrete mixture design (VCD)

Mixture proportions							
Mixture No. (V_{NF}-V_{MF})	Cement, kg/m^3	MS, kg/m^3	Water, kg/m^3	HRWRA, kg/m^3	QS, kg/m^3	NF, kg/m^3	MF, kg/m^3
0.0%-0.0%	1276	142	233	64	645	0.0	0
0.0%-0.5%	1275	142	230	67	632	0.0	39
0.0%-1.0%	1274	142	228	69	619	0.0	79
0.0%-2.0%	1273	141	225	72	593	0.0	157
0.2%-0.0%	1269	141	221	77	645	2.8	0
0.2%-0.5%	1268	141	219	80	632	2.8	39
0.2%-1.0%	1267	141	213	86	619	2.8	79
0.2%-2.0%	1266	141	211	89	593	2.8	157
0.4%-0.0%	1263	141	210	90	645	5.6	0
0.4%-0.5%	1262	141	207	93	632	5.6	39
0.4%-1.0%	1260	141	202	99	619	5.6	79
0.4%-2.0%	1258	140	196	106	593	5.6	157
0.6%-0.0%	1256	140	199	103	645	8.4	0
0.6%-0.5%	1254	140	193	109	632	8.4	39
0.6%-1.0%	1252	140	188	115	619	8.4	79
0.6%-2.0%	1252	140	186	118	593	8.4	157
Mixture parameters							
Mixture No. (V_{NF}-V_{MF})	CPV, %	*w*/*cm*	MS, %	HRWRA, %	NF, %	MF, %	Type
0.0%-0.0%	75	0.20	10.0	4.5	0.00	0.0	Plain
0.0%-0.5%	75	0.20	10.0	4.7	0.00	0.5	FRC
0.0%-1.0%	75	0.20	10.0	4.9	0.00	1.0	FRC
0.0%-2.0%	75	0.20	10.0	5.1	0.00	2.0	FRC
0.2%-0.0%	75	0.20	10.0	5.5	0.20	0.0	FRC
0.2%-0.5%	75	0.20	10.0	5.7	0.20	0.5	FRC
0.2%-1.0%	75	0.20	10.0	6.1	0.20	1.0	FRC
0.2%-2.0%	75	0.20	10.0	6.3	0.20	2.0	FRC
0.4%-0.0%	75	0.20	10.0	6.4	0.40	0.0	FRC
0.4%-0.5%	75	0.20	10.0	6.6	0.40	0.5	FRC
0.4%-1.0%	75	0.20	10.0	7.1	0.40	1.0	FRC
0.4%-2.0%	75	0.20	10.0	7.5	0.40	2.0	FRC
0.6%-0.0%	75	0.20	10.0	7.3	0.60	0.0	FRC
0.6%-0.5%	75	0.20	10.0	7.8	0.60	0.5	FRC
0.6%-1.0%	75	0.20	10.0	8.2	0.60	1.0	FRC
0.6%-2.0%	75	0.20	10.0	8.4	0.60	2.0	FRC

Note: 1 kg/m^3 = 0.0624 lb/ft^3.

NF volume (V_{NF}), and B represents the MF volume (V_{MF}). To further illustrate the experimental program, the mixture parameters are included in the lower section of Table 2, detailing the cementitious paste volume (CPV), *w*/*cm*, and MS content. The CPV, expressed as a percentage, refers to the volumetric ratio of cementitious paste relative to the total mixture volume. CPV is a key factor in concrete mixture design as it directly correlates with cement content and the sustainability of the mixture. Table 2 reports the HRWRA dosage used to maintain consistent workability across all mixtures and the variations in V_{NF} and V_{MF}.

Workability test

The workability of the mortar mixtures was determined using a mini-slump cone test.[24] In the mini-slump flow test, the slump was measured as the reduction in height of the fresh mortar after lifting the cone, while the flow diameter was obtained by averaging four equally spaced diameters of the mortar patty. Through HRWRA dosage adjustments, the slump was maintained within a narrow range of 40 to 46 mm (1.57 to 1.81 in.), while the flow diameter was controlled within a narrow range of 160 to 200 mm (6.30 to 7.87 in.). To further evaluate workability and self-leveling ability, the

degree of leveling was calculated from the slump and flow diameter results.[25]

Specimen preparation

Immediately after the workability tests, the mixture was remixed and cast into three 40 mm (1.57 in.) carbon steel cubic molds for compressive strength tests[26] and three 100 x 200 mm (3.94 x 7.87 in.) cylinder molds for indirect tensile tests at a designated curing age of 28 days. Most importantly, to evaluate direct tensile strength, three dumbbell-shaped specimens with dimensions of 60 x 15 x 350 mm (2.36 x 0.59 x 13.8 in.) (30 x 15 x 80 mm [1.18 x 0.59 x 3.15 in.] for the central portion) were cast for each mixture,[2,27] as shown in Fig. 2(a). The dumbbell-shaped mold was modified to provide a smooth transition between the two ends and the central prismatic portion to alleviate potential stress concentrations. In addition, the thickness of the tensile specimen was increased from 12.7 to 15.0 mm (0.5 to 0.6 in.) to accommodate longer fibers and ensure a more uniform fiber distribution.[27] After demolding the next day, all specimens were cured in a water tank at 27 ± 3°C (81 ± 5.4°F).

Compressive strength test and indirect tensile test

In accordance with BS EN 12390-3:2019, compression tests were conducted using a hydraulic servo-controlled machine. During testing, the loading rate was maintained at 0.6 MPa/s (87 psi/s). It is noteworthy that ASTM C39/C39M-21 specifies a loading rate of 0.25 ± 0.05 MPa/s (35 ± 7 psi/s). The compressive strength of each mixture was determined as the average of three specimens cast from the same batch and tested on the same day. To evaluate indirect tensile strength, splitting tensile tests were performed on cylindrical specimens in accordance with BS EN 12390-6:2009. The splitting tensile strength of each mixture was similarly calculated as the average of three specimens cast from the same batch and tested on the same day.

Direct tensile test

Referring to the method developed by the authors' team,[7] direct tensile tests were conducted on dumbbell-shaped specimens, as shown in Fig. 2(b). To mitigate stress concentrations, the two ends of the specimens were wrapped with a thin layer of aluminum plates, and laser calibration was used periodically throughout the preparation process to ensure accurate alignment. A tensile load was applied to both ends of the specimen using a universal testing machine at a constant loading rate of 0.6 mm/min (0.0236 in./min) for all specimens. Beyond the ultimate strain, the loading rate was increased to 3.0 mm/min (0.118 in./min) during the final stage of testing. The loading process continued until the complete fracture of the specimen, during which the tensile strain was recorded.

RESULTS AND DISCUSSION

HRWRA demand and workability

Figure 3 presents photographs of the mortar patties formed after the mini-slump flow tests. For a clearer illustration, the HRWRA dosage required to achieve consistent workability is plotted against V_{MF} at various V_{NF} values in Fig. 4(a). It

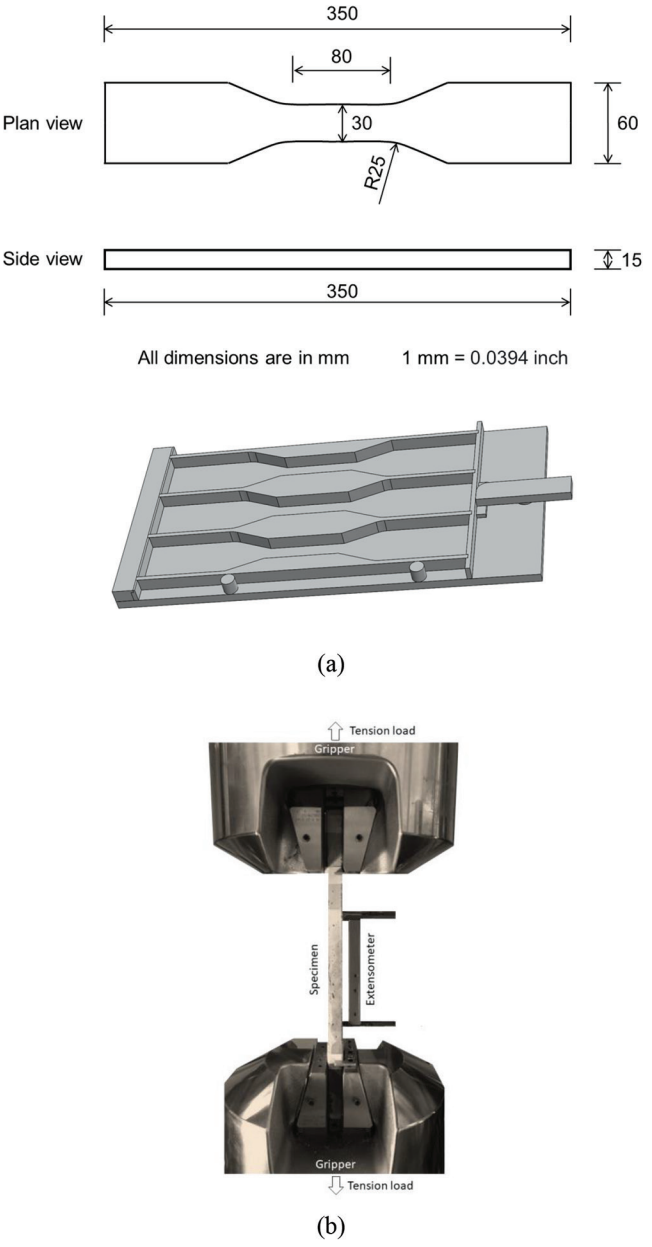

Fig. 2—(a) Sketch of dumbbell tensile specimen; and (b) FRC under direct tension test.

is evident that the HRWRA dosage increased with both V_{MF} and V_{NF}. Notably, the rate of increase in HRWRA dosage for FRC with V_{NF} is significantly higher than that for FRC with V_{MF}. For instance, the HRWRA dosage increased from 4.5 to 4.7% when V_{MF} increased from 0.0 to 0.5%, whereas it increased from 4.5 to 6.4% when V_{NF} increased from 0.0 to 0.4%. This trend is likely attributed to the higher fiber count per unit volume and the larger specific surface area of NF compared to MF. From a particle-packing perspective, NF is more likely to affect nanoparticle packing within the cementitious matrix at the nanoscale, while MF primarily disrupts the packing of sand particles at the microscale.

As a graphical illustration, Fig. 4(b) and Fig. 5(a) depict the variation of slump and flow diameter with V_{NF} at various V_{MF} values. Regarding the slump, the data points in Fig. 4(b) fluctuated within a narrow range of 40 to 46 mm (1.57 to 1.81 in.). Similarly, for the flow diameter, the data points in

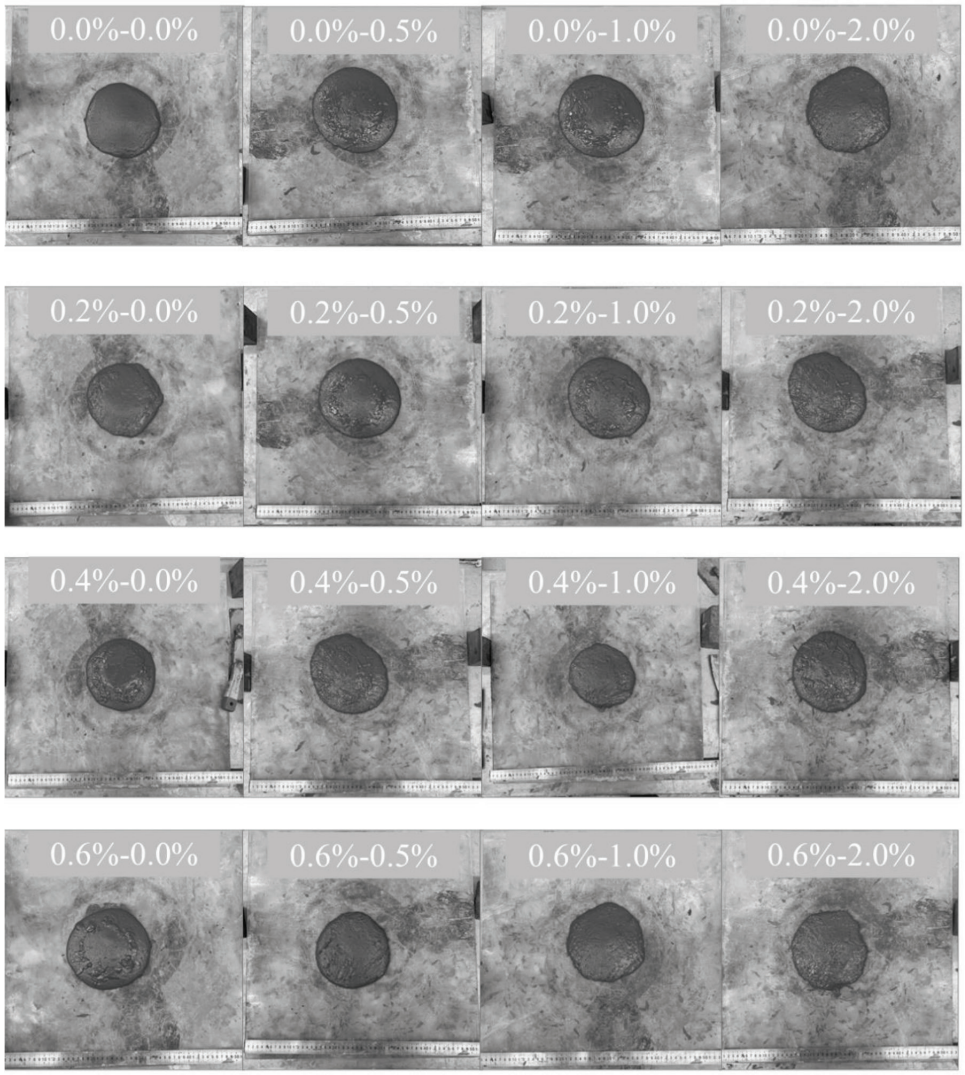

Fig. 3—Photographs of typical mortar patties formed after mini-slump flow tests.

Fig. 5(a) fluctuated within a range of 160 to 200 mm (6.30 to 7.87 in.). Although both the slump and flow diameter varied within a narrow range, the degree of leveling, as shown in Fig. 5(b), exhibited certain notable patterns. The degree of leveling ranged from 0.713 to 0.845, indicating that the mixtures experienced no segregation or fiber balling that could affect flowability.[22] Overall, an optimum NF content appeared to exist for achieving the maximum degree of leveling, beyond which the degree of leveling decreased. Generally, the mixture with V_{MF} = 0.5% and V_{NF} = 0.4% exhibited a slightly higher degree of leveling than both the plain matrix and the mixture containing the maximum NF and MF contents in this study. For instance, the incorporation of NF in mixtures can result in higher viscosity, which in turn enhances resistance to the uneven collapse of the paste microstructure compared to plain mixtures. This phenomenon explains why NF-containing mixtures tend to exhibit a higher degree of leveling.[28]

Compressive strength and indirect tensile strength

Figure 6(a) illustrates the relationship between compressive strength and V_{MF} at various V_{NF} values. The figure reveals an interesting trend, indicating that an optimum V_{NF}—0.4% in this study—exists for achieving the highest compressive strength at a given V_{MF}. For instance, at V_{MF} = 2.0%, the compressive strength increased slightly from 155.5 to 162.9 MPa (22.6 to 23.6 ksi) as V_{NF} increased from 0.0 to 0.4%. However, beyond 0.4% V_{NF}, the strength decreased again to 156.3 MPa (22.7 ksi). This phenomenon can be attributed to the uniform dispersion and effective nanoscale reinforcement provided by NF at low dosages (≤0.4%). However, at higher dosages (>0.4%), NF particles may agglomerate, negatively affecting particle packing and compromising matrix integrity. Moreover, the addition of NF did not alter the failure mode of specimens under compression.

In general, the incorporation of MF consistently enhanced compressive strength across the observed V_{MF} values, as evidenced by the increasing trend of compressive strength with V_{MF}. In addition, the failure mode under compression was notably transformed from brittle failure to ductile failure in the presence of MF, attributed to the fiber-bridging effect. Although not highly pronounced, the strength enhancement can largely be attributed to the confining effect provided by MF.[23] A comparison between the individual addition of

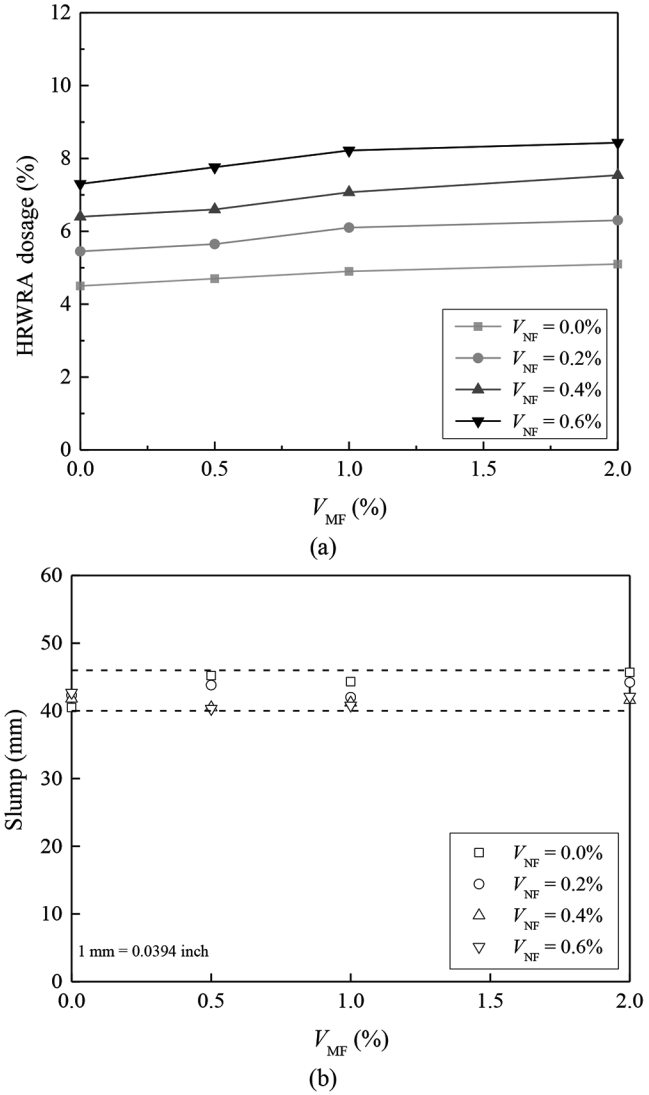

Fig. 4—(a) HRWRA dosage versus V_{MF}*; and (b) slump versus* V_{MF}.

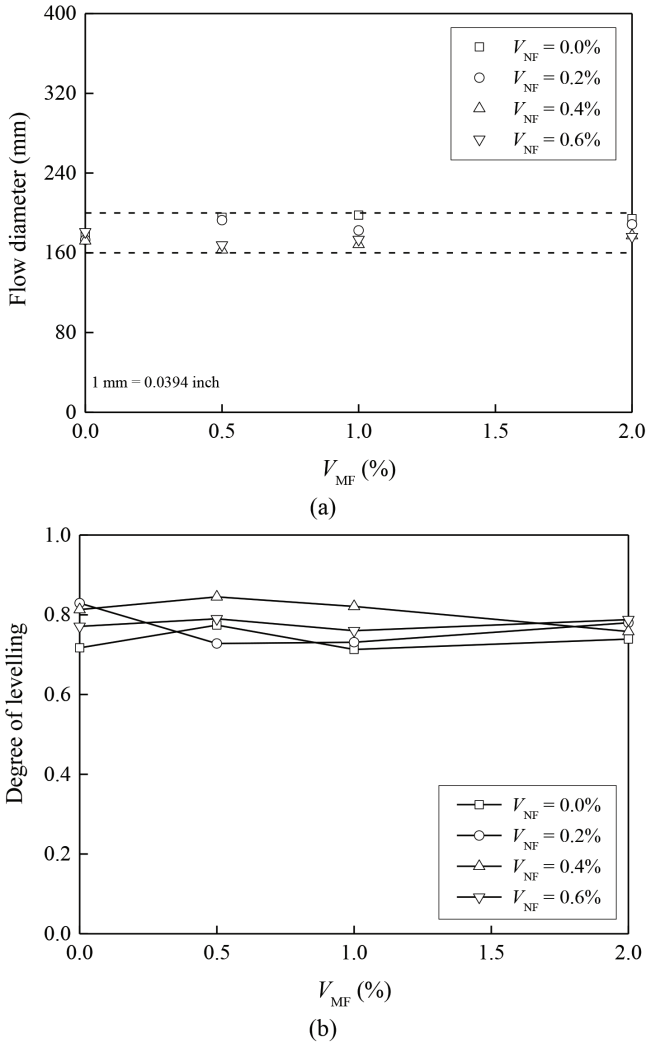

Fig. 5—(a) Flow diameter versus V_{MF}*; and (b) degree of leveling versus* V_{MF}.

0.5% MF and 0.4% NF revealed their similar effectiveness in strength enhancement. However, when NF and MF were used together, the compressive strength increased significantly beyond that achieved by the individual addition of NF or MF, suggesting a synergistic effect between NF and MF, which will be elaborated in the next section.

Figure 6(b) illustrates the indirect tensile strength. The overall trend of indirect tensile strength was similar to that of compressive strength. However, the increase in indirect tensile strength was more pronounced than that of compressive strength, particularly due to the addition of MF. Compared to plain mixtures without fibers, the incorporation of 0.4% NF and 2.0% MF resulted in less than a 10% increase in compressive strength. However, the same combination improved indirect tensile strength by approximately 200%, consistent with findings reported in the literature.[29,30] Additionally, the use of NF enhanced the matrix intrinsically, leading to an increase in indirect tensile strength of up to 50%.

Direct tensile strength and ductility

For strain-hardening FRC (also referred to as engineered cementitious composite [ECC] in certain cases), the post-cracking strength exceeds the first-cracking strength. At the peak tensile stress of the stress-strain curve, the direct tensile strength (ultimate tensile strength) was calculated using Eq. (1)

$$f_t = \frac{F}{A} \tag{1}$$

where f_t is the direct tensile strength; F is the maximum tensile load; and A is the cross-sectional area of the central prismatic portion of the specimen. For each mixture, the direct tensile strengths of three specimens cast from the same batch and tested at the same curing age were averaged to obtain the final tensile strength of the mixture.

Graphically, the direct tensile strengths are plotted against V_{NF} in Fig. 7(a) to illustrate the influence of NF and MF on tensile performance. As shown in Fig. 7(a), an optimum NF content exists for achieving the highest direct tensile strength. For instance, the direct tensile strength increased from 5.33 to 6.40 MPa (0.77 to 0.93 ksi) and then to 6.86 MPa

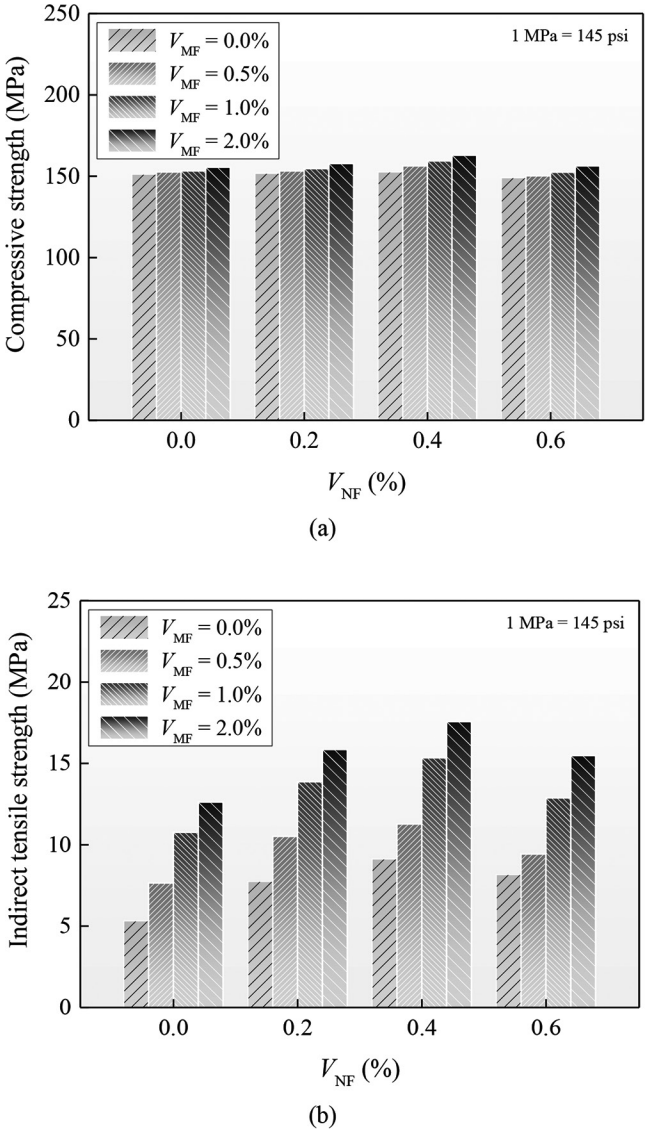

Fig. 6—Mechanical properties: (a) compressive strength; and (b) indirect tensile strength.

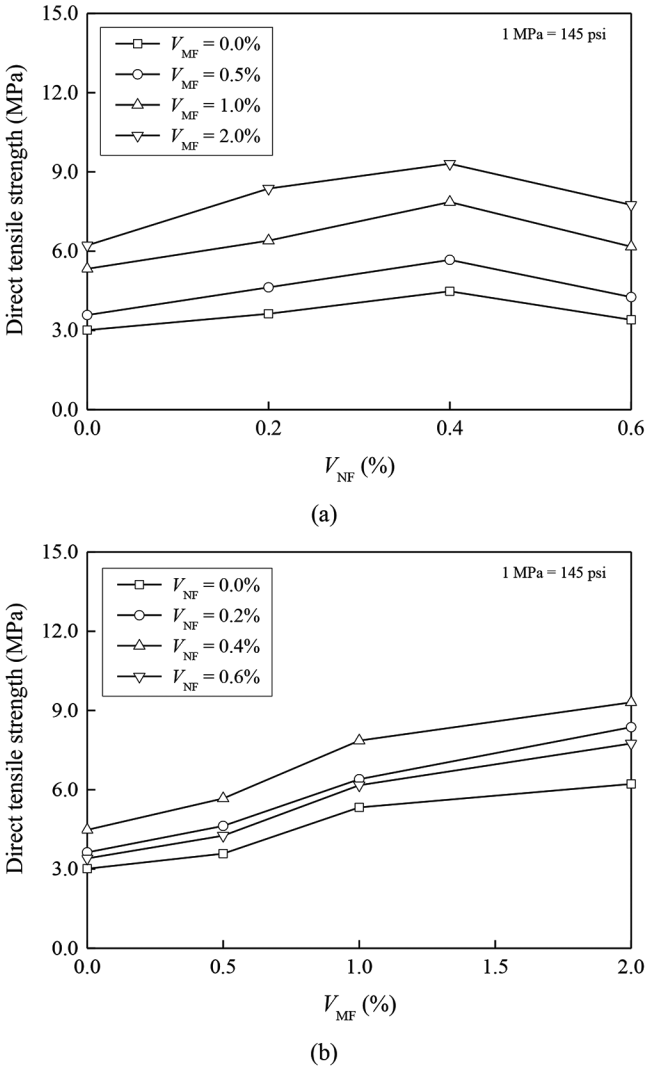

Fig. 7—Direct tensile strength versus: (a) V_{NF}; and (b) V_{MF}.

(0.99 ksi) as V_{NF} increased from 0.0 to 0.2% and then to 0.4%. However, beyond 0.4% V_{NF}, the direct tensile strength decreased to 6.17 MPa (0.89 ksi), resulting in inverted bowl-shaped curves in Fig. 7(a). This phenomenon can be attributed to the intrinsic reinforcement effect of NF, which enhances matrix resistance to tensile loads and bridges nanocracks at relatively low fiber dosages. However, when V_{NF} exceeds a certain threshold (0.4% in this study), the particle packing of cementitious materials may be disrupted,[31] compromising matrix quality and strength. This explains why, macroscopically, the relationship between direct tensile strength and V_{NF} exhibits an inverted bowl shape.

A clear trend demonstrating the beneficial effect of MF on direct tensile strength can be observed in Fig. 7(b). Visually, the most distinct feature of FRC specimens compared to plain concrete specimens under direct tension tests was the change in failure mode from brittle to ductile failure, accompanied by multiple cracking behavior. The attainment of ductile failure mode and multi-cracking behavior is particularly significant for the design and construction of earthquake-resistant concrete structures as well as blast- and impact-resistant structures. Compared to NF, MF was more effective in modifying the failure mode and promoting multiple cracking behavior. This can be largely attributed to the larger dimensions of MF, which are comparable to the size of sand or even aggregate particles (if present), whereas NF, with its smaller dimensions, aligns with the size of binder particles. Reinforcement at the nanoscale contributes to intrinsic tensile strength, whereas reinforcement at the microscale enhances pseudo-ductile tensile performance.

Mechanically, with the increase in V_{MF}, the direct tensile strength increased steadily, regardless of V_{NF}, indicating that with proper mixture design—considering the loosening effect of rigid fibers on particle packing[32]—the addition of steel fibers consistently enhances direct tensile strength through fiber bridging and the confining effect. However, unlike compressive strength, the combined use of NF and MF demonstrated greater effectiveness in improving direct tensile strength. More importantly, the incorporation of 0.4% NF together with 2.0% MF resulted in the largest increase in direct tensile strength, achieving a peak value of 9.31 MPa (1.35 ksi). This tensile strength level could not be attained using either NF or MF alone under the prescribed

experimental conditions, suggesting a synergistic effect between them.

To analyze the effect of the individual and combined use of NF and MF on direct tensile behavior throughout the elastic and post-cracking stages, as well as on tensile strain (ductility), the tensile stress-strain curves are presented in Fig. 8. In Fig. 8, tensile stress-strain curves are shown for four representative scenarios: 1) plain mixture; 2) mixture with only NF; 3) mixture with only MF; and 4) mixture with the combined use of NF and MF. For each scenario, three replicated tensile stress-strain curves are provided to ensure comprehensive data representation. Tensile parameters—such as first-cracking strength, first-cracking strain, ultimate strength, ultimate strain up to 80% of ultimate strength in the descending branch, ultimate strain up to the tensile strength of the corresponding plain mixture, and energy absorption up to 80% of ultimate strength in the descending branch—derived from the tensile stress-strain curves in Fig. 8, are reported in Table 3. The results indicate that, compared to the plain mixture without fibers, the individual use of NF increased tensile strength but did not alter the failure mode from brittle to ductile failure, suggesting that NF effectively enhanced the intrinsic tensile strength of the matrix through extensive and uniform nanoscale reinforcement.

The individual use of MF transformed the failure mode from brittle failure in the plain mixture to ductile failure in FRC, significantly enhancing tensile strain capacity and energy absorption. More importantly, the combined use of NF and MF further increased tensile strength, tensile strain capacity, and energy absorption. This improvement can be attributed to both multiscale reinforcement and the strengthening of the matrix, which enhances its intrinsic tensile strength. The increase in energy absorption—approximately 50 to 60 times higher than that of the plain mixture—demonstrates its potential for earthquake-resistant and blast- or impact-resistant concrete structures.

SYNERGY BETWEEN NF AND MF ON DIRECT TENSILE STRENGTH

The results presented in the previous section indicate a potential synergy between NF and MF in terms of direct tensile strength, contributing to the development of MSFRC with high intrinsic tensile strength. To further explore this potential synergy, a systematic quantitative evaluation is presented in the following section. First, it is essential to determine the individual contributions of NF and MF at various volume fractions in enhancing direct tensile strength. Although both NF and MF positively influence direct tensile strength, their effectiveness varies. Specifically, at a given V_{NF} or V_{MF}, the individual impact of incorporating MF or NF must be quantified. The individual effects of NF and MF will be assessed in comparison to their combined effect on direct tensile strength, providing insight into possible synergistic interactions between the two fiber types. To achieve this, the percentage increases in direct tensile strength resulting from the inclusion of NF and/or MF are tabulated in Table 4. Table 4 presents the percentage increases in direct tensile strength due to MF incorporation at a given V_{NF} (rows 3 to 14) and NF incorporation at a given V_{MF} (rows 15 to 26).

The increase in direct tensile strength induced by the same amount of MF as NF generally showed an increasing trend with rising V_{NF}. For instance, the incorporation of 0.5%, 1.0%, and 2.0% MF by volume resulted in 18.9%, 77.1%, and 106.6% increases in direct tensile strength at V_{NF} = 0.0%, whereas the corresponding increases at V_{NF} = 0.2% were 27.5%, 76.3%, and 130.6%, and at V_{NF} = 0.4%, they were 26.6%, 75.4%, and 107.8%, respectively. These results suggest that MF was generally more effective in enhancing direct tensile strength at higher V_{NF}. Conversely, the incorporation of NF up to a certain volume fraction at increasing V_{MF} also led to larger percentage increases in direct tensile strength. For example, adding 0.2% NF resulted in increases of 20.6%, 29.3%, 20.1%, and 34.6% in direct tensile strength at V_{MF} = 0.0%, 0.5%, 1.0%, and 2.0%, respectively. However,

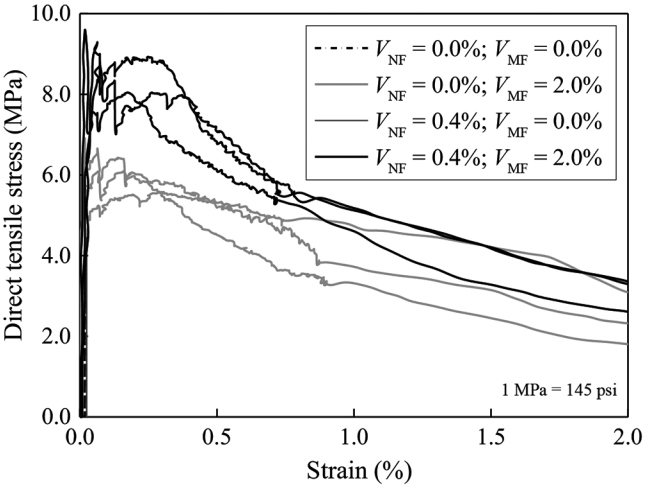

Fig. 8—Tensile stress-strain curves for plain mixture, mixtures with individual use of NF and MF, and mixtures with combined use of NF and MF.

Table 3—Direct tensile performance

Mixture No. (V_{NF}-V_{MF})	First-cracking strength, MPa	First-cracking strain	Ultimate strength, MPa	Ultimate strain*	Ultimate strain†	Energy absorption, N·m
0.0%-0.0%	3.01	0.00018	3.01	0.00018	0.00018	0.06
0.0%-2.0%	5.57	0.00019	6.22	0.00603	0.01552	3.16
0.4%-0.0%	4.48	0.00025	4.48	0.00025	0.00025	0.12
0.4%-2.0%	9.18	0.00048	9.31	0.00370	0.02012	3.55

*Ultimate strain up to 80% of ultimate strength at descending branch.

†Ultimate strain up to tensile strength of corresponding plain mixture.

Note: Each result was averaged from triplicated results; for plain mixture, assume all strains coincide with failure strain; 1 MPa = 145 psi; 1 N·m = 0.7376 ft·lb.

Table 4—Synergistic effect of NF and MF on direct tensile strength

Percentage increase in direct tensile strength	
Adding	Percentage increase, %
0.5% MF at 0.0% NF	18.9
0.5% MF at 0.2% NF	27.5
0.5% MF at 0.4% NF	26.6
0.5% MF at 0.6% NF	25.3
1.0% MF at 0.0% NF	77.1
1.0% MF at 0.2% NF	76.3
1.0% MF at 0.4% NF	75.4
1.0% MF at 0.6% NF	81.5
2.0% MF at 0.0% NF	106.6
2.0% MF at 0.2% NF	130.6
2.0% MF at 0.4% NF	107.8
2.0% MF at 0.6% NF	127.9
0.2% NF at 0.0% MF	20.6
0.2% NF at 0.5% MF	29.3
0.2% NF at 1.0% MF	20.1
0.2% NF at 2.0% MF	34.6
0.4% NF at 0.0% MF	48.8
0.4% NF at 0.5% MF	58.4
0.4% NF at 1.0% MF	47.5
0.4% NF at 2.0% MF	49.7
0.6% NF at 0.0% MF	13.0
0.6% NF at 0.5% MF	19.0
0.6% NF at 1.0% MF	15.8
0.6% NF at 2.0% MF	24.6

Synergistic effects of NF and MF		
Mixture No.	Percentage increase, %	Synergistic effect, %
0.2% NF + 0.5% MF	53.8	14.3
0.2% NF + 1.0% MF	112.6	14.9
0.2% NF + 2.0% MF	178.1	50.8
0.4% NF + 0.5% MF	88.4	20.6
0.4% NF + 1.0% MF	161.1	35.3
0.4% NF + 2.0% MF	209.3	53.9
0.6% NF + 0.5% MF	41.5	9.6
0.6% NF + 1.0% MF	105.0	8.9
0.6% NF + 2.0% MF	157.5	37.9

when V_{NF} exceeded 0.4%, a decline in percentage increases was observed, with values of 13.0%, 19.0%, 15.8%, and 24.6% at V_{MF} = 0.0%, 0.5%, 1.0%, and 2.0%, respectively. These observations indicate that the effectiveness of NF in enhancing direct tensile strength became more pronounced in the presence of increasing amounts of MF, regardless of V_{NF}. Therefore, it can be concluded that the effectiveness of NF and MF in enhancing direct tensile strength is synergistic, with their combined effect being greater than the sum of their individual effects.

To facilitate comparison and demonstrate the synergistic effect of NF and MF, the percentage increases in direct tensile strength resulting from the addition of both fibers are presented in the lower section of Table 4, relative to the direct tensile strength of the plain matrix. The combined use of NF and MF in various combinations resulted in a synergistic effect, as evidenced by the greater percentage increases in direct tensile strength compared to the sum of the percentage increases from the individual additions of NF and MF. For instance, the mixture containing 0.2% NF and 1.0% MF exhibited a 112.6% increase in direct tensile strength compared to the mixture containing 0.0% NF and 0.0% MF. This increase exceeded the sum of the percentage increase induced by adding 0.2% NF at 0.0% MF (20.6%) and the percentage increase induced by adding 1.0% MF at 0.0% NF (77.1%). Similarly, for the mixture containing 0.4% NF and 2.0% MF, the direct tensile strength was 209.3% higher than the plain matrix. Notably, this value of 209.3% exceeded the sum of the percentage increases induced by adding 0.4% NF at 2.0% MF (48.8%) and 2.0% MF at 0.0% NF (106.6%). These results confirm the synergistic effect of combining NF and MF in enhancing direct tensile strength.

The spillover values of 112.6% – (20.6% + 77.1%) = 14.9% and 209.3% – (48.8% + 106.6%) = 53.9% demonstrate the synergistic effect of NF and MF on direct tensile strength. To quantify this effect, the additional percentage increases in direct tensile strength resulting from the combined use of NF and MF, after subtracting the percentage increases due to their individual effects, were adopted as a quantitative measure of the synergistic effect.[33] Table 4 presents the calculated values for all mixtures containing both NF and MF. Overall, for mixtures incorporating NF ≥ 0.2% and MF ≥ 2.0%, the values of the synergistic effect exceeded 37.9% and reached as high as 53.9%. These values are significant and highlight the potential for developing high-tensile-strength MSFRC by leveraging the synergistic effect between NF and MF. The underlying mechanism behind this effect will be discussed in the next section.

FURTHER DISCUSSION

Qualitative cost-benefit analysis

Cost-benefit analysis is a valuable tool in materials design, providing designers and decision-makers with insights to strike a balance or achieve optimization between investment and potential benefits. In this study, the negative aspect of adding NF and MF is that it generally reduces workability, necessitating the increased use of HRWRA to compensate for this loss, thereby raising material costs. On the positive side, the incorporation of NF and MF enhances strength. As a result, evaluating the overall benefits of adding NF and MF is not straightforward. To indirectly assess the cost-benefit performance, the envelope of direct tensile strength against HRWRA dosage is depicted in Fig. 9. This analysis emphasizes the material cost associated with increased HRWRA demand. In Fig. 9, the data points along the same black lines and the same gray lines represent mixtures with the same V_{NF} and V_{MF}, respectively.

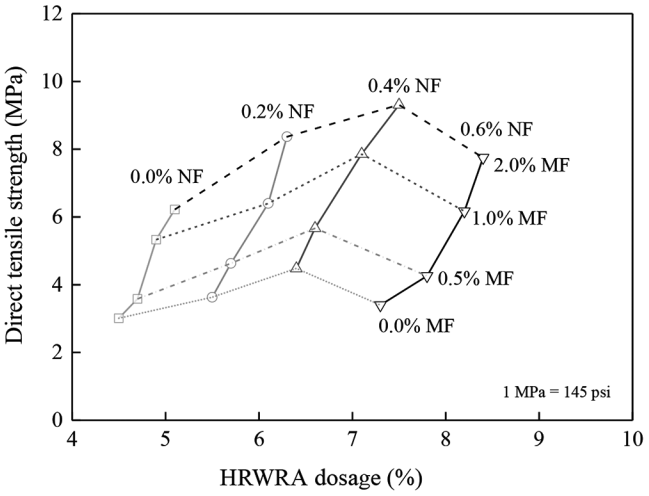

Fig. 9—Envelope of direct tensile strength and HRWRA dosage.

From the envelope in Fig. 9, it can be inferred that, at the same HRWRA dosage, the direct tensile strength increased significantly with V_{MF}, as evidenced by the relative positions of the of the dashed curves representing 0.0%, 0.5%, 1.0%, and 2.0% MF. Although adding either NF or MF increased HRWRA demand, mixtures that achieved both high direct tensile strength and low HRWRA dosage were primarily those incorporating both NF and MF (with the moisture content of QS kept constant). The plain matrix, which required the least HRWRA demand, exhibited relatively lower direct tensile strength, measuring 68% lower than the highest direct tensile strength attained in this study. In addition, the highest direct tensile strength was observed in the mixture containing 0.4% NF and 2.0% MF. However, the HRWRA demand for this mixture was 11% lower than that of the mixture with the highest HRWRA demand, indicating a promising trend that high direct tensile strength and low HRWRA demand can be achieved simultaneously.

Another important observation from this study is that the use of a very small amount of low-cost mineral NFs not only enhances the intrinsic tensile strength of the matrix but also improves the overall performance of FRC at a low cost. For instance, the direct tensile strength of FRC with only 1.0% MF by volume increased from 5.33 to 6.22 MPa (0.77 to 0.90 ksi) when the MF volume was increased from 1.0 to 2.0%. However, instead of adding an additional 1.0% MF, incorporating a small volume (0.2%) of low-cost mineral NF into FRC with 1.0% MF also increased the tensile strength from 5.33 to 6.40 MPa (0.77 to 0.93 ksi). This suggests that 1.0% MFs can be reduced, while only 0.2% mineral NFs are needed to achieve a similar direct tensile strength, resulting in material savings. Notably, this trend was also observed in indirect tensile strength. In summary, using NFs to reinforce the matrix and enhance intrinsic tensile strength is cost-effective and demonstrates promising potential for practical construction applications.

Mechanisms behind

Considering the aforementioned findings, the mechanisms behind the synergy between NF and MF merit in-depth exploration. The beneficial effects of NF and MF on strength development can be attributed to the following factors. First, nanoscale cracks form in the plain matrix when subjected to tensile loading beyond the elastic stage. The presence of NF helps arrest these nanoscale cracks and prolong the elastic stage, thereby enhancing tensile performance. Second, nanoscale cracks eventually localize into microcracks, where NF alone exhibits limited effectiveness. This transition is marked by the first drop in the tensile stress-strain curve, at which point the stress is defined as the first-cracking strength.[7]

Third, MF played a reinforcing role in strengthening the nanofiber-reinforced matrix (NFRC) through its fiber-bridging effect. When a microcrack formed, the stress in the surrounding matrix dropped to zero, while the stress was transferred to the adjacent matrix through MFs. If the overall bond force of MF within the NF-reinforced matrix were sufficient to enable effective load transfer without sudden failure, another microcrack would form once the tensile stress exceeded the strength of the NF-reinforced matrix—a process known as strain hardening.[34] During this process, both NF and MF contributed to the reinforcement mechanism, operating at the nanoscale and microscale to enhance the tensile performance of MSFRC. In fact, the effectiveness of combining other types of NFs and MFs has been reported in the literature,[35,36] further supporting this mechanism. Thus, it is recommended that NF be used in conjunction with MF, and vice versa, to maximize synergistic reinforcement effects.

An important issue arising from the use of fibers, particularly the combined use of NF and MF, is particle packing, as elongated particles are incompatible with spherical and quasi-spherical particles at different scales within the mixture. The needle-like particles, being smaller in size but having a larger aspect ratio, and the rod-like particles, being larger in size but having a smaller aspect ratio, exert different influences on particle packing. It is conceived that aggregate particles, including sand particles, mix with rod-like MFs or even macrofibers, forming a fiber-aggregate skeleton (FAS). Meanwhile, the cementitious particles and fillers combine with needle-like NFs, forming an NFRC, which fills the voids within the FAS. These two processes involve the loosening effect of fibers on particle packing, which must be actively controlled.[37] At the nanoscale, an adverse effect may occur when excessive NF is incorporated, as evidenced by a drop in both compressive strength and direct tensile strength at V_{NF} = 0.6%. At the microscale, when the geometric mean size ratio of aggregate/sand particles to fiber diameter falls below a threshold prescribed by the cubic root of a constant divided by the aspect ratio,[37] the packing of the mixture remains largely unaffected, which is consistent with the findings of this study.

CONCLUSIONS

Nanofibers (NFs), composed of nanoscale hydrated magnesium aluminosilicate materials with high corrosion resistance, reinforce the matrix at the nanoscale, while microfibers (MFs) are widely used in the development of high- or ultra-high-performance concrete (UHPC)/fiber-reinforced

concrete (FRC) (UHPFRC). In this study, a total of 16 plain, FRC, and multiscale FRC (MSFRC) mixtures with varying V_{NF} and V_{MF} were produced to develop intrinsically high-tensile-strength MSFRC and explore the potential synergy between NF and MF. Workability and mechanical strengths were consistently evaluated for all mixtures. In addition to the cost-benefit analysis, both qualitative and quantitative analyses were conducted to investigate the synergy between NF and MF. The underlying mechanisms of the observed synergistic effects were examined from a multiscale perspective. Based on these findings, the following conclusions were drawn:

1. The high-range water-reducing admixture (HRWRA) demand required to maintain consistent workability increased with both NF volume (V_{NF}) and MF volume (V_{MF}) due to the intensifying fiber entanglement effect. Additionally, a slight increase in compressive strength was observed with the addition of NF and MF.

2. The individual use of NF up to 0.6% and MF up to 2.0% by volume improved direct tensile strength by 13% and 107%, respectively. However, when NF and MF were used together, the direct tensile strength increased by 209%, which was significantly higher than their individual contributions.

3. Analysis revealed that the effectiveness of NF and MF in enhancing direct tensile strength became more pronounced when used in increasing amounts of the other fiber type. Consequently, the combined use of NF and MF resulted in significantly greater percentage increases in strength than the sum of their individual contributions.

4. The synergistic effect of NF and MF on direct tensile strength, quantified as the additional increase due to their combined use, reached as high as 53.8%. This beneficial effect demonstrates great potential and practical value in the development of intrinsically high-tensile-strength MSFRC.

5. Cost-benefit analysis indicated that the mixture containing 0.4% NF and 2.0% MF achieved the highest direct tensile strength. Additionally, the effectiveness of incorporating a low dosage of NF (for example, 0.2%) into FRC for enhanced tensile strength was found to be equivalent to doubling the MF volume.

The synergy between NF and MF arises from their ability to reinforce the matrix simultaneously at both the nanoscale and microscale. This synergistic effect has the potential to enhance other performance attributes, including reinforcing bar bond strength, tensile strength, shear and torsional strength, crack resistance, and blast and impact resistance. Further research is highly recommended to advance the development of sustainable MSFRC from a material perspective and to establish micromechanical models from a mechanical perspective.

AUTHOR BIO

ACI member **S. H. Chu** *serves as a Principal Investigator endowed by Vice-President for Research at Columbia University, New York, NY. He was educated and trained at various universities, including The University of Hong Kong, Pokfulam, Hong Kong; the University of Cambridge, Cambridge, UK; Nanyang Technological University, Singapore; and The Chinese University of Hong Kong, Shatin, New Territories, Hong Kong. He is a member of ACI Committees 239, Ultra-High-Performance Concrete, and 544, Fiber Reinforced Concrete. His research interests include sustainable, intelligent, and resilient infrastructure and structural engineering.*

ACKNOWLEDGMENTS

The author would like to express gratitude to The University of Hong Kong and the University of Cambridge for their support and resources. Insightful discussions with S. P. Shah and A. E. Naaman are also sincerely appreciated.

DATA AVAILABILITY STATEMENT

All data, models, and code generated or used during the study appear in the submitted paper.

REFERENCES

1. Gopalaratnam, V. S.; Shah, S. P.; Batson, G. B.; Criswell, M. E.; Ramakrishnan, V.; and Wecharatana, M., "Fracture Toughness of Fiber Reinforced Concrete," *ACI Materials Journal*, V. 88, No. 4, July-Aug. 1991, pp. 339-353.

2. Li, J.; Weng, J.; and Yang, E. H., "Stochastic Model of Tensile Behavior of Strain-Hardening Cementitious Composites (SHCCs)," *Cement and Concrete Research*, V. 124, Oct. 2019, Article No. 105856.

3. Boulekbache, B.; Hamrat, M.; Chemrouk, M.; and Amziane, S., "Flexural Behaviour of Steel Fibre-Reinforced Concrete Under Cyclic Loading," *Construction and Building Materials*, V. 126, Nov. 2016, pp. 253-262.

4. Chu, S. H.; Li, L. G.; and Kwan, A. K. H., "Fibre Factors Governing the Fresh and Hardened Properties of Steel FRC," *Construction and Building Materials*, V. 186, Oct. 2018, pp. 1228-1238.

5. Chu, S. H., and Kwan, A. K. H., "A New Method for Pull Out Test of Reinforcing Bars in Plain and Fibre Reinforced Concrete," *Engineering Structures*, V. 164, June 2018, pp. 82-91.

6. Chu, S. H., and Kwan, A. K. H., "A New Bond Model for Reinforcing Bars in Steel Fiber Reinforced Concrete," *Cement and Concrete Composites*, V. 104, Nov. 2019, Article No. 103405.

7. Kwan, A. K. H., and Chu, S. H., "Direct Tension Behaviour of Steel Fibre Reinforced Concrete Measured by a New Test Method," *Engineering Structures*, V. 176, Dec. 2018, pp. 324-336.

8. Leung, C. K. Y.; Zhang, X.; and Xia, Q., "The Application of Pseudo-Ductile Cementitious Composites in the Anchorage Zone of Post-Tensioned Concrete Members," *Materials and Structures*, V. 42, No. 9, Nov. 2009, pp. 1221-1231.

9. Yoo, D.-Y.; Yoon, Y-S.; and Banthia, N., "Predicting the Post-Cracking Behavior of Normal- and High-Strength Steel-Fiber-Reinforced Concrete Beams," *Construction and Building Materials*, V. 93, Sept. 2015, pp. 477-485.

10. Zhang, D.; Yu, J.; Wu, H.; Jaworska, B.; Ellis, B. R.; and Li, V. C., "Discontinuous Micro-Fibers as Intrinsic Reinforcement for Ductile Engineered Cementitious Composites (ECC)," *Composites Part B: Engineering*, V. 184, Mar. 2020, Article No. 107741.

11. Teng, L.; Zhu, J.; Khayat, K. H.; and Liu, J., "Effect of Welan Gum and Nanoclay on Thixotropy of UHPC," *Cement and Concrete Research*, V. 138, Dec. 2020, Article No. 106238.

12. Muhd Norhasri, M. S.; Hamidah, M. S.; and Mohd Fadzil, A., "Inclusion of Nano Metaclayed as Additive in Ultra High Performance Concrete (UHPC)," *Construction and Building Materials*, V. 201, Mar. 2019, pp. 590-598.

13. Arunothayan, A. R.; Nematollahi, B.; Khayat, K. H.; Ramesh, A.; and Sanjayan, J. G., "Rheological Characterization of Ultra-High Performance Concrete for 3D Printing," *Cement and Concrete Composites*, V. 136, Feb. 2023, Article No. 104854.

14. Muhd Norhasri, M. S.; Hamidah, M. S.; Mohd Fadzil, A.; and Mohd Faizal, M. J., "Characteristic and Strength Properties of Nano Metaclayed UHPC," *InCIEC 2015: Proceedings of the International Civil and Infrastructure Engineering Conference*, M. Yusoff, N. H. A. Hamid, M. F. Arshad, A. K. Arshad, A. R. M. Ridzuan, and H. Awang, eds., Springer, Singapore, 2016, pp. 689-697.

15. Irshidat, M. R., and Al-Saleh, M. H., "Thermal Performance and Fire Resistance of Nanoclay Modified Cementitious Materials," *Construction and Building Materials*, V. 159, Jan. 2018, pp. 213-219.

16. Mohd Faizal, M. J.; Hamidah, M. S.; and Muhd Norhasri, M. S., "Strength and Chloride Content of Nanoclayed Ultra-High Performance Concrete," *Proceeding on Structure, Materials and Construction Engineering Conference (CONS ENG'14)*, Istanbul, Turkey, 2014, pp. 99-111.

17. Mohd Faizal, M. J.; Hamidah, M. S.; Muhd Norhasri, M. S.; Noorli, I.; and Mohamad Ezad Hafez, M. P., "Chloride Permeability of Nanoclayed Ultra-High Performance Concrete," *InCIEC 2014: Proceedings of the International Civil and Infrastructure Engineering Conference*

2014, R. Hassan, M. Yusoff, A. Alisibramulisi, N. M. Amin, and Z. Ismail, eds., Springer, Singapore, 2015, pp. 613-623.

18. Mohd Faizal, M. J.; Hamidah, M. S.; Muhd Norhasri, M. S.; and Noorli, I., "Effect of Clay as a Nanomaterial on Corrosion Potential of Steel Reinforcement Embedded in Ultra-High Performance Concrete," *InCIEC 2015: Proceedings of the International Civil and Infrastructure Engineering Conference*, M. Yusoff, N. H. A. Hamid, M. F. Arshad, A. K. Arshad, A. R. M. Ridzuan, and H. Awang, eds., Springer, Singapore, 2016, pp. 679-687.

19. Hamed, N.; El-Feky, M. S.; Kohail, M.; and Nasr, E.-S. A. R., "Effect of Nano-Clay De-agglomeration on Mechanical Properties of Concrete," *Construction and Building Materials*, V. 205, Apr. 2019, pp. 245-256.

20. Morsy, M. S.; Alsayed, S. H.; and Aqel, M., "Hybrid Effect of Carbon Nanotube and Nano-Clay on Physico-Mechanical Properties of Cement Mortar," *Construction and Building Materials*, V. 25, No. 1, Jan. 2011, pp. 145-149.

21. Yoo, D.-Y.; Oh, T.; and Banthia, N., "Nanomaterials in Ultra-High-Performance Concrete (UHPC) – A Review," *Cement and Concrete Composites*, V. 134, Nov. 2022, Article No. 104730.

22. Wille, K.; El-Tawil, S.; and Naaman, A. E., "Properties of Strain Hardening Ultra High Performance Fiber Reinforced Concrete (UHP-FRC) Under Direct Tensile Loading," *Cement and Concrete Composites*, V. 48, Apr. 2014, pp. 53-66.

23. Chu, A. S. H., "Volume-Based Concrete Mixture Design," *ACI Materials Journal*, V. 120, No. 1, Jan. 2023, pp. 243-255.

24. Chu, S. H.; Ye, H.; Huang, L.; and Li, L. G., "Carbon Fiber Reinforced Geopolymer (FRG) Mix Design Based on Liquid Film Thickness," *Construction and Building Materials*, V. 269, Feb. 2021, Article No. 121278.

25. Chu, S. H., and Kwan, A. K. H., "Co-addition of Metakaolin and Silica Fume in Mortar: Effects and Advantages," *Construction and Building Materials*, V. 197, Feb. 2019, pp. 716-724.

26. EN 1015-11/A1:2019, "Methods of Test for Mortar for Masonry - Part 11: Determination of Flexural and Compressive Strength of Hardened Mortar," European Committee for Standardization, Brussels, Belgium, 2019.

27. Boughanem, S.; Jesson, D. A.; Mulheron, M. J.; Smith, P. A.; Eddie, C.; Psomas, S.; and Rimes, M., "Tensile Characterisation of Thick Sections of Engineered Cement Composite (ECC) Materials," *Journal of Materials Science*, V. 50, No. 2, Jan. 2015, pp. 882-897.

28. Chu, S. H.; Yang, E. H.; and Unluer, C., "Development of Nanofiber Reinforced Reactive Magnesia-Based Composites for 3D Printing," *Construction and Building Materials*, V. 366, Feb. 2023, Article No. 130270.

29. Shafieifar, M.; Farzad, M.; and Azizinamini, A., "Experimental and Numerical Study on Mechanical Properties of Ultra High Performance Concrete (UHPC)," *Construction and Building Materials*, V. 156, Dec. 2017, pp. 402-411.

30. Song, P. S., and Hwang, S., "Mechanical Properties of High-Strength Steel Fiber-Reinforced Concrete," *Construction and Building Materials*, V. 18, No. 9, Nov. 2004, pp. 669-673.

31. Chu, S. H.; Lam, W. L.; Li, L.; and Poon, C. S., "Packing Density of Ternary Cementitious Particles Based on Wet Packing Method," *Powder Technology*, V. 405, June 2022, Article No. 117493.

32. Chu, S. H.; Jiang, Y.; and Kwan, A. K. H., "Effect of Rigid Fibres on Aggregate Packing," *Construction and Building Materials*, V. 224, Nov. 2019, pp. 326-335.

33. Chu, S. H.; Khan, M.; Deng, X.; and Unluer, C., "Bio-Inspired Self-Prestressing Concrete (SPC) Involving Basalt Fibers and Expansive Agent," *Cement and Concrete Research*, V. 155, May 2022, Article No. 106735.

34. Li, V. C., and Wu, H.-C., "Conditions for Pseudo Strain-Hardening in Fiber Reinforced Brittle Matrix Composites," *Applied Mechanics Reviews*, V. 45, No. 8, Aug. 1992, pp. 390-398.

35. Rodriguez, A. J.; Guzman, M. E.; Lim, C.-S.; and Minaie, B., "Mechanical Properties of Carbon Nanofiber/Fiber-Reinforced Hierarchical Polymer Composites Manufactured with Multiscale-Reinforcement Fabrics," *Carbon*, V. 49, No. 3, Mar. 2011, pp. 937-948.

36. Martins, A.; Pinho, E. D.; Correlo, V. M.; Faria, S.; Marques, A. P.; Reis, R. L.; and Neves, N. M., "Biodegradable Nanofibers-Reinforced Microfibrous Composite Scaffolds for Bone Tissue Engineering," *Tissue Engineering Part A*, V. 16, No. 12, Dec. 2010, pp. 3599-3609.

37. Bandelt, M. J.; Frank, T. E.; Lepech, M. D.; and Billington, S. L., "Bond Behavior and Interface Modeling of Reinforced High-Performance Fiber-Reinforced Cementitious Composites," *Cement and Concrete Composites*, V. 83, Oct. 2017, pp. 188-201.

ACI MATERIALS JOURNAL TECHNICAL PAPER

Title No. 122-M13

Tensile Properties of Polypropylene and Polyethylene Terephthalate Fiber Bundles in Outdoor Thermal Environment

by Zihao Shen and Wenguang Liu

To constitute an alternative to ordinary fiber-reinforced polymer in the strengthening of existing structures, the tensile properties of polypropylene (PP) and polyethylene terephthalate (PET) fiber bundles in outdoor thermal environments (80 and 105°C) were investigated. The fiber bundles were carefully removed from a woven textile, and test specimens with a gauge length of 25 mm were fabricated. Based on the experiments, a Weibull distribution model of the tensile strength of the PP and PET fiber bundles was developed. Test results show that exposure temperature and time significantly affect the tensile strength, rupture strain, and elastic modulus of the PP and PET fiber bundles. The strength degradation of PP and PET fiber bundles is not obvious when exposed to 80°C. In contrast, when exposed to 105°C, their use requires consideration of mechanical properties' degradation. This study provides exact data for the use of PP and PET fiber bundles in outdoor thermal environments.

Keywords: high temperature; polyethylene terephthalate (PET); polypropylene (PP); tensile properties.

INTRODUCTION

Polypropylene (PP) and polyethylene terephthalate (PET) are the most versatile polymers due to a combination of low cost and good mechanical and physical properties.[1,2] Their applications have been extended to nearly every aspect of human daily life, such as PP pipes and PET bottles. Because of the stable chemical molecular structure of PP and PET, some harsh environments such as acid or base solutions have little effect on their mechanical properties,[3,4] reflecting a strong environmental adaptability and commercial value. One of the most common applications in the construction field is to make these polymers into fibers, taking full advantage of their mechanical properties.[5] When PP or PET fibers are added to concrete as an additive, most studies have reportedly been able to prevent concrete from spalling in large quantities during fires,[6-8] which creates a network more permeable than the cement matrix. In addition to adding short fibers to concrete, the application of long continuous fibers impregnated with resin can also be used as a reliable structural material for external strengthening and confining applications of reinforced concrete (RC) structures.[9-11] Several studies have confirmed the feasibility of using large-rupture-strain fibers to enhance the seismic performance of RC column members. These measurements undoubtedly protect people's safety.

The use of fibers with large rupture strain has already been further studied and developed in civil engineering as an alternative to conventional fibers (for example, carbon and glass fibers). Although the tensile strength of conventional fibers is much higher than that of PP and PET fibers, the rupture strain of conventional fibers is generally less than 3%,[12-14] which lacks the capacity to consume energy in natural disasters. However, it was reported that the tensile strength of PET fiber bundles was between those of steel and conventional fiber bundles and that the tensile strength increased with increasing the strain rate.[15] In fact, the elongation of PP fibers is 20 to 25%, whereas that of PET fibers is within 15%. These desirable properties offer an economical and ductile solution for structural safety. PP and PET fibers have a higher rupture strain than conventional fibers, making the former suitable for use in areas with high ductility demand. To understand the mechanical behavior of PP/PET-strengthened RC structures, it is imperative to investigate the mechanical properties of PP and PET fiber bundles in outdoor thermal environments, which commonly occur during service life events.

Therefore, this study is the first investigation of the tensile properties of PP and PET fiber bundles in outdoor thermal environments. The variables include exposure temperature (80 and 105°C) and exposure time (1 and 5 hours). The effects of such parameters on the major mechanical characteristics of stress-strain curves are investigated—notably, the tensile strength, rupture strain, elastic modulus, and process of yielding. Furthermore, a Weibull distribution model of the tensile strength is constructed based on test data, and the corresponding constitutive model is proposed.

RESEARCH SIGNIFICANCE

According to the foregoing review, the application of PP and PET fiber bundles in civil engineering will provide an economical and ductile seismic reinforcement solution. The limited literature reported the working properties of PP and PET fiber bundles, but a better understanding of the tensile properties at thermal service temperatures is essential. The authors believe that these large-rupture-strain fiber materials have great potential in the field of seismic reinforcement.

ACI Materials Journal, V. 122, No. 3, May 2025.

MS No. M-2022-267.R1, doi: 10.14359/51746711, received February 16, 2023, and reviewed under Institute publication policies.

EXPERIMENTAL INVESTIGATION

Specimen characteristics

A total of 44 fiber bundles cut from PP and PET woven textiles were prepared and tested under tensile axial loads. The PP and PET fabrics were braided with warp and weft yarns, and there were no significant differences in their appearance. The PP fabric had a waxy feel to the touch, whereas the PET fabric felt soft. The specifications of the PP and PET woven textiles were 230 and 625 g/m^3, respectively.

The preparation process for the test specimens was similar to that adopted by Bai et al.[15,16] Continuous fiber bundles of 1800 mm in length were carefully extracted from the PP and PET fabrics, and the linear density was calculated by dividing the weight by the length. The cross-sectional area of a fiber bundle was determined by dividing the linear density by the bulk density, which was also the approach adopted by Bai et al.[15,16] In this study, the bulk density was measured instead of directly using the manufacturer's data. The test method to obtain the bulk density is described in the following section. A small fiber bun with a length of 200 mm was cut from an 1800 mm long fiber bundle to fabricate the test specimens. To avoid stress concentration and improve the stress transfer of the test specimens, aluminum alloy sheets (10 x 15 x 1 mm) were glued to both ends using epoxy resin. These sheets were clamped to two square glasses until the resin was fully cured. The gauge length of each test specimen was 25 mm, which is shown in Fig. 1.

Thermal environment conditions

Test specimens were fabricated in the laboratory and tested for failure to investigate the tensile properties under axial loads. The ultimate aim of this study is to evaluate the tensile properties of PP and PET fiber bundles in outdoor thermal environments. Considering that high temperatures only last for a few hours per day, this study tested the tensile properties of PP and PET fiber bundles after being exposed to high temperatures for a certain period of time. Two exposure temperatures (80 and 105°C) and two exposure times (1 and 5 hours) were selected as variables. The reason for choosing 80°C is that the surface temperature of the material directly exposed to the sun hardly exceeds 80°C,[17] which is used to observe the tensile properties of PP and PET fiber bundles in outdoor thermal environments. The reference studies reported that the working properties of PP material decreased when it exceeded 105°C.[18] Thus, the choice of 105°C was used to observe the tensile properties of fiber bundles at ultimate service temperature. The choice of 5 hours was made due to a day of high-temperature sunlight from approximately 11:00 a.m. to 4:00 p.m.,[19] while the choice of 1 hour was made for preliminary observations of its tensile properties. The high-temperature treatment was achieved by an oven.

Before the tests, the test specimens were kept under dry experimental conditions at room temperature (25°C) for 6 hours. Subsequently, the test specimens were placed in an oven for the specific temperature and time and then taken out and kept under the same dry experimental conditions for 12 hours up to the test. Finally, all the tests were conducted at room temperature. Three or more specimens were tested in parallel under the same working conditions. The main characteristics and test results of all test specimens are summarized in Table 1. In the specimen labeling convention used in the table: 1) the first letter "T" represents a tensile specimen; 2) the second number represents the thermal treatment temperature in °C; and 3) the third number refers to the thermal treatment duration in hours. The last number denotes the fiber type, where 1 implies a PP fiber bundle, and 2 implies a PET fiber bundle. For example, "T-80-1-1" refers to a PP fiber bundle exposed to 80°C for 1 hour.

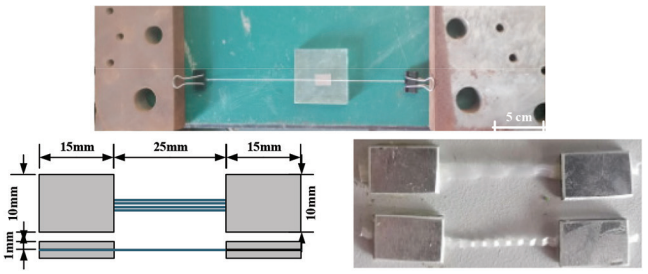

Fig. 1—Schematic diagram of fabricating PP and PET fiber bundles.

Table 1—Main characteristics and test results of PP and PET fiber bundle specimens

No.	A, mm^2	L, mm	E_1, GPa (SD)	E_2, GPa (SD)	σ_y, MPa (SD)	ε_t, % (SD)	f_t, MPa	Number
T-25-0-1	0.141	25	2.94 (0.32)	0.92 (0.39)	164.3 (42.8)	23.03 (0.04)	397	5
T-25-0-2	0.258	25	9.08 (0.80)	4.54 (0.61)	172.2 (18.2)	14.03 (2.25)	742	4
T-80-1-1	0.141	25	3.25 (0.15)	1.21 (0.17)	154.0 (34.9)	21.52 (1.92)	355	5
T-80-1-2	0.258	25	7.99 (1.57)	4.63 (0.44)	151.5 (46.4)	13.40 (0.63)	668	5
T-80-5-1	0.141	25	3.70 (0.39)	1.11 (0.31)	133.6 (56.3)	31.55 (4.39)	421	4
T-80-5-2	0.258	25	6.24 (1.25)	3.64 (0.17)	194.9 (22.5)	18.21 (0.91)	740	4
T-105-1-1	0.141	25	1.36 (0.21)	1.21 (0.11)	139.7 (15.6)	32.81 (0.02)	470	4
T-105-1-2	0.258	25	4.11 (0.38)	3.06 (0.09)	63.78 (21.31)	21.00 (0.02)	650	3
T-105-5-1	0.141	25	1.92 (0.12)	0.90 (0.16)	130.7 (37.0)	32.65 (2.86)	371	6
T-105-5-2	0.258	25	5.12 (1.17)	1.89 (0.37)	96.8 (30.8)	28.24 (3.38)	598	4

Note: A is cross-sectional area; M is mass; L is gauge length; E_1 is initial elastic modulus; E_2 is second elastic modulus; σ_y is yield strength; ε_t is rupture strain; f_t is tensile strength; SD is standard deviation.

Determination of cross-sectional area

The cross-sectional area, A, of a fiber bundle was determined using the linear and bulk densities. The test method for the linear density was described previously, and the following method for measuring the bulk density is crucial. Owing to the poor water absorption of the PP and PET fiber bundles, water molecules could be fully immersed in the gap between the filaments. Hence, the density-bottle method was selected as a useful and convenient method to measure the bulk density, as it only requires calculating the mass of a density bottle filled with distilled water. To ensure the accuracy of the test results, nine samples were tested in parallel, and both mean values and standard deviations of the linear and bulk densities of the PP and PET fiber bundles are listed in Table 2. In the density-bottle method, first, the fiber mass, m_1, was weighed on a high-precision electronic weighing scale (0.001 g), and subsequently, the mass of the density bottle filled with distilled water, m_2, was weighed. Following this, the fiber sample was gradually placed into the density bottle. Finally, the density bottle was heated over an alcohol lamp to remove bubbles from the surface of the filament, and the density-bottle mass, m_3, was weighed after it was kept standing for >2 hours at room temperature. Figure 2 shows the process of bulk density determination. The bulk density of a fiber bundle, ρ, is calculated using the following formula

$$\rho = \frac{m_1}{m_1 + m_2 - m_3} \quad (1)$$

Table 2—Measured physical properties of fiber bundles

Materials	Linear density, g/m		Bulk density, g/m^3	
	Mean	SD	Mean	SD
PP	0.12	1.06×10^{-5}	878×10^3	1.44%
PET	0.35	1.29×10^{-4}	1345×10^3	5.49%

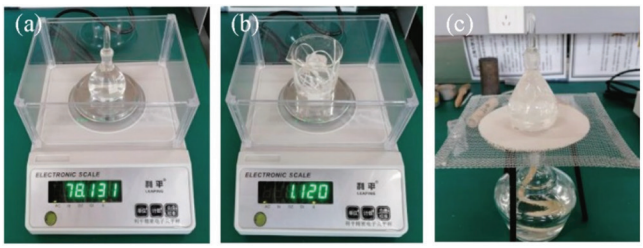

Fig. 2—Bulk density determination process of PP and PET fiber bundles: (a) density-bottle mass; (b) fiber bundle mass; and (c) removing bubbles.

Testing procedure

All specimens were tested under displacement control using a universal testing machine, which is shown in Fig. 3. The system had a maximum loading capacity of 50 kN with a wide test speed range from 0.001 to 500 mm/min. Owing to the small cross-sectional areas of the fiber bundles, their failure forces were very small, and the selected test machine was sufficient to conduct this test. All test specimens were loaded at a displacement rate of 2 mm/min. Ou and Zhu[20] demonstrated that the stiffness of a fiber bundle is much lower than that of the beam of a test machine, and the displacement of the beam can replace that of the fiber bundle during tensile axial loading. Therefore, in this study, considering the aforementioned conditions, the displacement of a fiber bundle was recorded using that of the beam. The stress and strain values were calculated from the cross-sectional area, A, and the gauge length (25 mm).

EXPERIMENTAL RESULTS

Failure modes

Figures 4 and 5 show the typical characteristics of the failure modes and scanning electron microscopy (SEM) micrographs of PP and PET fiber bundle specimens under a quasi-static load. From left to right, the failure specimens are in order those untreated and exposed to 80°C for 1 hour, 80°C for 5 hours, 105°C for 1 hour, and 105°C for 5 hours (Fig. 4); the experimental phenomena of loading to failure of PP and PET fiber bundles are essentially the same and can be described as follows. First, each filament is elongated during the initial loading. No filament breaking was observed at this stage, so the loading environment was quiet. Second, after the loading has continued for some time,

Fig. 3—Universal testing machine for quasi-static tensile test.

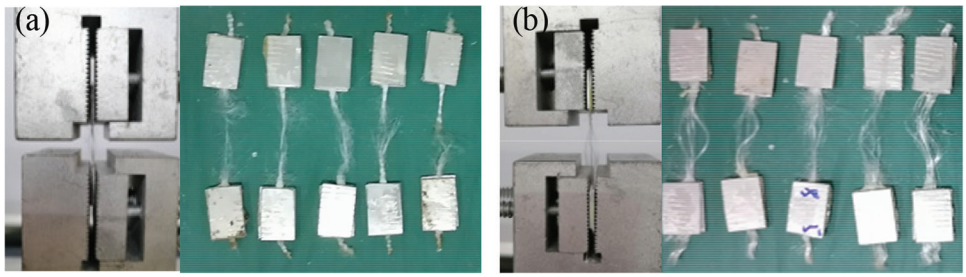

Fig. 4—Failure modes of fiber bundles exposed to high temperatures for different exposure times: (a) PP fiber bundle; and (b) PET fiber bundle.

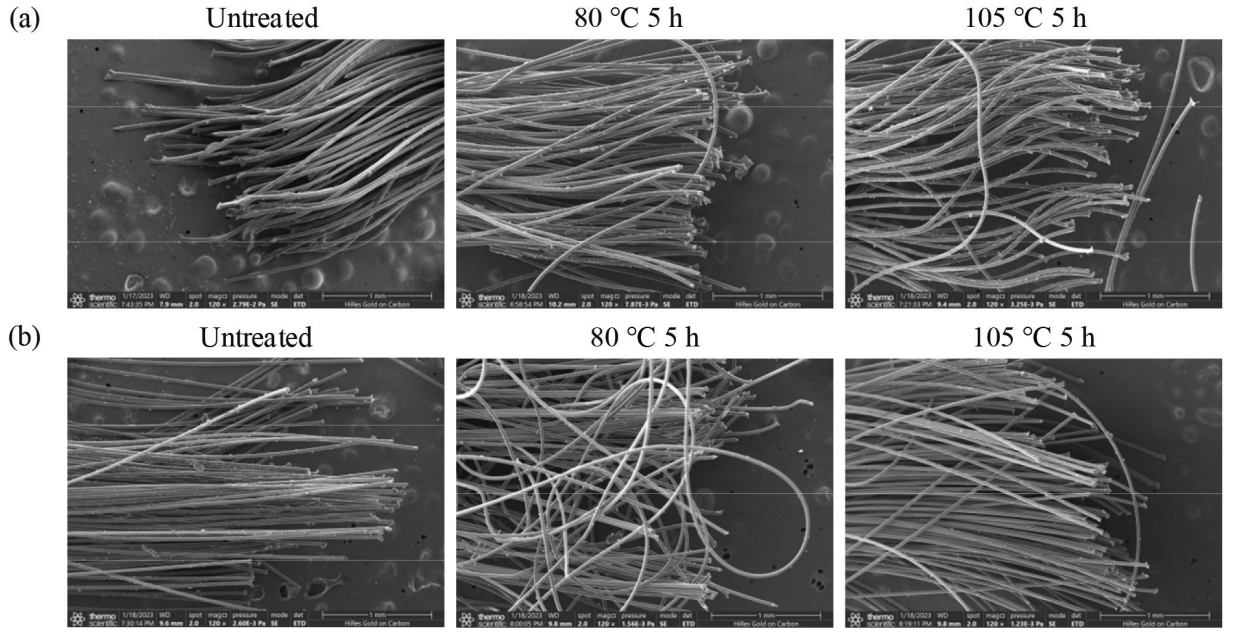

Fig. 5—SEM micrographs of typical failure modes of fiber bundles exposed to high temperatures for different exposure times: (a) PP fiber bundle; and (b) PET fiber bundle.

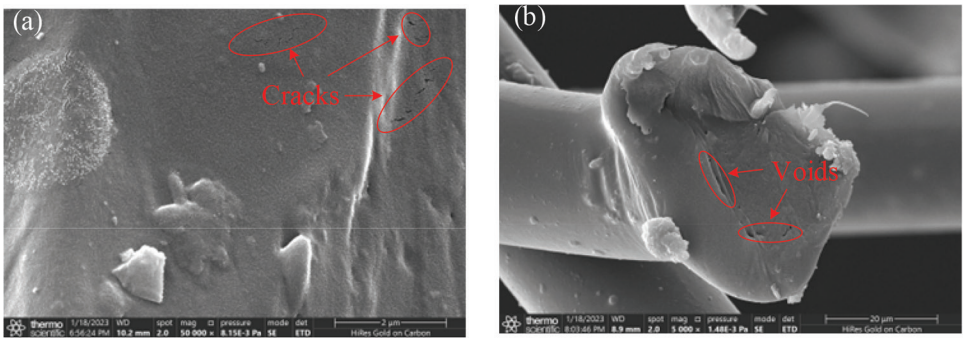

Fig. 6—Cracks and voids in rupture surface: (a) PP fiber bundle; and (b) PET fiber bundle.

some of the defective filaments break off one by one. There was a cracking sound as the filaments broke. The time for the development of inherent defects in each filament under quasi-static loading is sufficient, and a defect-containing and low-strength filament is expected to break first in the final state. The force originally borne by it is distributed over the other fibers, causing a stress mutation. It should be noted that the fiber bundle specimens were not destroyed immediately after the initial breaking of some filaments. Finally, the remaining filaments are unable to sustain the increasing load, resulting in stress reduction. The test was subsequently terminated. It can be seen from the tested fiber bundle specimen that there are still some PP and PET filaments with few defects that are not broken, and the figure of the PET fiber bundle specimens is the most obvious (Fig. 4(b)). This may be due to the fact that the bearing load of the PET fiber bundle is much higher than that of the PP fiber bundle and that the bearing load of the fiber bundle specimen decreases rapidly after a fraction of the PET filament is broken. Unbroken filaments give rise to plastic deformations such that after testing, the unbroken filament cannot remain in its initial collimated state. In addition, a partial melting of PET fiber bundles was observed at 105°C; however, this phenomenon did not occur at 80°C. The melting temperature of PP fiber was in the range of 145 to 180°C,[21] but the melting progress was not observed in the test. Typical SEM micrographs of PP and PET fiber bundle specimens were used to further explain the failure modes under different thermal conditions. Figure 5 shows that the PP and PET fiber bundles failed with a disordered rupture surface. The similarity of the failure modes of the fiber bundle specimens at different thermal conditions may be explained by their internal defects (for example, tiny cracks and voids), as shown in Fig. 6. The internal defects are located randomly along the direction of the filament, resulting in a disordered rupture surface. However, all filaments in the high-temperature treatment are uniformly heated, and the initial defects may expand but not disappear due to the local inhomogeneous deformation of the filaments. The failure modes of PP and PET fiber bundles under different thermal conditions are still determined by the random distribution of internal defects. This evidence shows that the failure modes are essentially the same for all fiber bundles at room temperature and exposed to high temperatures for a period of time (below 105°C).

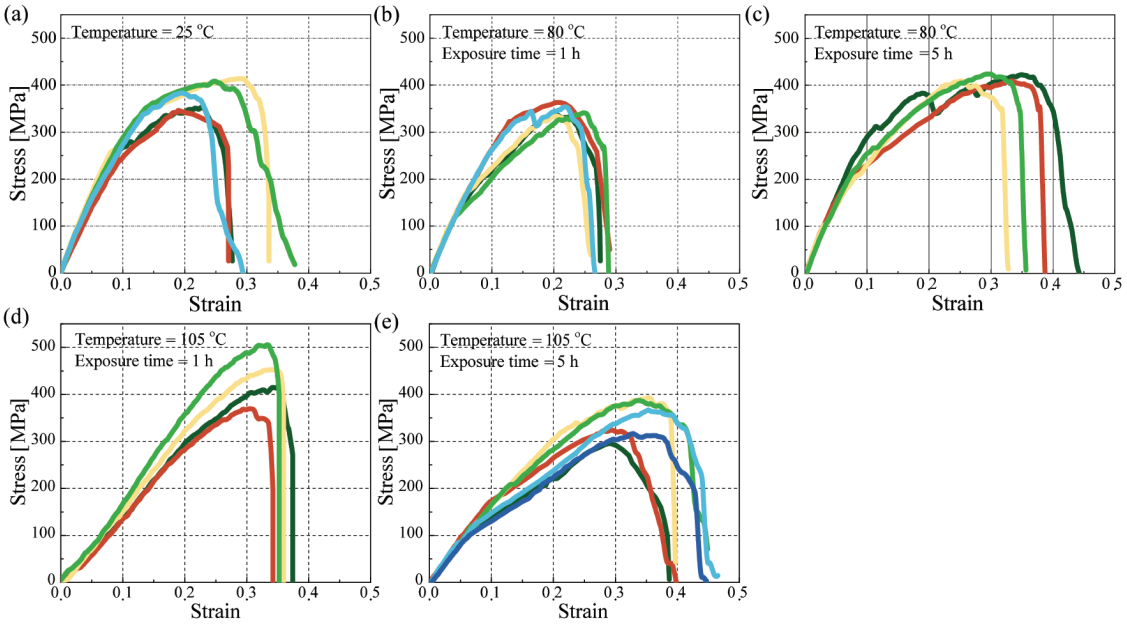

Fig. 7—Stress-strain curves of PP fiber bundles at room temperature and exposed to high temperatures for different exposure times: (a) T-25-0-1; (b) T-80-1-1; (c) T-80-5-1; (d) T-105-1-1; and (e) T-105-5-1.

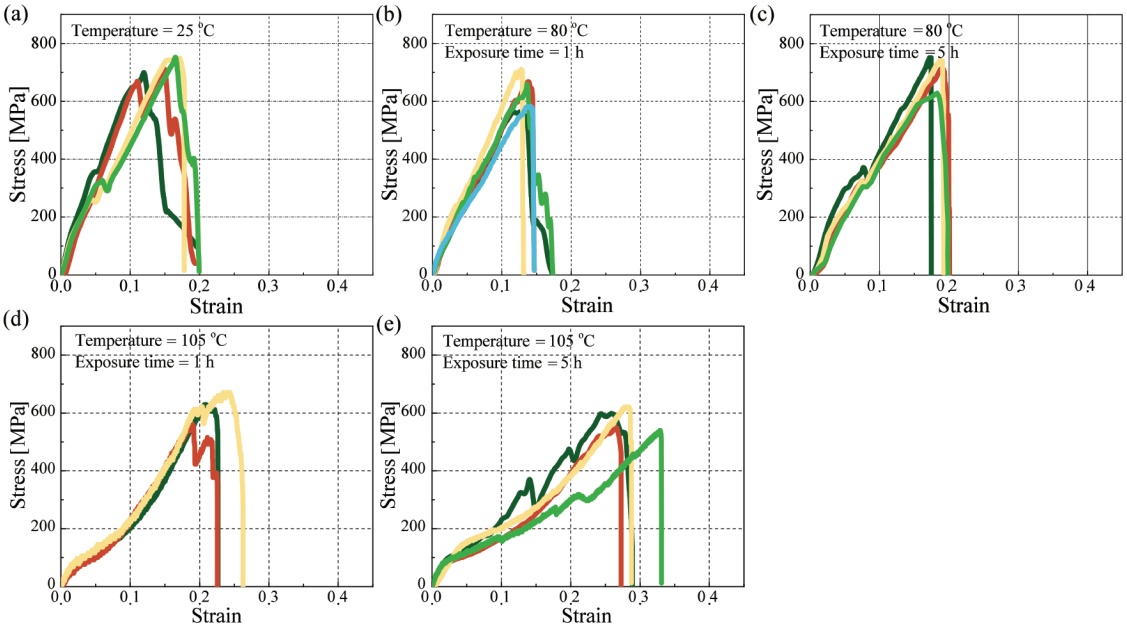

Fig. 8—Stress-strain curves of PET fiber bundles at room temperature and exposed to high temperatures for different exposure times: (a) T-25-0-2; (b) T-80-1-2; (c) T-80-5-2; (d) T-105-1-2; and (e) T-105-5-2.

Stress-strain relationship

Figures 7 and 8 show the experimental stress-strain relationships of the PP and PET fiber bundles. The stress-strain relationships of the specimens tested parallel were close to each other, demonstrating the accuracy of the test results. Note that a fiber bundle may experience slip failure accompanied by an abrupt loss of strength. Consequently, imperfect test data were excluded from this study.

The stress-strain curves of the fiber bundles are different from the curves of the mild steel with a long yield plateau, as shown in Fig. 9. Because the fiber bundles have no obvious inflection point in stress-strain curves, in this study, the yield point of the fiber bundle was obtained by the point when the fiber produced a plastic strain of 0.002 under tensile axial loads, as shown in Fig. 9(b). The definition of a yield point originates from metallic materials and is taken from a critical state point on the stress-strain curve that marks the transition from elasticity to plasticity. In general, for stress-strain curves with a distinct turning point, the turning point is the yield point; whereas, for stress-strain curves without a distinct turning point, the yield point is usually taken to be the moment when a small amount of plastic deformation occurs. The value of 0.002 is obtained by a great deal of engineering experience; therefore, this method is reliable.[22]

The stress-strain relationships of the PP and PET tensile specimens exhibited a three-stage elastic hardening-softening

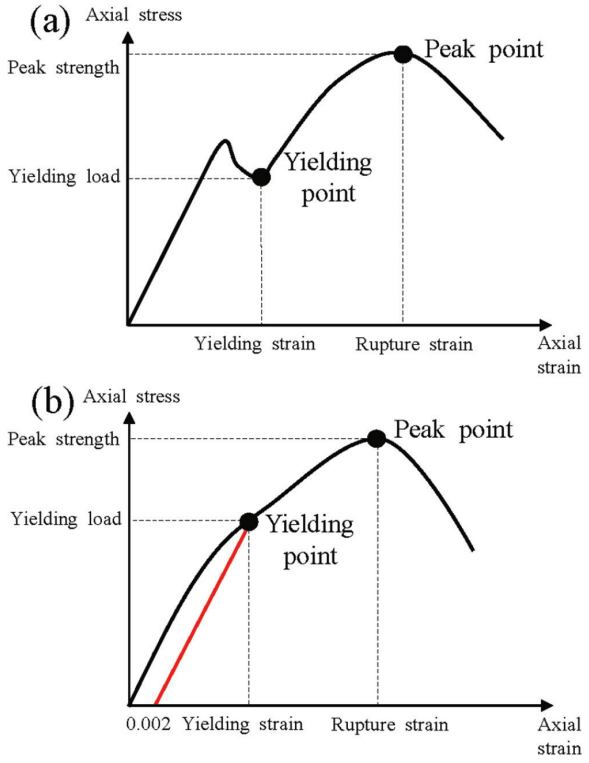

Fig. 9—Method to determine yield point: (a) with long yield plateau; and (b) without obvious inflection curves.

behavior: 1) an elastic stage showing a linear stress-strain relationship with an initial slope equal to the initial elastic modulus, E_1; 2) a strain-hardening stage from the yield point (σ_y, ε_y) with a slope equaling the second elastic modulus, E_2; and 3) a strain-softening stage from the stress maximum point (f_t, ε_t) with a declining curve.

The stress-strain curves of the PP and PET fiber bundles show some similarities and differences. During the initial elastic stage, the stress-strain relationships of the PP and PET fiber bundles exhibited high linear correlations, which remained constant after exposure to high temperatures. At this stage, the tiny cracks and voids inside the PP and PET fibers were unable to expand due to limited external forces. This characteristic remains unchanged, whether at 80 or 105°C, meaning that the integrity of PP and PET fiber bundles exposed to high temperatures is not affected. In the strain-hardening stage, the values of the second elastic modulus became scattered, and the linear correlation was reduced. Because the strain at the point of the maximum stress is generally considered to be a constant value under the same conditions, the scatter of the second elastic modulus directly affects the scatter of the strength. Such a scatter may be attributed to the damage evolution of the internal defects (for example, crack expansion), which was quantified by probabilistic models in studies. The probabilistic models are mainly classified as the Weibull model adopted by Bai et al.[15,16] and Out et al.[12] and the Bayesian model adopted by Pournamazian Najafabadi et al.[23] However, the initial elastic modulus and the second elastic modulus for the PP fiber bundles was smaller than that for the PET fiber bundles. This is because the molecular chain of PET consists of high-rigid benzene rings, which increase the forces between the molecules.[24] As observed in the failure

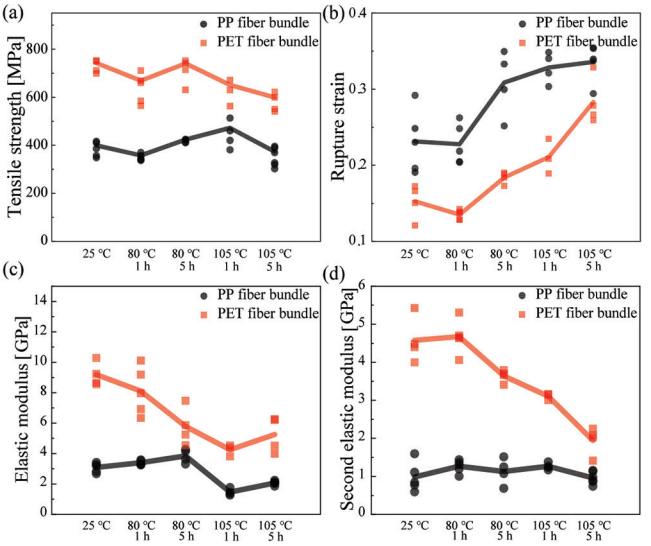

Fig. 10—Effect of exposure temperature and time on mechanical properties of PP and PET fiber bundles: (a) tensile strength; (b) rupture strain; (c) elastic modulus; and (d) second elastic modulus.

mode, both PP and PET filaments began to fail when the external load approached the maximum load point. The post-peak strain-softening behavior of the fiber bundle depends on the behavior of the remaining filaments. With a fiber bundle model, Bai et al.[15] reproduced the failure process of the fiber bundle and concluded the same. The post-peak behavior of some specimens of PP and PET fiber bundles shows a large amount of deformation up to final failure. This is due to premature failure of a few filaments in the fiber bundle due to internal defects caused by exposure to high temperatures. The remaining filaments continue to deform and bear the load, as they have not yet reached the failure strain. This will increase the dispersion of the tensile strength of the fiber bundle specimen, which can be quantified with a statistical model.

Major mechanical parameters

For further quantification of the mechanical behavior of the fiber bundle specimens, Table 1 summarizes the values of major experimental characteristics of the mechanical parameters (E_1, E_2, σ_y, ε_t, and f_t). Considering most studies confirm that the tensile strength of a fiber bundle conforms to a Weibull distribution,[12,15,16] f_t listed in Table 1 are calculated based on the Weibull distribution equation, as will be specified in the "Weibull analysis of tensile strength" section.

ANALYSIS AND DISCUSSION

Temperature effect on mechanical properties

Figure 10(a) shows the effects of the exposure temperature and exposure time on the tensile strengths of the PP and PET fiber bundles. Specifically, when exposed to 80°C for 1 hour, the tensile strengths of the PP and PET fiber bundles decreased by 10.6% and 9.97%, respectively, whereas they correspondingly increased by 6% and decreased by 0.27% on increasing the exposure time to 5 hours. These results showed that the tensile strengths of PP and PET fiber decreased when exposed to 80°C for 1 hour and then increased with the increase of exposure time (1 to 5 hours). Because both PP

and PET are crystalline polymers, the change in the tensile strength is most likely related to changes in crystallinity. It has been reported that the crystallinity of PP treated in hot air is significantly affected by increasing temperature; the crystallinity of PP increases when the temperature rises from 25 to 100°C and then decreases with increasing temperature,[25] whereas the crystallinity of PET increases with increasing temperature.[26] As the orientation of the molecules in the crystal region increases, the size and content of cracks and voids in the fiber increase, and eventually, some of the macromolecules break down. In addition to crystallinity, the mechanical properties of polymers are also related to the size of crystalline particles.[27] The increase in the tensile strength with increasing exposure time is probably related to the refinement of the crystalline particles.

When exposed to 105°C for 1 hour, the tensile strengths of the PP and PET fiber bundles increased by 18.4% and decreased by 12.4%, respectively, whereas they correspondingly decreased by 6.5% and 19.4% on increasing the exposure time to 5 hours. Similar to before, the change in the tensile strength can be attributed to changes in crystallinity when exposed to 105°C for 1 hour. At 105°C (exposure time of 1 hour), the decrease in the crystallinity of PP leads to the increase in strength, whereas the increase in the crystallinity of PET leads to the decrease in strength.[25,26] With increasing exposure time (1 to 5 hours), the tensile strength of the PP and PET fiber bundles decreased compared to the 1-hour exposure time. The abnormal trend can be explained by the observed partial melting when PET fiber bundles were exposed to 105°C for 5 hours, although the melting temperature of PET was reported to be 248°C in the reference study.[28] The melting temperature of PP was lower than that of PET, in the range of 145 to 180°C.[21] A partial melting of the PP fiber bundle was not observed in the thermal treatment, possibly due to the thin thickness of the selected PP fabric used.

The relationships between the rupture strain and the exposure temperature are illustrated in Fig. 10(b), and the average values are listed in Table 1. The rupture strains of the PP and PET fiber bundles tended to increase with the increase in the exposure temperature from 25 to 105°C, except for a slight decrease when exposed to 80°C for 1 hour. As the exposure temperature increased, the orientation of macromolecular chains increased, and the elongation of fibers increased gradually. However, a thermomechanical analysis for PP showed a turning point of approximately 80°C concerning the expansion and shrinkage of the molecular chain.[18] The slight decrease in the rupture strain when exposed to 80°C for 1 hour can be attributed to the change of molecular chain. The rupture strain of the PP fiber bundle increased from 23.03 to 32.65% with an increase in the exposure temperature from 25 to 105°C, whereas that of the PET fiber bundle increased from 14.03 to 28.24%.

The change rules of the initial and second elastic moduli of the PP and PET fiber bundle specimens exposed to high temperatures are plotted in Fig. 10(c) and (d), respectively, and the average values are listed in Table 1. The initial elastic modulus of the PP fiber bundle increased when exposed to 80°C and decreased when exposed to 105°C, whereas the corresponding second elastic modulus slightly changed when exposed to high temperatures for a period. In contrast, those of the PET fiber bundle decreased with increasing exposure temperature, except for a slight increase in the second elastic modulus when exposed to 80°C for 1 hour. As before, the orientation of macromolecular chains increased with increasing exposure temperature, and the elastic modulus of the polymer tended to decrease. The increase in the initial elastic modulus of the PP fiber bundle was probably related to the change of molecular chain when exposed to 80°C for 1 hour.[18]

Yield process for fiber bundles

Observations from the stress-strain curves of PP and PET fiber bundle specimens showed that the yield processes are within different strain ranges. The range of yield strain for both grew with the increase in exposure temperature. Specifically, the strains of the PP fiber bundle specimens in yield corresponded to a range of 0.03597 to 0.07989 for the exposure temperature of 25°C, 0.0362 to 0.06285 for the exposure temperature of 80°C (exposure time of 1 hour), 0.0298 to 0.07343 for the exposure temperature of 80°C (exposure time of 5 hours), 0.04013 to 0.09732 for the exposure temperature of 105°C (exposure time of 1 hour), and 0.04584 to 0.10611 for the exposure temperature of 105°C (exposure time of 5 hours). For comparison, the yield of the PET fiber bundle specimens was within the strain range 0.01783 to 0.02846 for the exposure temperature of 25°C, 0.01081 to 0.02879 for the exposure temperature of 80°C (exposure time of 1 hour), 0.01821 to 0.03433 for the exposure temperature of 80°C (exposure time of 5 hours), 0.01721 to 0.03122 for the exposure temperature of 105°C (exposure time of 1 hour), and 0.01614 to 0.04148 for the exposure temperature of 105°C (exposure time of 5 hours). All these values of PET fiber bundles are much lower than those of PP ones.

The average values of the yield strength for the PP and PET fiber bundles are listed in Table 1. Based on these values, the yield strengths of PP and PET fiber bundles decreased under exposure to high temperatures, except for T-80-5-2 and T-105-5-2. The effect of high temperatures on the axial yield strengths of these materials is compared. Results from the PP and PET fiber bundle specimens show that high temperatures affected load degeneration at approximately 20.5% and 43.8% of the yield strengths, respectively. The yield strength of the PET fiber bundle is more sensitive to high temperatures than that of the PP fiber bundle.

Weibull analysis of tensile strength

According to the literature,[12,15,16] a Weibull probability distribution provides sufficiently accurate tensile strengths for fiber bundles. Therefore, a Weibull distribution model was considered to be sufficiently accurate in describing the dispersion of the tensile strengths of PP and PET fiber bundles exposed to high temperatures for a period. The cumulative probability density function is expressed as

$$F(\sigma) = 1 - \exp\left[-\left(\frac{\sigma}{\sigma_0}\right)^m\right] \quad (2)$$

Table 3—Weibull parameters of tensile strengths of PP and PET fiber bundle specimens after exposure to high temperatures

Materials	Exposure temperature, °C	Exposure time, hours	Scale parameter σ_0, MPa	Shape parameter m	R^2
PP	25	—	397	11.0	0.93
	80	1	355	20.8	0.85
		5	421	46.7	0.85
	105	1	470	6.5	0.99
		5	371	7.2	0.92
PET	25	—	742	21.7	0.90
	80	1	668	8.8	0.94
		5	740	10.0	0.89
	105	1	650	8.7	0.99
		5	598	12.0	0.91

where F is the cumulative probability of the failure of a PP or PET fiber bundle at applied tensile stress σ; and σ_0 and m are the Weibull scale and shape parameters, respectively. m represents the degree of data dispersion, and a small m value implies a high dispersion of the tensile strength. At the stress level, σ, the failure probability, F, can be expressed as

$$F = \frac{i}{N+1} \tag{3}$$

where N is the total number of filaments in a fiber bundle; and i is the number of fibers broken at or below a certain stress level. Substituting Eq. (3) into Eq. (2) yields

$$1 - \exp\left[-\left(\frac{\sigma}{\sigma_0}\right)^m\right] = \frac{i}{N+1} \tag{4}$$

Equation (5) is obtained by taking double natural logarithms of both sides of Eq. (4).

$$\ln\left[-\ln\left(1 - \frac{i}{N+1}\right)\right] = m\ln\sigma - m\ln\sigma_0 \tag{5}$$

Assuming $X_i = \ln\sigma$ and $Y_i = \ln\left[-\ln\left(1 - \frac{i}{N+1}\right)\right]$, Eq. (5) can be rewritten as

$$Y_i = mX_i - m\ln\sigma_0 \tag{6}$$

The previous equation realizes a linear regression of a Weibull distribution. In this specific case, X_i and Y_i are calculated from experimental data, and based on them, linear fitting is performed. According to the equation obtained by the linear fitting, parameters m and σ_0 can be calculated under various thermal conditions, and the results for this study are summarized in Table 3.

In Table 3, the values of R^2 are between 0.85 and 0.99, reflecting that the tensile strengths of the PP and PET fiber bundles conform to a Weibull distribution. Shape parameter m of the PP fiber bundle increased when exposed to 80°C, whereas it decreased when exposed to 105°C compared to that at room temperature. By contrast, the shape parameter m of the PET fiber bundle decreased as the temperature increased. According to the statistical data, the tensile strength of the PP fiber bundle exposed to 80°C was stable, whereas the strength stability was not guaranteed at higher temperatures. The tensile strength of the PET fiber bundle was discrete at temperatures of 80°C and higher.

CONSTITUTIVE MODEL OF FIBER BUNDLES

The constitutive model can not only evaluate the stress-strain behavior of fiber bundle materials but also provide theoretical support for the design of novel composite materials. A proper fiber bundle constitutive model can be used to explain some experimental phenomena that cannot be observed. For example, experimental observations cannot explain the failure mechanism of fiber-reinforced concrete, whether the initial crack in concrete originates in the interfacial transition zone between the cement mortar and coarse aggregate or in the interfacial transition zone between the cement mortar and fiber. A more intuitive application is that by Bai et al.,[15] who adopted a bilinear stress-strain model to reproduce the failure process of the PET fiber bundle.

In this study, the corresponding constitutive models considering the scatter of tensile strength are proposed according to the stress-strain behaviors of PP and PET fiber bundles after exposure to high temperatures. As described in the previous sections, the stress and strain values presented a high linear correlation until the inflection point; they subsequently still presented a linear correlation in each high-temperature working condition. However, the second linear correlation was reduced between different parallel specimens. Thus, based on the observed behaviors of specimens, a bilinear stress-strain model is adopted in this study. The slope of the second part is represented by the Weibull distribution. The stress-strain model is given with the Weibull parameters as follows

$$\sigma = \begin{cases} E_1\varepsilon, & 0 \le \varepsilon \le \dfrac{\sigma_y}{E_1} \\ \dfrac{E_1\sigma_0\left[-\ln\left(1 - \dfrac{i}{N+1}\right)\right]^{\frac{1}{m}} - E_1\sigma_y}{E_1\varepsilon_t - \sigma_y}\left(\varepsilon - \dfrac{\sigma_y}{E_1}\right), & \dfrac{\sigma_y}{E_1} < \varepsilon \le \varepsilon_t \end{cases} \tag{7}$$

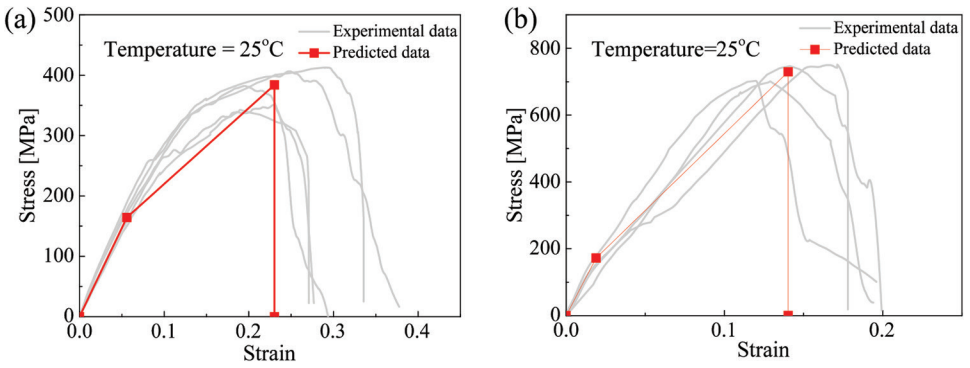

Fig. 11—Comparison of stress-strain curves of PP and PET fiber bundles at room temperature obtained from proposed model and tests.

Given the strain ε at the range of 0 to ε_t, the stress values can be predicted using Eq. (7). For other model parameters under different working conditions, refer to Tables 1 and 3. Assuming $i/(N + 1) = 0.5$, the comparisons of predicted and test stress-strain curves of PP and PET fiber bundles at room temperature are presented in Fig. 11. It can be seen from the figure that the prediction curves are in good agreement with the test results.

CONCLUSIONS

Quasi-static tests were conducted to investigate the tensile properties of polypropylene (PP) and polyethylene terephthalate (PET) fiber bundles exposed to high temperatures for different exposure times. Furthermore, the statistical distribution of the tensile strength of a fiber bundle was precisely quantified by a two-parameter Weibull analysis. The following key conclusions were drawn:

1. The PP and PET fiber bundles at room temperature and when exposed to high temperatures (80 and 105°C) for different exposure times (1 and 5 hours) show a bilinear stress-strain relationship. In the initial elastic stage, the stress-strain relationships of the PP and PET fiber bundles present a high linear correlation until the inflection point, which remains constant even when exposed to high temperatures. In the subsequent hardening stage, the experimental data became scattered, and the linear correlation was reduced.

2. Exposure temperature and time significantly affect the tensile strength, rupture strain, and elastic modulus of the PP and PET fiber bundles. PP and PET fibers are safe for use at service temperatures up to 80°C, while at 105°C, consideration of mechanical properties degradation is required.

3. In the comparison between PP and PET fiber bundles, the PP fiber bundle exhibited a wider range of yield strain, and the high temperatures extended the range of yield strain. Also, high temperatures affected load degeneration of PP and PET fiber bundles at approximately 20.5 and 43.8% of the yield strengths.

4. The tensile strengths of the PP and PET fiber bundles at room temperature and exposed to high temperatures (80 and 105°C) for different exposure times (1 and 5 hours) conform to a Weibull distribution. Thus, a Weibull distribution model is developed to describe the tensile strength of PP and PET fiber bundles.

The findings of this research will help the construction industry develop and market new hybrid fiber-reinforced polymer (FRP) members with high specific strength and deformability. The manufacturing process for producing new hybrid FRP members and the relevant working performance require further research.

AUTHOR BIOS

Zihao Shen *is a PhD Candidate at Shanghai University, Shanghai, China. His research interests include polymer shock-absorbing materials.*

Wenguang Liu *is a Professor at Shanghai University. His research interests include seismic and shock absorption techniques for major engineering structures, isolation structure analysis and design theory, polymer shock-absorbing materials, and seismic analysis and design of rail transit.*

REFERENCES

1. Afroughsabet, V., and Ozbakkaloglu, T., "Mechanical and Durability Properties of High-Strength Concrete Containing Steel and Polypropylene Fibers," *Construction and Building Materials*, V. 94, Sept. 2015, pp. 73-82. doi: 10.1016/j.conbuildmat.2015.06.051

2. Zeng, J.-J.; Gao, W.-Y.; Duan, Z.-J.; Bai, Y.-L.; Guo, Y.-C.; and Ouyang, L.-J., "Axial Compressive Behavior of Polyethylene Terephthalate/Carbon FRP-Confined Seawater Sea-Sand Concrete in Circular Columns," *Construction and Building Materials*, V. 234, Feb. 2020, Article No. 117383. doi: 10.1016/j.conbuildmat.2019.117383

3. Shukla, S. R., and Mathur, M. R., "Action of Alkali on Polybutylene Terephthalate and Polyethylene Terephthalate Polyesters," *Journal of Applied Polymer Science*, V. 75, No. 9, Feb. 2000, pp. 1097-1102. doi: 10.1002/(SICI)1097-4628(20000228)75:9<1097::AID-APP2>3.0.CO;2-7

4. Wardani, A. K.; Ariono, D.; Yespin, Y.; Sihotang, D. R.; and Wenten, I. G., "Preparation of Hydrophilic Polypropylene Membrane by Acid Dipping Technique," *Materials Research Express*, V. 6, No. 7, July 2019, Article No. 075308. doi: 10.1088/2053-1591/ab10cf

5. López-Buendía, A. M.; Romero-Sánchez, M. D.; Climent, V.; and Guillem, C., "Surface Treated Polypropylene (PP) Fibres for Reinforced Concrete," *Cement and Concrete Research*, V. 54, Dec. 2013, pp. 29-35. doi: 10.1016/j.cemconres.2013.08.004

6. Ju, Y.; Wang, L.; Liu, H.; and Tian, K., "An Experimental Investigation of the Thermal Spalling of Polypropylene-Fibered Reactive Powder Concrete Exposed to Elevated Temperatures," *Science Bulletin*, V. 60, No. 23, Dec. 2015, pp. 2022-2040.

7. Hager, I., and Mróz, K., "Role of Polypropylene Fibres in Concrete Spalling Risk Mitigation in Fire and Test Methods of Fibres Effectiveness Evaluation," *Materials*, V. 12, No. 23, Dec. 2019, Article No. 3869. doi: 10.3390/ma12233869

8. Cai, R.; Liu, J.-C.; and Ye, H., "Spalling Prevention of Ultrahigh-Performance Concrete: Comparative Effectiveness of Polyethylene Terephthalate and Polypropylene Fibers," *Journal of Materials in Civil Engineering*, ASCE, V. 33, No. 12, Dec. 2021, p. 04021344. doi: 10.1061/(ASCE)MT.1943-5533.0003980

9. Saleem, S.; Pimanmas, A.; Qureshi, M. I.; and Rattanapitikon, W., "Axial Behavior of PET FRP-Confined Reinforced Concrete," *Journal of Composites for Construction*, ASCE, V. 25, No. 1, Feb. 2021, p. 04020079. doi: 10.1061/(ASCE)CC.1943-5614.0001092

10. Cerniauskas, G.; Tetta, Z.; Bournas, D. A.; and Bisby, L. A., "Concrete Confinement with TRM versus FRP Jackets at Elevated Temperatures," *Materials and Structures*, V. 53, No. 3, June 2020, Article No. 58. doi: 10.1617/s11527-020-01492-x

11. Dai, J.-G.; Bai, Y.-L.; and Teng, J. G., "Behavior and Modeling of Concrete Confined with FRP Composites of Large Deformability," *Journal of Composites for Construction*, ASCE, V. 15, No. 6, Dec. 2011, pp. 963-973. doi: 10.1061/(ASCE)CC.1943-5614.0000230

12. Ou, Y.; Zhu, D.; Zhang, H.; Huang, L.; Yao, Y.; Li, G.; and Mobasher, B., "Mechanical Characterization of the Tensile Properties of Glass Fiber and Its Reinforced Polymer (GFRP) Composite under Varying Strain Rates and Temperatures," *Polymers*, V. 8, No. 5, May 2016, Article No. 196. doi: 10.3390/polym8050196

13. Wang, Y., and Xia, Y., "Dynamic Tensile Properties of E-Glass, Kevlar49 and Polyvinyl Alcohol Fiber Bundles," *Journal of Materials Science Letters*, V. 19, No. 7, Apr. 2000, pp. 583-586. doi: 10.1023/A:1006730312279

14. Sabet, S. M. M.; Akhlaghi, F.; and Eslami-Farsani, R., "The Effect of Thermal Treatment on Tensile Properties of Basalt Fibers," *Journal of Ceramic Science and Technology*, V. 6, No. 3, Sept. 2015, pp. 245-248.

15. Bai, Y.-L.; Yan, Z.-W.; Ozbakkaloglu, T.; Han, Q.; Dai, J.-G.; and Zhu, D.-J., "Quasi-Static and Dynamic Tensile Properties of Large-Rupture-Strain (LRS) Polyethylene Terephthalate Fiber Bundle," *Construction and Building Materials*, V. 232, Jan. 2020, Article No. 117241. doi: 10.1016/j.conbuildmat.2019.117241

16. Bai, Y.-L.; Yan, Z.-W.; Ozbakkaloglu, T.; Gao, W.-Y.; and Zeng, J.-J., "Mechanical Behavior of Large-Rupture-Strain (LRS) Polyethylene Naphthalene Fiber Bundles at Different Strain Rates and Temperatures," *Construction and Building Materials*, V. 297, Aug. 2021, Article No. 123786. doi: 10.1016/j.conbuildmat.2021.123786

17. Benmokrane, B.; Mousa, S.; Mohamed, K.; and Sayed-Ahmed, M., "Physical, Mechanical, and Durability Characteristics of Newly Developed Thermoplastic GFRP Bars for Reinforcing Concrete Structures," *Construction and Building Materials*, V. 276, Mar. 2021, Article No. 122200. doi: 10.1016/j.conbuildmat.2020.122200

18. Wu, X.; Tang, S.; Song, G.; Zhang, Z.; and Tan, D. Q., "High-Temperature Resistant Polypropylene Films Enhanced by Atomic Layer Deposition," *Nano Express*, V. 2, No. 1, Mar. 2021, Article No. 010025. doi: 10.1088/2632-959X/abe518

19. Lu, J.; Chen, J.-H.; Tang, Y.; and Wang, J.-S., "High-Rise Buildings versus Outdoor Thermal Environment in Chongqing," *Sensors*, V. 7, No. 10, Oct. 2007, pp. 2183-2200. doi: 10.3390/s7102183

20. Ou, Y., and Zhu, D., "Tensile Behavior of Glass Fiber Reinforced Composite at Different Strain Rates and Temperatures," *Construction and Building Materials*, V. 96, Oct. 2015, pp. 648-656. doi: 10.1016/j.conbuildmat.2015.08.044

21. Ríos, J. D.; Cifuentes, H.; Leiva, C.; García, C.; and Alba, M. D., "Behavior of High-Strength Polypropylene Fiber-Reinforced Self-Compacting Concrete Exposed to High Temperatures," *Journal of Materials in Civil Engineering*, ASCE, V. 30, No. 11, Nov. 2018, p. 04018271. doi: 10.1061/(ASCE)MT.1943-5533.0002491

22. Abdul Jalil, S.; Anwar, A.; Chou, S. M.; and Tai, K., "Material Yield Strain Identification Using Energy Absorption," *The Journal of Strain Analysis for Engineering Design*, V. 53, No. 6, Aug. 2018, pp. 463-469. doi: 10.1177/0309324718774950

23. Pournamazian Najafabadi, E.; Houshmand Khaneghahi, M.; Ahmadie Amiri, H.; Estekanchi, H. E.; and Ozbakkaloglu, T., "Experimental Investigation and Probabilistic Models for Residual Mechanical Properties of GFRP Pultruded Profiles Exposed to Elevated Temperatures," *Composite Structures*, V. 211, Mar. 2019, pp. 610-629.

24. Mittal, A.; Soni, R. K.; Dutt, K.; and Singh, S., "Scanning Electron Microscopic Study of Hazardous Waste Flakes of Polyethylene Terephthalate (PET) by Aminolysis and Ammonolysis," *Journal of Hazardous Materials*, V. 178, No. 1-3, June 2010, pp. 390-396. doi: 10.1016/j.jhazmat.2010.01.092

25. Akolekar, D. B.; Nair, S.; Adsul, S.; and Virkar, S., "Functionalization of Polypropylene at High Temperature Under Oxidative/Inert Environment," *Journal of Applied Polymer Science*, V. 123, No. 1, Jan. 2012, pp. 1-11. doi: 10.1002/app.34442

26. Hirai, T.; Matsunaga, T.; Sato, N.; Katagiri, Y.; Kawada, J.; and Usuki, A., "High-Temperature Crystallization of Immiscible Polymer Blends Induced by the Shear Flow in Injection Molding," *Polymer Crystallization*, V. 2, No. 4, 2019, Article No. e10069. doi: 10.1002/pcr2.10069

27. Chen, X.; Zhang, Z.; Chen, B.; Liu, C.; Zhang, S.; Cao, W.; and Wang, Z., "Crystalline Grain Refinement Toughened Isotactic Polypropylene Through Rapid Quenching of Stretched Melt," *Polymer*, V. 216, Feb. 2021, Article No. 123435. doi: 10.1016/j.polymer.2021.123435

28. Albano, C.; Camacho, N.; Hernández, M.; Matheus, A.; and Gutiérrez, A., "Influence of High Temperatures on PET-Concrete Properties," *Macromolecular Symposia*, V. 286, No. 1, Nov. 2009, pp. 195-202. doi: 10.1002/masy.200951224

ACI MATERIALS JOURNAL TECHNICAL PAPER

Title No. 122-M14

Properties, Durability, and Environmental Analysis of Fiber-Reinforced Concrete Mixtures

by Ali Farhat, Adel Chahrour, Bilal Hamad, Joseph J. Assaad, and Alissar Yehya

This investigation attempted to analyze the environmental impact of fibers, including their effect on the cost and durability of concrete mixtures, especially given the variety of fibers that are available in the market. Five types of fibers (polypropylene [PP], glass, basalt, polyvinyl alcohol [PVA], and steel) possessing different aspect ratios were considered in this study. The concrete mechanical properties—including the resistance to sorptivity, heat, and freezing-and-thawing cycles—were evaluated. Test results showed that the best environmental/cost/durability indicator was achieved for concrete prepared with 0.25% PVA or PP fibers by volume. This indicator gradually degraded with the use of basalt, glass, and steel fibers because of higher cost and greenhouse gas emissions generated during the fiber manufacturing. The use of PVA fibers significantly enhanced the resistance to heat and freezing-and-thawing cycles, while the least-performing concrete contained basalt fibers with relatively reduced flexural properties and increased sorptivity.

Keywords: durability; effect of heat; fibers; life-cycle assessment (LCA); mechanical properties.

INTRODUCTION

The use of fiber-reinforced concrete (FRC) mixtures has remarkably increased in the construction industry, especially because of their superior load-carrying and post-cracking capacities (Matar and Assaad 2019; Söylev and Özturan 2014). Fibers incorporated in concrete delay the formation and propagation of cracks, making them particularly beneficial for members subjected to fatigue and cyclic loadings (Ramezanianpour et al. 2013; Abou Rachied et al. 2023).

The existence of different fibers in the market often creates confusion among civil engineers when selecting the proper type for a given application (Hannawi et al. 2016). ASTM C1116/C1116M-10a (2010) outlines four types of fibers, including steel, alkali-resistant glass, synthetic (that is, polypropylene [PP], polymeric, or polyester), and natural. MPC 17-342 (Ghadban et al. 2017) reported that the lack of comparative data and guidance for proper fiber selection often led to reduced durability and an unbalanced cost-to-performance ratio. Generally, it is understood that the type of fibers, along with their concentration and geometry, have a direct impact on the concrete mechanical properties and durability, such as water absorption and resistance to fire and freezing-and-thawing cycles (Jamshaid and Mishra 2016; Jabbour et al. 2022).

Velayutham and Cheah (2014) reported that the FRC strength (compressive and flexural) gradually increased at higher steel fiber volume rates up to 3%. Li et al. (2021) showed that the steel FRC mass loss reduced by 15 to 30% after 25 freezing-and-thawing cycles, while the relative dynamic elastic modulus increased by 5 to 15%. Beigi et al. (2013) found that the PP fibers slightly reduced the FRC compressive strength, contrarily to the glass fibers, which led to higher compressive and tensile strengths. Ramesh and Eswari (2021) noticed a compression ductile behavior for basalt FRC specimens, with the modulus of rupture increased by 13% to 57% when the fibers were added at 0.5% to 1.5%, respectively. The optimum dosage was 0.15%, at which the improvement in tensile strength reached 23%. Regardless of the fiber type (PP, steel, carbon, or glass), Ali et al. (2021) concluded that the durability of concrete containing 0.5% carbon or PP fibers was better than the glass or steel FRC mixtures. Polyvinyl alcohol (PVA) fibers are commonly used in engineered cementitious composite (ECC) applications requiring high strain-hardening and ductility performances (Li et al. 2001). Such fibers have shown superior properties due to increased chemical and frictional bonds with the cement paste, albeit their use in FRC mixtures is still relatively limited.

Thermal gradients induced by elevated temperatures can deteriorate the hardened cement matrix, leading to internal cracking and reduced mechanical properties (Bezerra et al. 2019). Arioz (2009) reported a slight reduction in the concrete strengths at 400°C, while signs of surface cracking started showing at temperatures above 600°C. Drzymała et al. (2017) reported that the compressive strength of PP-type FRC increased slightly at 300°C but experienced a significant reduction at 600°C. This trend did not apply to the tensile and flexural strengths, which gradually dropped at higher temperatures. Wu et al. (2020) showed that high-tensile-strength fibers (such as steel) could prevent the growth of microcracks by creating a barrier when the concrete is heated and cooled. In contrast, low-melting-point fibers (such as PP) could offer pathways for water vapor to escape at elevated temperatures, thus reducing the gradient effects and internal pore pressure. Varghese et al. (2023) evaluated the effect of 12 mm fibers (basalt, carbon, glass, PP, and PVA) on the strength of concrete exposed to elevated temperatures for different time intervals. Regardless of the fiber type, such additions improved the concrete plastic deformation without rapid failure, increased energy absorption, and reduced the post-fire damage.

ACI Materials Journal, V. 122, No. 3, May 2025.

MS No. M-2023-343.R4, doi: 10.14359/51746712, received October 3, 2024, and reviewed under Institute publication policies.

Table 1—Physical properties and cost of different fibers (Al Ghali et al. 2023)

Fiber type	Density, kg/m^3	Tensile strength, MPa	Length (L), mm	Diameter (D), mm	Aspect ratio (L/D)	Thermal degradation temperature, °C	Fibers per m^3 at 0.25% rate, millions	Average cost, €/kg
PP-42	910	600 to 730	38	0.9	42	300 to 350	0.01	10.55
PP-270	910	570 to 660	19	0.07	270	300 to 350	3.4	14.07
Glass	2700	1700	12	0.013	920	300 to 500	157	8.74
Basalt	2670	2900 to 3100	12	0.017	700	350 to 500	92	15.73
PVA	1300	1600	8	0.037	210	230 to 250	29.1	8.00
Steel	7850	1100 to 1600	30	1	30	600 to 800	0.01	1.76

Unlike durability, the life cycle and environmental impacts of FRC mixtures incorporating various types of fibers are not yet fully understood (Song et al. 2009). In fact, the rapid advancements in the construction industry have accelerated the depletion of natural resources, contributing directly to hazardous emissions and climate change (Wernet et al. 2016; Akbar and Liew 2021). In 2022, the International Energy Agency (IEA) estimated that up to 13% of global greenhouse gas emissions are attributed to the embodied carbon in construction materials (IEA 2023).

Although some studies have reported on the environmental aspect of specific fibers, the results are derived from different studies that employed varying methods and baselines for comparison. Consequently, no single study has normalized these methods and provided a comprehensive comparison of different fibers in terms of environmental impact, performance, and cost. This lack of standardized comparison further complicates the understanding of FRC performance and highlights the need for more uniform and holistic research in this area. For instance, Van den Heede et al. (2018) reported that PVA fibers had a higher environmental impact than cement, reaching approximately 130%, 230%, and 220% in ozone depletion, human toxicity, and freshwater ecotoxicity, respectively. The effect of PVA fibers on climate change was estimated to be 3.4 times higher than that of PP fibers (Van den Heede et al. 2018). Basalt fibers are assumed to be green and safe (Zhang et al. 2021) because they are derived from natural sources. These fibers are created from the melting of rocks derived from volcanic origin, with diameters ranging between 13 and 20 μm (Özkan and Demir 2020).

RESEARCH SIGNIFICANCE

This paper is part of a comprehensive work undertaken at the American University of Beirut (AUB) to evaluate the environmental impact of fibers, including their effect on the cost and durability of FRC mixtures (Al Ghali et al. 2023). Two monofilament PP fibers, along with glass, basalt, PVA, and steel fibers, were tested. Investigated properties include compressive strength, tensile strength, flexural strength, modulus of elasticity, sorptivity, and resistance to moderate heat and freezing-and-thawing cycles. The significance of this work stems from civil engineers' interest in acquiring more knowledge on FRC properties and life-cycle assessment (LCA), thus offering solutions for optimized durability-to-cost-to-environmental impact for the building and construction industry.

EXPERIMENTAL PROCEDURE

Materials

As already noted, this paper is the continuation of a previous work undertaken by Al Ghali et al. (2023), where the description of materials used is detailed. In brief, a Type I portland cement conforming to ASTM C150/C150M, natural siliceous sand, and two types of limestone coarse aggregates were used. The high-range water-reducer (HRWR) complied with ASTM C494/C494M and had a solid content and specific gravity of 42% and 1.22, respectively. The manufacturer's recommended dosage varies between 0.25 and 2% of the cement mass; increased additions are expected to delay the setting times.

The fibers' physical properties and cost are summarized in Table 1 (Al Ghali et al. 2023). Two types of monofilament PP fibers are considered (Tuladhar and Yin 2019), with their melting points and degradation temperatures hovering at approximately 170 to 190°C and 300 to 350°C, respectively. Those PP fibers had different length-to-diameter (L-to-D) sizes of 38 x 0.9 mm and 19 x 0.07 mm, which resulted in an aspect ratio (L/D) of 42 and 270, respectively (referred to as PP-42 and PP-270, respectively). The scanning electron microscope (SEM) images reflect their surface morphology, which comprised smooth-texture single-strand fibers (Fig. 1).

The glass and basalt fiber filaments (Fig. 2) are produced from molten glassy or crushed basalt rocks. Many researchers, such as Jamshaid and Mishra (2016), Dopko (2018), and Ali et al. (2021), found that FRC made with basalt fibers exhibited improved strength and durability properties compared to other mixtures prepared with glass fibers. The average tensile strengths for glass and basalt fibers are 1700 and 3000 MPa, respectively, while their L-to-D sizes are 12 x 0.013 mm and 12 x 0.017 mm, respectively (Table 1). The PVA fibers are produced by polymerizing the vinyl acetate polymers and then treating the resulting monofilaments with alkaline catalysts (Li et al. 2001). This type of fiber degrades at approximately 230 to 250°C; their length, diameter, and tensile strength are 8 mm, 0.037 mm, and 1600 MPa, respectively. The SEM images for the glass, basalt, and PVA fibers reflect their smooth texture (Fig. 2).

Hooked-end steel fibers with tensile strength values ranging between 1100 and 1600 MPa were used (Fig. 2).

Fig. 1—Photos and SEM images for PP-42 and PP-270 fibers (Al Ghali et al. 2023).

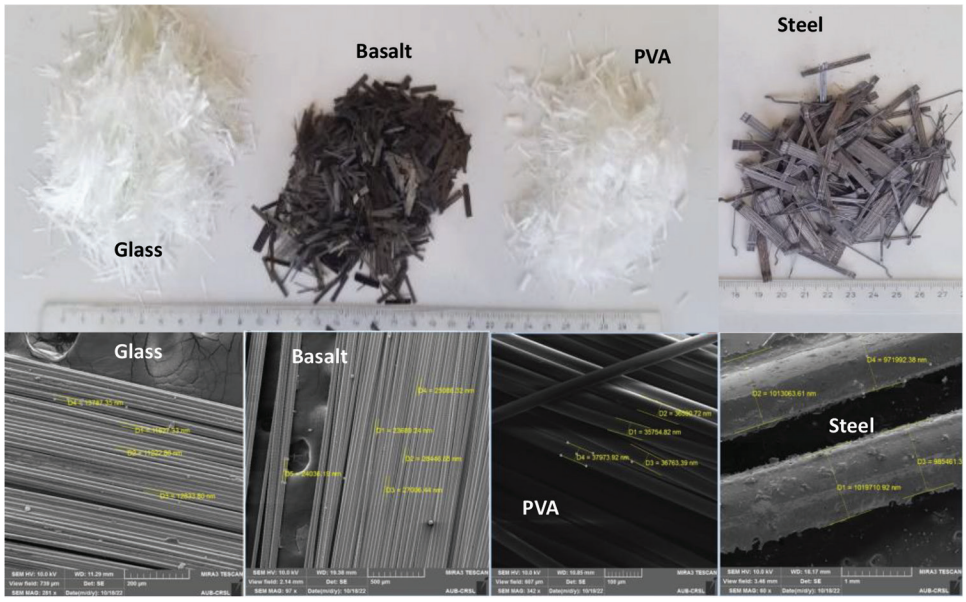

Fig. 2—Photos and SEM images for glass, basalt, PVA, and steel fibers (Al Ghali et al. 2023).

The deformed hooked ends would improve anchorage and friction with the hardened cement mortar (Hamad and Abou Haidar 2011; Marcos-Meson et al. 2020). The length and diameter of the steel fibers are 30 and 1 mm, respectively. The SEM images reveal the presence of very light irregularities and potholes on their top surfaces, which could improve the bond properties with the cement matrix (Hwang et al. 2015; Frazão et al. 2016).

Concrete proportions and batching

The concrete used in this work contained 400 kg/m^3 cement and 200 L of water (that is, a water-cement ratio [*w*/*c*] of 0.5), while the natural sand, fine aggregate, and coarse aggregate were 702, 611, and 407 kg/m^3, respectively. The expected 28-day characteristic compressive strength was approximately 40 ± 2.5 MPa. The HRWR dosage was adjusted in the control mixture (that is, fiber-free) at 0.25% of the cement mass to secure a slump of 200 ± 20 mm.

The volume of various fibers used was 0.25%, except for the steel fibers, which were tested at 0.25 and 0.5%. The HRWR demand (Table 2) remarkably increased with fiber additions to attain the targeted workability due to increased internal friction and fiber clumping (Khayat et al. 2003; Assaad and Khayat 2006). The steel fibers required the least HRWR demand, given their nonabsorbent nature and increased relative density. The glass and basalt fibers required 1.5% HRWR, compared to 1% and 1.25% for the PP-42 and PP-270 fibers, respectively. Larger fiber volumes would increase the HRWR demand beyond the manufacturer's recommendations, which could detrimentally affect the stability of the concrete mixture.

The procedure used for concrete mixing consisted of homogenizing the aggregates with the fibers and half the mixing water for approximately 1 minute. After securing proper fiber dispersion, cement was added with the remaining water, followed by HRWR, and the concrete was mixed for 2 minutes. After a resting period of half a minute, the concrete mixing resumed for 1 additional minute.

Testing procedures

The compressive strength (f_c') of concrete specimens, splitting tensile strength (f_t), and modulus of elasticity (E) were measured as per ASTM C39/C39M-18 (2018), ASTM C496/C496M-17 (2017), and ASTM C469/C469M-22 (2022), respectively, using 100 x 200 mm cylinders. The flexural strength (f_r) was determined by third-point bending using 75 x 100 mm cross-sectional beams having 400 mm length, as per ASTM C78/C78M-18 (2018). Linear variable differential transducers (LVDTs) were used to measure the

Table 2—HRWR demand and mechanical properties for mixtures under ambient temperature or after being exposed to moderate heat of 230 ± 10°C

Fiber type	HRWR, % of cement	Ambient temperature					After heat exposure		
		f_c', MPa	f_t, MPa	E, GPa	f_r, MPa	δ_r, mm	f_c', MPa	f_r, MPa	δ_r, mm
Control	0.25	43.6	2.75	29.8	5.06	0.29	27.9	4.83	0.212
PP-42	1	49.2	3.29	30.9	11.08	0.86	31.4	5.96	0.59
PP-270	1.25	40.1	3.18	29.9	10.14	0.76	25.2	5.12	0.44
Glass	1.5	42	3.69	31.9	9.97	0.71	28	5.91	0.47
Basalt	1.5	48.5	3.57	30.1	10.51	0.66	30.1	6.11	0.59
PVA	1	43.2	3.41	29	8.75	0.74	35.3	7.07	0.66
Steel (0.25%)	0.75	47.5	3.04	31.3	8.35	0.7	28	5.23	0.47
Steel (0.5%)	1.5	51.9	3.41	36.7	10.43	0.84	33.4	6.04	0.56

midspan deflection (δ_r). All specimens were cured in water for 7 and 28 days.

The behavior of FRC mixtures at moderate heat was assessed by compression (100 x 200 mm cylinders) and flexure (75 x 100 x 400 mm beams) testing. Initially, the 28-day hardened specimens were removed from the water curing tanks and kept for 5 days at ambient temperature with 50 ± 10% relative humidity. The specimens were then placed for a period of 120 minutes in an electric oven whose temperature was already preset at 230 ± 10°C. It is important to note that the specimens were not oven-dried prior to heat exposure to maintain the risk of spalling and assess the fiber-bridging effect for the different FRC mixtures (Arioz 2009; Ramezanianpour et al. 2013). Earlier studies showed that higher temperatures would cause the fibers to thermally decompose and lose their bridging effect, causing the degradation of concrete strength to be attributed to other mechanisms, such as the decomposition of calcium-silicate-hydrate (C-S-H) compounds, the transformation of the aggregate skeleton, and cracking of interfacial transition zones (Drzymała et al. 2017). After heating was completed, the specimens were left to cool down for 7 days at ambient temperature. Averages of two to three responses were considered.

The effect of repeated freezing-and-thawing cycles on strength degradation was determined as per ASTM C666-97 (1997). At the age of 28 days, the 75 x 100 x 400 mm prisms were placed in a chamber where temperature varied from 4 to –18°C for approximately 3.5 hours and then back again to produce 36 cycles every week. This process was continued for 2 additional weeks, making a total of 72 and 108 cycles. The degradation level due to freezing and thawing after each set of cycles was determined using the fundamental transverse frequency, as per ASTM C215-19 (2019). A so-called relative dynamic modulus of elasticity (P_c) was measured, as expressed in Eq. (1), where n and n_c are the fundamental transverse frequency after 0 and c cycles, respectively. Higher P_c values mean fewer cracks and voids created in the concrete sample and, thus, better durability and resistance against freezing-and-thawing cycles.

$$P_c\ (\%) = \frac{n_c^2}{n^2} \times 100 \quad (1)$$

The rate of water absorption, or sorptivity, was determined using concrete discs 100 mm in diameter and 75 mm in height, following ASTM C1585-20 (2020). The sides of the discs were sealed with epoxy resins to prevent evaporation, while the exposed surface was immersed in a 1 mm bed of water. The concrete mass was measured every hour for 6 hours and then daily for 7 days. The absorption index (I, mm) was determined as given in Eq. (2), whereby the initial rate of water absorption (W_i, mm/h$^{0.5}$) is the slope calculated from the linear regression of I versus the square root of time for values up to 6 hours. Similarly, the secondary rate of water absorption (W_s, mm/h$^{0.5}$) is the slope calculated from the linear regression of I versus the square root of time for values between 1 and 7 days. Averages of two to three responses were considered for the freezing-and-thawing cycles and sorptivity measurements. The I values are expressed as follows

$$I\,(\text{mm}) = \frac{\text{Change of mass at given time (g)}}{\text{Exposed surface area (mm}^2) \times \text{Density of water}\left(\frac{\text{g}}{\text{mm}^3}\right)} \quad (2)$$

MECHANICAL PROPERTIES AND DURABILITY

The 28-day mechanical properties—including f_c', f_t, E, f_r, and δ_r (maximum beam deflection)—determined under ambient temperature or after exposure to moderate heat are summarized in Table 2. The coefficient of variation (COV) was computed as the ratio between the mean values divided by the standard deviation, multiplied by 100. Hence, the maximum COV for f_c', E, and f_r, determined under ambient temperature, was 6.6%, 10.2%, and 9%, respectively, reflecting acceptable repeatability. The COV reached 10% and 13.5% for f_c' and f_r, respectively, when the specimens were exposed to heat. It is to be noted that the air content and unit weight of the tested concrete mixtures varied within 2.6 ± 0.4% and 2320 ± 35 kg/m^3, respectively.

The variation of any given mechanical property (Δ(Property), %) due to fiber additions was normalized with respect to the corresponding control concrete as indicated in Eq. (3)

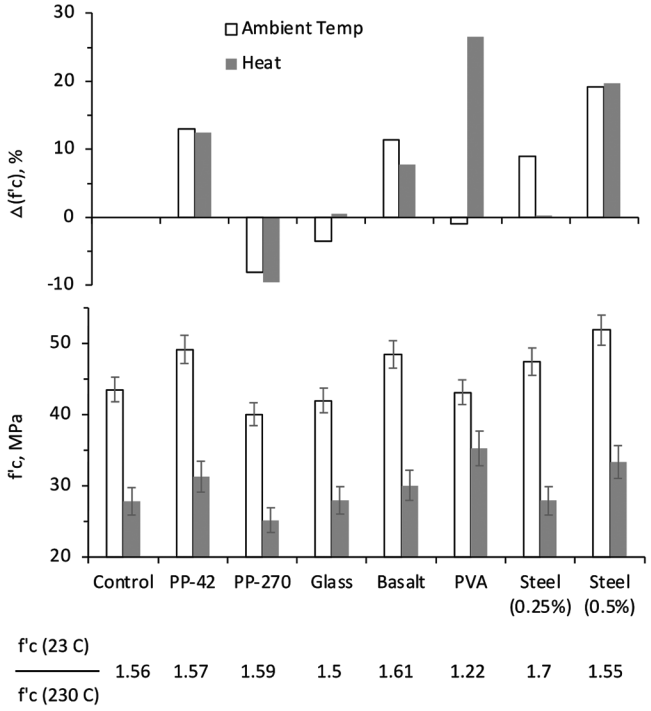

Fig. 3—Variations in f_c' *responses for mixtures cured in ambient temperature or after exposure to heat of 230 ± 10°C.*

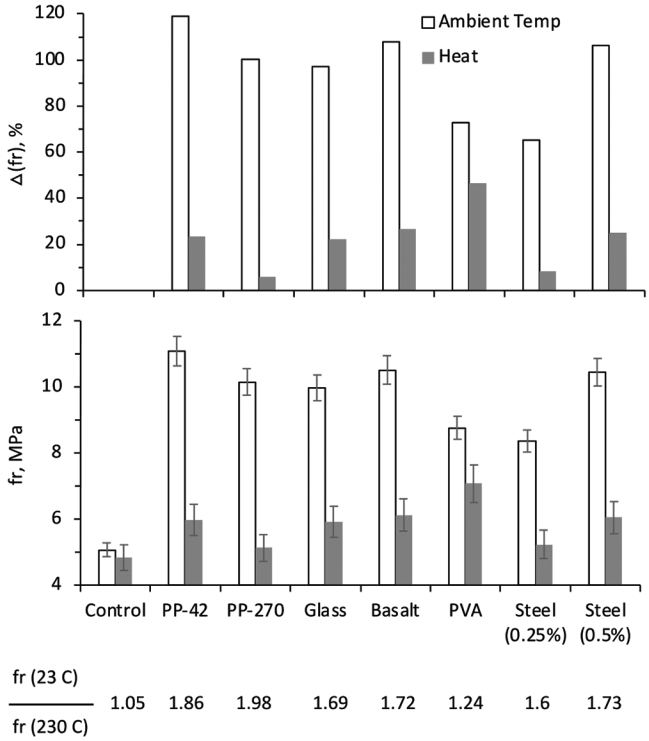

Fig. 4—Variations in f_r *responses for mixtures cured in ambient temperature or after exposure to heat of 230 ± 10°C.*

$$\Delta(\text{Property}) \text{ at given temperature, \%} = \frac{(\text{Property of FRC} - \text{Property of control mixture})}{\text{Property of control mixture}} \times 100 \quad (3)$$

Figure 3 plots the f_c' and $\Delta(f_c')$ responses determined under ambient temperature for various mixtures and shows the responses obtained after exposing the specimens to heat (which will be discussed later). Similar plots are given in Fig. 4 for the f_r responses.

Properties under ambient temperature

In general, the effect of fibers incorporated at a 0.25% rate on f_c' and E is relatively limited; the resulting $\Delta(f_c')$ and $\Delta(E)$ varied between –8% and 12% and between –3% and 7%, respectively. Similar trends are often reported in the literature, reflecting the marginal effect of fibers incorporated at moderate rates on the cement matrix porosity and interfacial transition zones of normal-strength concrete mixtures (Mastali and Dalvand 2017; Yuan and Jia 2021). However, as shown in Fig. 3, the incorporation of 0.5% steel fibers seems efficient for strengthening the concrete skeleton in compression, which increased the f_c' and E responses (that is, the $\Delta(f_c')$ and $\Delta(E)$ reached 19.7% and 23.2%, respectively). This can be attributed to the high-density nature of this kind of fiber, including its hooked-end shape, which enhances the capacity to control the propagation of cracks during loading (Hamad and Abou Haidar 2011). It is to be noted that a relatively weak relationship with a correlation coefficient (R^2) of 0.4 can be established between f_c' and E responses for all tested mixtures, given as: E (GPa) = 0.369(f_c', MPa) + 14.33.

Regardless of the fiber type, the tensile-related properties (f_r and f_t) improved for FRC mixtures (Fig. 4), which can be mainly attributed to the fiber-bridging effect, which increases the resistance to tensile stresses and restrains the propagation of cracks (Hannawi et al. 2016). As shown in Fig. 4, the improvement in f_r determined for specimens cured and tested under ambient temperature was particularly significant, with $\Delta(f_r)$ varying between 65 and 118%, reflecting the relevance of fibers for beams tested under flexure. Hence, the f_r increased from 5.06 MPa for the control mixture to 9.97, 10.51, and 11.08 MPa for mixtures incorporating 0.25% of glass, basalt, and PP-42 fibers, respectively. During the splitting tensile testing, such values varied from 2.75 MPa for the control mixture to 3.69, 3.57, and 3.29 MPa, respectively. The f_r and f_t responses for FRC containing PVA fibers were 8.75 and 3.41 MPa, respectively. Because of the higher bridging effect, the tensile-related properties improved when the steel fibers dosage increased from 0.25 to 0.5%; the resulting f_r increased from 8.35 to 10.43 MPa, and f_t varied from 3.04 to 3.41 MPa. A good relationship with R^2 of 0.85 can be established between f_r and f_t responses determined for specimens cured and tested under ambient temperature, expressed as follows: f_r (MPa) = –10.8(f_t, MPa)^2 + 74.6(f_t, MPa) – 118.3.

The improvement in f_r responses due to fiber additions was accompanied by a remarkable increase in maximum beam deflection (δ_r) recorded at failure (Table 2). For example, δ_r varied from 0.29 mm for the control mixture to 0.66, 0.74, and 0.86 mm for mixtures containing basalt, PVA, or PP-42 fibers, respectively; the resulting $\Delta(\delta_r)$ was 126%, 155%, and 196%, respectively. Such an increase is normally associated with the fiber-bridging effect, which limits the cracking and propagation of fissures, transmitting the stresses to the surrounding concrete and leading to improved ductility and

higher energy transfer before beam failure (Ridha et al. 2020). Figure 5 plots the relationships between f_r and δ_r measurements for all tested beams, whether under ambient temperature or after being exposed to heat; the resulting R^2 values were 0.81 and 0.75, respectively.

Effect of moderate heat on hardened properties

Exposing the concrete cylinders to moderate heat of 230 ± 10°C led to reduced f_c' responses for the different fibers used (Fig. 3); for example, the value decreased from 43.6 to 27.9 MPa ($f_{c23}'/f_{c230}' = 1.56$) for the control mixture and from 48.5 to 30.1 MPa ($f_{c23}'/f_{c230}' = 1.61$) for the basalt FRC mixture. This can be attributed to a number of concurrent physical and chemical changes, such as the decomposition of the ettringite between 50 and 110°C and the loss of water that vaporizes from the macropores when the temperature exceeds 100°C. This causes a loss in concrete weight accompanied by pressure build-up and thermal expansion within the skeleton, leading to the formation of fissures and, eventually, explosive spalling. Explosive spalling is often assumed to occur at high temperatures; however, many researchers have observed it at early heat stages (that is, at approximately 200°C), mostly depending on the initial moisture state, heating rate, and material's tensile strength (Arioz 2009; Akca and Özyurt 2018). Typically, when the temperature reaches approximately 350°C, the calcium hydroxide in the cement begins to dehydrate, while the aggregate phase starts decomposing at 700°C, generating significant strength reduction (Paul et al. 2020).

Signs of explosive spalling were observed on the exterior surfaces of specimens (whether cylinders or beams) containing glass and basalt fibers, reflecting that the concrete was not able to dissipate the pressure build-up during heating. In contrast, FRC mixtures prepared with PP (PP-42 and PP-270), PVA, and steel fibers exhibited limited signs of explosive spalling. The mechanism that prevented spalling in PP-type FRC can be attributed to the creation of microchannels in the concrete mass after reaching the melting point (170 to 190°C), thus allowing the water vapor to evacuate and release the pore pressure. The FRC specimens prepared with PVA or steel fibers combated spalling either because of their relatively stable nature against moderate heat of 230°C or because of their hooked-end shape, which enhanced the bridging effect within the concrete skeleton (Tiberti et al. 2015; Issa and Assaad 2015).

With the exception of the PVA-type FRC mixture, the $\Delta(f_c')$ values determined under ambient temperature are pretty similar to those obtained after exposing the specimens to moderate heat (Fig. 3). This physically reflects that the PP, glass, basalt, and steel fibers have marginal influence on the concrete compressive strength, whether tested under ambient or elevated temperatures. In contrast, the $\Delta(f_c')$ significantly varied from –1% to +26.5% for the PVA-based mixture, and the resulting f_{c23}'/f_{c230}' ratio of 1.22 was the lowest among all other FRC and control mixtures (Fig. 3). This suggests that PVA fibers appear to maintain efficiency at moderate heat exposure of 230°C and efficiently contribute to minimizing the loss in strength; similar trends were obtained for the flexure testing, as will be discussed later. Magalhães et al. (2013) reported that although melting of PVA fibers starts at approximately 220°C, the thermal analysis showed that complete mass loss does not occur before 600°C. Liu and Tan (2018) studied the effect of elevated temperature on residual properties of PVA-based cementitious composites and found that the melting of fibers might have created a network that was much more permeable than the plain matrix and reduced the likelihood of spalling.

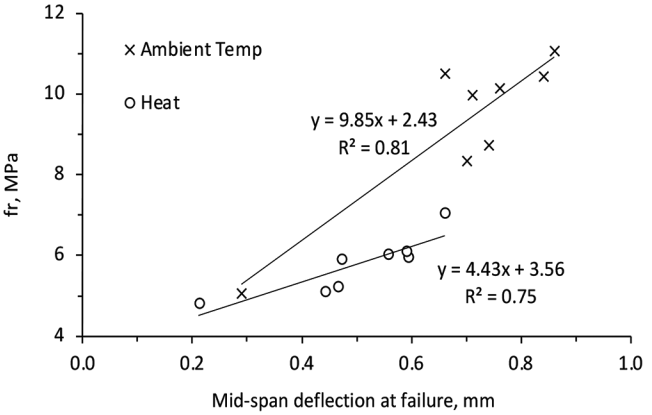

Fig. 5—Relationships between f_r *and* δ_r *for beams tested under ambient temperature or after being exposed to heat of 230 ± 10°C.*

The effect of exposing the concrete beams to heat curtailed the strength properties, leading to reduced f_r responses (Fig. 4). As explained earlier, this can be related to a combination of physical and chemical changes associated with weight loss, thermal shrinkage, and microcracking in the interfacial transition zones that could deteriorate the hardened properties. Nevertheless, it is interesting to note that the control mixture exhibited the lowest f_{r23}/f_{r230} ratio of 1.05; that is, the corresponding f_r varied from 5.06 to 4.83 MPa when testing under ambient or moderate temperature, respectively. The f_r remarkably dropped for the other FRC mixtures; for example, it varied from 11.08 to 5.96 MPa for the PP-42 mixture and from 10.51 to 6.11 MPa for the basalt mixture (the corresponding f_{r23}/f_{r230} ratios are 1.86 and 1.72, respectively). This can be attributed to the nature of the flexural strength test, in which the presence of fibers plays a determinant role in limiting the propagation of cracks in the tensile zone (Wang et al. 2019; Jabbour et al. 2022). The relatively increased f_{r23}/f_{r230} values recorded for FRC mixtures reflect the significant loss in the fiber-bridging effect due to moderate heat exposure. Hence, the $\Delta(f_r)$ significantly varied from 119 to 23.4% for the PP-42 mixture and from 108 to 26.5% for the basalt mixture. The $\Delta(f_r)$ determined under moderate heat increased from 8.3% to 25% for the FRC containing 0.25% or 0.5% steel fibers, respectively, reflecting the importance of increasing the steel fibers content to enhance the bridging effect and mitigate the drop in strength.

As with f_c', the lowest f_{r23}/f_{r230} ratio of 1.24 among other FRC mixtures corresponded to the mixture containing PVA fibers, corroborating their proper efficiency at moderate heat exposure of 230°C to minimize the loss in strength. The resulting $\Delta(f_r)$ varied from 73% to 46.4% when testing under ambient or moderate temperature conditions, respectively.

Table 3—Resistance to freezing-and-thawing cycles and sorptivity measurements

	Resistance to freezing and thawing							Sorptivity, mm/hr$^{0.5}$	
	n_0, Hz	n_{36}, Hz	n_{72}, Hz	n_{108}, Hz	P_{c36}, %	P_{c72}, %	P_{c108}, %	W_i	W_s
Control	1553	1264.5	ND	ND	66.3	ND	ND	0.619	0.309
PP-42	1775	954	ND	ND	28.9	ND	ND	0.341	0.189
PP-270	1708.5	1420	910	754.5	69.1	28.4	19.5	0.331	0.207
Glass	1730.5	1353.5	780	ND	61.2	20.3	ND	0.933	0.325
Basalt	1775	1598	495	ND	81.1	7.8	ND	0.882	0.306
PVA	1753	1398	843	743.5	63.6	23.1	18	0.424	0.279
Steel (0.25%)	1642	1131.5	ND	ND	47.5	ND	ND	0.638	0.346
Steel (0.5%)	1708.5	821	ND	ND	23.1	ND	ND	—	—

Note: ND means that the specimen collapsed after the specified number of freezing-and-thawing cycles.

Pourfalah (2018) concluded that after exposure to temperatures beyond 150°C (that is, near the melting point of PVA fibers), the failure mode of dog-bone-shaped samples used for direct tensile assessment changed from rupture to pullout, which changed the behavior from deflection hardening to deflection softening.

Effect of fibers on freezing-and-thawing resistance

Table 3 summarizes the n (fundamental transverse frequency) and corresponding P_c (relative dynamic modulus of elasticity) responses determined after subjecting the various concrete specimens to 0, 36, 72, and 108 freezing-and-thawing cycles. It also reports the sorptivity measurements (W_i and W_s).

The variations in P_c responses after 36, 72, and 108 cycles are plotted in Fig. 6. Generally speaking, the incorporation of medium-to-high-aspect-ratio fibers (that is, PP-270, glass, basalt, and PVA) seems to marginally affect the concrete resistance against freezing and thawing after 36 cycles; the resulting P_c varied within 70 ± 10% compared to the control mixture, which yielded a value of 66.3%. Most researchers agree that fibers can improve frost resistance due to the reduced development of microcracks under freezing-and-thawing cycles and the increased number of closed pores that can relieve the water pressure upon freezing in the cement matrix (Paul et al. 2020; Li et al. 2021). Yet, the frost resistance remarkably degraded with the use of PP-42 and steel fibers possessing low aspect ratios of 42 and 30, respectively. Hence, the P_c dropped to 28.9% for the mixture containing PP-42 fibers and to 47.5% and 23.1% for mixtures prepared with 0.25% or 0.5% steel fibers, respectively. This may be attributed to the long fiber shapes (that is, low aspect ratio), which reduce the resistance against microcrack formations, causing damage to the cement matrix. The control and FRC mixtures containing PP-42 or steel fibers completely broke after 72 cycles, reflecting their vulnerability against frost attack.

As shown in Fig. 6, the FRC mixtures prepared using the medium-to-high aspect ratio fibers did not fully degrade after 72 cycles, while only those containing PP-270 and PVA fibers resisted frost up to 108 cycles. Hence, the P_c values reached 28.4 and 19.5% after 72 and 108 cycles, respectively, for the FRC made using PP-270, while those values were 23.1

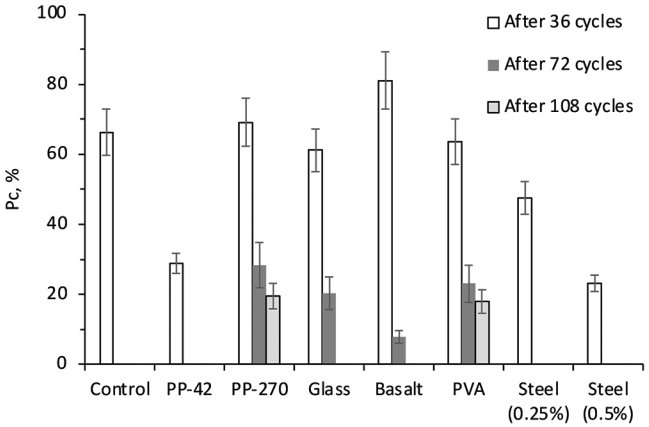

Fig. 6—Variations in P_c *responses determined after 36, 72, and 108 freezing-and-thawing cycles.*

and 18% for the PVA fiber mixture. Such results agree pretty well with others reported in the literature, confirming the benefits of PP and PVA fibers for the durability of concrete exposed to frost conditions. For example, Ma et al. (2018) studied the frost resistance of concrete containing PP fibers and showed that such additions positively contributed to the reduction of frost damage to the cement matrix. Nam et al. (2016) proved the benefits of PVA and PP fibers to the durability of concrete subjected to freezing-and-thawing cycles, albeit the PVA fibers were more efficient because of enhanced adhesion and better tensile properties than the PP. Li et al. (2021) reported that the mass loss is not a relevant index for frost damage evaluation of FRC mixtures; rather, the P_c measurements could be much more informative.

Effect on sorptivity

As expected, the absorption index (I) varied linearly over time, reflecting that water absorption increases at a constant rate with R^2 values larger than 0.97. The W_i and W_s responses are computed as the slope of the straight lines fitted between the square root of time and I measurements. Figure 7 plots the W_i and W_s responses for the various tested mixtures. As shown, the W_i remarkably decreased from 0.619 to 0.424 mm/h$^{0.5}$ for the control and PVA-based concrete, respectively. This was also the case with the incorporation of PP fibers, which reduced the W_i measurements to 0.341 and 0.331 mm/h$^{0.5}$ for mixtures containing PP-42 and

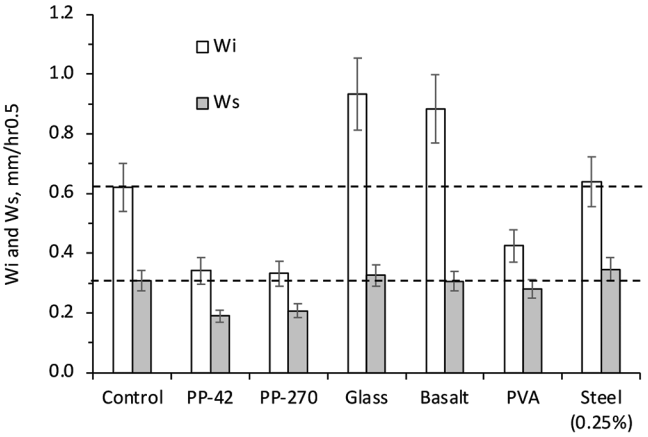

Fig. 7—Variations in W_i *and* W_s *responses for various tested mixtures.*

PP-270 fibers, respectively. This reveals that the PP and PVA fibers are beneficial in attenuating the level of water absorption during the first 6 hours of immersion in water. Many researchers attributed this behavior to the fiber-bridging effect, which reduces the development of cracks and the material's proneness toward water absorption by capillarity (Paul et al. 2020). Nevertheless, mixtures prepared using glass or basalt fibers exhibited relatively higher W_i values that reached 0.933 and 0.882 mm/h$^{0.5}$, respectively. It is worth noting that for longer-duration testing times (from 1 to 7 days), the influence of fibers seems to become marginal, reflecting that sorptivity becomes more affected by the level of porosity and compacity of the matrix. Hence, the resulting W_s values remained pretty close to the control value (within 0.309 ± 0 .1 mm/h$^{0.5}$).

COST AND ENVIRONMENTAL IMPACT ANALYSIS

Traditionally, the cost and performance aspects have been decisively adopted for developing concrete mixtures. Yet, nowadays, the environmental impact of material production and embodied carbon emissions have become additional concerns, especially with the pledges to decrease Global Warming Potential and mitigate climate change (UNFCCC 2015). In this study, the cost analysis for the different FRC mixtures is performed, followed by an LCA and environmental impact analysis, followed by an overall holistic analysis taking into consideration cost, environment, and performance.

Cost of control and FRC mixtures

Table 1 summarizes the average market prices provided by different suppliers for the various considered fibers. While the control mixture is estimated to cost 70 euros (€)/m^3, the basalt FRC mixture had the highest cost of 175 €/m^3, followed by the mixture containing steel (0.5%) fibers, glass, and then steel (with 0.25%) with a cost of 140, 129, and 104.5 €/m^3, respectively. The PP fibers mixtures had the lowest cost of 94 and 102 €/m^3, mostly because of the relatively cheap cost of the PP, including its relatively lower density, which reduces the amount used in the concrete mixture. In summary, the increase in cost due to fiber additions ranged between 34% (that is, the PP-42 fiber mixture) and 150% (that is, the basalt fiber mixture) compared to the control mixture.

Table 4—LCI to produce 1 kg of PP, glass, basalt, PVA, and steel fibers

Type of fibers	Input material/energy	Quantity/1 kg of fibers	Reference
PP	Polypropylene granules	1 kg	Akbar and Liew (2021)
	Water	22.78 kg	
	Lubricating oil	0.01585 kg	
	Heat (industrial furnace)	0.6 MJ	
Glass	Nylon 6 granules	0.28 kg	Akbar and Liew (2021)
	Silica sand	0.37 kg	
	Clay	0.464 kg	
	Limestone	0.351 kg	
	Electricity mixture	1.61 kW·h	
	Process steam from natural gas	14.5 MJ	
Basalt	Basalt	1 kg	Jamshaid and Mishra (2016)
	Heat and electricity	8 MJ	
PVA	PVA granules	1 kg	Van den Heede et al. (2018)
	Water	22.78	
	Heat (industrial furnace)	0.6 MJ	
Steel	Steel fibers	1 kg	ecoinvent database (Wernet et al. 2016)

Environmental cost

LCA is a useful technique for estimating the environmental emissions generated from any given production process (Song et al. 2009). The study herein considered a cradle-to-gate cycle analysis, which included the extraction and production phases. The functional unit is taken as one cubic meter for each FRC containing a specified fiber volume, cement, aggregates, and HRWR. The information related to the materials flow and energy consumption of the production cycles is gathered in a life-cycle inventory (LCI), as shown in Table 4.

To produce PP fibers, the raw PP granules are melted using an industrial furnace and then transformed into fibers using the wet-spinning method (Akbar and Liew 2021), consuming 0.6 MJ of energy. For glass fibers, different raw materials (including clay, limestone, silica sand, and boric acid) are melted into monofilament fibers at an energy of 14.5 MJ (Akbar and Liew 2021). Basalt fibers are manufactured using basalt rocks that are crushed and melted at extremely high temperatures of 1450 to 1500°C, then passed into bushings to produce the monofilament fibers. For PVA fibers, ethers or vinyl esters are polymerized with vinyl acetate to form PVA granules, which are then melted and turned into fibers (Van den Heede et al. 2018). The data for the production of steel fibers is collected from the ecoinvent databases (Wernet et al. 2016). As inferred from Table 5, the

Table 5—Normalized values of mechanical properties, cost, environmental impact, and durability-to-cost-to-environmental indicator (I_n)

	f_c'*	f_t*	f_r*	(f_{c230}'/f_{c23}')*	(f_{r230}/f_{r23})*	P_{c36}*	$(1/W_i)$*	Cost*	ECI*	Indicator I_n
Control	1.00	1.00	1.00	1.00	1.00	1.00	1.00	1.00	1.00	1.00
PP-42	**1.13**	1.20	**2.19**	1.00	0.56	0.44	1.82	**1.34**	**1.04**	**1.00**
PP-270	0.92	1.16	2.00	0.98	0.53	1.04	**1.87**	1.46	**1.04**	0.97
Glass	0.96	**1.34**	1.97	1.04	0.62	0.92	0.66	1.84	1.09	0.73
Basalt	1.11	1.30	2.08	0.97	0.61	**1.22**	0.70	2.50	1.05	0.64
PVA	0.99	1.24	1.73	**1.28**	**0.85**	0.96	1.46	1.37	1.06	**1.00**
Steel (0.25%)	1.09	1.11	1.65	0.92	0.66	0.72	0.97	1.49	**1.04**	0.80
Steel (0.5%)	1.19	1.24	2.06	1.01	0.61	0.35	—	2.00	1.08	0.70

Table 6—Environmental impacts for studied categories calculated using openLCA and ECI estimated for all FRC mixtures

	Environmental impacts				
	Global Warming Potential, kg CO_2-eq	Ozone depletion, kg CFC-11-eq	Acidification of soil and water, kg SO_2-eq	Eutrophication, kg PO_4^{3-} eq	ECI, €
Control	366.465	1.9×10^{-5}	0.897	0.1035	22.84
PP-42	373.291	1.9×10^{-5}	0.929	0.151	23.73
PP-270	373.805	1.9×10^{-5}	0.931	0.151	23.77
Glass	392.187	1.9×10^{-5}	1.05	0.116	24.86
Basalt	383.633	1.9×10^{-5}	0.984	0.1035	24.05
PVA	385.429	1.9×10^{-5}	1.008	0.1035	24.24
Steel (0.25%)	382.329	1.9×10^{-5}	0.916	0.1035	23.71
Steel (0.5%)	398.705	1.9×10^{-5}	0.950	0.116	24.78

main inputs for the environmental impact are the materials used and the energy consumed during production.

The environmental impacts are calculated for different environmental impact categories using openLCA software and based on ecoinvent databases (Wernet et al. 2016). The calculated impacts are transferred into a common unit: the Environmental Cost Indicator (ECI). The ECI is a monetary amount (in euros) that is equivalent to the cost of repairing the environmental damage caused throughout the life cycle of the studied product (Wernet et al. 2016). The studied environmental categories include the Global Warming Potential, ozone depletion, acidification of soil and water, and eutrophication, and their ECI values are 0.05 €/kg CO_2-eq, 30 €/kg CFC-11-eq, 4 €/kg SO_2-eq, and 9 €/kg PO_4-eq, respectively (Wernet et al. 2016). The ECI factors are used to transform the environmental impact obtained for each category into a common unit, which is a monetary cost in euros. For the category of Global Warming Potential, to remediate the damage to the environment caused by 1 kg of CO_2-eq emissions, a cost of €0.05 is needed.

The environmental impacts for the various tested mixtures at different categories are presented in Table 6, along with the overall ECI (in euros), which represents the cost needed to repair the environmental damage caused by producing each mixture. Clearly, the most significant environmental impact is in the global warming category. This is due to the cement production, which emits large amounts of carbon and thus contributes, on average, to more than 92% of the total environmental impact of the mixtures, as inferred from the detailed LCA reports obtained in this study. Although the impacts on the ozone depletion category are minimal (Table 6), this category was considered because its ECI factor is relatively high (600 times that of Global Warming Potential). Moreover, the estimated impacts on acidification of soil and water and on eutrophication are not negligible, as those categories have ECI factors that are 80 and 180 times higher than that of global warming, respectively. The mixture that has the highest overall environmental impact, indicated by the highest ECI, is the FRC with glass fibers, followed by the FRC with steel (0.5%), and then the FRC with PVA. However, the increase in the environmental impact resulting from adding fibers is less than 10% compared to the control mixture.

Durability-to-cost-to-environmental impact indicator (I_n)

A durability-to-cost-to-environmental impact indicator (I_n) is defined as the sum of the normalized performance obtained from the experimental work divided by the normalized cost and ECI values (refer to Eq. (4)). The asterisk (*) indicates that the values are normalized with respect to the control mixture. The values in the numerator correspond to the mechanical properties whose increase is beneficial; these include the compressive, splitting tensile, and flexural strengths, the concrete's ability to maintain compressive and flexural strengths at elevated temperatures, resistance to

freezing and thawing, and the inverse of sorptivity (because the W_i values are desired to be low). The values in the denominator correspond to those whose increase is not beneficial to the overall evaluation, including the purchasing cost and environmental impact.

$$I_n = \frac{2}{7} \times \frac{f_{c_{23}}'^{*} + f_t^{*} + f_r^{*} + (f_{c_{230}}'/f_{c_{23}}')^{*} + (f_{r_{230}}/f_{r_{23}})^{*} + P_{c_{36}}{}^{*} + \left(\frac{1}{W_i}\right)^{*}}{\text{Cost}^{*} + \text{ECI}^{*}} \quad (4)$$

The normalized values are listed in Table 5 (with the best values for each property shown in bold). The seven terms in the numerator, which are related to the performance, are considered to be of equal importance; thus, they are each given a weighting factor of 1/7. The two terms in the denominator represent the cost and the environmental impact and are given a weighting factor of 1/2. Values of I_n greater than or equal to 1.00 indicate that the overall enhancement in performance justifies the increase in cost and environmental impacts that result from fiber additions.

Except for FRC mixtures containing PP-42 and PVA fibers, the I_n values are less than 1.00 (Table 5). This means that the incorporation of PP-270, glass, basalt, and steel fibers does not significantly enhance the concrete durability to justify the additional costs of the fibers. As indicated previously, the environmental impact of adding fibers is not substantial because the main contributor is the cement, which was the same in all mixtures. The increase in ECI varies between 4 and 9%, with limited effect on I_n. However, the purchasing cost of the fibers appears to considerably affect I_n; for example, the cost of FRC with basalt fibers is 2.5 times higher than the control mixture, which significantly reduced I_n to 0.64 (although this mixture showed the highest resistance to freezing and thawing, with a normalized P_{c36} value of 1.22, and enhancement in flexural strength of 108%). The highest I_n corresponds to FRC prepared with PP-42 or PVA fibers with a value of 1.00, indicating that the enhancement in durability is just enough to justify the additional fiber costs (which are 34% and 37% higher than the control, respectively). The second highest I_n is for the FRC containing PP-270 fibers with a value of 0.97, pretty close to 1.00. This mixture has the highest normalized inverse of the sorptivity indicator and increased resistance to freezing-and-thawing cycles, which is beneficial for durability.

When taking all factors into consideration, the best FRC mixtures are those containing PP-42 and PVA fibers. In the case of PP-42, the increased I_n value can be attributed to higher compressive and flexural strengths and a low normalized cost and environmental impact. For PVA, the increased I_n value is due to improved resistance to heat and sorptivity, in addition to the fibers' relatively low cost and environmental impact. In other words, even though PP-42 and PVA mixtures have the same I_n value, their "winning" points are different. When the FRC is expected to be exposed to elevated temperature or freezing-and-thawing cycles, PVA fibers should be selected. In contrast, the PP-42 fibers are recommended because of their reduced cost and concrete enhancement in flexural strength (119% better than the control) and resistance to water absorption (82% better than the control).

CONCLUDING REMARKS

Unlike durability, the life cycle and environmental impacts of fiber-reinforced concrete (FRC) incorporating various types of fibers are not yet fully understood. In fact, no single study has normalized the assessment methods and provided a comprehensive comparison of different fibers in terms of environmental impact, performance, and cost. In this context, the research reported in this paper sought to assess the effect of different fibers (polypropylene [PP], glass, basalt, polyvinyl alcohol [PVA], and steel) on the concrete mechanical properties, along with their impact on concrete costs and environmental emissions.

Based on the foregoing, test results showed that the tensile-related properties (f_r and f_t) increased with fiber additions due to a higher bridging effect. The improvement in flexural strength was accompanied by a remarkable increase in the beam's deflection, reflecting better ductility. Signs of explosive spalling were observed on the exterior surfaces of glass- and basalt-type FRC specimens exposed to moderate heat of 230 ± 10°C. In contrast, mixtures containing PP, PVA, and steel fibers exhibited limited signs of explosive spalling. The best resistance to heat was achieved for PVA fibers, as reflected by the minimized strength loss.

The resistance to frost remarkably degraded with the use of fibers possessing low aspect ratios (PP-42 and steel). The FRC prepared using the medium-to-high-aspect-ratio fibers did not fully degrade after 72 cycles, with the best performance achieved with PP-270 and PVA fibers. Unlike the glass, basalt, and steel fibers, the use of PP and PVA fibers is beneficial to reducing the concrete's proneness toward water absorption by capillarity. The influence of fibers becomes marginal for longer test durations (that is, from 1 to 7 days), reflecting that sorptivity becomes more affected by the porosity and compacity of the matrix.

The increase in concrete cost due to fiber additions ranged between 34 and 150%, with basalt fibers being the most expensive and PP-42 fibers the cheapest. The increase in the environmental impact varied from 4 to 9%, with glass fibers having the largest impact. When accounting for the concrete durability, cost, and environmental impact, the PP-42 and PVA fibers were found to be the most effective, with a durability-to-cost-to-environmental impact indicator of 1.0. This indicator dropped to 0.64 and 0.73 for mixtures containing basalt and glass fibers, respectively.

AUTHOR BIOS

Ali Farhat *is a Graduate Student in the Department of Civil and Environmental Engineering at the American University of Beirut (AUB), Beirut, Lebanon.*

Adel Chahrour *is a Graduate Student in the Department of Civil and Environmental Engineering at AUB.*

Bilal Hamad, *FACI, is a Professor in the Department of Civil and Environmental Engineering at AUB. He received his BE from AUB and his MS and PhD from The University of Texas at Austin, Austin, TX. He received the ACI Structural Research Award in 1995. His research interests include*

the design, behavior, and strengthening of reinforced concrete structures, concrete technology, and sustainable construction materials.

Joseph J. Assaad *is a Professor in the Department of Civil and Environmental Engineering at the University of Balamand, Balamand, Lebanon. He received his PhD from the University of Sherbrooke, Sherbrooke, QC, Canada. His research interests include composite materials, durability, three-dimensional (3-D) printing, recycling of aggregates and other waste materials, and sustainability in construction.*

Alissar Yehya *is an Assistant Professor in the Department of Civil and Environmental Engineering at AUB. Her research interests include the mechanics and physics of earth and environmental processes, thermo-hydro-mechanical behavior of porous materials and permeability evolution by subsurface damage and healing processes, and sustainable engineering.*

ACKNOWLEDGMENTS

The authors wish to thank the American University of Beirut (AUB) for funding this research through the University Research Board grant number 104111. Also, the authors highly appreciate the assistance of the laboratory staff at the CEE Materials Lab of AUB in the fabrication and testing of the concrete specimens.

REFERENCES

Abou Rachied, T.; Dbouk, F.; Hamad, B.; and Assaad, J. J., 2023, "Structural Behavior of Beams Cast Using Normal and High Strength Concrete Containing Blends of Ceramic Waste Powder and Blast Furnace Slag," *Cleaner Materials*, V. 7, Mar., Article No. 100179. doi: 10.1016/j.clema.2023.100179

Akbar, A., and Liew, K. M., 2021, "Multicriteria Performance Evaluation of Fiber-Reinforced Cement Composites: An Environmental Perspective," *Composites Part B: Engineering*, V. 218, Aug., Article No. 108937. doi: 10.1016/j.compositesb.2021.108937

Akca, A. H., and Özyurt, N., 2018, "Effects of Re-Curing on Microstructure of Concrete after High Temperature Exposure," *Construction and Building Materials*, V. 168, pp. 431-441. doi: 10.1016/j.conbuildmat.2018.02.122

Al Ghali, A. E.; El Ezz, N. E.; Hamad, B.; Assaad, J.; and Yehya, A., 2023, "Comparative Study on Shear Strength and Life Cycle Assessment of Reinforced Concrete Beams Containing Different Types of Fibers," *Case Studies in Construction Materials*, V. 19, Dec., Article No. e02497. doi: 10.1016/j.cscm.2023.e02497

Ali, B.; Raza, S. S.; Hussain, I.; and Iqbal, M., 2021, "Influence of Different Fibers on Mechanical and Durability Performance of Concrete with Silica Fume," *Structural Concrete*, V. 22, No. 1, Feb., pp. 318-333. doi: 10.1002/suco.201900422

Arioz, O., 2009, "Retained Properties of Concrete Exposed to High Temperatures: Size Effect," *Fire and Materials*, V. 33, No. 5, Aug./Sept., pp. 211-222. doi: 10.1002/fam.996

Assaad, J. J., and Khayat, K. H., 2006, "Effect of Mixture Consistency on Formwork Pressure Exerted by Highly Flowable Concrete," *Journal of Materials in Civil Engineering*, ASCE, V. 18, No. 6, Dec., pp. 786-791. doi: 10.1061/(ASCE)0899-1561(2006)18:6(786)

ASTM C39/C39M-18, 2018, "Standard Test Method for Compressive Strength of Cylindrical Concrete Specimens," ASTM International, West Conshohocken, PA, 8 pp.

ASTM C78/C78M-18, 2018, "Standard Test Method for Flexural Strength of Concrete (Using Simple Beam with Third-Point Loading)," ASTM International, West Conshohocken, PA, 5 pp.

ASTM C215-19, 2019, "Standard Test Method for Fundamental Transverse, Longitudinal, and Torsional Resonant Frequencies of Concrete Specimens," ASTM International, West Conshohocken, PA, 7 pp.

ASTM C469/C469M-22, 2022, "Standard Test Method for Static Modulus of Elasticity and Poisson's Ratio of Concrete in Compression," ASTM International, West Conshohocken, PA, 6 pp.

ASTM C496/C496M-17, 2017, "Standard Test Method for Splitting Tensile Strength of Cylindrical Concrete Specimens," ASTM International, West Conshohocken, PA, 5 pp.

ASTM C666-97, 1997, "Standard Test Method for Resistance of Concrete to Rapid Freezing and Thawing," ASTM International, West Conshohocken, PA, 6 pp.

ASTM C1116/C1116M-10a, 2010, "Standard Specification for Fiber-Reinforced Concrete," ASTM International, West Conshohocken, PA, 7 pp.

ASTM C1585-20, 2020, "Standard Test Method for Measurement of Rate of Absorption of Water by Hydraulic-Cement Concretes," ASTM International, West Conshohocken, PA, 6 pp.

Beigi, M. H.; Berenjian, J.; Lotfi Omran, O.; Sadeghi Nik, A.; and Nikbin, I. M., 2013, "An Experimental Survey on Combined Effects of Fibers and Nanosilica on the Mechanical, Rheological, and Durability Properties of Self-Compacting Concrete," *Materials & Design*, V. 50, Sept., pp. 1019-1029. doi: 10.1016/j.matdes.2013.03.046

Bezerra, A. C. S.; Maciel, P. S.; Corrêa, E. C. S.; Soares Junior, P. R. R.; Aguilar, M. T. P.; and Cetlin, P. R., 2019, "Effect of High Temperature on the Mechanical Properties of Steel Fiber-Reinforced Concrete," *Fibers*, V. 7, No. 12, Dec., Article No. 100. doi: 10.3390/fib7120100

Dopko, M., 2018, "Fiber Reinforced Concrete: Tailoring Composite Properties with Discrete Fibers," master's thesis, Iowa State University, Ames, IA, 177 pp.

Drzymała, T.; Jackiewicz-Rek, W.; Tomaszewski, M.; Kuś, A.; Gałaj, J.; and Šukys, R., 2017, "Effects of High Temperature on the Properties of High Performance Concrete (HPC)," *Procedia Engineering*, V. 172, pp. 256-263. doi: 10.1016/j.proeng.2017.02.108

Frazão, C.; Barros, J.; Camões, A.; Alves, A. C.; and Rocha, L., 2016, "Corrosion Effects on Pullout Behavior of Hooked Steel Fibers in Self-Compacting Concrete," *Cement and Concrete Research*, V. 79, Jan., pp. 112-122. doi: 10.1016/j.cemconres.2015.09.005

Ghadban, A. A.; Wehbe, N. I.; and Underberg, M., 2017, "Fiber-Reinforced Concrete for Structure Components," Report No. MPC 17-342, Mountain-Plains Consortium, Fargo, ND, 166 pp.

Hamad, B. S., and Abou Haidar, E. Y., 2011, "Effect of Steel Fibers on Bond Strength of Hooked Bars in High-Strength Concrete," *Journal of Materials in Civil Engineering*, ASCE, V. 23, No. 5, May, pp. 673-681. doi: 10.1061/(ASCE)MT.1943-5533.0000230

Hannawi, K.; Bian, H.; Prince-Agbodjan, W.; and Raghavan, B., 2016, "Effect of Different Types of Fibers on the Microstructure and the Mechanical Behavior of Ultra-High Performance Fiber-Reinforced Concretes," *Composites Part B: Engineering*, V. 86, Feb., pp. 214-220. doi: 10.1016/j.compositesb.2015.09.059

Hwang, J. P.; Jung, M. S.; Kim, M.; and Ann, K. Y., 2015, "Corrosion Risk of Steel Fibre in Concrete," *Construction and Building Materials*, V. 101, Part 1, Dec., pp. 239-245. doi: 10.1016/j.conbuildmat.2015.10.072

IEA, 2023, "CO2 Emissions in 2022," International Energy Agency, Paris, France, 19 pp.

Issa, C. A., and Assaad, J. J., 2015, "Bond of Tension Bars in Underwater Concrete: Effect of Bar Diameter and Cover," *Materials and Structures*, V. 48, No. 11, Nov., pp. 3457-3471. doi: 10.1617/s11527-014-0414-4

Jabbour, R.; Assaad, J. J.; and Hamad, B., 2022, "Cost-to-Performance Assessment of Polyvinyl Alcohol Fibers in Concrete Structures," *Mechanics of Advanced Materials and Structures*, V. 29, No. 20, pp. 2973-2983. doi: 10.1080/15376494.2021.1882625

Jamshaid, H., and Mishra, R., 2016, "A Green Material from Rock: Basalt Fiber – A Review," *The Journal of the Textile Institute*, V. 107, No. 7, pp. 923-937. doi: 10.1080/00405000.2015.1071940

Khayat, K. H.; Pavate, T. V.; Assaad, J.; and Jolicoeur, C., 2003, "Analysis of Variations in Electrical Conductivity to Assess Stability of Cement-Based Materials," *ACI Materials Journal*, V. 100, No. 4, July-Aug., pp. 302-310.

Li, D.; Guo, Q.; and Liu, S., 2021, "Influence of Steel Fiber on Durability Performance of Concrete under Freeze-Thaw Cycles," *Advances in Materials Science and Engineering*, V. 2021, No. 1, Article No. 5460844. doi: 10.1155/2021/5460844

Li, V. C.; Wang, S.; and Wu, C., 2001, "Tensile Strain-Hardening Behavior of Polyvinyl Alcohol Engineered Cementitious Composite (PVA-ECC)," *ACI Materials Journal*, V. 98, No. 6, Nov.-Dec., pp. 483-492.

Liu, J.-C., and Tan, K. H., 2018, "Mechanism of PVA Fibers in Mitigating Explosive Spalling of Engineered Cementitious Composite at Elevated Temperature," *Cement and Concrete Composites*, V. 93, Oct., pp. 235-245. doi: 10.1016/j.cemconcomp.2018.07.015

Ma, H.; Yu, H.; Li, C.; Tan, Y.; Cao, W.; and Da, B., 2018, "Freeze–Thaw Damage to High-Performance Concrete with Synthetic Fibre and Fly Ash due to Ethylene Glycol Deicer," *Construction and Building Materials*, V. 187, Oct., pp. 197-204. doi: 10.1016/j.conbuildmat.2018.07.189

Magalhães, M. S.; Toledo Filho, R. D.; and Fairbairn, E. M. R., 2013, "Durability Under Thermal Loads of Polyvinyl Alcohol Fibers," *Matéria*, V. 18, No. 4, Dec., pp. 1587-1595. doi: 10.1590/S1517-70762013000400018

Marcos-Meson, V.; Solgaard, A.; Fischer, G.; Edvardsen, C.; and Michel, A., 2020, "Pull-Out Behavior of Hooked-End Steel Fibres in Cracked Concrete Exposed to Wet-Dry Cycles of Chlorides and Carbon Dioxide – Mechanical Performance," *Construction and Building Materials*, V. 240, Apr., Article No. 117764. doi: 10.1016/j.conbuildmat.2019.117764

Mastali, M., and Dalvand, A., 2017, "Fresh and Hardened Properties of Self-Compacting Concrete Reinforced with Hybrid Recycled Steel–Polypropylene Fiber," *Journal of Materials in Civil Engineering,* ASCE, V. 29, No. 6, June, p. 04017012. doi: 10.1061/(ASCE)MT.1943-5533.0001851

Matar, P., and Assaad, J. J., 2019, "Concurrent Effects of Recycled Aggregates and Polypropylene Fibers on Workability and Key Strength Properties

of Self-Consolidating Concrete," *Construction and Building Materials*, V. 199, Feb., pp. 492-500. doi: 10.1016/j.conbuildmat.2018.12.091

Nam, J.; Kim, G.; Lee, B.; Hasegawa, R.; and Hama, Y., 2016, "Frost Resistance of Polyvinyl Alcohol Fiber and Polypropylene Fiber Reinforced Cementitious Composites Under Freeze Thaw Cycling," *Composites Part B: Engineering*, V. 90, Apr., pp. 241-250. doi: 10.1016/j.compositesb.2015.12.009

Özkan, Ş., and Demir, F., 2020, "The Hybrid Effects of PVA Fiber and Basalt Fiber on Mechanical Performance of Cost Effective Hybrid Cementitious Composites," *Construction and Building Materials*, V. 263, Dec., Article No. 120564. doi: 10.1016/j.conbuildmat.2020.120564

Paul, S. C.; van Zijl, G. P. A. G.; and Šavija, B., 2020, "Effect of Fibers on Durability of Concrete: A Practical Review," *Materials*, V. 13, No. 20, Oct., Article No. 4562. doi: 10.3390/ma13204562

Pourfalah, S., 2018, "Behaviour of Engineered Cementitious Composites and Hybrid Engineered Cementitious Composites at High Temperatures," *Construction and Building Materials*, V. 158, Jan., pp. 921-937. doi: 10.1016/j.conbuildmat.2017.10.077

Ramesh, B., and Eswari, S., 2021, "Mechanical Behaviour of Basalt Fibre Reinforced Concrete: An Experimental Study," *Materials Today: Proceedings*, V. 43, Part 2, pp. 2317-2322. doi: 10.1016/j.matpr.2021.01.071

Ramezanianpour, A. A.; Esmaeili, M.; Ghahari, S. A.; and Najafi, N. H., 2013, "Laboratory Study on the Effect of Polypropylene Fiber on Durability, and Physical and Mechanical Characteristic of Concrete for Application in Sleepers," *Construction and Building Materials*, V. 44, July, pp. 411-418. doi: 10.1016/j.conbuildmat.2013.02.076

Ridha, M. M. S.; Al-Shaarbaf, I. A. S.; and Sarsam, K. F., 2020, "Experimental Study on Shear Resistance of Reactive Powder Concrete Beams Without Stirrups," *Mechanics of Advanced Materials and Structures*, V. 27, No. 12, pp. 1006-1018. doi: 10.1080/15376494.2018.1504258

Song, Y. S.; Youn, J. R.; and Gutowski, T. G., 2009, "Life Cycle Energy Analysis of Fiber-Reinforced Composites," *Composites Part A: Applied Science and Manufacturing*, V. 40, No. 8, Aug., pp. 1257-1265. doi: 10.1016/j.compositesa.2009.05.020

Söylev, T. A., and Özturan, T., 2014, "Durability, Physical and Mechanical Properties of Fiber-Reinforced Concretes at Low-Volume Fraction," *Construction and Building Materials*, V. 73, Dec., pp. 67-75. doi: 10.1016/j.conbuildmat.2014.09.058

Tiberti, G.; Minelli, F.; and Plizzari, G., 2015, "Cracking Behavior in Reinforced Concrete Members with Steel Fibers: A Comprehensive Experimental Study," *Cement and Concrete Research*, V. 68, Feb., pp. 24-34. doi: 10.1016/j.cemconres.2014.10.011

Tuladhar, R., and Yin, S., 2019, "Production of Recycled Polypropylene (PP) Fibers from Industrial Plastic Waste Through Melt Spinning Process," *Use of Recycled Plastics in Eco-efficient Concrete*, F. Pacheco-Torgal, J. Khatib, F. Colangelo, and R. Tuladhar, eds., Woodhead Publishing, Sawston, UK, pp. 69-84. doi: 10.1016/B978-0-08-102676-2.00004-9

UNFCCC, "Paris Agreement," United Nations Framework Convention on Climate Change, Paris France, Dec. 12, 2015, 30 pp.

Van den Heede, P.; Mignon, A.; Habert, G.; and De Belie, N., 2018, "Cradle-to-Gate Life Cycle Assessment of Self-Healing Engineered Cementitious Composite with In-House Developed (Semi-)Synthetic Superabsorbent Polymers," *Cement and Concrete Composites*, V. 94, Nov., pp. 166-180. doi: 10.1016/j.cemconcomp.2018.08.017

Varghese, A.; Anand, N.; Andrushia, D.; Lubloy, E.; and Arulraj, P., 2023, "Investigation of the Post-Fire Performance and Flexural Behaviour Modeling of FRC Exposed to a Standard Fire," *Structural Engineering International*, V. 33, No. 2, pp. 238-257. doi: 10.1080/10168664.2021.1953427

Velayutham, G., and Cheah, C. B., 2014, "The Effects of Steel Fibre on the Mechanical Strength and Durability of Steel Fibre Reinforced High Strength Concrete (SFRHSC) Subjected to Normal and Hygrothermal Curing," *MATEC Web of Conferences*, V. 10, Article No. 02004. doi: 10.1051/matecconf/20141002004

Wang, X.; He, J.; Mosallam, A. S.; Li, C.; and Xin, H., 2019, "The Effects of Fiber Length and Volume on Material Properties and Crack Resistance of Basalt Fiber Reinforced Concrete (BFRC)," *Advances in Materials Science and Engineering*, V. 2019, No. 1, Article No. 7520549. doi: 10.1155/2019/7520549

Wernet, G.; Bauer, C.; Steubing, B.; Reinhard, J.; Moreno-Ruiz, E.; and Weidema, B., 2016, "The ecoinvent Database Version 3 (Part I): Overview and Methodology," *The International Journal of Life Cycle Assessment*, V. 21, No. 9, Sept., pp. 1218-1230. doi: 10.1007/s11367-016-1087-8

Wu, H.; Lin, X.; and Zhou, A., 2020, "A Review of Mechanical Properties of Fibre Reinforced Concrete at Elevated Temperatures," *Cement and Concrete Research*, V. 135, Sept., Article No. 106117. doi: 10.1016/j.cemconres.2020.106117

Yuan, Z., and Jia, Y., 2021, "Mechanical Properties and Microstructure of Glass Fiber and Polypropylene Fiber Reinforced Concrete: An Experimental Study," *Construction and Building Materials,* V. 266, Part A, Jan., Article No. 121048.

Zhang, C.; Wang, Y.; Zhang, X.; Ding, Y.; and Xu, P., 2021, "Mechanical Properties and Microstructure of Basalt Fiber-Reinforced Recycled Concrete," *Journal of Cleaner Production*, V. 278, Jan., Article No. 123252. doi: 10.1016/j.jclepro.2020.123252

ACI MATERIALS JOURNAL TECHNICAL PAPER

Title No. 122-M15

Fatigue Tension-Softening Constitutive Model of Normal-Strength Concrete

by Hong Chen, Meng-Di Jia, Rena C. Yu, Jian-Jun Zheng, and Zhi-Min Wu

The fatigue tension-softening constitutive model of concrete is a crucial material property for the nonlinear analysis of fatigue crack propagation processes. However, existing models are derived and calibrated based on concrete with a single strength grade, which limits their applicability. To address this issue, this study develops a fatigue tension-softening constitutive model applicable to normal-strength grade concrete. First, based on the fracture test results of three-point bending (TPB) beams, the relationship between the external work and the energy consumed for fatigue crack propagation is established using the principle of energy conservation. The second-order derivative of this relationship is then used to determine the cohesive stress under fatigue loading. It is found that the cohesive stress decreases with the increase in both fatigue crack opening displacement and the number of fatigue cycles. For a given fatigue load level, the higher the tensile strength of the concrete, the slower the degradation rate of cohesive stress. Subsequently, by introducing the number of fatigue cycles, crack opening displacement, and tensile strength as key parameters, the fatigue tension-softening constitutive model for normal-strength concrete is formulated. Finally, the model is validated by using it to predict the fatigue crack propagation length, fatigue life, and stress intensity factor at the fatigue failure of TPB beams and comparing these predictions with experimental results. The model proposed in this study provides essential parameters for evaluating the fatigue fracture performance of concrete.

Keywords: compressive strength grade; crack propagation; fatigue fracture; tension-softening constitutive model.

INTRODUCTION

Concrete structures such as bridge decks, airport runways, pavements, and offshore structures are subjected to fatigue loading during their service life. This loading can lead to the initiation and propagation of fatigue cracks, ultimately resulting in the fatigue failure of the structures. Accurately predicting the fatigue crack propagation process is critical to implementing appropriate strengthening measures. According to the fictitious crack model,[1] quantifying the degradation of cohesive stress under fatigue loading, also referred to as the tension-softening constitutive model, is a crucial input for such predictions. Consequently, the modeling of the fatigue constitutive model of concrete has garnered significant attention, and extensive research has been conducted in this area.

Currently, research on the fatigue tension-softening constitutive model of concrete can be broadly categorized into two main areas. The first category focuses on the quantitative analysis of the unloading-reloading characteristics of cohesive stress under cyclic loading. Reinhardt et al.[2] and Yankelevsky and Reinhardt[3] proposed the relationship between the cohesive stress and the crack opening displacement (COD) (σ-w) of concrete under cycle loading and reported that the degradation of cohesive stress was influenced by the COD and the number of cycles. Gylltoft[4] proposed a theoretical model to characterize the tensile failure of concrete subjected to cyclic loading and demonstrated that fatigue failure occurs when all the energy consumed in the fracture process zone (FPZ) by unloading-reloading cycles is equal to the fracture energy of concrete under monotonic loading. Based on the aforementioned studies, Hordijk[5] presented a continuous σ-w relationship for predicting the fatigue crack propagation in four-point bending beams and introduced the envelope curve, the unloading curve, the gap in the envelope curve, and the reloading curve to describe the degradation of cohesive stress. Subsequently, Hordijk[6] and Zhang et al.[7,8] found that the cohesive stress varies linearly with the logarithm of the number of fatigue cycles and presented a fatigue σ-w relationship of concrete by considering the unloading-reloading hysteresis. In the frame of dimensionless stress-deformation coordinates, Zhang et al.[9] proposed a model to describe the hysteretic behaviors of concrete under cyclic tension and tension-compression loading according to the crack closing-opening mechanism. As uniaxial fatigue tension tests have some eccentricity in the testing process, three-point bending (TPB) tests on concrete beams under fatigue loading were conducted by Toumi and Bascoul[10] to determine the fatigue σ-w relationship with the fracture energy and tensile strength of concrete and the unloading and reloading hysteresis loop. By considering the unloading-reloading hysteresis and the cohesive stress degradation, Horii et al.[11] proposed an analytical fatigue σ-w relationship for predicting the fatigue crack propagation process of concrete under low-cycle fatigue loading. However, the proposed relationship ignores the effect of the unloading process and is not suitable for high-cycle fatigue crack propagation. By considering the difference between unloading and reloading paths, Yang et al.[12] presented a fatigue σ-w relationship to characterize the irreversible damage process in the FPZ and simulated the propagation of mode I and mixed-mode fatigue cracks. With the assumption that the unloading and reloading paths were linear, Xu and Yuan[13,14] presented a fatigue σ-w relationship suitable for mixed-mode

ACI Materials Journal, V. 122, No. 3, May 2025.

MS No. M-2024-044.R2, doi: 10.14359/51746713, received February 26, 2025, and reviewed under Institute publication policies.

fracture, in which the extended finite element method was combined to simulate the mixed-mode fatigue crack propagation in single-edge notched beams. Toyama et al.[15] proposed a constitutive model by considering the degradation of traction stress caused by cyclic loading, and the finite element method was combined to simulate the fatigue crack growth in concrete. With the energy-based method, a fatigue σ-w relationship of concrete was reported by Skar et al.,[16] which could characterize the fatigue fracture behavior of concrete with a hinge model. By considering the stiffness degradation and the irreversible displacement accumulation, Xi and Yang[17] proposed a new cyclic cohesive zone model of concrete for low-cycle fatigue, and the predicted fatigue life was in reasonable agreement with experimental results. Subsequently, Lima and Bittencourt[18] presented a low-cycle cohesive fatigue model of concrete by considering the size dependence and simulated the crack propagation in TPB beam specimens with different sizes. Kumar and Ray[19] proposed a fatigue crack propagation rate law of concrete under fatigue loads by considering the influence of size, loading frequency, and stress amplitude. It was found that the fatigue life and the critical fatigue crack length increase with the increase of specimen size and loading frequency but decrease with the increase of stress amplitude. Baktheer et al.[20] introduced a phase-field cohesive zone method to simulate the fatigue crack propagation in concrete, which contributes to the unified modeling of high-cycle fatigue and low-cycle fatigue of concrete. Although these studies can effectively capture the fatigue fracture mechanism of concrete and provide reasonable predictions of fatigue crack propagation length and fatigue life, the determination and application of these tension-softening constitutive models are complex and time-consuming. This is particularly true when considering the hysteretic behavior of concrete under high-cycle fatigue. As a result, there is a strong demand for the development of a simpler fatigue tension-softening constitutive model for concrete. This need has spurred the emergence and advancement of the second category of research, which focuses solely on the degradation of cohesive stress corresponding to the fatigue peak load.

Specifically, by assuming that the cohesive stress only exists during loading, Simon and Chandra Kishen[21] proposed a fatigue σ-w relationship of concrete by considering the interfacial fracture energy between the cement mortar and coarse aggregates. Based on the energy equivalence, Zhang et al.[22,23] derived a fatigue σ-w relationship for the polymer cement mortar-concrete interface and found that the degradation rate of the cohesive stress increases with the increase of fatigue COD and number of fatigue cycles. Jia et al.[24] tested notched TPB beams of C30 concrete under static loading, fatigue loading, and fatigue-static loading and proposed a σ-w relationship of concrete under fatigue loading from the view of energy for simulating mode I fatigue crack propagation. Although these models offer the advantage of ease of application, the empirical coefficients within them are highly dependent on the material properties of the concrete. For instance, the constitutive model proposed by Jia et al.[24] becomes invalid for concrete with compressive strength grades other than C30. From the perspective of evaluating the fatigue fracture performance of concrete, there is an urgent need to develop a fatigue tension-softening constitutive model that can be applied to concrete with varying compressive strength grades.

The purpose of this paper is to propose a fatigue tension-softening constitutive model applicable to normal-strength concrete (with compressive strength not exceeding 50 MPa [7.25 ksi]). First, based on the fatigue fracture test results of TPB beams designed with concrete compressive strengths of C20, C30, and C40, a fatigue tension-softening constitutive model for normal-strength concrete is derived and formulated. Second, the proposed model is integrated with an initial fracture toughness-based crack propagation criterion to simulate the mode I fatigue crack propagation process in concrete with different compressive strength grades. Finally, the predicted crack propagation length, fatigue life, and stress intensity factor (SIF) at fatigue failure are compared with experimental results to validate the effectiveness of the proposed fatigue tension-softening constitutive model.

RESEARCH SIGNIFICANCE

From the previous literature review, it is evident that for fatigue tension-softening constitutive models considering the evolution of cohesive stress under unloading-reloading cycles, accurately determining the mathematical form of the σ-w relationship is complex and challenging. This is particularly true when accounting for the fact that the degradation of cohesive stress in high-cycle fatigue does not reach the envelope curve of the σ-w relationships. For constitutive models focused on cohesive stress degradation under fatigue peak load, the fitted empirical coefficients are dependent on the material properties of concrete. However, to the best of the authors' knowledge, a universal constitutive model applicable to concrete with different compressive strengths has not yet been reported. Therefore, this study aims to investigate and develop a fatigue tension-softening constitutive relationship for concrete that features a simple mathematical expression and broad applicability. Based on the proposed model, it is anticipated that the nonlinear fatigue crack propagation and fatigue life of concrete structures can be predicted with reasonable accuracy. This would enable timely implementation of appropriate strengthening and repair measures, ultimately contributing to a reduction in the maintenance costs of concrete structures over their life cycle.

EXPERIMENTAL PROGRAM

Concrete materials and specimens

According to the authors' previous investigation,[25] concrete with designed compressive strength grades of C20, C30, and C40 was used to study its fatigue fracture properties. The mixture proportions of the concrete are detailed in Table 1, where the cementitious material consists of ordinary portland cement with a 28-day compressive strength of 42.5 MPa (6.16 kpsi). The fine aggregate is natural river sand, and the coarse aggregate is crushed limestone with particle sizes ranging from 5 to 10 mm (0.20 to 0.39 in.). The measured compressive strength (f_{cu}), tensile strength (f_t), elastic modulus (E), and Poisson's ratio (ν) of the concrete

Table 1—Mixture proportions of concrete, kg/m³

Strength grade	Cement	River sand	Lime-stone	Water	Fly ash	Water-binder ratio
C20	216	715	1167	210	92	0.68
C30	327	657	1204	195	—	0.60
C40	446	593	1102	214	—	0.48

Note: 1 kg/m³ = 1.6855 lb/yd³.

Table 2—Mechanical properties of concrete

Strength grade	f_{cu}, MPa	f_t, MPa	E, GPa	v
C20	29.71 ± 2.35	2.59 ± 0.13	28.63 ± 1.63	0.23 ± 0.02
C30	38.34 ± 2.06	3.16 ± 0.28	35.32 ± 1.51	0.24 ± 0.01
C40	49.12 ± 1.86	3.74 ± 0.34	38.49 ± 1.92	0.24 ± 0.02

Note: 1 MPa = 145 psi; 1 GPa = 145 ksi.

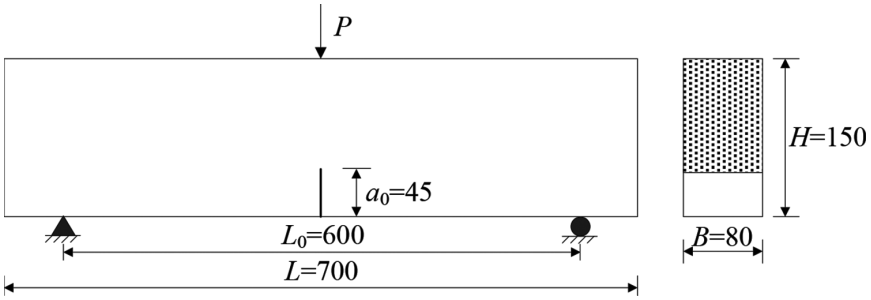

Fig. 1—Geometry of TPB beam. (Note: Units in mm; 1 mm = 0.0394 in.)

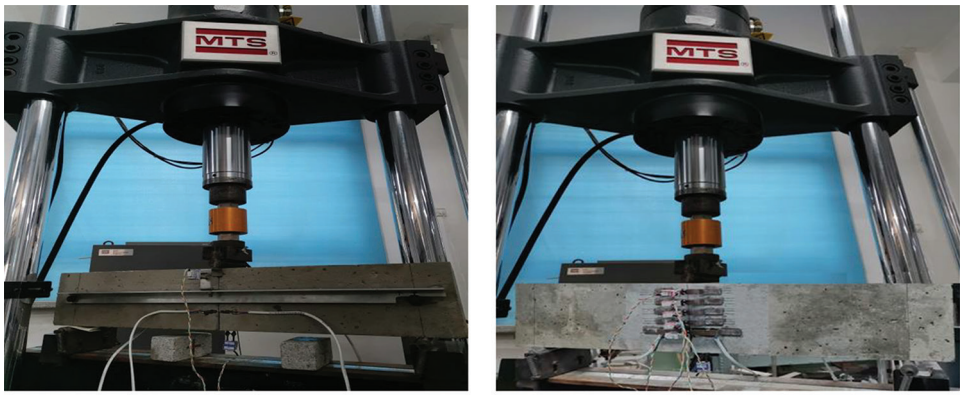

(a) Measurement of *CMOD* and δ (b) Measurement of *COD*

Fig. 2—Fatigue test setup.

for each designed strength grade are listed in Table 2. The geometry of the TPB beam specimen is illustrated in Fig. 1, where the span (L_0), height (H), width (B), and initial crack length (a_0) of the beams are 600, 150, 80, and 45 mm (23.64, 5.91, 3.15, and 1.70 in.), respectively.

Test setup

The fracture tests were conducted in three steps. First, nine TPB beams, comprising three different concrete compressive strength grades (three specimens per group), were tested under static loading to obtain the necessary parameters for conducting the fatigue tests. Second, 45 TPB beams with the same three compressive strength grades were tested under fatigue loading. For each strength grade, three load levels (0.7, 0.8, and 0.9) were selected, with five specimens tested at each load level. Finally, 210 TPB beams were initially subjected to fatigue loading until specific fatigue cycles were reached, followed by static loading until specimen failure. This procedure is referred to as fatigue-static testing. All fracture tests were performed using a closed-loop electro-hydraulic testing machine with a capacity of 250 kN (56,180 lbf), as illustrated in Fig. 2. An external load sensor with a capacity of 30 kN (6741.6 lbf) was used to record the load (P). The crack mouth opening displacement (CMOD) was measured using a clip gauge fixed at the crack mouth with a pair of knife edges. Simultaneously, the midspan deflection (δ) of the beam was recorded using a clip gauge positioned at the loading point, as shown in Fig. 2(a). To determine the initial cracking load, two strain gauges (10 x 2 mm [0.394 x 0.0788 in.]) were symmetrically installed 5 mm (0.197 in.) away from the crack tip on both lateral sides of the TPB beam to monitor strain variations. To measure the COD, five clip gauges were installed along the ligament at equal intervals of 20 mm (0.788 in.) from the crack tip to the top of the beam, as depicted in Fig. 2(b). All data were collected using a data acquisition system operating at a frequency of 20 Hz. Further details regarding the materials and fracture tests can be found in the original literature.[25]

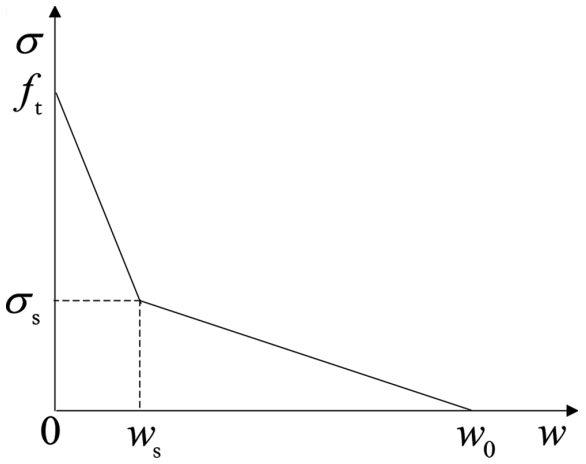

Fig. 3—Bilinear softening curve.

Table 3—Parameters of bilinear curves

Strength grade	f_t, MPa	G_f, N/m	w_0, mm	σ_s, MPa	w_s, mm
C20	2.59	128.94	0.18	0.86	0.040
C30	3.16	131.61	0.15	1.05	0.033
C40	3.74	135.42	0.13	1.25	0.029

Note: 1 MPa = 145 psi; 1 N/m = 0.205 bf/yd; 1 mm = 0.0394 in.

STATIC TENSION-SOFTENING CONSTITUTIVE MODEL

The static tension-softening constitutive model of concrete, including linear, bilinear, and exponential curves,[1,2,26,27] has been extensively studied. Among these, the bilinear curve has been widely adopted in practical engineering to predict crack propagation in concrete under static loading due to its simplicity and accuracy. Based on Petersson's investigation,[26] the bilinear model, as illustrated in Fig. 3, can be expressed as follows

$$\sigma_s = \frac{f_t}{3} \tag{1}$$

$$w_s = \frac{0.8\,G_f}{f_t} \tag{2}$$

$$w_0 = \frac{3.6\,G_f}{f_t} \tag{3}$$

where G_f and f_t represent the fracture energy and tensile strength of concrete, respectively; σ_s and w_s denote the cohesive stress and COD at the turning point of the curve; and w_0 is the critical COD. Based on the authors' previous test results,[25] the parameters σ_s, w_s, and w_0 for concrete with different compressive strength grades were determined and are listed in Table 3.

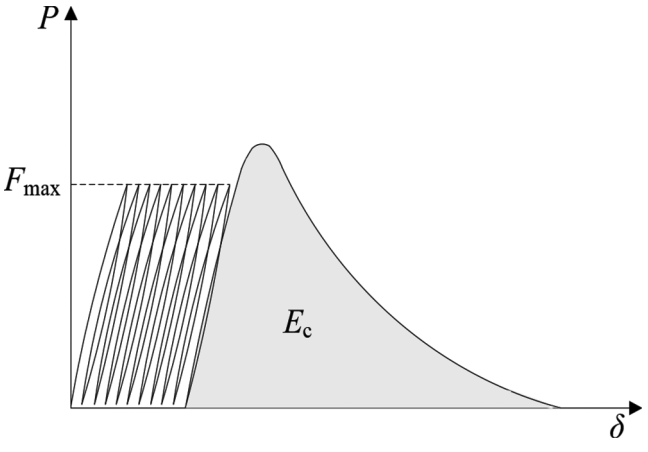

Fig. 4—Schematic P-δ *curve.*

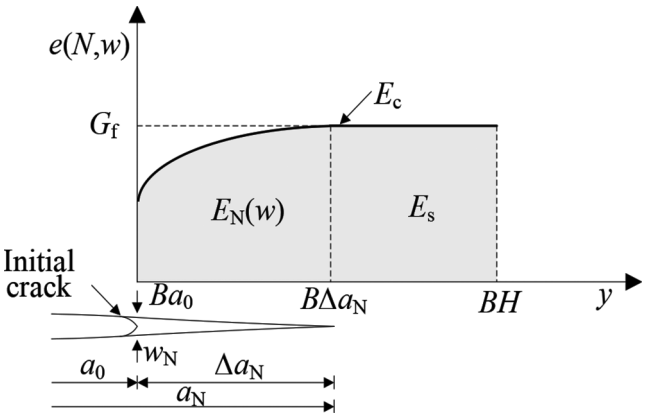

Fig. 5—Energy distribution.

FATIGUE TENSION-SOFTENING CONSTITUTIVE MODEL

Derivation process of fatigue tension-softening constitutive model

First, it should be clarified that this investigation is conducted at the macroscale. The effects of microstructure and aggregate bridging of concrete at the mesoscale on fatigue crack propagation are quantified through the degradation of cohesive stress. The core idea behind the derivation of the fatigue tension-softening constitutive model is energy conservation. Specifically, because the notched TPB beams tested in the aforementioned experiments have a relatively large span-depth ratio, the influence of shear force on energy dissipation is negligible. The mechanical behavior of the concrete outside the FPZ is approximately linear elastic during the fatigue crack propagation process. Therefore, it is assumed that the energy consumed by crack propagation is equal to the external work, and the energy dissipated outside the FPZ is ignored. Based on this quantitative relationship, the cohesive stress under fatigue loading is formulated as follows.

Figure 4 illustrates the schematic load versus deflection (P-δ) curve of a TPB beam subjected to N fatigue cycles followed by static loading. The area under the static P-δ curve represents the external work E_c. After N fatigue cycles, the distribution of the energy required for crack propagation under static loading is shown in Fig. 5, where $E_N(w)$ denotes the required energy within the FPZ, and E_s represents the

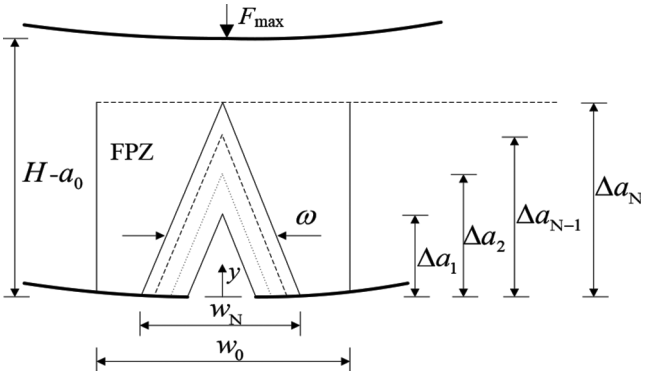

Fig. 6—Schematic fatigue crack propagation.

required energy in the undamaged zone, which can be calculated based on the fracture energy. According to the principle of energy conservation, $E_N(w)$ can be expressed as

$$E_N(w) = E_c - E_s \tag{4}$$

After N fatigue cycles, the fatigue crack propagation length is illustrated in Fig. 6. To simplify the theoretical derivation, the continuous fatigue crack propagation process is divided into N increments, with each increment corresponding to one fatigue cycle. The crack propagation length after i ($1 \le i \le N$) fatigue cycles is denoted as Δa_i. By considering the energy consumed under static loading for each increment, the residual energy $E_N(w)$ can be formulated and expressed as

$$E_N(w) = B\int_0^{\Delta a_1} e(N,\omega)\,\mathrm{d}y + B\int_{\Delta a_1}^{\Delta a_2} e(N-1,\omega)\,\mathrm{d}y + \cdots + B\int_{\Delta a_{N-1}}^{\Delta a_N} e(1,\omega)\,\mathrm{d}y \tag{5}$$

where $e(i,w)$ is the required energy for the crack-propagating unit area under static loading, and can be calculated by

$$e(i,w) = \int_{w_i}^{w_0} \sigma(i,\omega)\,\mathrm{d}\omega \tag{6}$$

where w_i is the COD after i fatigue cycles; w_0 is the critical COD; $\sigma(N, \omega)$ is the static cohesive stress after N fatigue cycles; and ω is the COD under static loading.

In previous investigations, it was verified that the assumption of a linearly distributed COD along the ligament has a negligible influence on the prediction of the fracture properties of concrete.[8] Therefore, based on this assumption, the relationship between Δa_N and the crack tip opening displacement w_N can be derived as

$$\mathrm{d}y = -(\Delta a_N / w_N)\,d\omega \tag{7}$$

Substituting Eq. (7) into Eq. (5) yields

$$\frac{w_N E_N(w)}{B\Delta a_N} = \int_{w_N\left(1-\frac{\Delta a_1}{\Delta a_N}\right)}^{w_N} e(N,\omega)\mathrm{d}\omega + \int_{w_N(1-\Delta a_1/\Delta a_N)}^{w_N(1-\Delta a_2/\Delta a_N)} e(N-1,\omega)\mathrm{d}\omega + \cdots \int_0^{w_N\left(1-\frac{\Delta a_{N-1}}{\Delta a_N}\right)} e(1,\omega)\mathrm{d}\omega \tag{8}$$

Defining the parameter T_N as

$$T_N = \frac{w_N E_N(w)}{B\Delta a_N} \tag{9}$$

Substituting Eq. (9) into Eq. (8) and taking the second-order derivative of Eq. (8) yields

$$\frac{\mathrm{d}^2 T_N}{\mathrm{d}w_N^2} = -\sigma(N,w) + \left(1-\frac{\Delta a_1}{\Delta a_N}\right)\sigma\left[N,\ w_N\left(1-\frac{\Delta a_1}{\Delta a_N}\right)\right] - \left(1-\frac{\Delta a_1}{\Delta a_N}\right)\sigma\left[N-1, w_{N-1}\left(1-\frac{\Delta a_1}{\Delta a_N}\right)\right] + \left(1-\frac{\Delta a_2}{\Delta a_N}\right)\sigma\left[N-1, w_{N-1}\left(1-\frac{\Delta a_2}{\Delta a_N}\right)\right] - \cdots - \left(1-\frac{\Delta a_{N-1}}{\Delta a_N}\right)\sigma\left[1, w_1\left(1-\frac{\Delta a_{N-1}}{\Delta a_N}\right)\right] \tag{10}$$

It should be noted that, theoretically, the fatigue cycle-related COD would be discontinuous. However, it is assumed here that the COD evolves continuously to enable the second-order derivation of this equation. Additionally, the crack tip after i fatigue cycles serves as the starting point for the $i + 1$ fatigue cycles. This implies that the cohesive stress must be continuous at this location, leading to the relationship given by

$$\sigma\left[N-i+1, w_N\left(1-\frac{\Delta a_i}{\Delta a_N}\right)\right] = \sigma\left[N-i, w_N\left(1-\frac{\Delta a_i}{\Delta a_N}\right)\right] \tag{11}$$

Substituting Eq. (11) into Eq. (10), the cohesive stress of concrete after experiencing N fatigue cycles and with a COD of w, denoted as $\sigma(N, w)$, can be obtained by

$$\sigma(N,w) = -\frac{\mathrm{d}^2 T_N}{\mathrm{d}w_N^2} \tag{12}$$

Procedure for determining model

According to the theoretical derivation process outlined previously, the determination of the cohesive stress of concrete under fatigue loading can be conducted as follows:

1. Based on the static-fatigue fracture test results obtained by Chen et al.,[25] the four key parameters w_N, $E_N(w)$, B, and Δa_N for concrete with different compressive strength grades can be determined;
2. Substituting these four parameters into Eq. (9), the quantitative mathematical relationship between T_N and w_N can be fitted; and
3. Substituting the fitted equation from step (2) into Eq. (12), the cohesive stress of concrete under fatigue loading can finally be determined.

Specifically, Fig. 7 illustrates the experimentally determined T_N and w_N for concrete with different compressive strength grades, where "C20-0.9" denotes the TPB beam with a designed concrete compressive strength grade of C20 and a fatigue load level S of 0.9. Considering the physical meaning of these two parameters, the following two boundary conditions should be satisfied when fitting the quantitative relationship between T_N and w_N:

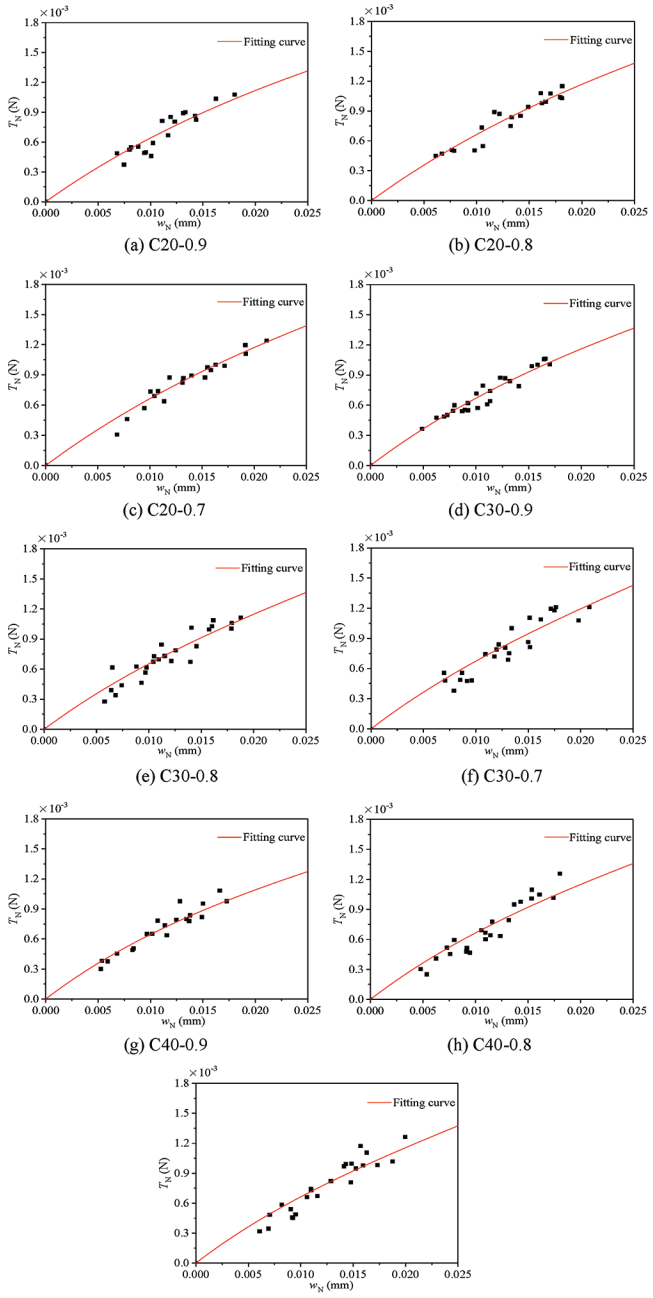

Fig. 7—Relationship between T_N *and* w_N. *(Note: 1 N = 0.225 bf; 1 mm = 0.0394 in.)*

1. when $w_N = 0$, $T_N = 0$; and
2. when $w_N = 0$, $\frac{d^2 T_N}{d w_N^2} = -f_t$.

After extensive attempts, the following Eq. (13), which satisfies the two aforementioned conditions, was used to fit the quantitative relationship between T_N and w_N

$$T_N = b_1 w_N [1 + b_2 \exp(-b_3 w_N)] \quad (13)$$

where b_1, b_2, and b_3 are empirical coefficients. Figure 7 presents the fitted curves based on nonlinear regression analysis. The values of these three coefficients for concrete with different compressive strength grades are listed in Table 4, along with the coefficients of determination r. It can be observed that all r are greater than 0.90, indicating a good fit. By substituting the fitting equations into Eq. (12), the cohesive stress of concrete under fatigue loading, $\sigma(N,w)$, can finally be determined.

Table 4—Fitted parameters in Eq. (13)

Strength grade	S	b_1	b_2	b_3	r
C20	0.9	0.02	2.13	23.74	0.91
	0.8	0.03	1.65	25.13	0.94
	0.7	0.04	0.97	32.68	0.96
C30	0.9	0.03	1.86	28.96	0.94
	0.8	0.03	1.52	31.95	0.92
	0.7	0.04	0.96	39.24	0.91
C40	0.9	0.03	1.85	34.82	0.93
	0.8	0.03	1.38	38.11	0.91
	0.7	0.04	1.21	39.95	0.92

To facilitate the final modeling of the constitutive model, $\sigma(N, w)$ is normalized by $\sigma_s(w)$, where $\sigma_s(w)$ is the cohesive stress of concrete under static loading. Figure 8 depicts the relationship between $\sigma(N, w)/\sigma_s(w)$ and w_N/w_0 under different fatigue load levels. When w_N is equal to or smaller than the crack tip opening displacement after the first loading cycle w_1, $\sigma(N, w)$ is equal to the cohesive stress of concrete under static loading—that is, $\sigma(N, w) = \sigma_s(w)$. Obviously, the values of w_1 for load levels of 0.7 and 0.8 are close but smaller compared with that for a load level of 0.9. The reason for this is that before the peak load P_{max}, the closer the load is to the peak load, the larger the nonlinear deformation of the concrete beam is. In addition, $\sigma(N, w)/\sigma_s(w)$ decreases with an increase in w_N/w_0 and S. When w_N/w_0 is 0.04 and S is 0.9, 0.8, and 0.7, $\sigma(N, w)/\sigma_s(w)$ decreases by 6.6%, 8.9%, and 11.2% for C20 concrete, respectively. Likewise, for a given S at 0.9, 0.8, and 0.7, $\sigma(N, w)/\sigma_s(w)$ decreases by 7.1%, 10.4%, and 11.5% for C30 concrete and 8.7%, 13.0%, and 16.1% for C40 concrete, respectively. This can be explained as follows. The lower the fatigue load level is, more fatigue cycles are required to reach the same opening displacement for the fatigue crack. For a given COD, more loading cycles are needed to overcome the bridging resistance along the crack surface caused by lower fatigue loading, and more severe degradation of cohesive stress is induced, which is consistent with the conclusions reported by Zhang et al.[22]

The relationship between $\sigma(N, w)/\sigma_s(w)$ and N under different fatigue load levels is shown in Fig. 9. For a given compressive strength of concrete, $\sigma(N, w)/\sigma_s(w)$ decreases with the increase of N. When N is 10 and S is 0.9, 0.8, and 0.7, $\sigma(N, w)/\sigma_s(w)$ decreases by 10.9%, 4.8%, and 2.1% for C20 concrete, respectively. Likewise, for a given S at 0.9, 0.8, and 0.7, $\sigma(N, w)/\sigma_s(w)$ decreases by 8.6%, 3.1%, and 1.9% for C30 concrete and 6.4%, 2.7%, and 1.5% for C40 concrete, respectively. The cohesive stress decreases as the fatigue load level decreases. The reason for this is that under a lower fatigue load level, more fatigue cycles are needed to reach the same value of N and more severe stress degradation is induced by the cyclic opening and closing of the fictitious crack surface.

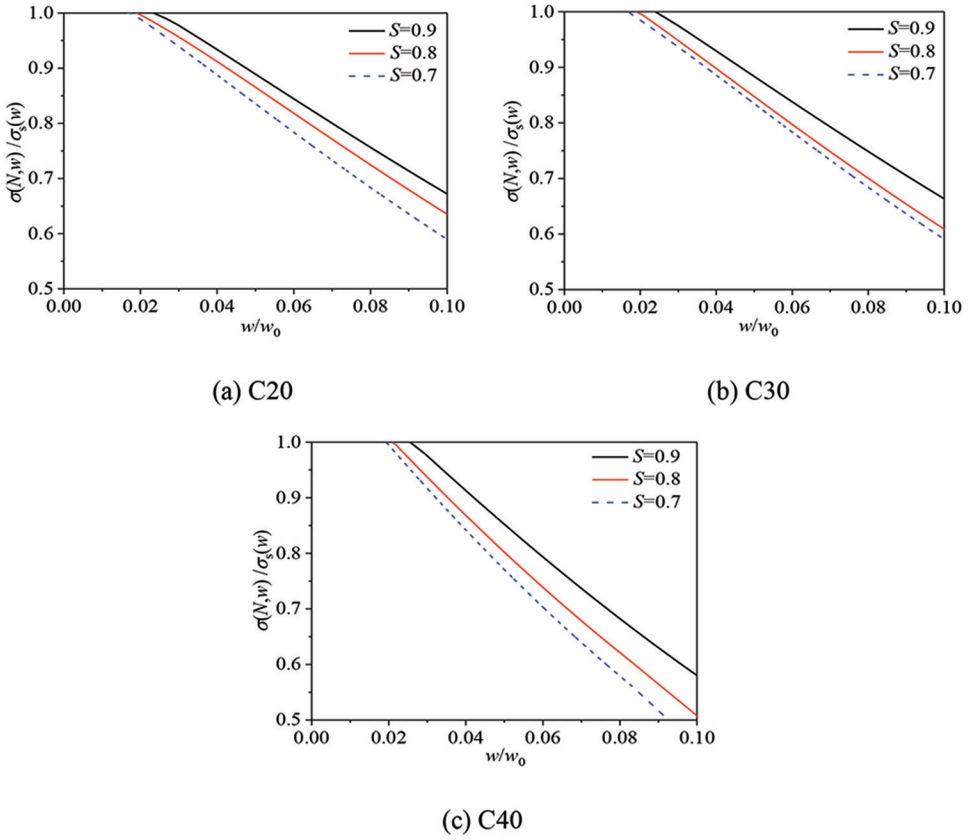

Fig. 8—Relationship between $\sigma(N,w)/\sigma_s(w)$ *and* w/w_0.

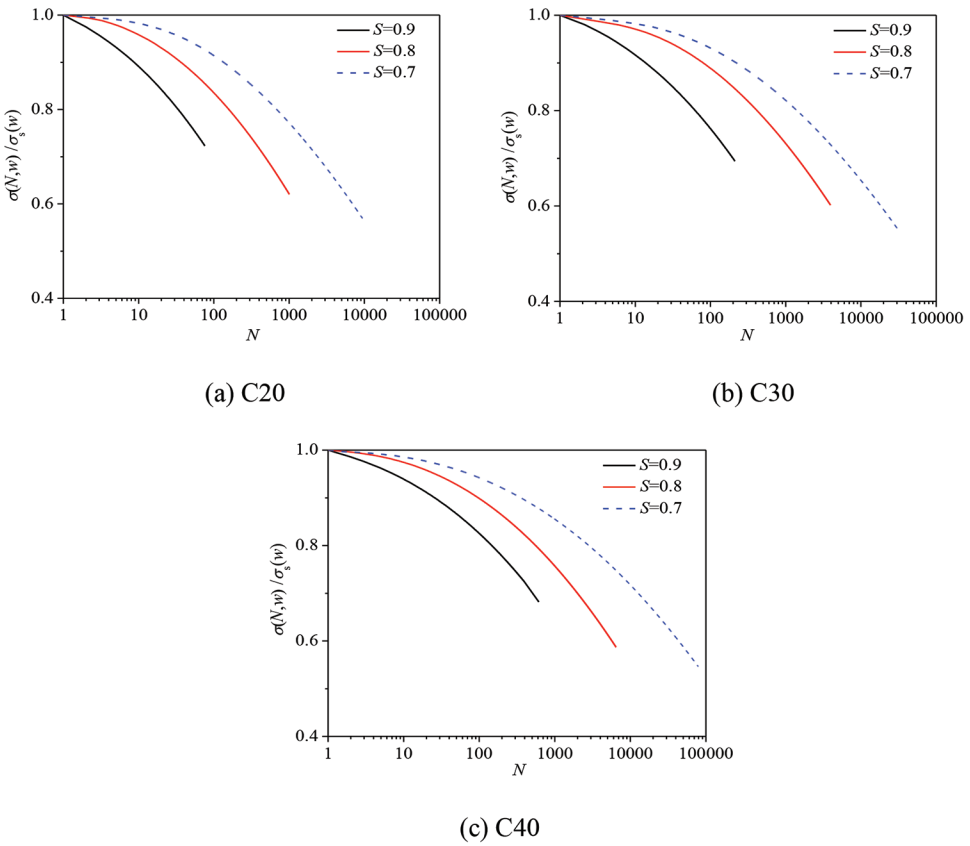

Fig. 9—Relationship between $\sigma(N,w)/\sigma_s(w)$ *and* N *under different fatigue load levels.*

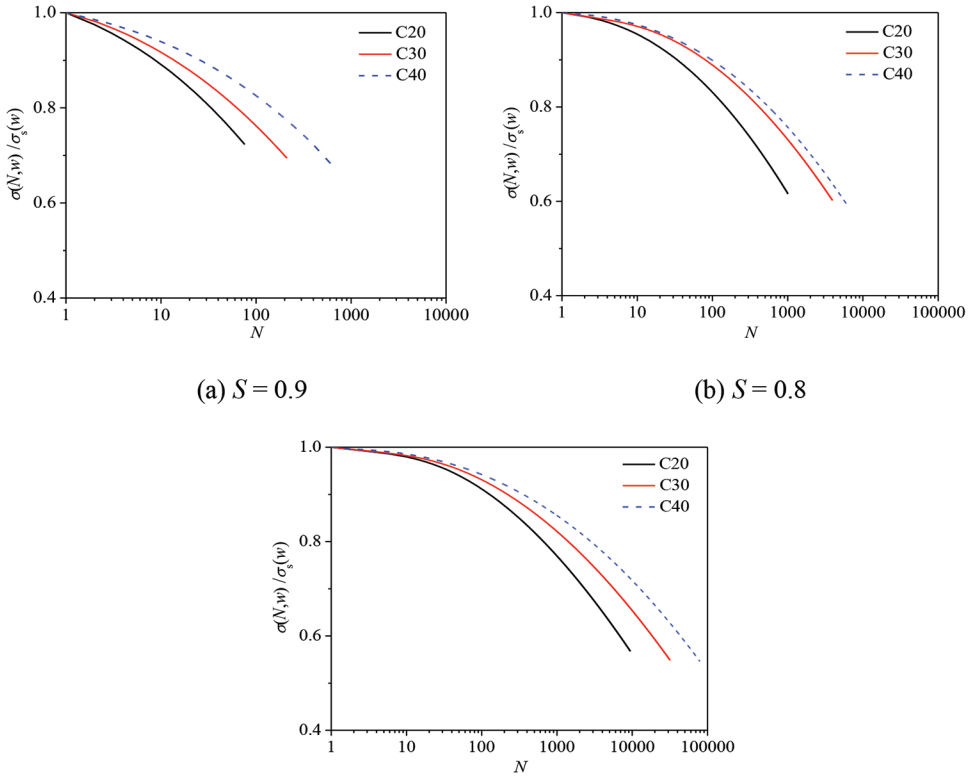

Fig. 10—Relationship between $\sigma(N,w)/\sigma_s(w)$ *and* N *for different strengths of concrete.*

The relationship between $\sigma(N, w)/\sigma_s(w)$ and N for concrete with different compressive strengths is shown in Fig. 10. When N is 10 and S is 0.9, $\sigma(N, w)/\sigma_s(w)$ decreases to 89.1%, 91.4%, and 93.6% for C20, C30, and C40 concrete, respectively. Likewise, for C20, C30, and C40 concrete, $\sigma(N, w)/\sigma_s(w)$ decreases to 95.2%, 96.9%, and 97.3% for a given S at 0.8 and 97.9%, 98.1%, and 98.5% for a given S at 0.7, respectively. For a given fatigue load level, a higher tensile strength of concrete results in a slower decrease of the normalized cohesive stress.

Based on the results presented in Fig. 8 to 10, regression analysis was performed to fit the mathematical expression of the fatigue tension-softening constitutive model of concrete. By taking the fatigue cycle (N) and COD (w) as the key parameters, numerous attempts were made to determine the mathematical form of the constitutive model. Balancing the model's accuracy and simplicity, the constitutive model was finally formulated as

$$\frac{\sigma(N,w)}{\sigma_s(w)} = 1 - [\log(N)](0.02 + 1.58\frac{w}{w_0} - 0.04 f_t \frac{w}{w_0}\log(N)) \quad (14)$$

It should be highlighted that in the model, the tensile strength of concrete f_t is also introduced to quantify the influence of concrete compressive strength grade on the degradation of cohesive stress. Figure 11 illustrates the comparison of the predicted $\sigma(N, w)/\sigma_s(w)$ using Eq. (14) with the experimental results. The predicted $\sigma(N, w)/\sigma_s(w)$ agrees well with the experimental results with a coefficient of determination

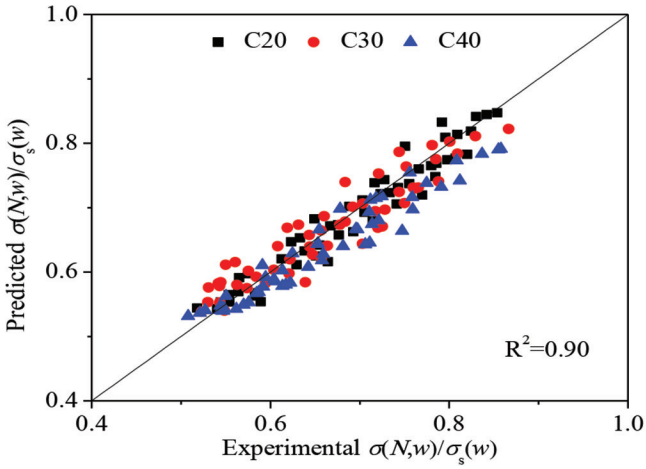

Fig. 11—Comparison of $\sigma(N,w)/\sigma_s(w)$ *between predictions and experimental results.*

of 0.90, indicating that the proposed model can capture the degradation of the cohesive stress for normal-strength concrete.

Through the analysis mentioned earlier, when the tensile strength (f_t) and fracture energy (G_f) of concrete are determined in advance, the cohesive stress of concrete under static loading, $\sigma_s(w)$, can be calculated using Eq. (1) to (3). Subsequently, by substituting $\sigma_s(w)$, f_t, and w_0 into Eq. (14), the fatigue tension-softening constitutive model of concrete can be finalized. In practical engineering applications, when the fatigue cycles (N) and COD are known and input into the proposed constitutive model, the cohesive stress $\sigma(N, w)$ can

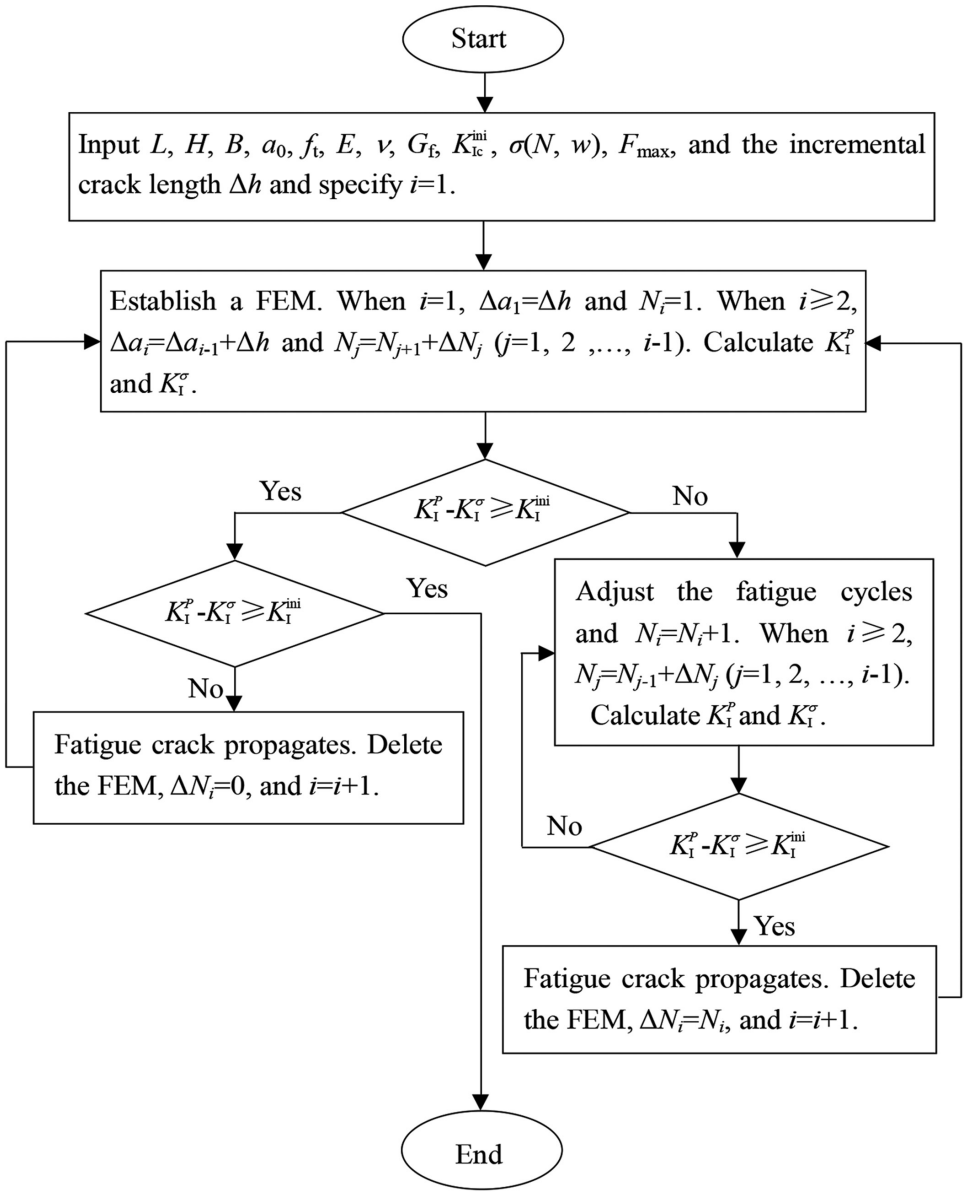

Fig. 12—Flowchart of numerical computation.

be determined. This cohesive stress can then be introduced into the FPZ of concrete to describe its quasi-brittle properties, thereby quantifying the nonlinear crack propagation process in concrete structures.

NUMERICAL VALIDATION

To verify the proposed fatigue tension-softening constitutive model, it is combined with an initial fracture toughness-based crack propagation criterion[28] to predict the fatigue crack propagation process of the TPB beams. The predicted results are then compared with the experimental results. According to the initial fracture toughness-based crack propagation criterion, the fatigue crack propagation is evaluated as follows:

1. When $K_I^P - K_I^\sigma < K_{Ic}^{ini}$, the fatigue crack does not propagate;
2. When $K_I^P - K_I^\sigma = K_{Ic}^{ini}$, the fatigue crack is in the critical state; and
3. When $K_I^P - K_I^\sigma > K_{Ic}^{ini}$, the fatigue crack propagates.

where K_I^P is the SIF caused by the applied fatigue load; K_I^σ is the SIF generated by the cohesive stress in the FPZ; and K_{Ic}^{ini} is the initial fracture toughness of concrete. This criterion has the advantage of reflecting the resistance of concrete to cracking and is unaffected by the stress singularity at the crack tip.

Figure 12 shows the flowchart of the numerical calculation procedure for the fatigue crack propagation process, which is elaborated in detail as follows:

1. Input the required geometric and material parameters, including the span (L), depth (H), thickness (B), initial crack length (a_0), tensile strength (f_t), elastic modulus (E), Poisson's ratio (ν), initial fracture toughness (K_{Ic}^{ini}), fracture energy (G_f), fatigue peak load (F_{max}), and the proposed fatigue tension-softening constitutive model.

2. Establish the finite element model of the TPB beam and set the incremental fatigue crack length Δh. For the first crack propagation step (i = 1), $\Delta a_1 = \Delta h$. For $i \geq 2$, $\Delta a_i = \Delta a_{i-1} + \Delta h$. The fatigue cycle at the i-th crack propagation

Table 5—Parameters adopted in numerical simulation

Strength grade	S	f_t, MPa	E, GPa	v	K_{Ic}^{ini}, MPa·m$^{1/2}$	G_f, N/m	F_{max}, kN
C20	0.9	2.59	28.63	0.23	0.45	128.94	3.46
	0.8						3.07
	0.7						2.69
C30	0.9	3.16	35.32	0.24	0.58	131.61	4.46
	0.8						3.96
	0.7						3.47
C40	0.9	3.74	38.49	0.24	0.64	135.42	4.82
	0.8						4.29
	0.7						3.75

Note: 1 MPa = 145 psi; 1 GPa = 145 kpsi; 1 MPa·m$^{1/2}$ = 138.62 psi·yd$^{1/2}$; 1 N/m = 0.205 bf/yd; 1 kN = 224.72 bf.

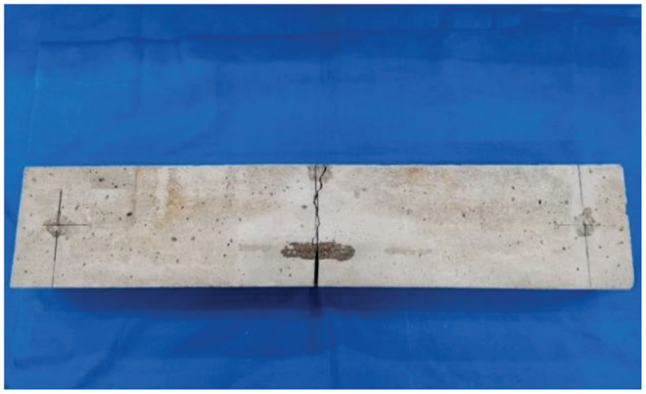

Fig. 13—Mode-I fatigue fracture for specimen C20-0.9.

step is denoted by N_i. When $i = 1$, $N_i = 1$, and when $i \geq 2$, $N_j = N_{j+1} + \Delta N_j$ ($j = 1, 2, \ldots, i–1$), where N_j is the total number of fatigue cycles after the j-th step, and ΔN_j is the number of fatigue cycles at the j-th crack propagation step. Compute K_I^P and K_I^σ.

3. According to the given crack propagation criterion, the calculation procedure is divided into the following two cases:

(a) If $K_I^P - K_I^\sigma \geq K_{Ic}^{ini}$, the fatigue crack initiates and propagates, $\Delta N_i = 0$, and $i = i + 1$; and

(b) If $K_I^P - K_I^\sigma < K_{Ic}^{ini}$, the fatigue crack does not propagate and the fatigue cycles should be increased. When $i = 1$, $N_i = N_i + 1$. When $i \geq 2$, $N_j = N_{j+1} + \Delta N_j$ ($j = 1, 2, \ldots, i–1$). Based on the update fatigue cycles, recompute K_I^P and K_I^σ. Repeat this step until the crack propagation condition is satisfied. Then the fatigue cycles at the i-th crack propagation step are determined, $\Delta N_i = N_i$, and $i = i + 1$;

4. Repeat steps (2) and (3). When the fatigue crack propagation length exceeds the threshold, the program is terminated. The numerical results, including the fatigue crack propagation length, the fatigue life, and the SIF at the fatigue failure of the beams, are then outputted.

In the authors' previous investigation,[25] mode I fatigue fracture tests of TPB beams were conducted using concrete with different compressive strength grades (C20, C30, and C40) and under different load levels (0.7, 0.8, and 0.9). The TPB beams had a span of 600 mm (23.64 in.), a depth of 150 mm (5.91 in.), a thickness of 80 mm (3.15 in.), and an initial crack length-to-depth ratio of 0.30. The material

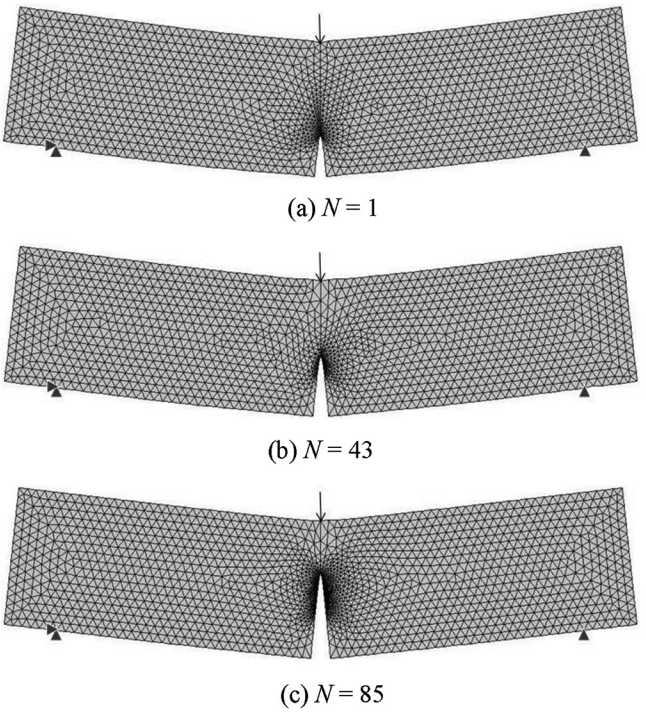

Fig. 14—Fatigue crack propagation process in specimen C20-0.9.

properties for concrete with different compressive strength grades, as well as the fatigue peak loads P_{max} at different load levels, are presented in Table 5. Figure 13 shows the experimentally observed fatigue failure form of the TPB beam with a concrete strength grade of C20 and an applied load level of 0.9, denoted as C20-0.9. Based on the provided geometric and material parameters, the fatigue crack propagation process of these TPB beams was simulated using the numerical procedure described earlier. The simulated fatigue crack propagation process for specimen C20-0.9 is illustrated in Fig. 14. It should be noted that in the numerical calculations, the increment of the fatigue crack length Δh was set to 2 mm (0.08 in.). This value was chosen based on a pre-conducted sensitivity analysis, which indicated that using this increment achieves a balance between computational accuracy and efficiency. Additionally, it should be clarified that both microcracking at the mesoscale and the reduction of stiffness at the macroscale can be attributed to

the degradation of cohesive stress under fatigue loading. Therefore, in the numerical model, the mechanical behavior of concrete outside the FPZ is assumed to be linear elastic.

Figure 15 presents a comparison of the predicted normalized $\Delta a_N/\Delta a_f$-N/N_f curves with the experimental results for concrete with different strength grades, where Δa_f denotes the crack propagation length at fatigue failure. It can be observed that all predicted $\Delta a_N/\Delta a_f$-N/N_f curves fall within the scatter band of the experimental results, indicating good agreement between the predicted and experimental data. The values of fatigue life (N_f), crack propagation length at fatigue failure (Δa_f), and SIF at fatigue failure (K_{If}) obtained from the numerical simulation and the experiments are listed in Table 6. The error between the predicted results and the experimental values, as well as the mean absolute percentage error (MAPE) between the predicted results and the experimental results, are also provided. Figure 16 shows the comparison of fatigue life. It can be observed that all predicted fatigue life values fall within the scatter band of the experimental results. The significant discrepancy between the predicted fatigue life and the mean values of the experimental results can be explained from the following two aspects: 1) Due to the inherent inhomogeneity of concrete, the material properties of each specimen within a group may vary slightly. This variability leads to significant scatter in the measured fatigue life.[29] When only five TPB specimens are included in each group, the sample size is insufficient to obtain a statistically significant mean fatigue life; and 2) In the numerical model, deterministic material parameters of concrete are used to simulate the fatigue crack propagation process. As a result, only a unique fatigue life value can be obtained, which may not fully capture the variability observed in experimental results. Figures 17 and 18 show the comparison of Δa_f and K_{If}, respectively. For both parameters, the error and MAPE are less than 10% and 0.05. The predicted results demonstrate good agreement with the experimental results. Through these quantitative comparisons, the effectiveness of the proposed fatigue tension-softening constitutive model in simulating the fatigue fracture process of concrete with different strength grades is verified. Based on the predicted results, the fatigue fracture behavior of normal-strength concrete structures can be effectively assessed, enabling the implementation of appropriate strengthening measures to enhance structural service performance.

Although the general degradation law of cohesive stress under fatigue loading has been identified and formulated based on the test results of 264 TPB beams, and its effectiveness in predicting the fatigue crack propagation process has been verified, its accuracy and versatility require further investigation. Specifically, the experimental results used in this study included only five specimens for each group. Due to the significant scatter inherent in fatigue test results, the accuracy of the model may be affected. To address this, more fatigue fracture tests on concrete with different compressive strength grades should be conducted to expand the data set and further refine the model. Furthermore, given the complexity of fatigue loading conditions and service environments encountered by concrete structures in practical engineering applications, it is essential to employ the

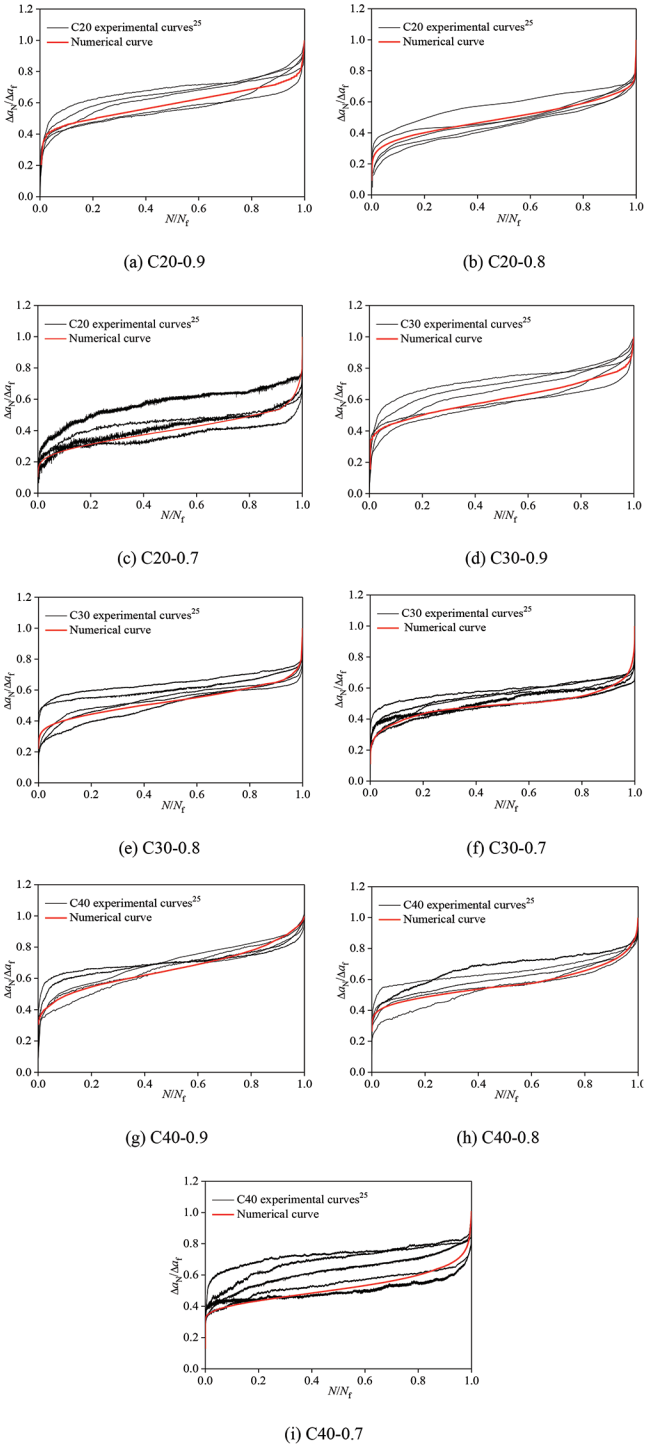

Fig. 15—$\Delta a_N/\Delta a_f$-N/N_f curves.

proposed model to predict the fatigue crack propagation process under diverse environmental conditions (including freezing-and-thawing cycles and wetting-and-drying cycles) and various loading parameters (including different stress amplitudes and frequencies), as well as to investigate the crack propagation behavior at the structural scale. Concurrently, systematic experimental investigations should be conducted to comprehensively characterize the fatigue fracture properties. Finally, through quantitative comparison between the predicted and experimental results, the robustness and applicability of the proposed model across different

Table 6—Numerical and experimental results under fatigue loading

Strength grade	S	N_f				Δa_f, mm				K_{If}, MPa·m$^{1/2}$			
		Num.	Exp.	Error, %	MAPE	Num.	Exp.	Error, %	MAPE	Num.	Exp.	Error, %	MAPE
C20	0.9	85	145	–41.38	0.90	39.40	40.97	–3.83	0.04	1.47	1.52	–3.29	0.04
			42	102.38			36.91	6.75			1.39	5.76	
			28	203.57			38.95	1.15			1.45	1.38	
			59	44.06			40.09	–1.72			1.49	–1.34	
			196	–56.63			41.85	–5.85			1.56	–5.77	
	0.8	2114	775	172.77	1.29	45.48	43.95	3.48	0.03	1.51	1.46	3.42	0.03
			671	215.05			42.95	5.89			1.44	4.86	
			597	254.10			44.52	2.15			1.49	1.34	
			2172	–2.67			48.13	–5.51			1.58	–4.43	
			2059	2.67			45.68	–0.44			1.52	-0.66	
	0.7	14,371	3896	268.87	1.04	51.38	48.81	5.27	0.03	1.56	1.45	7.59	0.04
			6856	109.61			49.90	2.97			1.49	4.70	
			20,619	–30.30			52.52	–2.17			1.61	–3.11	
			15,757	–8.80			51.04	0.67			1.54	1.30	
C30	0.9	111	311	–64.31	0.47	36.25	37.33	–2.89	0.04	1.79	1.80	–0.56	0.04
			472	–76.48			39.72	–8.74			1.91	–6.28	
			269	–58.74			36.27	–0.06			1.76	1.70	
			108	2.78			35.32	2.63			1.72	4.07	
			164	–32.32			33.99	6.65			1.67	7.19	
	0.8	6583	3761	75.03	0.85	42.33	42.15	0.43	0.03	1.80	1.80	0	0.03
			10,904	–39.63			44.93	–5.79			1.93	–6.74	
			3393	94.02			40.74	3.90			1.74	3.45	
			3717	77.11			41.95	0.91			1.79	0.56	
			2776	137.14			39.93	6.01			1.70	5.88	
	0.7	36,645	11,366	222.41	0.91	48.13	50.43	–4.56	0.03	1.84	1.96	–6.12	0.04
			97,376	–62.37			48.07	0.12			1.83	0.55	
			20,310	80.43			46.26	4.04			1.75	5.14	
			47,200	–22.36			47.97	0.33			1.83	0.55	
			22,006	66.52			45.89	4.88			1.73	6.36	
C40	0.9	422	107	294.39	0.89	34.35	33.38	2.91	0.04	1.82	1.78	2.25	0.03
			1211	–65.15			38.03	–9.68			1.98	–8.08	
			339	24.48			34.26	0.26			1.82	0	
			961	–56.09			33.07	3.87			1.77	2.82	
			450	-6.22			35.14	–2.24			1.85	–1.62	
	0.8	8945	10,779	–17.02	0.81	40.83	43.16	–5.40	0.04	1.88	1.99	–5.53	0.04
			3151	183.88			37.41	9.14			1.74	8.05	
			8577	4.29			41.15	–0.78			1.90	–1.05	
			5325	67.98			40.50	0.81			1.87	0.53	
			3893	129.77			39.27	3.97			1.82	3.30	
	0.7	68,588	44,580	53.85	0.76	45.88	43.61	5.21	0.03	1.87	1.76	6.25	0.04
			116,779	–41.27			48.50	–5.40			2.00	–6.50	
			154,668	–55.66			47.02	–2.43			1.93	–3.11	
			23,147	196.31			45.08	1.77			1.83	2.19	
			51,914	32.12			46.81	–1.99			1.92	–2.60	

Note: 1 mm = 0.0394 in.; 1 MPa·m$^{1/2}$ = 138.62 psi·yd$^{1/2}$.

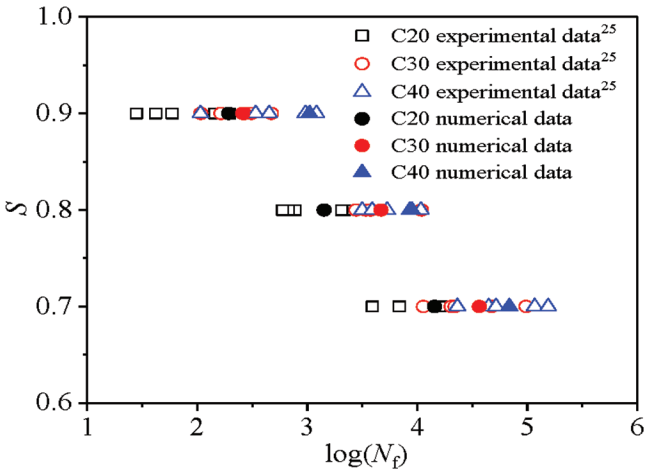

Fig. 16—Comparison of N_f.

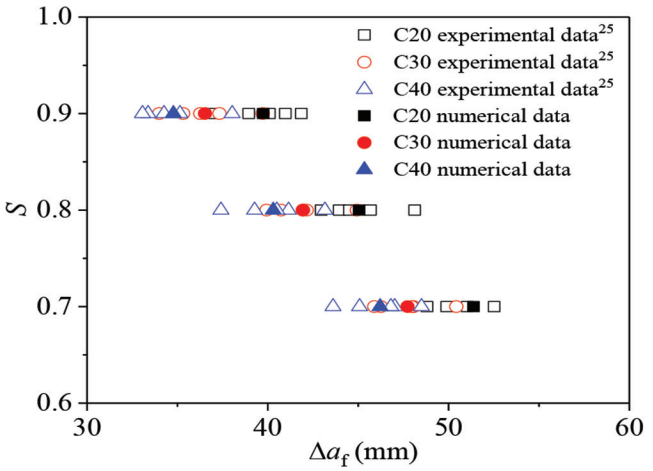

Fig. 17—Comparison of Δa_f.

conditions can be further verified, thereby facilitating its implementation in practical engineering scenarios.

CONCLUSIONS

Due to the lack of systematic and comprehensive studies on the fatigue tension-softening constitutive relationship of concrete, especially concerning the impact of concrete strength variations, the precise prediction of nonlinear fatigue crack propagation in concrete structures remains a significant challenge. This limitation consequently hinders the reliable assessment of structural fatigue performance. To address this research gap, a detailed investigation on the fatigue tension-softening constitutive model of normal-strength concrete was undertaken. The conclusions drawn are presented as follows:

1. The strength grade of concrete is a critical parameter influencing the degradation law of cohesive stress and should be carefully considered when formulating the fatigue tension-softening constitutive model. The results indicate that, under the same load levels and fatigue cycles, the higher the strength grade of concrete is, the slower the degradation of normalized cohesive stress is.

2. A fatigue tension-softening constitutive model for normal-strength concrete is proposed. From the perspective of energy conservation, a quantitative relationship between

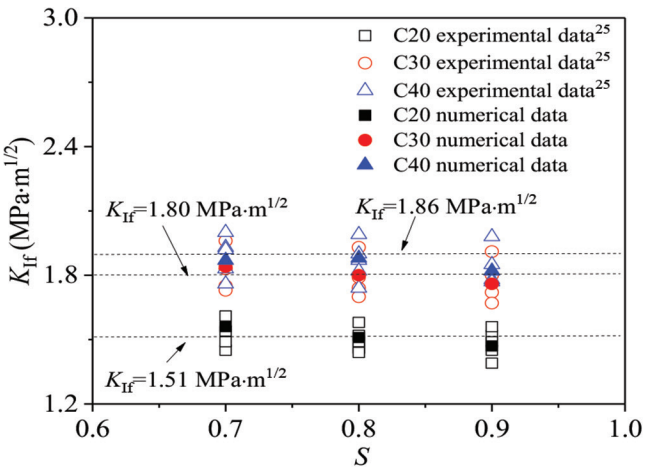

Fig. 18—Comparison of K_{If}. *(Note: 1 MPa·m*$^{1/2}$ *= 138.62 psi·yd*$^{1/2}$*.)*

the external work and the energy consumed by crack propagation in concrete is established, which is used to derive the degradation law of cohesive stress. By incorporating the influence of concrete strength grade, the fatigue tension-softening constitutive model is mathematically formulated.

3. When the fracture energy and tensile strength of normal-strength concrete are predetermined, the fatigue tension-softening constitutive model can be established by using these two parameters to determine the key variables within the model. Subsequently, this model can be employed to predict the nonlinear fatigue crack propagation in normal-strength concrete when combined with the stress intensity factor (SIF)-based fatigue crack propagation criterion. This approach provides a valuable reference for evaluating the fatigue performance of concrete structures.

AUTHOR BIOS

Hong Chen *is a PhD Candidate in the School of Civil Engineering and Architecture, Zhejiang University of Science & Technology, Hangzhou, China. Her research interests include fracture mechanics of concrete and fatigue damage in quasi-brittle materials.*

Meng-Di Jia *is a Lecturer in the School of Civil Engineering, Zhengzhou University, Zhengzhou, China. His research interests include fracture mechanics of concrete and applications of high-performance steel fiber-reinforced concrete in bridge engineering.*

Rena C. Yu *is a Professor in the School of Civil Engineering, Universidad de Castilla-La Mancha, Ciudad Real, Spain. Her research interests include computational mechanics of solids and structures and fatigue damage in quasi-brittle materials.*

Jian-Jun Zheng *is a Professor in the School of Civil Engineering, Zhejiang University of Technology, Hangzhou, China. His research interests include stereological analysis and numerical simulation of concrete mesostructure, mesomechanics of concrete, and durability of concrete materials and structures.*

Zhi-Min Wu *is a Professor in the School of Civil Engineering and Architecture, Zhejiang University of Science & Technology. His research interests include fracture mechanics of concrete, bond behavior of steel bars in concrete, and rehabilitation of existing concrete structures.*

ACKNOWLEDGMENTS

The financial support from the National Natural Science Foundation of China (Grants No. 52079021, 52278279, and 52308148) and the United Kingdom Royal Academy of Engineering through the Distinguished Visiting Fellow Scheme (Grant No. DVF1617_5_21) is greatly acknowledged.

NOTATION

a_0 = initial crack length of TPB beam
B = height of TPB beam
b_1, b_2, b_3 = empirical coefficients
E = elastic modulus
E_c = residual energy
$E_N(w)$ = residual energy in FPZ
E_s = energy in undamaged zone of beam along ligament
$e(N,w)$ = unit residual energy of crack after N fatigue cycles
F_{max} = fatigue peak load
f_{cu} = compressive strength
f_t = tensile strength
G_f = fracture energy
H = width of TPB beam
K_{If} = stress intensity factor at fatigue failure
K_I^P = stress intensity factor caused by applied load
K_{Ic}^{ini} = initial fracture toughness
K_I^q = stress intensity factor caused by cohesive stress
L = length of TPB beam
L_0 = span of TPB beam
N = number of fatigue cycles
N_f = fatigue life
P = applied load
P_{ini} = initial cracking load
S = fatigue load level
T_N = ratio of $w_N E_N(w)$ to $B\Delta a_N$
w = fatigue crack opening displacement
w_N = crack tip opening displacement after N fatigue cycles
w_s = crack opening displacement at turning point of bilinear model
w_0 = critical crack opening displacement
ν = Poisson's ratio
Δa_f = crack propagation length at fatigue failure
Δa_N = crack propagation length after N fatigue cycles
Δh = increment of fatigue crack length
δ = displacement at loading point
$\sigma(N,\omega)$ = cohesive stress-crack width relationship after N fatigue cycles
$\sigma(N,w)$ = fatigue tension-softening constitutive model
σ_s = cohesive stress at turning point of bilinear model
$\sigma_s(w)$ = static tension-softening constitutive model
ω = fictitious crack width

REFERENCES

1. Hillerborg, M.; Modéer, M.; and Petersson, P. E., "Analysis of Crack Formation and Crack Growth in Concrete by Means of Fracture Mechanics and Finite Elements," *Cement and Concrete Research*, V. 6, No. 6, 1976, pp. 773-781. doi: 10.1016/0008-8846(76)90007-7

2. Reinhardt, H. W.; Cornelissen, H. A. W.; and Hordijk, D. A., "Tensile Tests and Failure Analysis of Concrete," *Journal of Structural Engineering*, ASCE, V. 112, No. 11, 1986, pp. 2462-2477. doi: 10.1061/(ASCE)0733-9445(1986)112:11(2462)

3. Yankelevsky, D. Z., and Reinhardt, H. W., "Uniaxial Behavior of Concrete in Cyclic Tension," *Journal of Structural Engineering*, ASCE, V. 115, No. 1, 1989, pp. 166-182. doi: 10.1061/(ASCE)0733-9445(1989)115:1(166)

4. Gylltoft, K., "Fracture Mechanics Models for Fatigue in Concrete Structures," PhD thesis, Luleå University of Technology, Luleå, Sweden, 1983.

5. Hordijk, D. A., "Local Approach to Fatigue of Concrete," PhD thesis, Delft University of Technology, Delft, the Netherlands, 1991.

6. Hordijk, D. A., "Tensile and Tensile Fatigue Behaviour of Concrete, Experiments, Modelling and Analyses," *Heron*, V. 37, No. 1, 1992, pp. 1-79.

7. Zhang, J.; Stang, H.; and Li, V. C., "Fatigue Life Prediction of Fiber Reinforced Concrete under Flexural Load," *International Journal of Fatigue*, V. 21, No. 10, 1999, pp. 1033-1049. doi: 10.1016/S0142-1123(99)00093-6

8. Zhang, J.; Li, V. C.; and Stang, H., "Size Effect on Fatigue in Bending of Concrete," *Journal of Materials in Civil Engineering*, ASCE, V. 13, No. 6, 2001, pp. 446-453. doi: 10.1061/(ASCE)0899-1561(2001)13:6(446)

9. Zhang, P.; Ren, Q. W.; and Lei, D., "Hysteretic Model for Concrete under Cyclic Tension and Tension–Compression Reversals," *Engineering Structures*, V. 163, May, 2018, pp. 388-395. doi: 10.1016/j.engstruct.2018.02.051

10. Toumi, A., and Bascoul, A., "Mode I Crack Propagation in Concrete under Fatigue: Microscopic Observations and Modelling," *International Journal for Numerical and Analytical Methods in Geomechanics*, V. 26, No. 13, 2002, pp. 1299-1312. doi: 10.1002/nag.245

11. Horii, H.; Shin, H. C.; and Pallewatta, T. M., "Mechanism of Fatigue Crack Growth in Concrete," *Cement and Concrete Composites*, V. 14, No. 2, 1992, pp. 83-89. doi: 10.1016/0958-9465(92)90002-D

12. Yang, B.; Mall, S.; and Ravi-Chandar, K., "A Cohesive Zone Model for Fatigue Crack Growth in Quasibrittle Materials," *International Journal of Solids and Structures*, V. 38, No. 22-23, 2001, pp. 3927-3944. doi: 10.1016/S0020-7683(00)00253-5

13. Xu, Y. J., and Yuan, H., "Computational Analysis of Mixed-Mode Fatigue Crack Growth in Quasi-Brittle Materials Using Extended Finite Element Methods," *Engineering Fracture Mechanics*, V. 76, No. 2, 2009, pp. 165-181. doi: 10.1016/j.engfracmech.2008.08.011

14. Xu, Y. J., and Yuan, H., "Computational Modeling of Mixed-Mode Fatigue Crack Growth Using Extended Finite Element Methods," *International Journal of Fracture*, V. 159, No. 2, 2009, pp. 151-165. doi: 10.1007/s10704-009-9391-y

15. Toyama, H.; Kishida, H.; and Yonezu, A., "Characterization of Fatigue Crack Growth of Concrete Mortar under Cyclic Indentation Loading," *Engineering Failure Analysis*, V. 83, Jan, 2018, pp. 156-166. doi: 10.1016/j.engfailanal.2017.10.004

16. Skar, A.; Poulsen, P. N.; and Olesen, J. F., "A Simple Model for Fatigue Crack Growth in Concrete Applied to A Hinge Beam Model," *Engineering Fracture Mechanics*, V. 181, Aug, 2017, pp. 38-51. doi: 10.1016/j.engfracmech.2017.06.018

17. Xi, X., and Yang, S. T., "A Non-Linear Cohesive Zone Model for Low-Cycle Fatigue of Quasi-Brittle Materials," *Theoretical and Applied Fracture Mechanics*, V. 122, Dec. 2022, p. 103641. doi: 10.1016/j.tafmec.2022.103641

18. Lima, G., and Bittencourt, E., "A Cohesive Model for the Rupture of Concrete by Low-Cycle Fatigue," *Fatigue and Fracture of Engineering Materials and Structures*, V. 47, No. 6, 2024, pp. 2215-2227. doi: 10.1111/ffe.14298

19. Kumar, B., and Ray, S., "A Multi-Scale Based Fracture Characterization in Concrete under Fatigue Loading Using Critical Energy Dissipation," *International Journal of Fatigue*, V. 165, Dec. 2022, p. 107165. doi: 10.1016/j.ijfatigue.2022.107165

20. Baktheer, A.; Martínez-Pañeda, E.; and Aldakheel, F., "Phase Field Cohesive Zone Modeling for Fatigue Crack Propagation in Quasi-Brittle Materials," *Computer Methods in Applied Mechanics and Engineering*, V. 422, Mar. 2024, p. 116834. doi: 10.1016/j.cma.2024.116834

21. Simon, K. M., and Chandra Kishen, J. M., "Influence of Aggregate Bridging on the Fatigue Behavior of Concrete," *International Journal of Fatigue*, V. 90, Sept. 2016, pp. 200-209. doi: 10.1016/j.ijfatigue.2016.05.009

22. Zhang, D. W.; Furuuchi, H.; Hori, A.; Seiji, F.; and Ueda, T., "Determination of Tensile Crack Bridging of PCM-Concrete Interface Subjected to Fatigue Loading by Means of Bending Test," *Journal of Structural Engineering*, V. 55A, July 2009, pp. 861-870.

23. Zhang, D. W.; Furuuchi, H.; Hori, A.; and Ueda, T., "Fatigue Degradation Properties of PCM-Concrete Interface," *Journal of Advanced Concrete Technology*, V. 7, No. 3, 2009, pp. 425-438. doi: 10.3151/jact.7.425

24. Jia, M. D.; Wu, Z. M.; Yu, R. C.; and Zhang, X. X., "Tension-Softening Constitutive Relation and Numerical Simulation Method for Mode I Fatigue Crack Propagation in Concrete," *International Journal of Fracture*, V. 238, No. 2, 2022, pp. 133-163. doi: 10.1007/s10704-022-00642-2

25. Chen, H.; Wang, H. W.; Zheng, J. J.; and Wu, Z. M., "Residual Fracture Toughness and Fracture Energy of Concrete with Different Strengths after Fatigue Loading," *Construction and Building Materials*, V. 408, Dec. 2023, p. 133563. doi: 10.1016/j.conbuildmat.2023.133563

26. Petersson, P. E., "Crack Growth and Development of Fracture Zones in Plain Concrete and Similar Materials," Report No. TVBM-1006, Division of Building Materials, Lund University, Lund, Sweden, 1981.

27. Cornelissen, H. A. W.; Hordijk, D. A.; and Reinhardt, H. W., "Experimental Determination of Crack Softening Characteristics of Normalweight and Lightweight Concrete," *Heron*, V. 31, No. 2, Jan. 1986, pp. 45-56.

28. Wu, Z. M.; Rong, H.; Zheng, J. J.; and Dong, W., "Numerical Method for Mixed-Mode I–II Crack Propagation in Concrete," *Journal of Engineering Mechanics*, ASCE, V. 139, No. 11, 2013, pp. 1530-1538. doi: 10.1061/(ASCE)EM.1943-7889.0000594

29. Ortega, J. J.; Ruiz, G.; Yu, R. C.; Afanador-García, N.; Tarifa, M.; Poveda, E.; Zhang, X.; and Evangelista, F., Jr., "Number of Tests and Corresponding Error in Concrete Fatigue," *International Journal of Fatigue*, V. 116, Nov. 2018, pp. 210-219. doi: 10.1016/j.ijfatigue.2018.06.022

ACI MATERIALS JOURNAL TECHNICAL PAPER

Title No. 122-M16

Artificial Intelligence Approach for Predicting Compressive Strength of Geopolymer Concrete

by Muhammad Naveed, Asif Hameed, Ali Murtaza Rasool, Rashid Hameed, and Danish Mukhtar

Geopolymer concrete (GPC) is a progressive material with the capability to significantly reduce global industrial waste. The combination of industrial by-products with alkaline solutions initiates an exothermic reaction, termed geopolymerization, resulting in a carbon-negative concrete that lessens environmental impact. Fly ash (FA)-based GPC displays noticeable variability in its mechanical properties due to differences in mixture design ratios and curing methods. To address this challenge, the authors optimized the constituent proportions of GPC through a meticulous selection of nine independent variables. A thorough experimental database of 1242 experimental observations was assembled from the available literature, and artificial neural networks (ANNs) were employed for compressive strength modeling. The developed ANN model underwent rigorous evaluation using statistical metrics such as R*-values,* R^2 *values, and mean squared error (MSE). The statistical analysis revealed an absence of a direct correlation between compressive strength and independent variables, as well as a lack of correlation among the independent variables. However, the predicted compressive strength by the developed ANN model aligns well with experimental observations from the compiled database, with* R^2 *values for the training, validation, and testing data sets determined to be 0.84, 0.74, and 0.77, respectively. Sensitivity analysis identified curing temperature and silica-to-alumina ratio as the most crucial independent variables. Furthermore, the research introduced a novel method for deriving a mathematical expression from the trained model. The developed mathematical expressions accurately predict compressive strength, demonstrating minimal errors when using the tan-sigmoid activation function. Prediction errors were within the range of –0.79 to 0.77 MPa, demonstrating high accuracy. These equations offer a practical alternative in engineering design, bypassing the intricacies of the internal processes within the ANN.*

Keywords: artificial neural network (ANN); constituent ratios; fly ash (FA); geopolymer concrete (GPC) strength; green material; mathematical modeling.

INTRODUCTION

Geopolymer concrete (GPC) distinguishes itself as a green substitute for conventional concrete, providing a notable decrease in carbon dioxide (CO_2) emissions—up to five to six times less.[1] GPC is formulated with a blend of industrial waste materials serving as precursors, an alkaline activation solution, and aggregates.[2,3] The exothermic reaction known as geopolymerization is triggered when a precursor, notably copious in SiO_2 and Al_2O_3, dissolves in an alkaline solution.[4,5] Alkaline solution is typically composed by mixing caustic soda (NaOH) and water glass (Na_2SiO_3).[6-8] Curing conditions significantly influence the rate of geopolymerization and form a covalently bonded three-dimensional (3-D) macromolecular network that enhances compressive strength at early age.[9-11] Therefore, achieving the desired GPC compressive strength relies on selecting the appropriate proportions of these constituents.[12-14] Although experimental studies have showcased the advantages of GPC, especially concerning enhanced mechanical performance, it is crucial to acknowledge that such investigations can incur significant expenses, involve complexity, and demand considerable time.[15-17] To streamline the process and facilitate more economical and optimized mixture designs, the development of a reliable predictive model capable of replicating experimental outcomes for GPC's compressive strength becomes imperative. Numerous researchers have undertaken efforts for compressive strength prediction. While acknowledging the existing challenges, it is important to note that these endeavors provide valuable insights into different influencing variables for GPC. Dao et al.[18] employed various artificial intelligence (AI) approaches for compressive strength prediction by considering four input variables. Though the study involved a data set of 210 GPC samples with an approximate strength approximation error of 13%, it did not explore the impact of curing temperature and curing duration. Shahmansouri et al.[19] developed an artificial neural network (ANN) for GPC incorporating natural zeolite and silica fume, using a data set of 39 experimental samples. While the study considered input variables such as NaOH molarity, slag content, silica fume, and zeolite content, it did not include certain influential factors such as Na_2SiO_3 content, curing regimes, and aggregates ratio. Ahmad et al.[20] used different machine-learning algorithms to forecast GPC compressive strength with 154 data points and nine input variables. However, the effect of the curing regime, a crucial parameter for expediting the geopolymerization process, was not incorporated. Verma et al.[21] developed an ANN model for GPC compressive strength with a comprehensive data set of 540 data points and 12 input variables. Pratap et al.[22] explored the potential of the ANN to assess the mechanical properties of GPC using 20 samples and five input variables. While these studies offer valuable contributions, they did not explore the properties of Na_2SiO_3 and curing methods.

The available literature lacks in-depth modeling investigations exploring the impact of varying ratios of GPC

ACI Materials Journal, V. 122, No. 3, May 2025.

MS No. M-2024-060.R3, doi: 10.14359/51746714, received December 6, 2024, and reviewed under Institute publication policies.

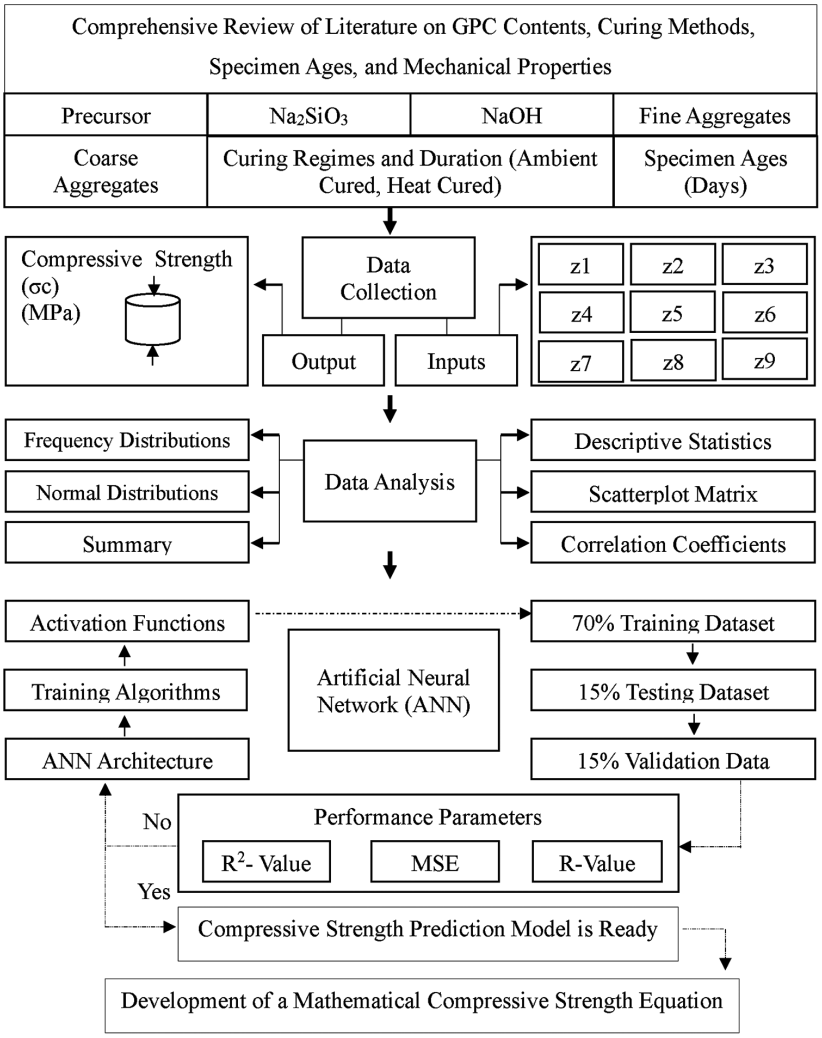

Fig. 1—Research methodology.

components on compressive strength under different curing temperatures and sample ages.[23] Additionally, the construction sector seldom employs a robust model for forecasting GPC compressive strength. This is primarily due to the restricted applicability of existing models, which fail to encompass a diverse range of experimental data.[24] The focus of this study is a comprehensive exploration of the factors influencing the compressive strength of fly ash (FA)-based GPC. The research uses AI methodology, integrating nine independent variables. The database collected by Naveed et al.[25] was considered, and ANNs were employed to model compressive strength. The model's accuracy was evaluated using mean squared error (MSE), *R*-value, and coefficient of determination (R^2). In addition, this research introduces a method for generating a mathematical expression from a trained ANN model. These expressions represent a pragmatic alternative in engineering design that circumvents the complexity of the internal processes within ANNs. This innovative strategy has the potential to yield GPC mixture designs that not only meet performance criteria but also reduce resource consumption and environmental impact, thereby contributing to green construction practices. The adopted research methodology is presented in Fig. 1.

EXPERIMENTAL DATABASE

In this study, the test database used by Naveed et al.[25] was meticulously compiled by aggregating experimental findings from various published research articles. This comprehensive database comprised a total of 1242 data points, encompassing diverse constituent proportions. Notably, this research exclusively focused on data extracted from articles that employed FA as a primary binder.

From each of the chosen articles, the authors systematically extracted crucial data, encompassing the quantities of binder ($v1$), caustic soda ($v2$), water glass ($v3$), sand ($v4$), and coarse aggregates ($v5$), along with information regarding curing temperature, curing duration, and specimen age. The indispensable input variables, vital for the modeling of compressive strength, were carefully computed and are delineated in Table 1.

DESCRIPTIVE STATISTICS

Table 2 presents the descriptive statistics of the input variables, offering valuable insights into the fundamental attributes of the data set. These statistics aid in comprehending the data set's central tendencies, variability, and distribution patterns.[25,26] The standard deviation indicates the typical deviation from the mean value.[27] In the case of $z5$ and $z6$, it

Table 1—Nomenclature of selected variables

Notation	Description	Calculation
$z1$	Silicon dioxide to aluminum oxide ratio	SiO_2/Al_2O_3 (from X-ray fluorescence analysis)
$z2$	Alkaline solution (I)/precursor content (b) ratio	$v2 + (v3/v1)$
$z3$	Na_2SiO_3/NaOH ratio	$v2/v3$
$z4$	NaOH molarity, M	Concentration of solid NaOH in water
$z5$	Curing temperature, °C	Ambient curing and heat curing
$z6$	Curing duration, hours	Heat curing duration after specimen casting
$z7$	Specimen age, days	Number of days after which specimen was tested
$z8$	Sand-total aggregates ratio	$v4/(v4 + v5)$
$z9$	Total aggregates-mixture ratio	$(v4 + v5)/(v1 + v2v3 + v4 + v5)$

Table 2—Descriptive statistics of input variables

Statistic	$z1$	$z2$	$z3$	$z4$	$z5$	$z6$	$z7$	$z8$	$z9$
Mean	2.322	0.459	2.314	11.803	59.071	29.040	16.924	0.335	0.758
Standard error	0.035	0.003	0.017	0.085	0.728	0.509	0.451	0.001	0.001
Median	2.105	0.450	2.500	12.000	60.000	24.000	7.000	0.330	0.770
Mode	2.473	0.450	2.500	14.000	60.000	24.000	7.000	0.300	0.770
Standard deviation	1.249	0.109	0.614	2.984	25.642	15.313	15.887	0.044	0.042
Sample variance	1.561	0.012	0.377	8.906	657.499	234.50	252.388	0.002	0.002
Kurtosis	11.079	4.644	40.179	–0.878	–0.920	30.375	5.342	4.742	2.645
Skewness	3.138	1.588	3.427	0.004	–0.006	4.435	1.921	1.729	–1.36
Range	7.287	0.850	8.400	17.000	96.000	163.00	89.000	0.350	0.230
Minimum	0.483	0.250	0.400	3.000	24.000	5.000	1.000	0.200	0.600
Maximum	7.770	1.100	8.800	20.000	120.000	168.00	90.000	0.550	0.830
Count	1242	1242	1242	1242	1242	905	1242	1242	1242
Confidence level (95%)	±0.07	±0.006	±0.034	±0.17	±1.43	±0.99	±0.88	±0.002	±0.002

is noteworthy that the standard deviation is notably higher, suggesting that these variables exhibit a high degree of dispersion. Skewness is the measure of the asymmetry of data distributions. As the skewness for $z1$, $z2$, $z3$, $z6$, $z7$, and $z8$ positively deviates from zero, these variables are considered right-skewed, and for $z5$ and $z9$, the distribution is left-skewed. Kurtosis quantifies the degree of peakedness in the data distribution.[28] When the value exceeds 3, as seen in $z1$, $z3$, $z6$, and $z7$, it suggests a leptokurtic distribution with heavy tails. Conversely, $z5$ and $z6$ have values less than 3, pointing to a platykurtic distribution. The values for $z2$, $z8$, and $z9$ may be considered mesokurtic. Confidence level provides the uncertainties associated with the estimates.[29] For $z1$, the mean value is 2.322 with a 95% confidence interval of 2.252 to 2.392 with a margin of error of ±0.07. The relative frequency distributions for the input variables are presented in Fig. 2, which shows non-normal distributions for all input variables.

SCATTERPLOT MATRIXES

Scatterplot matrixes serve as a tool to visualize the complex relationships between input variables all at once.[30] This matrix helped to choose a proper method for model development of compressive strength.[31,32] The process involves plotting each variable against every other variable, resulting in a grid of plots, as depicted in Fig. 3. A nonlinear relationship exists between the input variables. This matrix also helps to identify the correlations between the input variables. In modeling studies, the input variables should not be highly correlated because such correlations can make it challenging to disentangle the individual effects of each variable. Pearson's correlation coefficient (r) was computed for each scatterplot shown in Fig. 3. The correlation coefficient's range spans from –1 to +1. When r is less than 0.3, it signifies a weak correlation, while values between 0.3 and 0.7 indicate a reasonable correlation.[26,33] A correlation exceeding 0.7 suggests a robust relationship. A positive correlation coefficient signifies a direct relationship between the input variables, while a negative coefficient signifies an inverse relationship.[34] Figure 3 depicts that all the input variables are poorly correlated and are independent of each other. Thus, the decision was made to harness the potential of ANNs in this research to model the compressive strength of GPC effectively.

ARTIFICIAL NEURAL NETWORK (ANN)

An ANN is a machine-learning algorithm that draws inspiration from the structure and function of the neural networks found in the human brain.[35] ANNs are adept at capturing intricate nonlinear relationships within the data

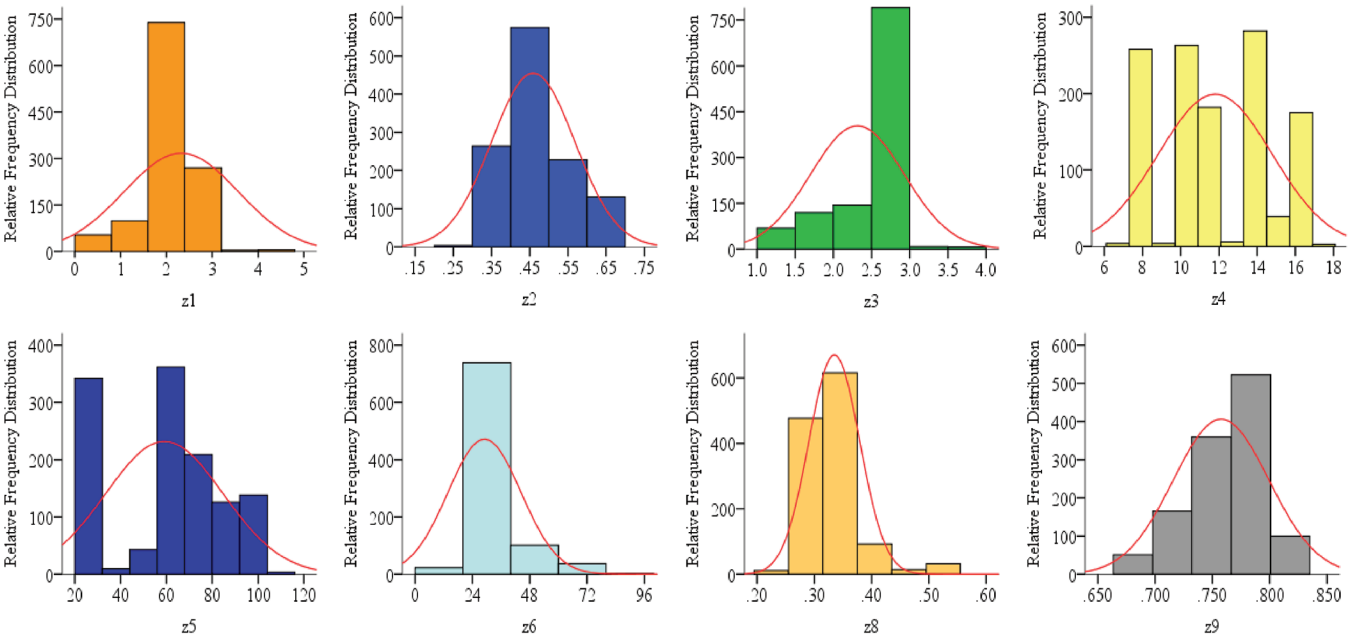

Fig. 2—Relative frequency distributions of input variables.

and do not require adherence to a normal distribution.[36,37] Every ANN solves a specific problem and comprises interconnected nodes to process and transmit information. Each node communicates information to another node through inter-unit connections whose strength (associated weights) is obtained and adjusted by a training algorithm.[38] The nodes are organized into layers, and the activation function assigns a value to the output of each layer.[39] The performance of an ANN was evaluated using MSE and regression performance indicators.[40,41] The process of ANNs is presented in Fig. 4.

The ANN model employed in this investigation comprised an input layer, a hidden layer, and an output layer. The input layer conveyed the initial data of input variables ($z1$, $z2$, …, $z9$) to the hidden layer without conducting any computations. The hidden layers served as intermediaries, carrying out computations using an activation function to introduce nonlinearity.[42] The selection of hidden layers and the number of neurons (nodes) in a solitary hidden layer are pivotal elements in the process of transforming and learning intricate patterns within the data.[24] Hornik et al.[43] affirmed that multilayer feedforward networks, even with just one hidden layer, can attain accurate universal approximations. Hence, for this study, a sole hidden layer was used. To ascertain the optimal number of neurons, a trial-and-error approach was implemented. Numerous ANNs underwent training with different numbers of neurons in the hidden layer, and the configuration that yielded the highest correlation coefficient (R-value) and the lowest MSE was selected.[44] In the context of this study, the authors determined that the optimal number of neurons was 19 (as depicted in Fig. 5). The outcomes from the hidden layer were transmitted to the output layer, which was tasked with generating the final predictions for compressive strength.[45,46]

The compiled data set was divided into three sets for training, validation, and testing the neural network.[30] Specifically, 70% of the data set was allocated for fine-tuning the ANN by adjusting its weights and biases (training data set).[47] This adjustment process, known as network training, is essential for reducing errors in the neural network's predictions.[48] The Levenberg-Marquardt (LM) backpropagation algorithm was chosen for ANN training because it outperforms other algorithms in predicting nonlinear concrete properties. This algorithm calculated the error gradient with respect to the network weights and biases. This gradient indicates the direction and magnitude in which the weights and biases should be adjusted for error minimization.[49] Additionally, 15% of the data was reserved for preventing overfitting issues and performance monitoring (validation data set), while another 15% was designated to assess the accuracy of the trained network (testing data set).[50] In this research, data normalization, as defined in Eq. (1), was employed to address the issue of overfitting.[51] The inputs and outputs underwent processing using data normalization, restricting the values of each data point to the range of –1 to +1.[52]

$$N_i = \frac{2 \times (E - E(\min))}{E(\max) - E(\min)} - 1 \quad (1)$$

where N_i denotes the normalized data point; E indicates the experimental data point; and $E(\min)$ and $E(\max)$ represent the minimum and maximum experimental observations of each variable in the data set.

$$\text{tan-sigmoid}(x) = \frac{2}{1 + e^{-2x}} - 1 \quad (2)$$

$$\text{purelin}(x) = x \quad (3)$$

Activation functions introduce nonlinearity, aiding the ANN model approximating complex data relationships and influencing gradient flow during training. Pham and Hadi[24] stated that an ANN trained using a tan-sigmoid (tansig) transfer function in the hidden layer exhibited notably superior predictive accuracy. In prediction tasks, the choice for the output layer's activation function is linear (purelin). It is

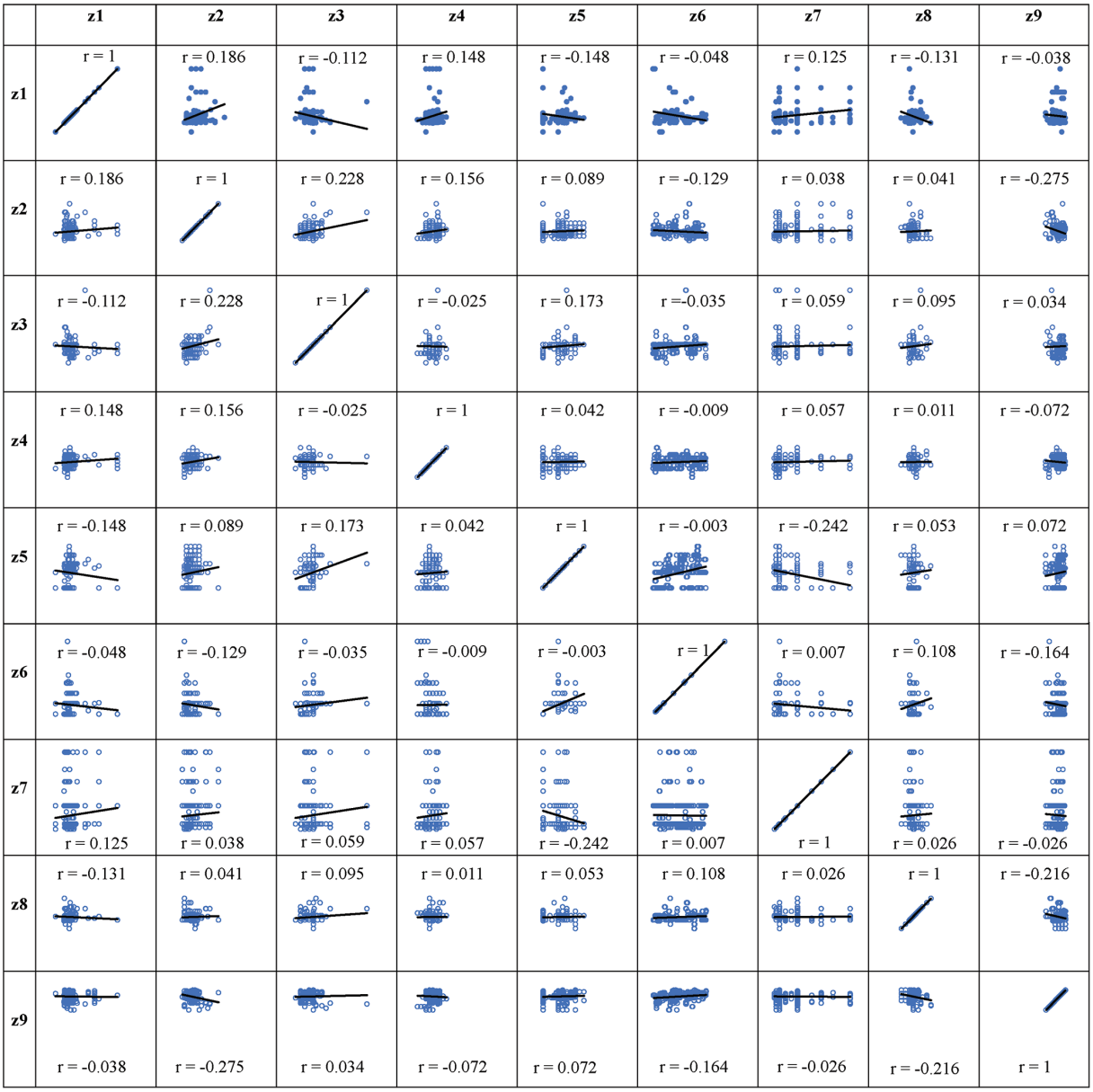

Fig. 3—Scatterplot matrix for all input variables used in present study.

preferred as it allows the neural network to produce a wide range of real-numbered outputs without constraints. Hence, this research used two activation functions, specifically tansig (Eq. (2)) for the hidden layer and purelin (Eq. (3)) for the output layer, in forecasting compressive strength.

RESULTS AND DISCUSSION

From the compiled database, 870 data points were designated for ANN training, 186 data points for validation, and another 186 data points were allocated for testing. The architecture of the proposed ANN consists of three layers following a feedforward backpropagation algorithm, as shown in Fig. 6. The input layer comprises nine neurons, the hidden layer has 19 neurons, and the output layer consists of one neuron. The training algorithm employed was LM, and the activation functions used in the hidden and output layers were tansig and purelin. The MSE, *R*-value, and R^2 value were used as the performance parameters. The performance parameters are presented in Eq. (4) to (6) as follows

$$\text{MSE} = \frac{1}{n}\sum_{i=1}^{n}(yi - yi')^2 \tag{4}$$

$$R\text{-value} = \sqrt{1 - \frac{\sum_{i=1}^{n}(yi - yi')^2}{\sum_{i=1}^{n}(yi - y)^2}} \tag{5}$$

$$R^2\text{-value} = 1 - \frac{\sum_{i=1}^{n}(yi - yi')^2}{\sum_{i=1}^{n}(yi - y)^2} \tag{6}$$

where n denotes the size of the data set; yi indicates the i-th experimental data point; and yi' represents the i-th predicted data point.

PERFORMANCE OF ANN

Figure 7 depicts the network's performance measured by MSE as it transitions from higher to lower values. The plot exhibits three lines, representing distinct stages of training, validation, and testing performance. Notably, the

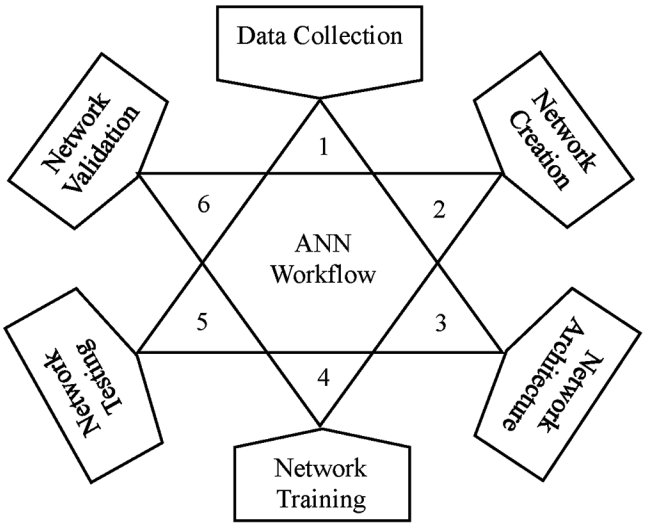

Fig. 4—Process of artificial neural network.

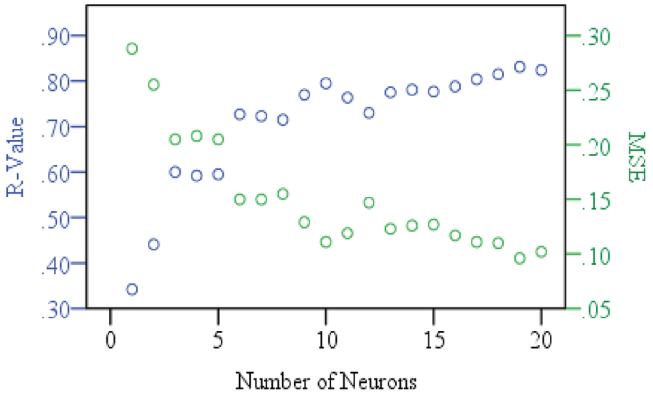

Fig. 5—Optimal number of neurons.

peak validation performance was attained at epoch 46, with subsequent error repetitions observed after this point. The training process was consequently halted at epoch 52. Therefore, the compressive strength model underwent 52 iterations (epochs) across the training data set to achieve minimal error.

TRAINING PROGRESS

Figure 8 illustrates the training progress of the ANN model. Notably, the error exhibited a repeated pattern three times after epoch 16 and continued progressing in the right direction. Typically, the training process halts when the error pattern repeats six times. It is evident from Fig. 8 that the error repeated itself six times after epoch 46, and testing continued until epoch 52. This consistent repetition of error, starting at epoch 46, indicates overfitting of the data. Consequently, epoch 46 was identified as the reference point, and its weights were designated as the final weights. A validation check was performed six times, corresponding to the number of error repetitions, before concluding the training process.

ERROR HISTOGRAM

When a specific distribution is followed, it offers valuable insights into the characteristics of the model itself. Figure 9 presents the error histogram of the ANN, segmented into 20 bins, for all data sets. Both the training and testing data sets exhibit conformity to a Gaussian distribution. This observation implies that the model underwent effective training, resulting in favorable outputs.

REGRESSION

The evaluation of the correlation between the network's outputs and target values used the *R*-value. To minimize MSE and maximize the correlation coefficient (*R*), a neural

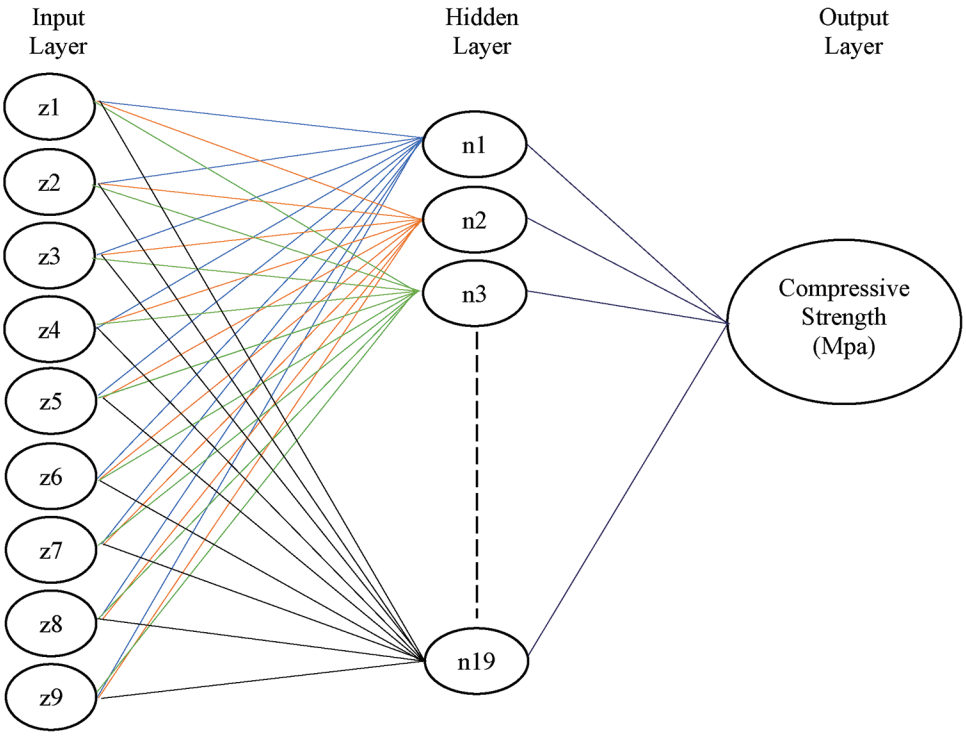

Fig. 6—Schematic representation of ANN compressive strength model.

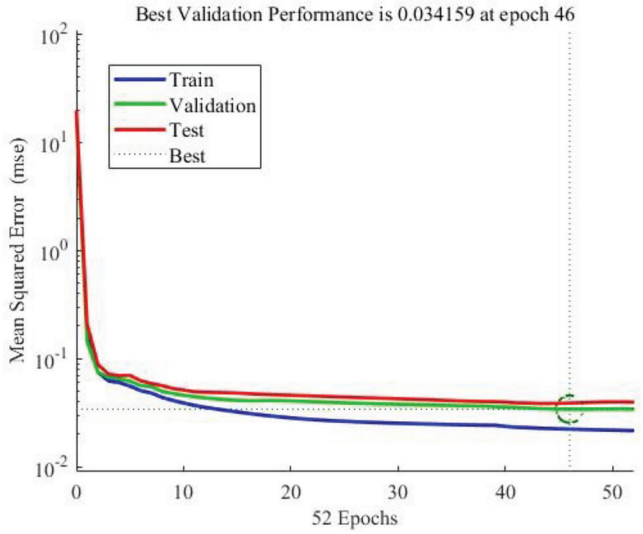

Fig. 7—Performance plot of ANN.

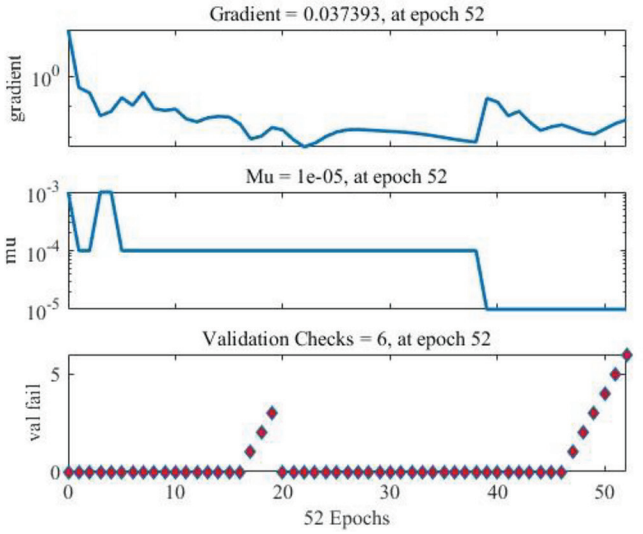

Fig. 8—Training state plot for ANN model.

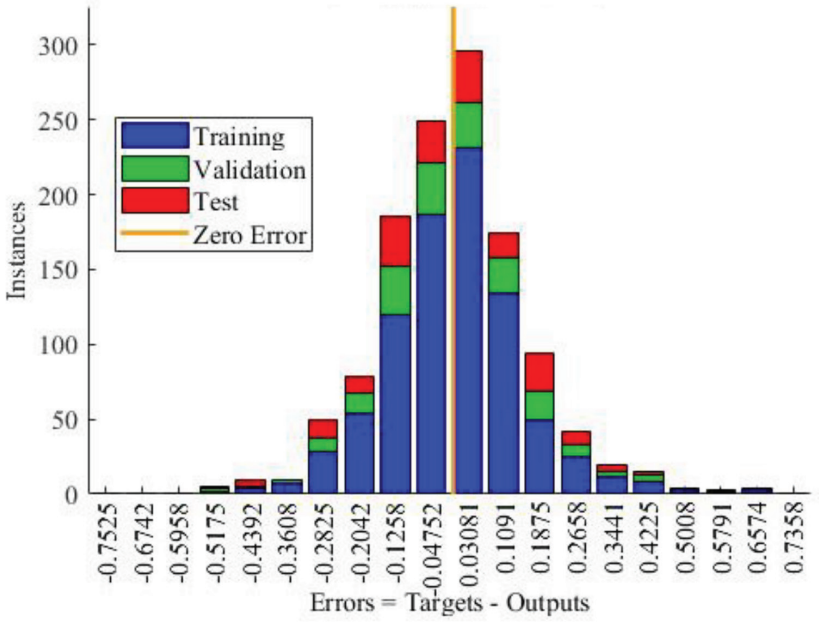

Fig. 9—Error histogram.

network featuring a hidden layer with 19 neurons was chosen, resulting in an R-value of 0.902 and an R^2 value of 0.814. In Fig. 10, a regression plot illustrates the performance of the validation, testing, and training data sets. The R^2 values for the training, testing, and validation data sets were 0.84, 0.74, and 0.77, respectively.

TAYLOR DIAGRAM

The Taylor diagram serves as a visual tool for a thorough assessment of the model's performance. In this study, a systematic evaluation was conducted to gauge the similarity between the ANN outputs and experimental observations, employing various statistical metrics, such as the correlation coefficient, standard deviation, and root-mean-square difference (RMSE). The alignment between the ANN outputs and experimental results is evident for the training, validation, and testing data sets, as illustrated in Fig. 11 and 12.

Figure 11 represents the correlation coefficient between the ANN outputs and experimental observations along the y-axis, and the x-axis illustrates the standard deviations, offering insight into the variability in predictions. A correlation coefficient of 1 indicates an exact match between the two data sets. Examining the distribution of points on the scatterplot allows for a visual assessment of how well the model aligns with the observed data, with clustering around a 45-degree line suggesting good agreement.

Displayed in Fig. 12 is the representation of the RMSE on the x-axis against the data set number on the y-axis. The RMSE serves as a tool to discern areas of over- or underprediction. The correlation between the predicted and experimental values is deemed satisfactory, affirming the validity of the model. The Taylor diagrams provided a holistic view of the statistical metrics guiding the evaluation of the agreement between ANN outputs and experimental data, consisting of 1242 data points.

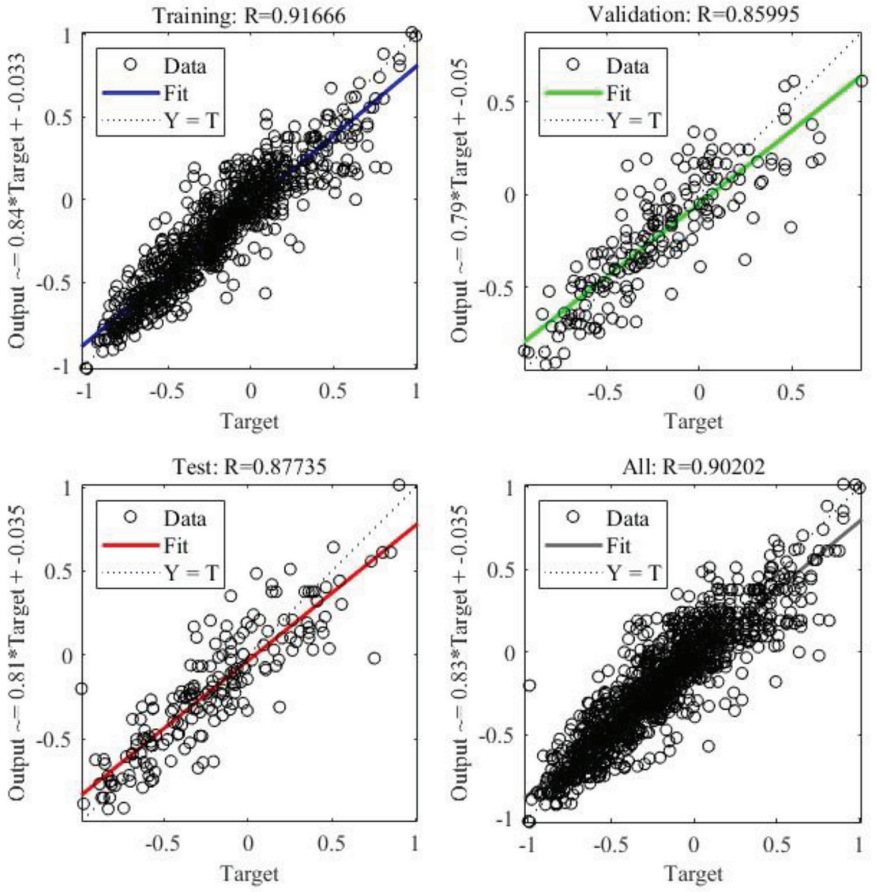

Fig. 10—Regression plots for different data sets.

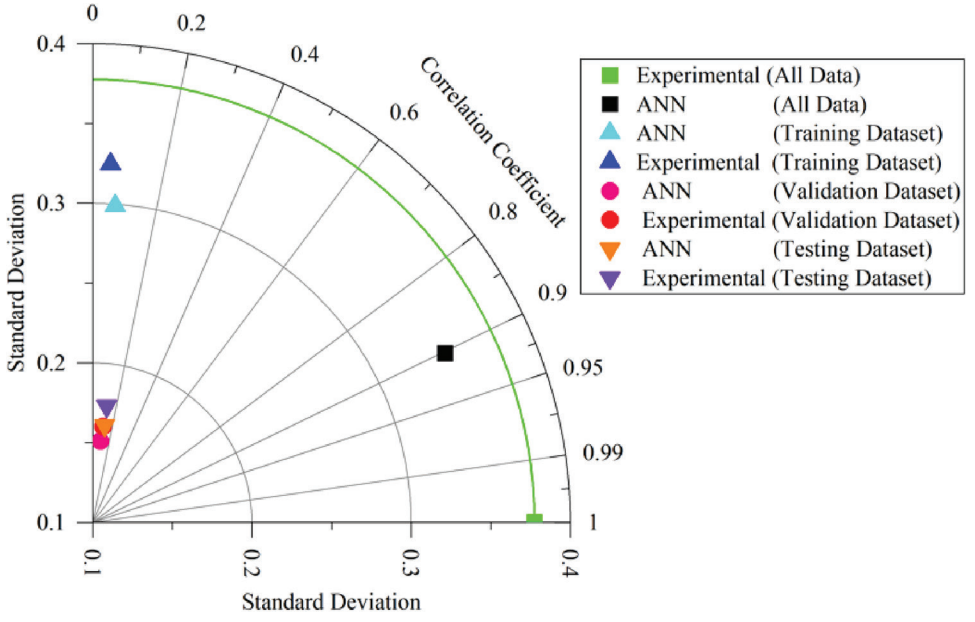

Fig. 11—Taylor diagram: standard deviation.

MATHEMATICAL FORMULATION OF DEVELOPED ANN MODEL

While the simulated outcomes from the proposed ANNs exhibit favorable concordance with the experimental data, they may not be the most convenient tools for engineers in practical engineering design due to their complex nature.[26] ANNs involve a network of interconnected nodes with weights and biases that are adjusted during training to learn patterns in the data.[53] It is reasonable and feasible to explicitly derive a functional-form mathematical equation from the trained networks by amalgamating the weight matrixes and the bias matrixes.[24,54] However, the eventual equations will become intricate due to the use of nonlinear transfer functions. In the preceding section, the tansig transfer function

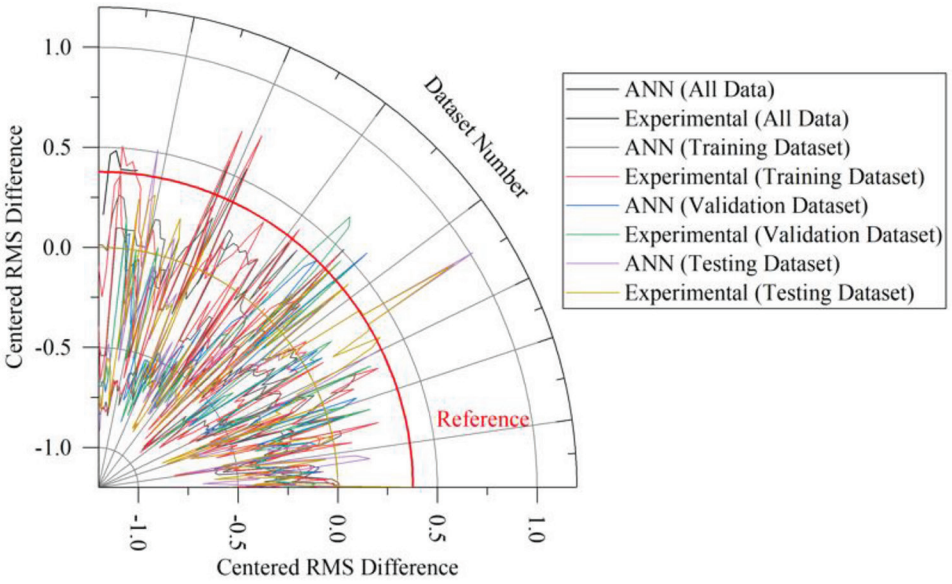

Fig. 12—Taylor diagram: root-mean-square difference (RMSE).

was employed in the hidden layer, chosen for its superior performance compared to the purelin transfer function.[55,56] In this research, an attempt was undertaken to formulate a mathematical equation based on the developed ANN model for the prediction of compressive strength in FA-based GPC. Figure 13 illustrates a typical ANN with weights, bias, activation function, and output. The squishification of each neuron, from input layer to the final output, has been assessed using Eq. (7) to (12).

$$X = [\, z1\ z2\ z3\ \ldots\ zn] \tag{7}$$

$$b = w_0 = \text{bias} \tag{8}$$

$$\text{net} = w_0 + w_1 z_1 + \ldots + w_n z_n \tag{9}$$

$$WX = w_1 z_1 + \ldots + w_n z_n \tag{10}$$

$$\text{net} = WX + b \tag{11}$$

$$y = f(\text{net}) = f(WX + b) \tag{12}$$

WEIGHT AND BIAS MATRIXES

From the trained ANN in the previous section, the matrixes of weights and biases, employing tansig in the hidden layer and purelin in the output layer, are outlined in Tables 3 and 4.

The mathematical design of the ANN implemented in this investigation is presented in Fig. 14. The input layer comprises nine neurons, the hidden layer comprises 19 neurons, and the output layer comprises one neuron. From the input layer, each neuron was transferred to the hidden layer, where its weights and biases were adjusted through the LM algorithm. Finally, the hidden layer provided an input weight matrix (IW) of size [19 × 9] and a bias matrix ($b1$) of size [19 × 1]. The output of the hidden layer ($y1$) consisted of a [19 × 1] matrix. The operation of the hidden layer is presented in Eq. (13) to (20)

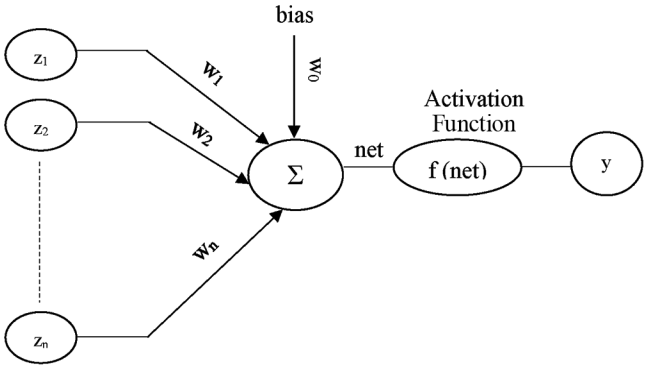

Fig. 13—Mathematical model of ANN.

$$\text{IW} = [19 \times 9] \text{ matrix} \tag{13}$$

$$X = [9 \times 1] \text{ matrix} \tag{14}$$

$$\text{IW}X = [19 \times \boxed{9}] \times [\boxed{9} \times 1] \tag{15}$$

$$\text{IW}X = [19 \times 1] \text{ matrix} \tag{16}$$

$$b1 = [19 \times 1] \text{ matrix} \tag{17}$$

$$\text{IW}X + b1 = [19 \times 1] \text{ matrix} \tag{18}$$

$$\text{net}1 = \text{IW}X + b1 \tag{19}$$

$$y1 = f(\text{net}1) \tag{20}$$

The output from the hidden layer served as the input for the output layer. Subsequently, adjustments to the weights and biases were made using the chosen training algorithm. The output layer provided a layer weight matrix (LW) of size [1 × 19] and a bias matrix ($b2$) of size [1 × 1]. The output of the output layer (y) consisted of a [1 × 1] matrix, which was the final result for one set of the inputs.

Table 3—Input weight matrix (IW)

2.204	3.013	–2.14	3.053	–1.272	–1.183	–0.301	0.484	–0.198
–0.339	–1.542	–0.576	–0.963	–0.629	–0.236	0.847	–0.91	–0.68
–0.542	0.044	–0.216	–0.643	–0.161	0.013	0.309	1.548	–0.067
–1.041	–2.324	1.305	–3.436	1.648	1.181	0.498	0.021	–0.307
1.897	0.07	1.466	0.206	–1.797	–2.183	–0.132	1.792	–2.451
–0.17	–1.834	0.66	–0.426	–0.651	2.117	–0.116	–1.944	–0.225
–0.677	–0.743	0.433	–0.42	–0.279	2.024	0.682	1.152	–0.502
–1.537	–0.323	–0.462	0.046	–2.175	1.472	0.208	–1.314	–0.047
–0.736	–3.612	0.921	1.033	0.722	1.801	0.353	0.233	–1.059
–1.527	1.642	1.627	–0.249	0.269	1.202	0.307	–0.612	2.279
–0.018	–1.54	–0.7	–0.825	0.326	0.059	–0.06	–1.139	0.094
–0.797	0.773	1.708	–1.86	0.271	2.234	–0.027	0.553	1.451
3.716	0.406	–0.751	0.132	1.635	–3.277	–0.064	1.712	0.059
–1.107	–1.406	0.114	0.53	1.056	0.927	0.31	1.362	–0.34
1.915	–0.813	–1.855	–0.686	–0.568	–0.686	–0.092	0.401	–1.573
2.25	0.205	3.247	0.238	0.424	–1.11	0.251	–0.212	1.341
0.737	–0.421	–0.19	0.51	–0.116	–0.1344	–0.807	0.5	–2
3.042	–0.28	0.1	0.115	1.984	–0.34	–0.134	1.612	–0.213
–0.312	–0.038	0.996	0.127	–0.076	0.974	0.296	0.786	0.856

$$\mathrm{LW} = [1 \times 19] \text{ matrix} \tag{21}$$

$$b2 = [1 \times 1] \text{ matrix} \tag{22}$$

$$\mathrm{LW}y1 = [1 \times 19] \times [19 \times 1] \tag{23}$$

$$\mathrm{LW}y1 + b2 = [1 \times 1] \text{ matrix} \tag{24}$$

$$\mathrm{net2} = \mathrm{LW}y1 + b2 \tag{25}$$

$$y = f(\mathrm{net2}) \tag{26}$$

Equation (26) is the final output from the developed ANN. To formulate a compressive strength equation, the subsequent procedure was employed.

$$y = f(\mathrm{LW}y1 + b2) \tag{27}$$

$$y = f(\mathrm{LW}(f(\mathrm{IW}X + b1)) + b2) \tag{28}$$

The purelin transfer function was applied in the output layer, resulting in Eq. (28) as follows

$$y = \mathrm{purelin}(\mathrm{LW}(f(\mathrm{IW}X + b1)) + b2) \tag{29}$$

APPLICATION OF PURELIN TRANSFER FUNCTION

Equation (3) signifies a pure linear (purelin) activation function, a simple function that imparts linear transformation to inputs without introducing nonlinearity. If the purelin function is applied in the hidden layer, Eq. (29) transforms as follows

$$y = \mathrm{purelin}(\mathrm{LW}(\mathrm{purelin}(\mathrm{IW}X + b1)) + b2) \tag{30}$$

Table 4—Layer weight matrix (LW), layer-1 bias, and layer-2 bias

LW^T	$b1$	$b2$
–2.116	2.834	
–1.181	1.831	
–2.123	0.929	
–1.82	–2.282	
0.657	–2.242	
–1.929	0.553	
2.133	3.161	
1.869	–2.151	
–0.912	0.57	
3.174	–0.731	–0.267
1.489	–0.865	
–1.539	0.466	
–1.423	–0.397	
1.639	0.336	
2.418	0.741	
0.918	1.834	
1.432	1.875	
1.335	3.347	
0.086	–2.227	

Note: Superscript "T" represents transpose of a matrix.

$$y = (\mathrm{LW}(\mathrm{IW}X + b1) + b2) \tag{31}$$

$$y = \mathrm{LW} \times \mathrm{IW}X + \mathrm{LW} \times b1 + b2 \tag{32}$$

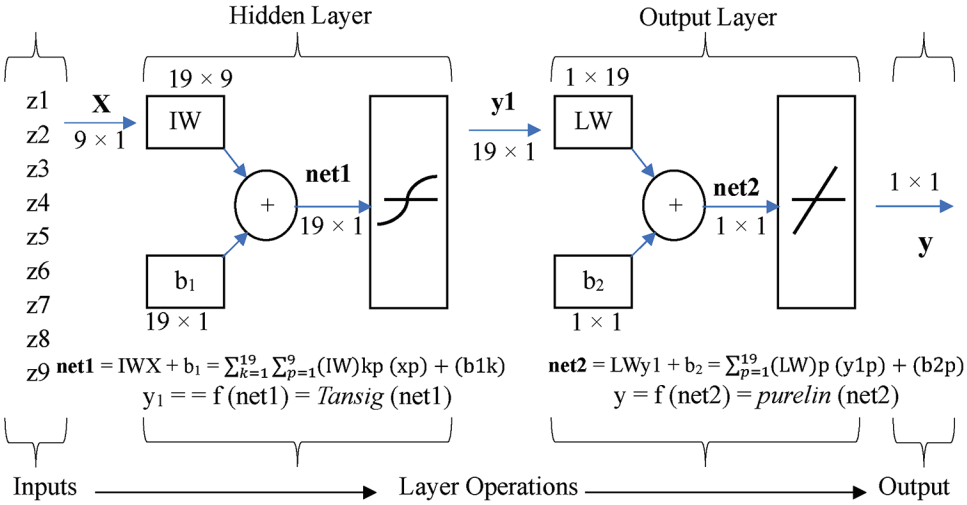

Fig. 14—ANN architecture of this study.

$$y = (\text{LW} \times \text{IW})X + (\text{LW} \times b1 + b2) \quad (33)$$

$$W = \text{LW} \times \text{IW} \quad (34)$$

$$y = WX + a \quad (35)$$

where W is characterized as a proportional matrix obtained through the multiplication of the LW and the IW; and the scalar a is defined as (LW$b1$ + $b2$). The dimensions of the W-matrix, the scalar a, and the output (y) were computed as follows

$$W = [1 \times \boxed{19}] \times [\boxed{19} \times 9] \quad (36)$$

$$W = [1 \times 9] \text{ matrix} = [w1\ w2\ w3\ w4\ w5\ w6\ w7\ w8\ w9] \quad (37)$$

$$a = [1 \times \boxed{19}] \times [\boxed{19} \times 1] + [1 \times 1] = [1 \times 1] \text{ matrix} \quad (38)$$

$$y = [1 \times \boxed{9}] \times [\boxed{9} \times 1] + [1 \times 1] = [1 \times 1] \text{ matrix} \quad (39)$$

If the purelin transfer function were applied in the hidden layer, Eq. (34) would yield the same output as Eq. (26). However, a user-friendly compressive strength equation (Eq. (35)) from the trained ANN has successfully been derived. The compressive strength equation for the n number of input variables is presented as follows

$$y = \sum_{p=1}^{n}(WpXp) + a \quad (40)$$

$$y = (w1z1 + w2z2 + w3z3 + w4z4 + w5z5 + w6z6 + w7z7 + w8z8 + w9z9) + a \quad (41)$$

For this study, the proportional weight matrix was calculated using Eq. (34) and is given as follows.

$w1$	$w2$	$w3$
−0.1469	−0.4413	−0.1418
$w4$	$w5$	$w6$
−0.0436	0.34109	0.19429
$w7$	$w8$	$w9$
0.25735	−0.1382	−0.2505

The predictive equation for the compressive strength of FA-based GPC is presented in Eq. (42).

$$y = -0.1469(z1) - 0.4413(z2) - 0.1418(z3) - 0.0436(z4) + 0.34109(z5) + 0.19429(z6) + 0.25735(z7) - 0.1382(z8) - 0.2505(z9) - 0.09842 \quad (42)$$

APPLICATION OF TAN-SIGMOID FUNCTION

Equation (2) denotes the tansig activation function, a nonlinear transformation applied to inputs to introduce nonlinearity. This study employed the tansig function in the hidden layer, thereby transforming Eq. (29) into the following expressions.

$$y = \text{purelin}(\text{LW}(\text{tansig}(\text{IW}X + b1)) + b2) \quad (43)$$

$$y = (\text{LW}(\text{tansig}(\text{IW}X + b1)) + b2) \quad (44)$$

$$\text{tansig}(\text{IW}X + b1) = \frac{2}{1 + e^{-2(\text{IW}X + b1)}} - 1 \quad (45)$$

$$y = (\text{LW}\left(\frac{2}{1 + e^{-2(\text{IW}X + b1)}} - 1\right) + b2) \quad (46)$$

The predictive equation for compressive strength is articulated in Eq. (47). This equation encapsulates the computations executed within the ANN, using the weight and bias matrixes outlined in Tables 4 and 5. Thus, for a given set of inputs, Eq. (47) calculates the output, representing the compressive strength of FA-based GPC.

$$y = \left[\sum_{p=1}^{19}(\text{LW})p \times \left(\sum_{k=1}^{19}\sum_{p=1}^{9}\left(\frac{2}{1 + e^{-2((\text{IW})kp(Xp) + b1k)}} - 1\right)\right)\right] + (b2p) \quad (47)$$

PERFORMANCE OF PROPOSED MATHEMATICAL EXPRESSIONS

The efficacy of the proposed compressive strength equations (Eq. (42) and (47)) is depicted in Fig. 15 to 18 across training, validation, and testing data sets. These visualizations

Table 5—Sensitivity analysis

Neural network	*z*1	*z*2	*z*3	*z*4	*z*5	*z*6	*z*7	*z*8	*z*9
ANN-1	0.131	0.132	0.072	0.087	0.115	0.180	0.098	0.088	0.098
ANN-2	0.145	0.105	0.082	0.071	0.154	0.124	0.097	0.117	0.105
ANN-3	0.146	0.103	0.059	0.085	0.158	0.147	0.099	0.104	0.099
ANN-4	0.148	0.116	0.107	0.071	0.134	0.107	0.112	0.100	0.105
ANN-5	0.155	0.125	0.104	0.061	0.148	0.140	0.093	0.095	0.078
ANN-6	0.151	0.094	0.076	0.079	0.189	0.134	0.093	0.099	0.085
ANN-7	0.176	0.097	0.097	0.082	0.138	0.121	0.105	0.101	0.082
ANN-8	0.152	0.098	0.070	0.081	0.209	0.122	0.080	0.099	0.089
ANN-9	0.146	0.092	0.083	0.085	0.198	0.100	0.108	0.111	0.078
ANN-10	0.155	0.098	0.093	0.073	0.154	0.136	0.098	0.101	0.092
Average importance	0.150	0.106	0.084	0.077	0.160	0.131	0.098	0.102	0.091
Normalized importance	94%	66%	53%	48%	100%	82%	61%	64%	57%

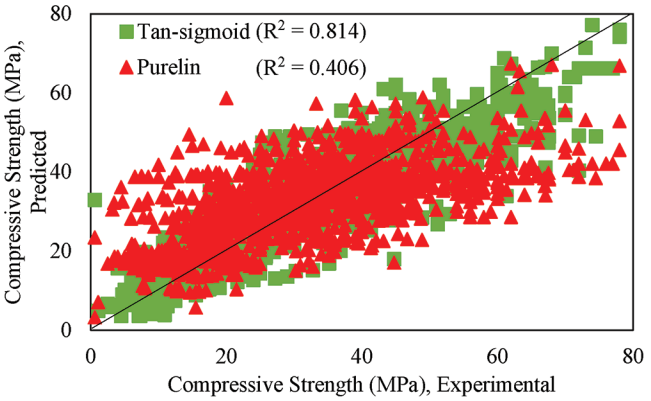

Fig. 15—Accuracy of activation functions (all data).

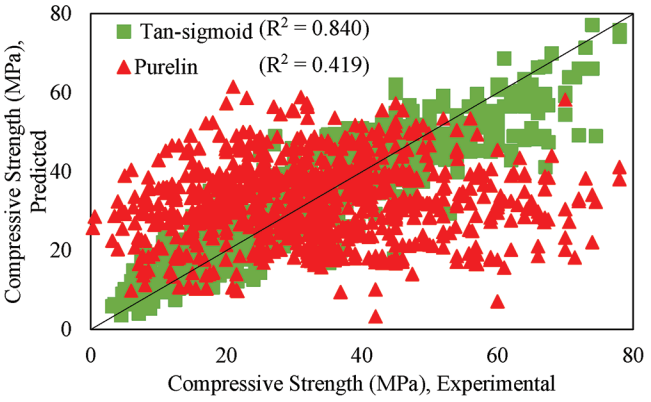

Fig. 16—Accuracy of activation functions (70% training data set).

underscore that the equation formulated with a tansig transfer function yields estimated compressive strength values that closely align with the experimental observations. Figure 19 shows the error in predictions by Eq. (42) and (47) for 1242 experimental observations. Notably, Eq. (47) exhibits minimal errors compared to Eq. (42). This observation underscores the significance of introducing nonlinearity through the tansig activation function for accurate predictions of the compressive strength of FA-based GPC.

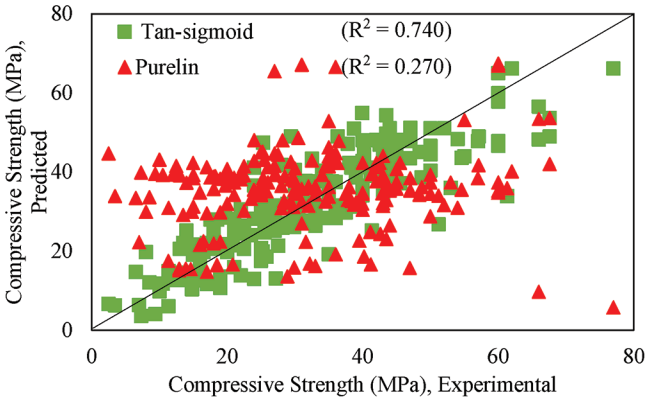

Fig. 17—Accuracy of activation functions (15% validation data set).

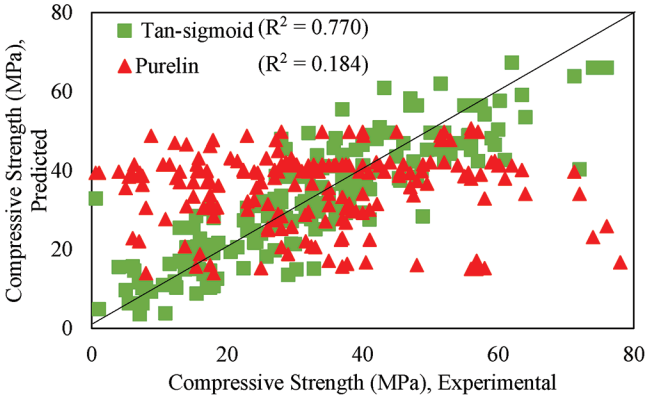

Fig. 18—Accuracy of activation functions (15% testing data set).

SENSITIVITY ANALYSIS

To assess the predictive capabilities of each independent variable, a sensitivity analysis was conducted (refer to Table 5 and Fig. 20). The normalized importance of these variables was determined by dividing their relative importance by the maximum importance and presenting the results as a percentage. The analysis revealed that curing temperature (*z*5) emerged as the most crucial predictor. Following

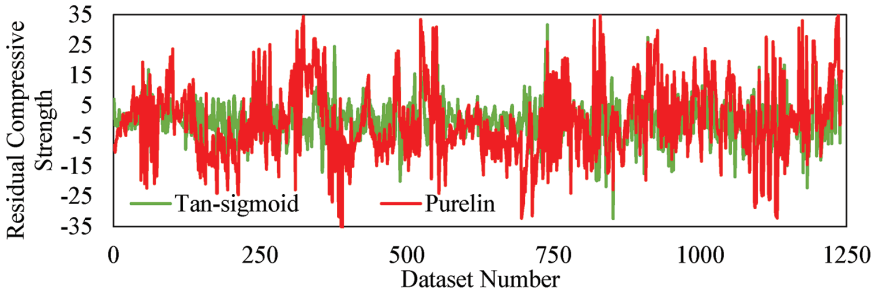

Fig. 19—Residual compressive strength.

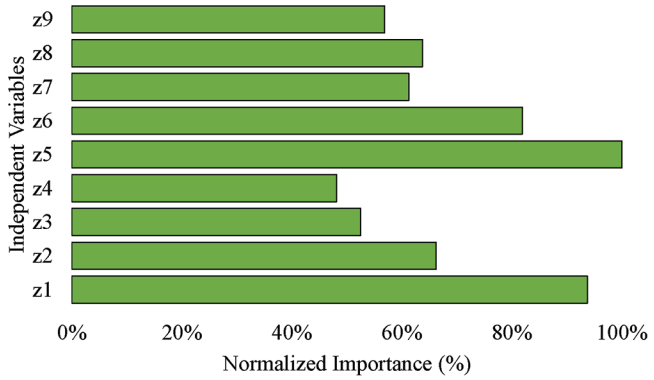

Fig. 20—Relative importance of independent variables.

closely is the silica-alumina ratio ($z1$) at 94%. Subsequent variables and their normalized importance include curing duration ($z6$) at 82%, activation solution to precursor ratio ($z2$) at 66%, fine aggregates to total aggregates ratio ($z8$) at 64%, age of specimen ($z7$) at 61%, aggregates to GPC mixture ratio ($z9$) at 57%, sodium silicate to hydroxide ratio ($z3$) at 53%, and NaOH molarity ($z4$) at 48%.

CONCLUSIONS

A comprehensive data set was curated through an extensive literature review,[25] aiming to forecast the compressive strength of geopolymer concrete (GPC) based on fly ash (FA). Using artificial neural networks (ANNs), predictive models were developed employing different activation functions. The validation process involved comparing the predicted strength with experimental observations. The investigation produced several noteworthy findings, summarized as follows:

1. The statistical analysis reveals no direct correlation between compressive strength and independent variables, and there is also an absence of correlation among the independent variables.

2. The ANN approach amalgamates the intricacy of various statistical and machine-learning techniques, functioning as a versatile black box applicable across diverse engineering disciplines. This approach proves to be the most effective model for precise prediction of the compressive strength of GPC.

3. It is noteworthy that the regression values (R-values) generated for the training, testing, and validation data sets were 0.91666, 0.87735, and 0.85995, respectively. The optimal performance in ANN modeling was achieved at epoch 46, demonstrating a high accuracy in predicting the compressive strength. Therefore, the developed ANN model can be used by engineers to calculate the compressive strength of FA-based GPC.

4. The proposed mathematical expressions provide a simplified form with minimal errors. The error for the proposed mathematical model was approximately 9% when the tan-sigmoid (tansig) activation function was used and 23.8% when the purelin activation function was applied, although both proposed equations predicted the compressive strength. Still, the tansig activation function (mean squared error [MSE] = 6.66 and R^2 = 0.814) exhibited superior performance compared to the purelin activation function (MSE = 11.9 and R^2 = 0.406).

5. The sensitivity analysis highlighted that the curing temperature ($z5$) and the SiO_2-Al_2O_3 ratio ($z1$) were the foremost parameters significantly influencing the compressive strength.

RESEARCH LIMITATIONS AND FUTURE DIRECTIONS

This study focuses on FA-based GPC, and it is important to exercise caution when generalizing the results to slag-based GPC or metakaolin-based GPC. Future research could broaden the scope by formulating compressive strength models for diverse GPC compositions. Furthermore, considering the primary emphasis on predicting compressive strength in this investigation, there is an opportunity to develop predictive models for tensile and flexural behavior. Lastly, as the current study uses an artificial intelligence approach for compressive strength prediction, validation through an experimental program is suggested to validate the outcomes.

AUTHOR BIOS

Muhammad Naveed *is a PhD Student in the Civil Engineering Department at the University of Engineering and Technology, Lahore, Lahore, Pakistan.*

Asif Hameed *is a Professor in the Civil Engineering Department at the University of Engineering and Technology, Lahore.*

Ali Murtaza Rasool *is a Structural Expert at Diamer Basha Dam Consultant Group (DBCG) – National Engineering Services Pakistan (NESPAK), Lahore, Pakistan.*

Rashid Hameed *is a Professor in the Civil Engineering Department at the University of Engineering and Technology, Lahore.*

Danish Mukhtar *is an MSc Student in the Department of Computer Science at the National University of Sciences and Technology, Islamabad, Pakistan.*

DECLARATION OF COMPETING INTEREST

The authors assert that there are no known financial or interpersonal conflicts that could potentially impact the integrity of the presented research.

ACKNOWLEDGMENTS

The authors express their gratitude to the Civil Engineering Department at the University of Engineering and Technology, Lahore, Lahore, Pakistan, for their generous support in both research and financial aspects.

REFERENCES

1. Zhong, J.-X.; Cao, L.-Y.; Li, M.; Wang, S.-P.; Liu, F.; Lv, X.-W.; and Peng, X.-Q., "Mechanical Properties and Durability of Alkali-Activated Steel Slag–Blast Furnace Slag Cement," *Journal of Iron and Steel Research International*, V. 30, No. 7, 2023, pp. 1342-1355. doi: 10.1007/s42243-023-01003-6

2. Srividya, T.; Kannan Rajkumar, P. R.; Sivasakthi, M.; Sujitha, A.; and Jeyalakshmi, R., "A State-of-the-Art on Development of Geopolymer Concrete and Its Field Applications," *Case Studies in Construction Materials*, V. 16, 2022, Article No. e00812. doi: 10.1016/j.cscm.2021.e00812

3. Verma, M., and Dev, N., "Sodium Hydroxide Effect on the Mechanical Properties of Flyash-Slag Based Geopolymer Concrete," *Structural Concrete*, V. 22, No. S1, 2021, pp. E368-E379. doi: 10.1002/suco.202000068

4. Rathnayaka, M.; Karunasinghe, D.; Gunasekara, C.; Wijesundara, K.; Lokuge, W.; and Law, D. W., "Machine Learning Approaches to Predict Compressive Strength of Fly Ash-Based Geopolymer Concrete: A Comprehensive Review," *Construction and Building Materials*, V. 419, 2024, Article No. 135519. doi: 10.1016/j.conbuildmat.2024.135519

5. Katlav, M.; Ergen, F.; and Donmez, I., "AI-Driven Design for the Compressive Strength of Ultra-High Performance Geopolymer Concrete (UHPGC): From Explainable Ensemble Models to the Graphical User Interface," *Materials Today Communications*, V. 40, 2024, Article No. 109915. doi: 10.1016/j.mtcomm.2024.109915

6. Zakka, W. P.; Lim, N. H. A. S.; and Khun, M. C., "A Scientometric Review of Geopolymer Concrete," *Journal of Cleaner Production*, V. 280, Part 1, 2021, Article No. 124353. doi: 10.1016/j.jclepro.2020.124353

7. Verma, M., and Dev, N., "Effect of Ground Granulated Blast Furnace Slag and Fly Ash Ratio and the Curing Conditions on the Mechanical Properties of Geopolymer Concrete," *Structural Concrete*, V. 23, No. 4, 2022, pp. 2015-2029. doi: 10.1002/suco.202000536

8. Podolsky, Z.; Liu, J.; Dinh, H.; Doh, J. H.; Guerrieri, M.; and Fragomeni, S., "State of the Art on the Application of Waste Materials in Geopolymer Concrete," *Case Studies in Construction Materials*, V. 15, 2021, Article No. e00637. doi: 10.1016/j.cscm.2021.e00637

9. Parathi, S.; Nagarajan, P.; and Pallikkara, S. A., "Ecofriendly Geopolymer Concrete: A Comprehensive Review," *Clean Technologies and Environmental Policy*, V. 23, No. 6, 2021, pp. 1701-1713. doi: 10.1007/s10098-021-02085-0

10. Yeşilyurt, M., and Kocadağistan, B., "Carbon Footprint Evaluation of a Ready-Mixed Concrete Plant," *NanoEra*, V. 3, No. 1, 2023, pp. 8-15. doi: 10.5152/NanoEra.2023.1233774

11. Ahmed, H. U.; Mostafa, R. R.; Mohammed, A.; Sihag, P.; and Qadir, A., "Support Vector Regression (SVR) and Grey Wolf Optimization (GWO) to Predict the Compressive Strength of GGBFS-Based Geopolymer Concrete," *Neural Computing & Applications*, V. 35, No. 3, 2023, pp. 2909-2926. doi: 10.1007/s00521-022-07724-1

12. Ahmed, H. U.; Mohammed, A. S.; Qaidi, S. M. A.; Faraj, R. H.; Hamah Sor, N.; and Mohammed, A. A., "Compressive Strength of Geopolymer Concrete Composites: A Systematic Comprehensive Review, Analysis and Modeling," *European Journal of Environmental and Civil Engineering*, V. 27, No. 3, 2023, pp. 1383-1428. doi: 10.1080/19648189.2022.2083022

13. Hossain, M. A. S.; Uddin, M. N.; and Hossain, M. M., "Prediction of Compressive Strength Fiber-Reinforced Geopolymer Concrete (FRGC) Using Gene Expression Programming (GEP)," *Materials Today: Proceedings*, 2023. doi: 10.1016/j.matpr.2023.02.458

14. Roshani, M. M.; Kargar, S. H.; Farhangi, V.; and Karakouzian, M., "Predicting the Effect of Fly Ash on Concrete's Mechanical Properties by ANN," *Sustainability*, V. 13, No. 3, 2021, Article No. 1469. doi: 10.3390/su13031469

15. Bajpai, R.; Soni, V.; Shrivastava, A.; and Ghosh, D., "Experimental Investigation on Paver Blocks of Fly Ash-Based Geopolymer Concrete Containing Silica Fume," *Road Materials and Pavement Design*, V. 24, No. 1, 2023, pp. 138-155. doi: 10.1080/14680629.2021.2012236

16. Su, M.; Zhong, Q.; and Peng, H., "Regularized Multivariate Polynomial Regression Analysis of the Compressive Strength of Slag-Metakaolin Geopolymer Pastes Based on Experimental Data," *Construction and Building Materials*, V. 303, 2021, Article No. 124529. doi: 10.1016/j.conbuildmat.2021.124529

17. Gharehbaghi, K.; Tee, K. F.; and Gharehbaghi, S., "Review of Geopolymer Concrete: A Structural Integrity Evaluation," *International Journal of Forensic Engineering*, V. 5, No. 1, 2021, pp. 59-71. doi: 10.1504/IJFE.2021.117384

18. Dao, D. V.; Trinh, S. H.; Ly, H.-B.; and Pham, B. T., "Prediction of Compressive Strength of Geopolymer Concrete Using Entirely Steel Slag Aggregates: Novel Hybrid Artificial Intelligence Approaches," *Applied Sciences*, V. 9, No. 6, 2019, Article No. 1113. doi: 10.3390/app9061113

19. Shahmansouri, A. A.; Yazdani, M.; Ghanbari, S.; Bengar, H. A.; Jafari, A.; and Ghatte, H. F., "Artificial Neural Network Model to Predict the Compressive Strength of Eco-Friendly Geopolymer Concrete Incorporating Silica Fume and Natural Zeolite," *Journal of Cleaner Production*, V. 279, 2021, Article No. 123697. doi: 10.1016/j.jclepro.2020.123697

20. Ahmad, A.; Ahmad, W.; Aslam, F.; and Joyklad, P., "Compressive Strength Prediction of Fly Ash-Based Geopolymer Concrete via Advanced Machine Learning Techniques," *Case Studies in Construction Materials*, V. 16, 2022, Article No. e00840. doi: 10.1016/j.cscm.2021.e00840

21. Verma, N. K.; Meesala, C. R.; and Kumar, S., "Developing an ANN Prediction Model for Compressive Strength of Fly Ash-Based Geopolymer Concrete with Experimental Investigation," *Neural Computing & Applications*, V. 35, No. 14, 2023, pp. 10329-10345. doi: 10.1007/s00521-023-08237-1

22. Pratap, B.; Shubham, K.; Mondal, S.; and Rao, B. H., "Exploring the Potential of Neural Network in Assessing Mechanical Properties of Geopolymer Concrete Incorporating Fly Ash and Phosphogypsum in Pavement Applications," *Asian Journal of Civil Engineering*, V. 24, No. 8, 2023, pp. 3575-3589. doi: 10.1007/s42107-023-00735-w

23. Naveed, M.; Hameed, A.; Rasool, A. M.; Mukhtar, D.; and Ahmed, T., "AI-Based Non-Linear Models for Mechanical and Toughness Properties of Sustainable Fiber-Reinforced Geopolymer Concrete (FRGPC)," *Mechanics of Advanced Materials and Structures*, 2024, pp. 1-25. doi: 10.1080/15376494.2024.2390182

24. Pham, T. M., and Hadi, M. N. S., "Predicting Stress and Strain of FRP-Confined Square/Rectangular Columns Using Artificial Neural Networks," *Journal of Composites for Construction*, ASCE, V. 18, No. 6, 2014, p. 04014019. doi: 10.1061/(ASCE)CC.1943-5614.0000477

25. Naveed, M.; Hameed, A.; Qureshi, M. U.; and Rasool, A. M., "Optimization of Constituent Proportions for Compressive Strength of Sustainable Geopolymer Concrete: A Statistical Approach," *Results in Engineering*, V. 20, 2023, Article No. 101575. doi: 10.1016/j.rineng.2023.101575

26. Ahmed, H. U.; Mohammed, A. S.; and Mohammed, A. A., "Proposing Several Model Techniques Including ANN and M5P-Tree to Predict the Compressive Strength of Geopolymer Concretes Incorporated with Nano-Silica," *Environmental Science and Pollution Research*, V. 29, No. 47, 2022, pp. 71232-71256. doi: 10.1007/s11356-022-20863-1

27. Waqas, R. M.; Butt, F.; Zhu, X.; Jiang, T.; and Tufail, R. F., "A Comprehensive Study on the Factors Affecting the Workability and Mechanical Properties of Ambient Cured Fly Ash and Slag Based Geopolymer Concrete," *Applied Sciences*, V. 11, No. 18, 2021, Article No. 8722. doi: 10.3390/app11188722

28. Salla, S. R.; Modhera, C. D.; and Babu, U. R., "An Experimental Study on Various Industrial Wastes in Concrete for Sustainable Construction," *Journal of Advanced Concrete Technology*, V. 19, No. 2, 2021, pp. 133-148. doi: 10.3151/jact.19.133

29. Ahmed, H. U.; Abdalla, A. A.; Mohammed, A. S.; Mohammed, A. A.; and Mosavi, A., "Statistical Methods for Modeling the Compressive Strength of Geopolymer Mortar," *Materials*, V. 15, No. 5, 2022, Article No. 1868. doi: 10.3390/ma15051868

30. Meesala, C. R.; Verma, N. K.; and Kumar, S., "Critical Review on Fly-Ash Based Geopolymer Concrete," *Structural Concrete*, V. 21, No. 3, 2020, pp. 1013-1028. doi: 10.1002/suco.201900326

31. Philip, S., and Nidhi, M., "A Review on the Material Performance of Geopolymer Concrete as Green Building Materials," *Materials Today: Proceedings*, 2023. doi: 10.1016/j.matpr.2023.04.110

32. Naveed, M.; Raza, M. A.; and Mehmood, R., "Performance Analyses of Conventional Hot Mix Asphalt with Waste Additives," *Case Studies in Construction Materials*, V. 16, 2022, Article No. e00850. doi: 10.1016/j.cscm.2021.e00850

33. Amin, M.; Elsakhawy, Y.; Abu El-Hassan, K.; and Abdelsalam, B. A., "Behavior Evaluation of Sustainable High Strength Geopolymer Concrete Based on Fly Ash, Metakaolin, and Slag," *Case Studies in Construction Materials*, V. 16, 2022, Article No. e00976. doi: 10.1016/j.cscm.2022.e00976

34. Asuero, A. G.; Sayago, A.; and González, A., "The Correlation Coefficient: An Overview," *Critical Reviews in Analytical Chemistry*, V. 36, No. 1, 2006, pp. 41-59. doi: 10.1080/10408340500526766

35. Veerapandian, V.; Pandulu, G.; Jayaseelan, R.; Sathish Kumar, V.; Murali, G.; and Vatin, N. I., "Numerical Modelling of Geopolymer Concrete In-Filled Fibre-Reinforced Polymer Composite Columns Subjected to Axial Compression Loading," *Materials*, V. 15, No. 9, 2022, Article No. 3390. doi: 10.3390/ma15093390

36. Kanwisher, N.; Khosla, M.; and Dobs, K., "Using Artificial Neural Networks to Ask 'Why' Questions of Minds and Brains," *Trends in Neurosciences*, V. 46, No. 3, 2023, pp. 240-254. doi: 10.1016/j.tins.2022.12.008

37. Worden, K.; Tsialiamanis, G.; Cross, E. J.; and Rogers, T. J., "Artificial Neural Networks," *Machine Learning in Modeling and Simulation: Methods and Applications*, T. Rabczuk and K.-J. Bathe, eds., Springer, Cham, Switzerland, 2023, pp. 85-119.

38. Hinton, G., "How to Represent Part-Whole Hierarchies in a Neural Network," *Neural Computation*, V. 35, No. 3, 2023, pp. 413-452. doi: 10.1162/neco_a_01557

39. Linka, K., and Kuhl, E., "A New Family of Constitutive Artificial Neural Networks towards Automated Model Discovery," *Computer Methods in Applied Mechanics and Engineering*, V. 403, Part A, 2023, Article No. 115731. doi: 10.1016/j.cma.2022.115731

40. Prem, P. R.; Thirumalaiselvi, A.; and Verma, M., "Applied Linear and Nonlinear Statistical Models for Evaluating Strength of Geopolymer Concrete," *Computers and Concrete*, V. 24, No. 1, 2019, pp. 7-17.

41. Saleh Dolamary, P. Y.; Jaf, D. K.; Arbili, M. M.; and Karpuzcu, M., "Validation of Feret Regression Model for Fly Ash Based Geopolymer Concrete," *Polytechnic Journal*, V. 8, No. 3, 2018, pp. 173-189.

42. Amran, M.; Debbarma, S.; and Ozbakkaloglu, T., "Fly Ash-Based Eco-Friendly Geopolymer Concrete: A Critical Review of the Long-Term Durability Properties," *Construction and Building Materials*, V. 270, 2021, Article No. 121857. doi: 10.1016/j.conbuildmat.2020.121857

43. Hornik, K.; Stinchcombe, M.; and White, H., "Multilayer Feedforward Networks Are Universal Approximators," *Neural Networks*, V. 2, No. 5, 1989, pp. 359-366. doi: 10.1016/0893-6080(89)90020-8

44. Alghannam, M.; Albidah, A.; Abbas, H.; and Al-Salloum, Y., "Influence of Critical Parameters of Mix Proportions on Properties of MK-Based Geopolymer Concrete," *Arabian Journal for Science and Engineering*, V. 46, No. 5, 2021, pp. 4399-4408. doi: 10.1007/s13369-020-04970-0

45. Ahmed, H. U.; Mohammed, A. S.; Mohammed, A. A.; and Faraj, R. H., "Systematic Multiscale Models to Predict the Compressive Strength of Fly Ash-Based Geopolymer Concrete at Various Mixture Proportions and Curing Regimes," *PLOS One*, V. 16, No. 6, 2021, Article No. e0253006. doi: 10.1371/journal.pone.0253006

46. Silva, G.; Kim, S.; Bertolotti, B.; Nakamatsu, J.; and Aguilar, R., "Optimization of a Reinforced Geopolymer Composite Using Natural Fibers and Construction Wastes," *Construction and Building Materials*, V. 258, 2020, Article No. 119697. doi: 10.1016/j.conbuildmat.2020.119697

47. Khan, Q. S.; Sheikh, M. N.; and Hadi, M. N. S., "Predicting Strength and Strain Enhancement Ratios of Circular Fiber-Reinforced Polymer Tube Confined Concrete under Axial Compression Using Artificial Neural Networks," *Advances in Structural Engineering*, V. 22, No. 6, 2019, pp. 1426-1443. doi: 10.1177/1369433218815229

48. Saravanan, S., and Elavenil, S., "Strength Properties of Geopolymer Concrete Using M-Sand by Assessing their Mechanical Characteristics," *ARPN Journal of Engineering and Applied Sciences*, V. 13, No. 13, 2018, pp. 4028-4041.

49. Zhang, H. Y.; Kodur, V.; Qi, S. L.; Cao, L.; and Wu, B., "Development of Metakaolin–Fly Ash Based Geopolymers for Fire Resistance Applications," *Construction and Building Materials*, V. 55, 2014, pp. 38-45. doi: 10.1016/j.conbuildmat.2014.01.040

50. Uwasu, M.; Hara, K.; and Yabar, H., "World Cement Production and Environmental Implications," *Environmental Development*, V. 10, 2014, pp. 36-47. doi: 10.1016/j.envdev.2014.02.005

51. Nguyen, K. T.; Nguyen, Q. D.; Le, T. A.; Shin, J.; and Lee, K., "Analyzing the Compressive Strength of Green Fly Ash Based Geopolymer Concrete Using Experiment and Machine Learning Approaches," *Construction and Building Materials*, V. 247, 2020, Article No. 118581. doi: 10.1016/j.conbuildmat.2020.118581

52. Pham, T. T.; Nguyen, T. T.; Nguyen, L. N.; and Nguyen, P. V., "A Neural Network Approach for Predicting Hardened Property of Geopolymer Concrete," *GEOMATE Journal*, V. 19, No. 74, 2020, pp. 176-184. doi: 10.21660/2020.74.72565

53. Mohammed, A.; Burhan, L.; Ghafor, K.; Sarwar, W.; and Mahmood, W., "Artificial Neural Network (ANN), M5P-Tree, and Regression Analyses to Predict the Early Age Compression Strength of Concrete Modified with DBC-21 and VK-98 Polymers," *Neural Computing & Applications*, V. 33, No. 13, 2021, pp. 7851-7873. doi: 10.1007/s00521-020-05525-y

54. Reed, M.; Lokuge, W.; and Karunasena, W., "Fibre-Reinforced Geopolymer Concrete with Ambient Curing for In Situ Applications," *Journal of Materials Science*, V. 49, No. 12, 2014, pp. 4297-4304. doi: 10.1007/s10853-014-8125-3

55. Kalinowska-Wichrowska, K.; Pawluczuk, E.; Bołtryk, M.; and Nietupski, A., "Geopolymer Concrete with Lightweight Artificial Aggregates," *Materials*, V. 15, No. 9, 2022, Article No. 3012. doi: 10.3390/ma15093012

56. Oyebisi, S., and Alomayri, T., "Artificial Intelligence-Based Prediction of Strengths of Slag-Ash-Based Geopolymer Concrete Using Deep Neural Networks," *Construction and Building Materials*, V. 400, 2023, Article No. 132606. doi: 10.1016/j.conbuildmat.2023.132606

aci Foundation

Building the Future

We're Building the Future

OUR MISSION

We make strategic investments in ideas, research, and people to create the future of the concrete industry.

Through its councils and programs, the ACI Foundation helps to keep the concrete industry at the forefront of advances in material composition, design, and construction.

OUR FOCUS

- Identifying technologies and innovations which provide needed solutions for the concrete industry
- Seeking concrete research projects that further the knowledge and sustainability of concrete materials, construction, and structures
- Supporting our future concrete innovators and leaders by administering fellowships and scholarships
- Helping honorably discharged veterans with our Veterans Rebate for ACI Certification program

www.acifoundation.org

ACI MATERIALS JOURNAL TECHNICAL PAPER

Title No. 122-M17

Predicting Mortar Behavior through Intrinsic and Rheological Properties

by Mouhcine Ben Aicha, Ayoub Aziz, Olivier Jalbaud, and Yves Burtschell

This study investigates the impact of air-entraining admixtures (AEAs) on mortar performance, focusing on fresh-state and hardened-state properties critical to durability and engineering applications. Ten distinct mortar mixtures were analyzed, following guidelines established by the European Federation of National Associations Representing Producers and Applicators of Specialist Building Products for Concrete (EFNARC). AEAs were introduced at varying proportions (0.01 to 0.5% of cement weight) to evaluate their effects on intrinsic properties (density, void ratio, and water absorption), rheological parameters (plastic viscosity and yield stress), and mechanical characteristics (compressive strength, ultrasonic velocity, and modulus of elasticity).

Regression models were developed and yielded high predictive accuracy, with R^2 *values exceeding 0.98. Notably, ultrasonic velocity and modulus of elasticity demonstrated strong correlations with intrinsic properties across all curing ages. Similarly, compressive strength showed significant associations with rheological parameters, highlighting the influence of air content and flow behavior on structural performance. These findings offer precise quantitative models for predicting mortar behavior and optimizing formulations for enhanced performance.*

Keywords: air-entraining admixtures (AEAs); mechanical characteristics; mortar; rheological parameters; ultrasonic velocity.

INTRODUCTION

Sand, cement, and water are thoroughly combined to create cement mortar. Depending on the specifications of the specifier, the applications, and the desired performances, the mortar can also be composed of mineral additions and chemical additives or fibers (Benaicha et al. 2015a; Gdoutos et al. 2016; Jeon et al. 2023; Ramakrishna and Sundararajan 2019).

In recent years, the use of different types of admixtures to improve mortars have been studied (Abarna Munisha et al. 2021; Abdulwahid and Fadhil Abdullah 2021; Ahmad et al. 2020; Ahmadi et al. 2018; Liu et al. 2021; Mao et al. 2022; Sheikh Hassani et al. 2021; Silva et al. 2021; Steiner et al. 2015; Wang et al. 2021) to address limitations in resistance while significantly enhancing their long-term performance.

Increasing the air content in cementitious materials can alter their intrinsic properties, significantly improving their resistance to freezing-and-thawing cycles (Fowler 2009; Ghantous et al. 2021; Lv et al. 2020; Ruegenberg et al. 2021; Zou et al. 2008). Research indicates that the total pore volume within the material plays a crucial role in determining freezing-and-thawing durability (Abadel and Alghamdi 2023; Hall 1989; Litvan 1980; Xue et al. 2010).

During the hydration and hardening of mortars, the consumption of water by the hydration phenomenon induces the appearance of pores in the paste, which affects fresh and hardened material behavior (Craipeau et al. 2021).

As a result of the chemical reaction between cement and water during the hydration and hardening process of mortars, hydration products such as calcium-silicate-hydrate (C-S-H) and CH are developed. Simultaneously, due to water consumption by the hydration process, pores start to appear within the paste because of incomplete filling of the microstructure by hydration products and evaporation of unbound water. Such pores can be classified into gel pores (of the nanometer scale), capillary pores, and larger micrometer-scale entrapped air voids (Hilal 2016; Powers 1958).

Their existence and distribution will have a dual consequence in material behavior: in the fresh state, workability and rheological parameters are directly related to the air content, potentially reducing density. In the hardened state, they are critical to the mechanical properties of compressive strength and modulus of elasticity while also affecting durability. For instance, according to Craipeau et al. (2021), increased porosity generally reduces mechanical strength and improves permeability but can also improve resistance to freezing-and-thawing cycles when properly controlled. The evolution of these pores must be understood for workability and performance to balance each other in mortar formulations.

This observation highlights how the material's intrinsic properties influence the long-term behavior and stability of mortars (Gao et al. 2022; Ge et al. 2023; Sasui et al. 2021; Silva et al. 2020; Zhao et al. 2021). The cyclical production of ice in the porous mortar's structure is a typical reason for the material deterioration in cold areas (where temperatures frequently drop below zero) (Cultrone et al. 2005; Darvish et al. 2021; Kim et al. 2019; Xu et al. 2017).

An air-entraining admixture (AEA) should be added to the mortar to increase its resistance to freezing and thawing (Backstrom et al. 1958; Baltrus and LaCount 2001; Benaicha et al. 2022; Chatterji 2003; Dolch 1996; Du and Folliard 2005; Gagné 2016; Ke et al. 2020; Ley et al. 2009; Öztürk and Kılınçkale 2023; Tunstall et al. 2021). These studies indicate that additional investigations are needed to interpret

ACI Materials Journal, V. 122, No. 3, May 2025.

MS No. M-2024-096.R2, doi: 10.14359/51746715, received December 3, 2024, and reviewed under Institute publication policies.

the effect of these additives on mortar behavior. For instance, Fowler (2009) and Du and Folliard (2005) demonstrate that AEAs significantly influence freezing-and-thawing resistance by modifying pore structure. However, these studies lack detailed quantitative models linking fresh-state parameters (for example, air content and rheological properties) to mechanical outcomes, such as compressive strength and modulus of elasticity. Similarly, research by Ghantous et al. (2021) and Lv et al. (2020) confirms the role of AEAs in improving freezing-and-thawing resistance but provides limited insights into how these effects vary across different AEA dosages.

Further, while Craipeau et al. (2021) explored the relationship between hydration-induced porosity and material behavior, they focused predominantly on pore pressure during early hydration, leaving a gap in understanding the long-term mechanical implications.

This work deals with the development of multivariable regression models for the prediction of the mechanical behavior of mortars with AEA, based on studying the correlation between the intrinsic characteristics (air content, water absorption, void ratio, and density), mechanical parameters (compressive strength, ultrasonic velocity, and modulus of elasticity), and rheological properties (plastic viscosity and yield stress).

First, the amount of air in the mixture containing AEA at different concentrations was examined. Subsequently, the effects of AEA proportions (that is, the weight percentage between the AEA solution and the cement) on the mechanical parameters and the rheological behavior of the mortars were studied in a rather large range. The correlation of these two behaviors with the intrinsic characteristics of samples was then investigated and validated by regression models. Based on the systematic examinations performed in this study, several models are proposed to evaluate the mechanical parameters of mortar mixtures. Finally, the statistical coefficients, standard errors, and residual deviation are provided based on the proposed model.

RESEARCH SIGNIFICANCE

This research is important because it thoroughly investigates how AEAs affect the performance of mortar mixtures. This study offers detailed insights into the correlations between air content, mechanical qualities, and rheological behavior by carefully examining 10 different mortar compositions in accordance with European Federation of National Associations Representing Producers and Applicators of Specialist Building Products for Concrete (EFNARC) requirements.

The research focuses on a critical requirement in the field of mortar engineering, specifically the improvement of freezing-and-thawing resistance. Given the growing focus on sustainability in construction materials, it is essential to comprehend the influence of AEA on the properties of mortar. This understanding is vital for the development of resilient infrastructure. This study provides useful methods for forecasting the behavior of mortar under different settings by developing strong regression models that correlate intrinsic traits, mechanical parameters, and rheological qualities. These models not only enhance the theoretical comprehension of mortar dynamics but also have practical ramifications for the design and optimization of mortar mixtures in real-world construction projects.

Moreover, the research emphasizes the complex relationship between porosity, mechanical strength, and sonic velocity, providing insights into fundamental elements of mortar behavior. This comprehensive approach enhances comprehension of mortar performance and establishes the foundation for future progress in the fields of material science and building engineering.

Table 1—Material proprieties

	CEM	AEA	HRWRA
C_3S, %	63.96	—	—
C_2S, %	10.2	—	—
C_3A, %	2.2	—	—
SiO_2, %	20.5	—	—
S^{2-}, %	0.01	—	—
NaO_2 eq., %	0.52	<4	<1
Cl^- (chloride ions)	0.01	<0.1	<0.1
Density	3.15	1.035 ± 0.02	1.085 ± 0.01
Blaine fineness, cm^2/g	4750	—	—
pH	—	11 ± 1	4.5 ± 1
Dry extract, %	—	9.3 ± 0.9	41 ± 1.5

MATERIALS AND EXPERIMENTAL METHOD

Starting materials and test procedures

The properties of the raw materials used in the manufacture of 10 mortars, such as cement (CEM), high-range water-reducing admixture (HRWRA), and AEA, are given in Table 1 and analyzed in detail in Benaicha et al. (2015b, 2019a,b,c, 2022).

These materials are manufactured according to the European standards EN 197-1, EN 480-8, and EN 934-2 for CEM, HRWRA, and AEA, respectively. In addition, all mortars have been manufactured according to EN 196-1. The percentages of AEA, related to cement weight and mixture proportions, are given in Table 2.

For better representativeness of the sample, each measurement was conducted three times for statistical reliability, resulting in a total of 30 data points for the analysis of 10 mortar mixtures.

Characterization methods

Fresh-condition tests—The fresh mortar is regarded from a rheological viewpoint as a Bingham suspension made up of a cement paste and dispersed aggregates (Flatt 2004; Tattersall and Banfill 1983; Murata 1984; Roussel et al. 2010). The tests used are: 1) air content measurement by aerometer test according to EN 12350-7 (Fig. 1); 2) fresh density of mortar according to EN 10156; and 3) rheological behavior, such as yield stress and plastic viscosity, using a rheometer (Fig. 2). The technical details of these tests are mentioned in Benaicha (2013) and Benaicha et al. (2022).

Table 2—Mortar mixture proportions

Codes	*w*/*c*, %	AEA, %	Cement, kg/m^3	HRWRA, kg/m^3	Water, kg/m^3	Sand 0/2, kg/m^3
Control (M0)	0.45	0	540	3.96	243.5	1460
M1	0.45	0.001	540	3.96	243.5	1460
M2	0.45	0.002	540	3.96	243.5	1460
M3	0.45	0.005	540	3.96	243.5	1460
M4	0.45	0.007	540	3.96	243.5	1460
M5	0.45	0.01	540	3.96	243.5	1460
M6	0.45	0.03	540	3.96	243.5	1460
M7	0.45	0.05	540	3.96	243.5	1460
M8	0.45	0.1	540	3.96	243.5	1460
M9	0.45	0.5	540	3.96	243.5	1460

Note: *w*/*c* is water-cement ratio.

Fig. 1—Aerometer test.

Hardened-state tests—The tests used are: 1) mechanical strength at 1, 7, and 28 days according to EN 1015-11 on cubic specimens measuring 40 x 40 x 40 mm; 2) ultrasonic velocity at 1, 7, and 28 days according to EN 12504-4 on prismatic specimens measuring 40 x 40 x 160 mm; 3) water absorption and void ratio tests by capillary absorption according to EN 1015-18; 4) hardened density of mortar at 28 days according to EN 1015-10; and 5) modulus of elasticity at 28 days by using Eq. (1) and according to Thomaz et al. (2021)

$$Ed = \rho V^2 \frac{(1+\mu)(1-2\mu)}{(1-\mu)} \quad (1)$$

where Ed is the dynamic modulus of elasticity of mortar (GPa); ρ is the hardened density of mortar (kg/m^3); V corresponds to the P-wave velocity (m/s); and μ is the Poisson's ratio. The Poisson's ratio was obtained in the literature, μ = 0.2, according to Rosell and Cantalapiedra (2011).

Before crushing the hardened specimens, their porosity was observed under a binocular microscope with 45× zoom (Fig. 3).

Fig. 2—Rheometer.

Fig. 3—Binocular microscope.

RESULTS AND DISCUSSION

Evaluation of compressive strength based on intrinsic properties

First, Fig. 4 graphically illustrates the evolution of water absorption, air content, and void ratio based on AEA content (Table 2). This figure shows that the values of these intrinsic properties rise as the percentage of AEA increases.

Mortar M0 (without AEA) had an air content of 1.6%, a void ratio of 8.1%, and a water absorption rate of 4.23%. Furthermore, the mortar M9 (with an AEA percentage of 0.5%) had an air content of 14%, a void ratio of 20.3%, and a water absorption rate of 10.04%.

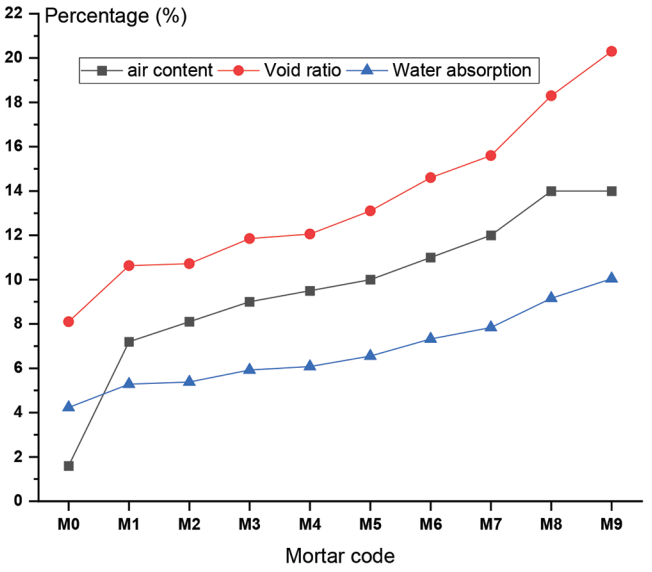

Fig. 4—Evolution of water absorption, void ratio, and air content.

This increase in the void ratio and the other intrinsic parameters is explained by the increase in air bubbles present in the samples (Fig. 5).

Second, Fig. 6 graphically illustrates the effect of AEA percentage on the hardened density of mortar. As can be seen by examining this graph, the hardened density values fall as the AEA percentage increases.

The M0 mortar had a hardened density of 2216 kg/m^3, while the M9 mortar showed a hardened density of 1939 kg/m^3. This decrease is primarily due to air bubbles that have been trapped in the elaborate mortar by the addition of AEA. As a result, the mass of the mixture will become less dense for the same volume.

Finally, Fig. 7 to 9 graphically illustrate the change in compressive strength of the synthesized mortars at 1, 7, and 28 days of curing according to the water absorption, void ratio, and hardened density, respectively. Analyzing these figures, as water absorption increases, the values of this resistance drop (Fig. 7), as well as the void ratio (Fig. 8). However, in Fig. 9, the greater the hardened density, the greater the compressive strength. For water absorption and void ratio, the best correlation was obtained with a polynomial fit of order 2, while for hardened density, the best relationship was obtained with a linear fit.

In this specific study, compressive strength was used as a dependent variable. However, from the results of the

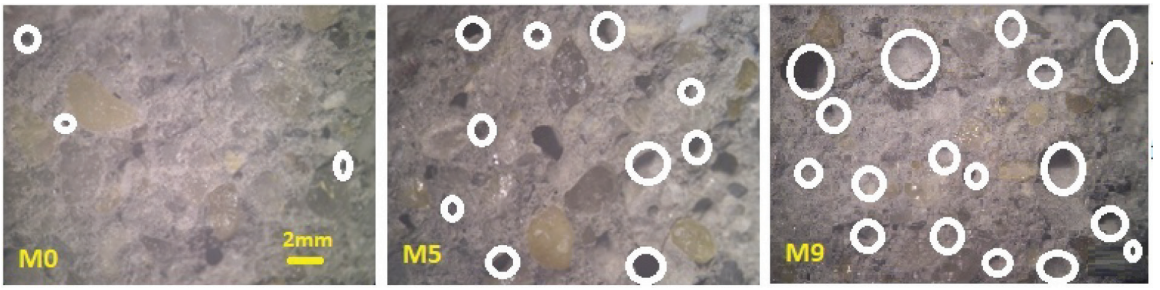

Fig. 5—Porosity analysis of samples by binocular microscope. White circles indicate air voids formed in mortar matrix due to inclusion of AEA.

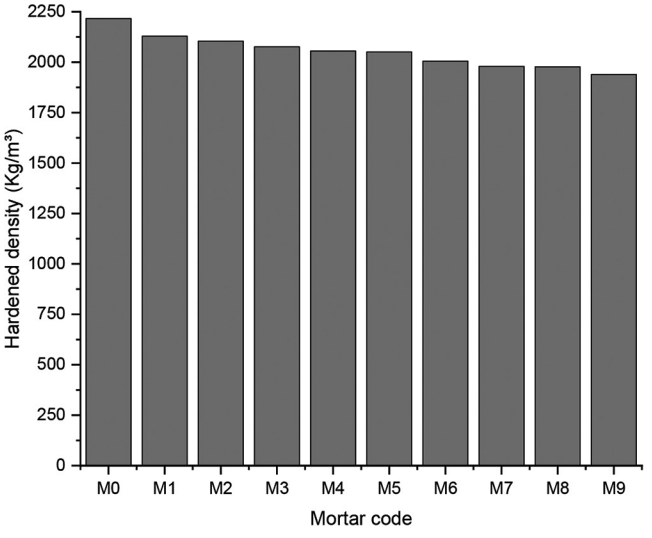

Fig. 6—Evolution of hardened density.

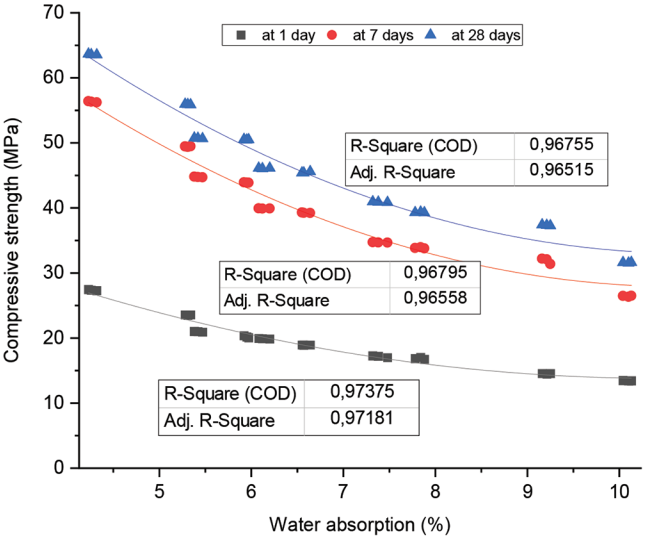

Fig. 7—Correlation between compressive strength and water absorption.

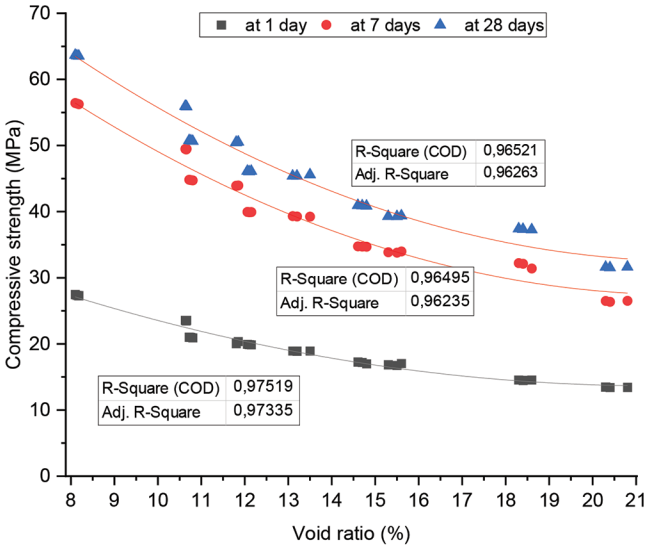

Fig. 8—Correlation between void ratio and compressive strength.

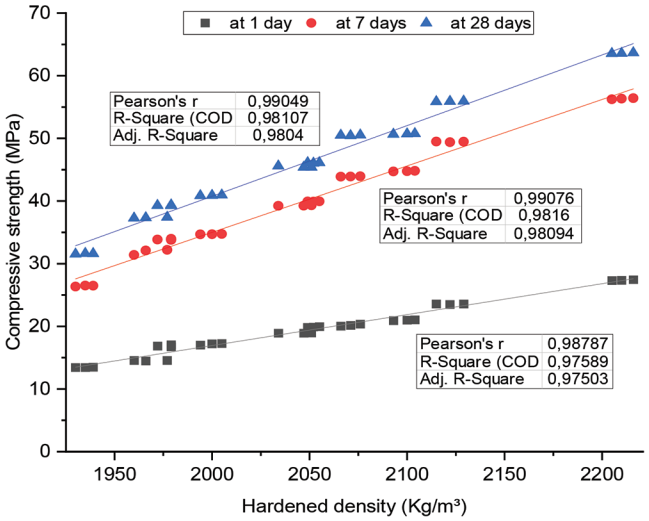

Fig. 9—Correlation between density and compressive strength.

Table 3—Results of regression model of compressive strength

Output	Model parameters	Value	SE	Adj. R^2	R^2
Compressive strength at 1 day	Intercept (A)	–62.31395	9.6939	0.98052	0.98074
	$B1$	1.49895	1.44584		
	$B2$	–0.91984	0.69023		
	$B3$	0.04096	0.00413		
Compressive strength at 7 days	Intercept (A)	–136.88382	18.40929	0.98313	0.98488
	$B1$	0.54725	2.74574		
	$B2$	–0.66261	1.31079		
	$B3$	0.08898	0.00784		
Compressive strength at 28 days	Intercept (A)	–138.56599	19.56297	0.98317	0.98491
	$B1$	0.66137	2.91781		
	$B2$	–0.77757	1.39294		
	$B3$	0.09316	0.00833		

experimental tests that were performed in the hardened state, three output factors were identified as having a primary influence on the mechanical response of mortars. Table 3 contains an analysis of these three different parameters.

For this experimental data set, a multiple linear regression model is constructed as follows, with the R^2 coefficient value as close to 1 as possible

$$\text{Compressive strength} = A + B1X1 + B2X2 + B3X3$$

where $X1$ is water absorption; $X2$ is void ratio; $X3$ is hardened density; and $B1$, $B2$, and $B3$ are the correlation coefficients (Table 3).

At all curing ages (1, 7, and 28 days), the statistical coefficients demonstrate a high degree of correlation between intrinsic parameters and compressive strength. The two coefficients have values greater than 0.98 (Table 3).

Evaluation of modulus of elasticity as function of intrinsic properties

The change in the modulus of elasticity according to the percentage of AEA added to the elaborate mortars is graphically shown in Fig. 10. It can be seen from this graph that the values of the modulus of elasticity decreased as the proportion of AEA increased (Table 2).

Mortar M0's modulus of elasticity was approximately 37.1 GPa. In contrast, for M9 (with 0.5% of AEA), this value was reduced to 25.61 GPa.

This decrease is mostly caused by the air bubbles that AEA's inclusion in the concrete caused to exist. The reduction in strength occurs because the increased air content introduces more voids within the mortar matrix. These voids disrupt the continuity of the material, making it less resistant to applied loads. When a load is applied, the stress concentrates around these voids, causing microcracks to form and propagate more easily, which weakens the overall structure and reduces its load-bearing capacity.

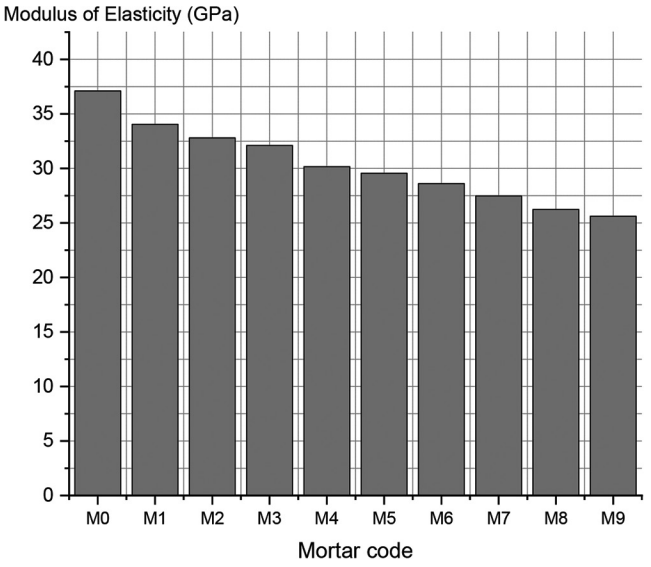

Fig. 10—Evolution of modulus of elasticity.

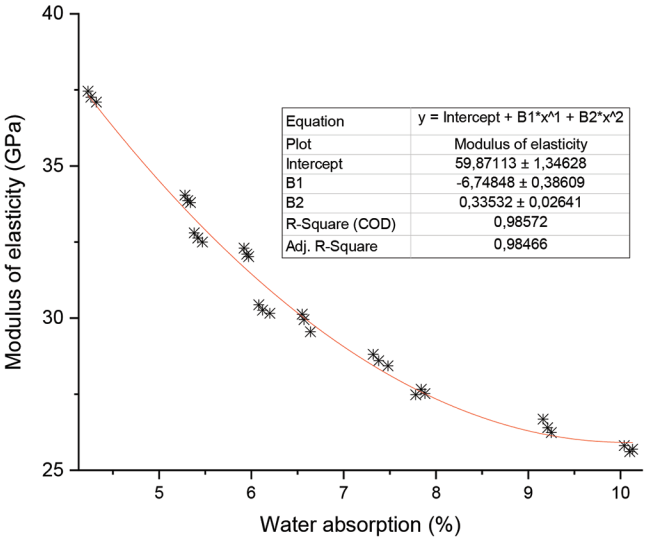

Fig. 11—Correlation between water absorption and modulus of elasticity.

Furthermore, the evolution of the modulus of elasticity with water absorption, void ratio, and density is shown in Fig. 11 to 13, respectively. These figures show that the modulus of elasticity values decrease as the water absorption (Fig. 11) and void ratio (Fig. 12) increase. However, the modulus of elasticity increases with the increase in the hardened density (Fig. 13).

The study's dependent variable was the modulus of elasticity. Experimental testing in the cured state revealed three output parameters that primarily affected the mechanical response of the different synthesized mortars. These output parameters are presented and discussed in Table 4.

The regression model for the data set generated in this experimental investigation that maintains a value of R^2 close to 1, achieved using multiple linear regression (by MATLAB program), is the following

$$\text{Modulus of elasticity} = A + B1X1 + B2X2 + B3X3$$

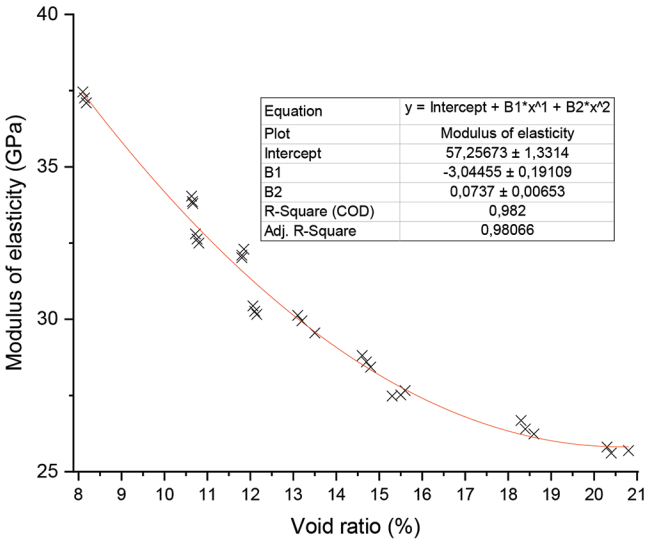

Fig. 12—Correlation between void ratio and modulus of elasticity.

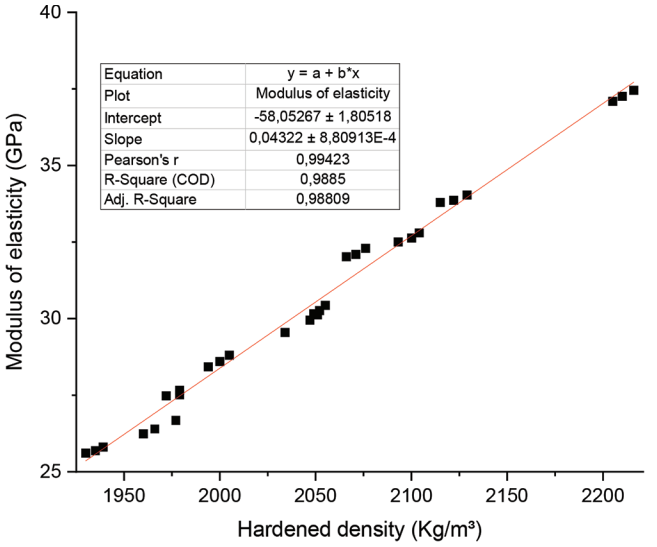

Fig. 13—Correlation between hardened density and modulus of elasticity.

Table 4—Regression model results of modulus of elasticity

Output	Model parameters	Value	SE	Adj. R^2	R^2
Modulus of elasticity	Intercept (A)	–48.66539	6.1934	0.98842	0.98962
	$B1$	–0.78382	0.92374		
	$B2$	0.28806	0.44099		
	$B3$	0.03933	0.00264		

where $X1$ is water absorption; $X2$ is void rate; $X3$ is hardened density; and the B coefficients, as well as their standard deviations (SEs), are shown in Table 4. The statistical parameters of the forecast coefficients, including the Adj. R^2 and R^2 values, are also reported.

Table 4 demonstrates that the statistical variables used to predict the coefficients, such as R^2 and Adj. R^2, showed a strong correlation between the intrinsic parameters and the

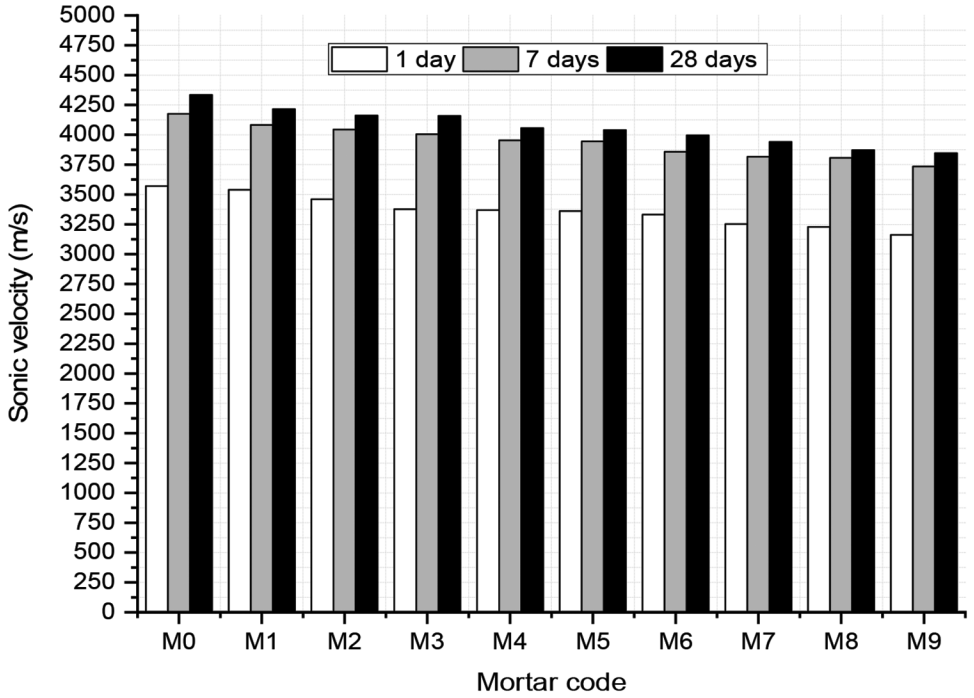

Fig. 14—Evolution of sonic velocity.

modulus of elasticity. These coefficients had values greater than 0.98.

The predictive models are underpinned by the intrinsic effects of AEA on the microstructure of mortar. The increased air content leads to a higher void ratio and reduced density, directly influencing the mechanical behavior by weakening the interfacial transition zone (ITZ) (Chen et al. 2021). This effect explains the observed decrease in compressive strength and modulus of elasticity as air content increases (Aghziel Sadfa et al. 2024; Benaicha et al. 2022). Similarly, rheological parameters, such as plastic viscosity and yield stress, are reduced due to the reduction in internal friction, which enhances flow but compromises structural integrity. These mechanisms align with the predictive models' coefficients, offering a quantitative framework for understanding these interactions.

Evaluation of *P*-wave velocity according to intrinsic properties

The *P*-wave velocities in mortars were measured on cured samples at 1, 7, and 28 days. Figure 14 shows the trend of *P*-wave velocity according to the content of AEA included in the mortar formulations. It should be noted in Fig. 14 that the velocities decrease with increasing AEA content.

P-wave velocity values for the reference mortar (M0) were 3571, 4175, and 4334 m/s at 1, 7, and 28 days, respectively. In contrast, these velocity values for the M9 mortar (which included 0.5% AEA) were 3162, 3735, and 3846 m/s at 1, 7, and 28 days, respectively.

This decrease is primarily caused by the air cavities that the AEA addition to the mortar induced to develop. The *P*-propagation wave's time accelerates due to these air bubbles, which leads to a decrease in the velocity (Mao et al. 2022; Rosell and Cantalapiedra 2011). In fact, the increase in

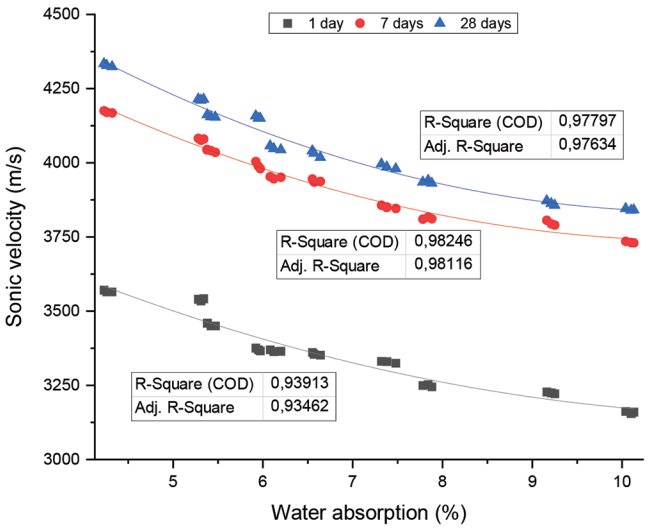

Fig. 15—Correlation between water absorption and sonic velocity.

the velocity with the age of curing of manufactured mortars is due to the increase in rigidity provided by the hydration process. The quality of the mortar for the same sample improved with time due to hydration, which increased the hardness of the mortar.

The evolution of *P*-wave velocity (at 1, 7, and 28 days) is displayed in Fig. 15 to 17 according to water absorption, void ratio, and hardened density, respectively. These figures show that the *P*-wave velocity values decrease with increasing water absorption (Fig. 15) and void ratio (Fig. 16). However, in Fig. 17, the propagation of *P*-wave velocity increases with the increase in hardened density. For water absorption and void ratio, the best correlation was obtained with a polynomial fit of order 2, while for hardened density, the best relationship was obtained with a linear fit.

The dependent parameter in this research was the sonic velocity propagation (*P*-wave) at 1, 7, and 28 days of curing.

Based on the findings of the experiments conducted in the cured condition, three output parameters that mainly affect the strength response of the elaborated mortars were established and evaluated in Table 5.

The regression model for the data set achieved in this experiment, using multiple linear regression (by MATLAB program) and holding the R^2 value close to 1, is developed as follows

$$\text{Sonic velocity} = A + B1X1 + B2X2 + B3X3$$

where $X1$ is water absorption; $X2$ is void rate; $X3$ is hardened density; and the B coefficients and the SEs are shown in Table 5. The statistical parameters of the expected coefficients, including the Adj. R^2 and R^2 values, are also reported.

All curing ages (1, 7, and 28 days) exhibited a significant correlation between the sonic velocity and the intrinsic parameters, as indicated by statistical parameters in the anticipated coefficients, such as R^2 and Adj. R^2. These two coefficients sometimes had values greater than 0.99 (the case of sonic velocity at 7 days).

Evaluation of compressive strength according to rheological properties

Plastic viscosity and yield stress are two variables that determine rheological behavior (Benaicha et al. 2017, 2019b).

As shown in Fig. 18, the percentage of AEA incorporated into the mortars has a direct effect on these parameters.

The reference mortar (M0) had a plastic viscosity of 13.8 Pa and a yield stress of roughly 36.61 Pa·s. For the M9 mortar (containing 0.5% AEA), the plastic viscosity was 5.51 Pa·s, and the yield stress was 2.94 Pa·s.

The density of the mortar decreased when AEA was introduced as a result of the formation of air bubbles. Due to voids between the two materials, the internal friction between their particles decreased, resulting in less yield stress. The cement paste's cohesion—and, as a result, its plastic viscosity—will be reduced if there are voids in the mixture.

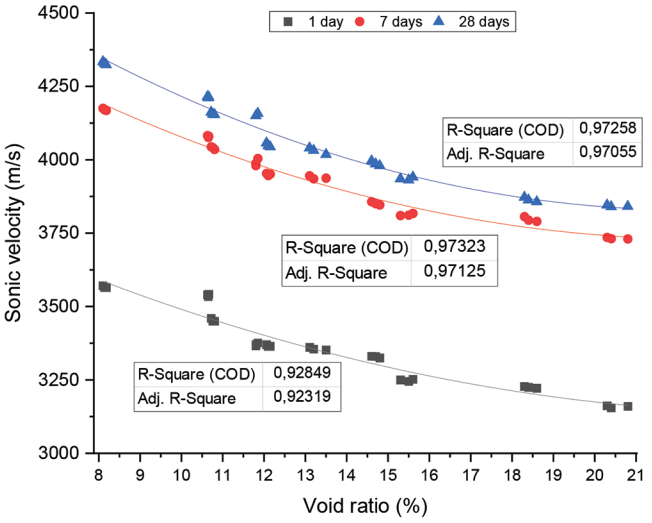

Fig. 16—Correlation between void ratio and sonic velocity.

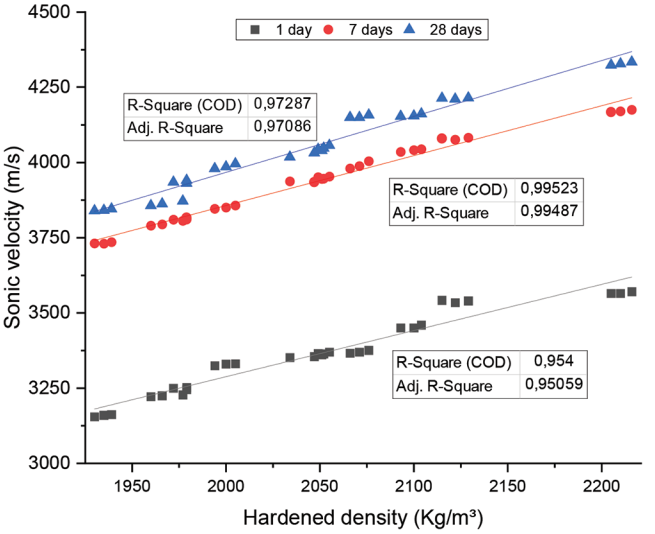

Fig. 17—Correlation between hardened density and sonic velocity.

Table 5—Results of regression model of sonic velocity

Output	Model parameters	Value	SE	Adj. R^2	R^2
Sonic velocity at 1 day	Intercept (A)	1552.90824	464.76581	0.95098	0.95605
	$B1$	–150.08311	69.31967		
	$B2$	59.7426	33.0926		
	$B3$	0.98668	0.19797		
Sonic velocity at 7 days	Intercept (A)	1595.78828	181.30561	0.99331	0.994
	$B1$	–129.69337	27.04167		
	$B2$	52.5731	12.90946		
	$B3$	1.22613	0.07723		
Sonic velocity at 28 days	Intercept (A)	1574.19493	395.96328	0.97497	0.97756
	$B1$	–96.37943	59.05779		
	$B2$	33.75734	28.19367		
	$B3$	1.30907	0.16866		

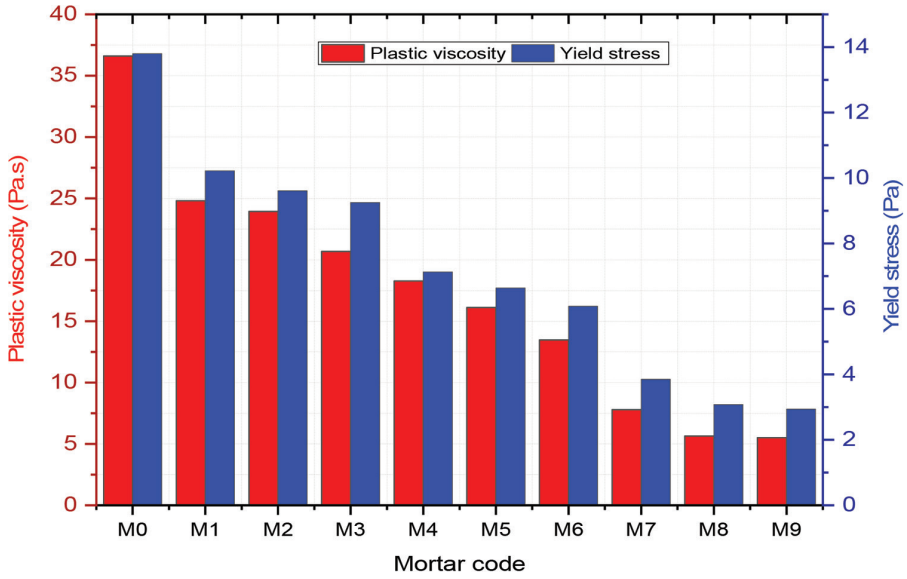

Fig. 18—Evolution of plastic viscosity and yield stress.

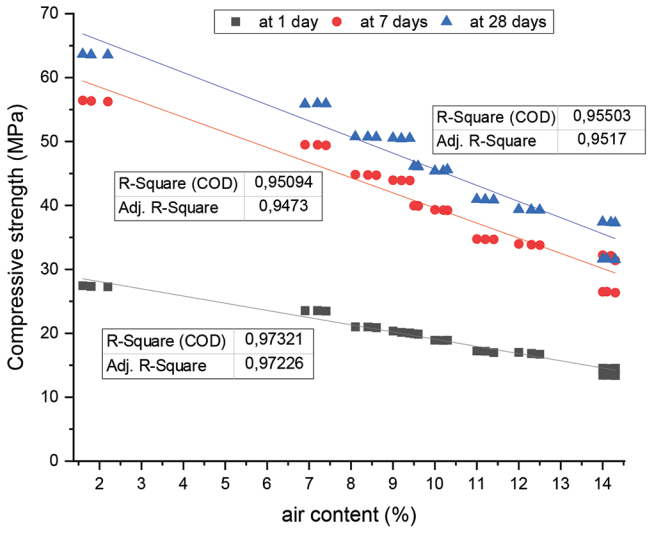

Fig. 19—Correlation curve between air content in mortar and compressive strength.

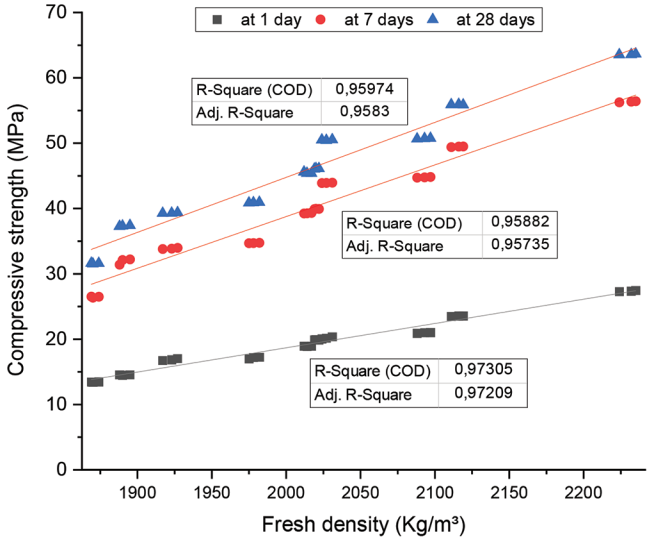

Fig. 20—Correlation between fresh density and compressive strength.

In other words, the term "plastic viscosity" refers to the amount of water that is able to dissipate in the pores of the sheared material due to friction between solid grains. A mixture's workability improves with decreasing yield stress and viscosity (El Asri et al. 2022a,b).

Furthermore, the fresh density values decreased similarly with an increase in the percentage of AEA, as shown in Fig. 6 with regard to the hardened density. The fresh density for the reference mortar (M0) was 2235 kg/m^3, while the density for the M9 mortar, which contained 0.5% AEA, was 1874 kg/m^3. The density of the mortar decreased when AEA was introduced due to the formation of air bubbles. This means that mass is reduced for a given volume.

The evolution of compressive strength at 1, 7, and 28 days is graphically shown in Fig. 19 to 22 according to air content (fresh porosity), fresh density, plastic viscosity, and yield stress, respectively. By examining these figures, it is possible to observe that compressive strength values decrease as air content increases (Fig. 19). In contrast, the compressive strength in Fig. 20 to 22 improves as fresh density, plastic viscosity, and yield stress values increase. The best relationship was obtained with a linear fit.

Compressive strength at 1, 7, and 28 days was the dependent parameter in this work. The experimental investigations conducted in the fresh state led to the establishment of four output parameters that mainly affected the mechanical response of the elaborated mortars. These are discussed in Table 6.

The regression model for the data set achieved in this experiment, using multiple linear regression (by MATLAB program) and holding the R^2 value close to 1, is developed as follows

$$\text{Compressive strength} = A + B1X1 + B2X2 + B3X3 + B4X4$$

where $X1$ is air content; $X2$ is fresh density; $X3$ is plastic viscosity; $X4$ is yield stress; and the B coefficients and the

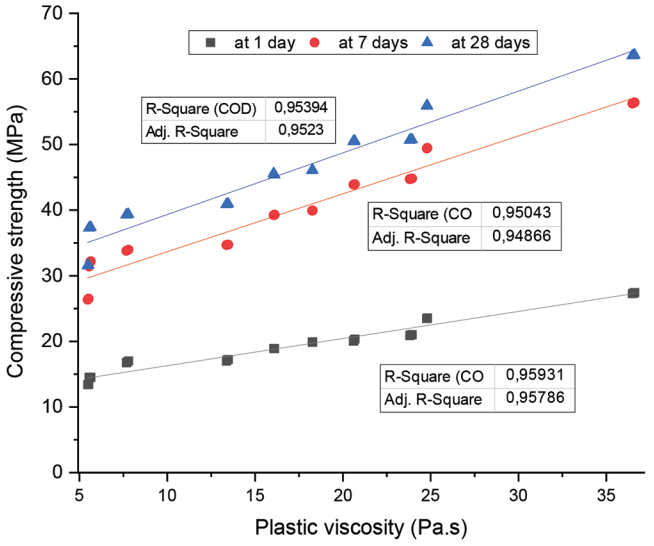

Fig. 21—Correlation between plastic viscosity and compressive strength.

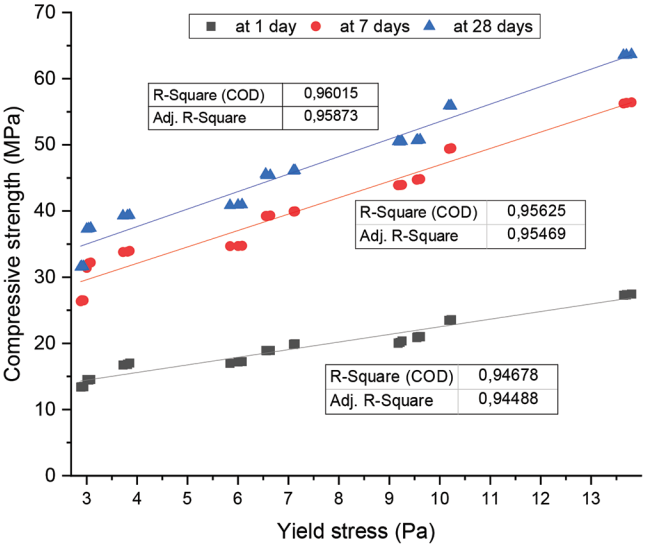

Fig. 22—Correlation between yield stress and compressive strength.

Table 6—Results of regression model of compressive strength from rheological parameters

Output	Model parameters	Value	SE	Adj. R^2	R^2
Compressive strength at 1 day	Intercept (*A*)	–26.86499	17.57138	0.98061	0.98329
	*B*1	–0.75682	0.1986		
	*B*2	0.02766	0.0089		
	*B*3	–0.41017	0.18203		
	*B*4	0.67676	0.32877		
Compressive strength at 7 days	Intercept (*A*)	–108.08172	47.58917	0.96903	0.9733
	*B*1	–0.63378	0.53787		
	*B*2	0.07653	0.0241		
	*B*3	–1.34069	0.49301		
	*B*4	3.21332	0.89042		
Compressive strength at 28 days	Intercept (*A*)	–91.66829	48.82478	0.9712	0.97517
	*B*1	–0.79599	0.55184		
	*B*2	0.07161	0.02472		
	B3	–1.37026	0.50581		
	*B*4	3.44762	0.91354		

SEs are shown in Table 6. The statistical parameters of the expected coefficients, including the Adj. R^2 and R^2 values, are also reported.

All curing ages (1, 7, and 28 days) exhibited a significant correlation between the compressive strength and rheological parameters, as indicated by statistical parameters in the anticipated coefficients, such as R^2 and Adj. R^2. These two coefficients sometimes had values greater than 0.99 (the case of compressive strength at 1 day).

CONCLUSIONS

This paper investigated the relationships between the mechanical, rheological, and intrinsic properties of mortars, considering the effect of porosity on rheology, compressive strength, and sonic velocity. Employing different multiple linear regression models, which were developed and analyzed using MATLAB, the results show the rationality and precision of the proposed models in predicting compressive strength at 1, 7, and 28 days. The main conclusions that can be drawn from this study are as follows:

- The increment in the dosage of air-entraining admixture (AEA) corresponded to increased air content, water absorption, and void ratio, a sign of modification by AEA that takes an active role in modifying porosity. With higher dosages, a decline was recorded in the value of fresh and hardened density, plastic viscosity, yield stress, compressive strength, and sonic velocity.
- A strong correlation between the compressive strength and the intrinsic characteristics was developed for all curing ages (1, 7, and 28 days) by statistically significant coefficients. The modulus of elasticity after 28 days

showed good agreement with intrinsic parameters, and the coefficients of determination were beyond 98%.
- The sonic velocity and intrinsic parameters were highly correlated at every curing age of 1, 7, and 28 days, where the coefficient reached over 0.99 in some parameters, such as sonic velocity at 7 days.
- The compressive strength and rheological parameters were highly statistically correlated at any curing age. For example, the coefficient of the compressive strength at 1 day was above 0.99.

These findings establish a solid foundation for optimizing mortar formulations by shedding light on the impact of AEA dosage and porosity on the mechanical and rheological properties. The developed regression models serve as reliable tools for predicting mortar behavior, enabling consistent performance in construction applications.

AUTHOR BIOS

Mouhcine Ben Aicha *is a Professor at the National School of Architecture, Rabat, Morocco. His research interests include self-consolidating concrete. This research work is attached to the Structure and Materials Laboratory.*

Ayoub Aziz *is a Professor at the Scientific Institute at Mohammed V University, Rabat, Morocco. This research work is attached to the Geo-Biodiversity and Natural Patrimony Laboratory (GEOBIO) and the Geophysics, Natural Patrimony and Green Chemistry Research Center (GEOPAC).*

Olivier Jalbaud *is a Professor at Polytech Marseille at Aix Marseille Université, Marseille, France. His research interests include self-consolidating concrete. This research work is attached to the University Institute of Industrial Thermal Systems (IUSTI) UMR 7343 Laboratory.*

Yves Burtschell *is a Professor at Polytech Marseille at Aix Marseille Université. His research interests include self-consolidating concrete. This research work is attached to the IUSTI UMR 7343 Laboratory.*

REFERENCES

Abadel, A. A., and Alghamdi, H., 2023, "Effect of High Volume Tile Ceramic Wastes on Resistance of Geopolymer Mortars to Abrasion and Freezing-Thawing Cycles: Experimental and Deep Learning Modelling," *Ceramics International*, V. 49, No. 10, May, pp. 15065-15081. doi: 10.1016/j.ceramint.2023.01.089

Abarna Munisha, M.; Sakthieswaran, N.; Ganeshbabu, O.; and Gaayathri, K. K., 2021, "Experimental Study on Effects of Natural Admixture on Blended Mortar," *Materials Today: Proceedings*, V. 37, Part 2, pp. 1023-1027. doi: 10.1016/j.matpr.2020.06.284

Abdulwahid, M. Y., and Fadhil Abdullah, S., 2021, "The Utilization of Walnut Shells as a Partial Replacement of Sand in Mortar Mixes," *Structural Concrete*, V. 22, No. S1, Jan., pp. E300-E307. doi: 10.1002/suco.202000108

Aghziel Sadfa, F.; Ben Aicha, M.; Jalbaud, O.; Zaher, M.; Hafidi Alaoui, A.; and Burtschell, Y., 2024, "Effects of Air Content on Rheological Behavior and Segregation of Self-Compacting Concrete," *Hybrid Advances*, V. 7, Dec., Article No. 100337. doi: 10.1016/j.hybadv.2024.100337

Ahmad, M. R.; Chen, B.; and Shah, S. F. A., 2020, "Influence of Different Admixtures on the Mechanical and Durability Properties of One-Part Alkali-Activated Mortars," *Construction and Building Materials*, V. 265, Dec., Article No. 120320. doi: 10.1016/j.conbuildmat.2020.120320

Ahmadi, Z.; Esmaeili, J.; Kasaei, J.; and Hajialioghli, R., 2018, "Properties of Sustainable Cement Mortars Containing High Volume of Raw Diatomite," *Sustainable Materials and Technologies*, V. 16, July, pp. 47-53. doi: 10.1016/j.susmat.2018.05.001

Backstrom, J. E.; Burrows, R. W.; Mielenz, R. C.; and Wolkodoff, V. E., 1958, "Origin, Evolution, and Effects of the Air Void System in Concrete. Part 2—Influence of Type and Amount of Air-Entraining Agent," *ACI Journal Proceedings*, V. 55, No. 8, Aug., pp. 261-272. doi: 10.14359/11354

Baltrus, J. P., and LaCount, R. B., 2001, "Measurement of Adsorption of Air-Entraining Admixture on Fly Ash in Concrete and Cement," *Cement and Concrete Research*, V. 31, No. 5, May, pp. 819-824. doi: 10.1016/S0008-8846(01)00494-X

Benaicha M., 2013, "Formulation des Différents Bétons (BAP, BHP et BFUP) à Haute Teneur en Additions Minérales : Optimisation pour Améliorer le Coulage, la Résistance au Jeune Âge et la Durabilité des Bétons," doctoral thesis, Aix Marseille Université, Marseille, France.

Benaicha, M.; Belcaid, A.; Alaoui, A. H.; Jalbaud, O.; and Burtschell, Y., 2019a, "Effects of Limestone Filler and Silica Fume on Rheology and Strength of Self-Compacting Concrete," *Structural Concrete*, V. 20, No. 5, Oct., pp. 1702-1709. doi: 10.1002/suco.201900150

Benaicha, M.; Belcaid, A.; Alaoui, A. H.; Jalbaud, O.; and Burtschell, Y., 2019b, "Rheological Characterization of Self-Compacting Concrete: New Recommendation," *Structural Concrete*, V. 20, No. 5, Oct., pp. 1695-1701. doi: 10.1002/suco.201900154

Benaicha, M.; Burtschell, Y.; Alaoui, A. H.; and Elharrouni, K., 2017, "Theoretical Calculation of Self-Compacting Concrete Plastic Viscosity," *Structural Concrete*, V. 18, No. 5, Oct., pp. 710-719. doi: 10.1002/suco.201600064

Benaicha, M.; Hafidi Alaoui, A.; Jalbaud, O.; and Burtschell, Y., 2019c, "Dosage Effect of Superplasticizer on Self-Compacting Concrete: Correlation Between Rheology and Strength," *Journal of Materials Research and Technology*, V. 8, No. 2, Apr., pp. 2063-2069. doi: 10.1016/j.jmrt.2019.01.015

Benaicha, M.; Jalbaud, O.; Hafidi Alaoui, A.; and Burtschell, Y., 2015a, "Marsh Cone Coupled to a Plexiglas Horizontal Channel: Rheological Characterization of Cement Grout," *Flow Measurement and Instrumentation*, V. 45, Oct., pp. 126-134. doi: 10.1016/j.flowmeasinst.2015.06.004

Benaicha, M.; Jalbaud, O.; Hafidi Alaoui, A.; and Burtschell, Y., 2022, "Porosity Effects on Rheological and Mechanical Behavior of Self-Compacting Concrete," *Journal of Building Engineering*, V. 48, May, Article No. 103964. doi: 10.1016/j.jobe.2021.103964

Benaicha, M.; Roguiez, X.; Jalbaud, O.; Burtschell, Y.; and Hafidi Alaoui, A., 2015b, "Influence of Silica Fume and Viscosity Modifying Agent on the Mechanical and Rheological Behavior of Self Compacting Concrete," *Construction and Building Materials*, V. 84, June, pp. 103-110. doi: 10.1016/j.conbuildmat.2015.03.061

Chatterji, S., 2003, "Freezing of Air-Entrained Cement-Based Materials and Specific Actions of Air-Entraining Agents," *Cement and Concrete Composites*, V. 25, No. 7, Oct., pp. 759-765. doi: 10.1016/S0958-9465(02)00099-9

Chen, Y.; Al-Neshawy, F.; and Punkki, J., 2021, "Investigation on the Effect of Entrained Air on Pore Structure in Hardened Concrete Using MIP," *Construction and Building Materials*, V. 292, July, Article No. 123441. doi: 10.1016/j.conbuildmat.2021.123441

Craipeau, T.; Perrot, A.; Toussaint, F.; Huet, B.; and Lecompte, T., 2021, "Mortar Pore Pressure Prediction During the First Hours of Cement Hydration," *Cement and Concrete Composites*, V. 119, May, Article No. 103998. doi: 10.1016/j.cemconcomp.2021.103998

Cultrone, G.; Sebastián, E.; and Ortega Huertas, M., 2005, "Forced and Natural Carbonation of Lime-Based Mortars with and without Additives: Mineralogical and Textural Changes," *Cement and Concrete Research*, V. 35, No. 12, Dec., pp. 2278-2289. doi: 10.1016/j.cemconres.2004.12.012

Darvish, P.; Alengaram, U. J.; Alnahhal, A. M.; Poh, Y. S.; and Ibrahim, S., 2021, "Enunciation of Size Effect of Sustainable Palm Oil Clinker Sand on the Characteristics of Cement and Geopolymer Mortars," *Journal of Building Engineering*, V. 44, Dec., Article No. 103335. doi: 10.1016/j.jobe.2021.103335

Dolch, W. L., 1996, "Air-Entraining Admixtures," *Concrete Admixtures Handbook: Properties, Science, and Technology*, second edition, V. S. Ramachandran, ed., William Andrew Inc., Norwich, NY, pp. 518-557. doi: 10.1016/B978-081551373-5.50012-X

Du, L., and Folliard, K. J., 2005, "Mechanisms of Air Entrainment in Concrete," *Cement and Concrete Research*, V. 35, No. 8, Aug., pp. 1463-1471. doi: 10.1016/j.cemconres.2004.07.026

El Asri, Y.; Benaicha, M.; Zaher, M.; and Hafidi Alaoui, A., 2022a, "Prediction of the Compressive Strength of Self-Compacting Concrete Using Artificial Neural Networks Based on Rheological Parameters," *Structural Concrete*, V. 23, No. 6, Dec., pp. 3864-3876. doi: 10.1002/suco.202100796

El Asri, Y.; Ben Aicha, M.; Zaher, M.; and Hafidi Alaoui, A., 2022b, "Modelization of the Rheological Behavior of Self-Compacting Concrete Using Artificial Neural Networks," *Materials Today: Proceedings*, V. 58, Part 4, pp. 1114-1121. doi: 10.1016/j.matpr.2022.01.257

Flatt, R. J., 2004, "Towards a Prediction of Superplasticized Concrete Rheology," *Materials and Structures*, V. 37, No. 5, June, pp. 289-300. doi: 10.1007/BF02481674

Fowler, D. W., 2009, "Repair Materials for Concrete Structures," *Failure, Distress and Repair of Concrete Structures*, N. Delatte, ed., Woodhead Publishing, Sawston, UK, pp. 194-207. doi: 10.1533/9781845697037.2.194

Gagné, R., 2016, "Air Entraining Agents," *Science and Technology of Concrete Admixtures*, P.-C. Aïtcin and R. J. Flatt, eds., Woodhead Publishing, Sawston, UK, pp. 379-391. doi: 10.1016/B978-0-08-100693-1.00017-5

Gao, Y.; Cui, X.; Lu, N.; Hou, S.; He, Z.; and Liang, C., 2022, "Effect of Recycled Powders on the Mechanical Properties and Durability of Fully Recycled Fiber-Reinforced Mortar," *Journal of Building Engineering*, V. 45, Jan., Article No. 103574. doi: 10.1016/j.jobe.2021.103574

Gdoutos, E. E.; Konsta-Gdoutos, M. S.; Danoglidis, P. A.; and Shah, S. P., 2016, "Advanced Cement Based Nanocomposites Reinforced with MWCNTs and CNFs," *Frontiers of Structural and Civil Engineering*, V. 10, No. 2, June, pp. 142-149. doi: 10.1007/s11709-016-0342-1

Ge, W.; Liu, W.; Ashour, A.; Zhang, Z.; Li, W.; Jiang, H.; Sun, C.; Qiu, L.; Yao, S.; Lu, W.; and Liu, Y., 2023, "Sustainable Ultra-High Performance Concrete with Incorporating Mineral Admixtures: Workability, Mechanical Property and Durability Under Freeze-Thaw Cycles," *Case Studies in Construction Materials*, V. 19, Dec., Article No. e02345. doi: 10.1016/j.cscm.2023.e02345

Ghantous, R. M.; Moradllo, M. K.; Becker, H. H.; Ley, M. T.; and Weiss, W. J., 2021, "Determining the Freeze-Thaw Performance of Mortar Samples Using Length Change Measurements During Freezing," *Cement and Concrete Composites*, V. 116, Feb., Article No. 103869. doi: 10.1016/j.cemconcomp.2020.103869

Hall, C., 1989, "Water Sorptivity of Mortars and Concretes: A Review," *Magazine of Concrete Research*, V. 41, No. 147, June, pp. 51-61. doi: 10.1680/macr.1989.41.147.51

Hilal, A. A., 2016, "Microstructure of Concrete," *High Performance Concrete Technology and Applications*, S. Yilmaz and H. B. Özmen, eds., InTech Open Limited, London, UK, pp. 3-24. doi: 10.5772/64574

Jeon, K.; Jeon, C.; and Choi, W., 2023, "Effect of Mixing Ratio on Fire Resistance of Cement Mortar with Polypropylene Fiber and Polymer," *Case Studies in Construction Materials*, V. 19, Dec., Article No. e02503. doi: 10.1016/j.cscm.2023.e02503

Ke, G.; Zhang, J.; Tian, B.; and Wang, J., 2020, "Characteristic Analysis of Concrete Air Entraining Agents in Different Media," *Cement and Concrete Research*, V. 135, Sept., Article No. 106142. doi: 10.1016/j.cemconres.2020.106142

Kim, J.; Suryanto, B.; and McCarter, W. J., 2019, "Conduction, Relaxation and Complex Impedance Studies on Portland Cement Mortars During Freezing and Thawing," *Cold Regions Science and Technology*, V. 166, Oct., Article No. 102819. doi: 10.1016/j.coldregions.2019.102819

Ley, M. T.; Chancey, R.; Juenger, M. C. G.; and Folliard, K. J., 2009, "The Physical and Chemical Characteristics of the Shell of Air-Entrained Bubbles in Cement Paste," *Cement and Concrete Research*, V. 39, No. 5, May, pp. 417-425. doi: 10.1016/j.cemconres.2009.01.018

Litvan, G. G., 1980, "Freeze-Thaw Durability of Porous Building Materials," *Durability of Building Materials and Components*, STP691-EB, P. J. Sereda and G. G. Litvan, eds., ASTM International, West Conshohocken, PA, pp. 455-463. doi: 10.1520/STP36080S

Liu, J.; Zhao, L.; Chang, F.; and Chi, L., 2021, "Mechanical Properties and Microstructure of Multilayer Graphene Oxide Cement Mortar," *Frontiers of Structural and Civil Engineering*, V. 15, No. 4, Aug., pp. 1058-1070. doi: 10.1007/s11709-021-0747-3

Lv, Z.; Xia, C.; Wang, Y.; and Lin, Z., 2020, "Frost Heave and Freezing Processes of Saturated Rock with an Open Crack Under Different Freezing Conditions," *Frontiers of Structural and Civil Engineering*, V. 14, No. 4, Aug., pp. 947-960. doi: 10.1007/s11709-020-0638-z

Mao, J.; Wang, Q.; Qu, L.; Zhang, H.; Shi, Z.; Xu, S.; and Li, X., 2022, "Study of Mortar Layer Property of Superhydrophobic Metakaolin Based Cement Mortar," *Journal of Building Engineering*, V. 45, Jan., Article No. 103578. doi: 10.1016/j.jobe.2021.103578

Murata, J., 1984, "Flow and Deformation of Fresh Concrete," *Materials and Structures*, V. 17, No. 2, Mar., pp. 117-129. doi: 10.1007/BF02473663

Öztürk, H., and Kılınçkale, F. M., 2023, "The Effect of Wetting-Drying / Freezing-Thawing Cycles on Properties of Non-Air Entrained Fly Ash Substituted Cement-Based Composites," *Ceramics International*, V. 49, No. 7, Apr., pp. 10993-11004. doi: 10.1016/j.ceramint.2022.11.294

Powers, T. C., 1958, "Structure and Physical Properties of Hardened Portland Cement Paste," *Journal of the American Ceramic Society*, V. 41, No. 1, Jan., pp. 1-6. doi: 10.1111/j.1151-2916.1958.tb13494.x

Ramakrishna, G., and Sundararajan, T., 2019, "A Novel Approach to Rheological and Impact Strength of Fibre-Reinforced Cement/Cementitious Composites for Durability Evaluation," *Durability and Life Prediction in Biocomposites, Fibre-Reinforced Composites and Hybrid Composites*, M. Jawaid, M. Thariq, and N. Saba, eds., Woodhead Publishing, Sawston, UK, pp. 389-406. doi: 10.1016/B978-0-08-102290-0.00017-9

Rosell, J. R., and Cantalapiedra, I. R., 2011, "Simple Method of Dynamic Young's Modulus Determination in Lime and Cement Mortars," *Materiales de Construcción*, V. 61, No. 301, Jan.-Mar., pp. 39-48. doi: 10.3989/mc.2010.53509

Roussel, N.; Lemaître, A.; Flatt, R. J.; and Coussot, P., 2010, "Steady State Flow of Cement Suspensions: A Micromechanical State of the Art," *Cement and Concrete Research*, V. 40, No. 1, Jan., pp. 77-84. doi: 10.1016/j.cemconres.2009.08.026

Ruegenberg, F.; Schidlowski, M.; Bader, T.; and Diekamp, A., 2021, "NHL-Based Mortars in Restoration: Frost-Thaw and Salt Resistance Testing Methods Towards a Field Related Application," *Case Studies in Construction Materials*, V. 14, June, Article No. e00531. doi: 10.1016/j.cscm.2021.e00531

Sasui, S.; Kim, G.; Nam, J.; van Riessen, A.; and Hadzima-Nyarko, M., 2021, "Effects of Waste Glass as a Sand Replacement on the Strength and Durability of Fly Ash/GGBS Based Alkali Activated Mortar," *Ceramics International*, V. 47, No. 15, Aug., pp. 21175-21196. doi: 10.1016/j.ceramint.2021.04.121

Sheikh Hassani, M.; Torki, A.; Asadollahfardi, G.; Saghravani, S. F.; and Shafaei, J., 2021, "The Effect of Water to Cement Ratio and Age on the Mechanical Properties of Cement Mortar and Concrete Made of Micro-Nano Bubbles without Adding Any Admixtures," *Structural Concrete*, V. 22, No. S1, Jan., pp. E756-E768. doi: 10.1002/suco.201800292

Silva, B.; Ferreira Pinto, A. P.; Gomes, A.; and Candeias, A., 2021, "Admixtures Potential Role on the Improvement of the Freeze-Thaw Resistance of Lime Mortars," *Journal of Building Engineering*, V. 35, Mar., Article No. 101977. doi: 10.1016/j.jobe.2020.101977

Silva, B. A.; Ferreira Pinto, A. P.; Gomes, A.; and Candeias, A., 2020, "Suitability of Different Surfactants as Air-Entraining Admixtures for Lime Mortars," *Construction and Building Materials*, V. 256, Sept., Article No. 118986. doi: 10.1016/j.conbuildmat.2020.118986

Steiner, L. R.; Bernardin, A. M.; and Pelisser, F., 2015, "Effectiveness of Ceramic Tile Polishing Residues as Supplementary Cementitious Materials for Cement Mortars," *Sustainable Materials and Technologies*, V. 4, July, pp. 30-35. doi: 10.1016/j.susmat.2015.05.001

Tattersall, G. H., and Banfill, P. F. G., 1983, *The Rheology of Fresh Concrete*, Pitman Books Limited London, UK, 356 pp.

Thomaz, W. A.; Miyaji, D. Y.; and Possan, E., 2021, "Comparative Study of Dynamic and Static Young's Modulus of Concrete Containing Basaltic Aggregates," *Case Studies in Construction Materials*, V. 15, Dec., Article No. e00645. doi: 10.1016/j.cscm.2021.e00645

Tunstall, L. E.; Ley, M. T.; and Scherer, G. W., 2021, "Air Entraining Admixtures: Mechanisms, Evaluations, and Interactions," *Cement and Concrete Research*, V. 150, Dec., Article No. 106557. doi: 10.1016/j.cemconres.2021.106557

Wang, C.; Sun, K.; Niu, H.; Sun, G.; Zhang, Z.; and Kong, L., 2021, "Effect of Binary Admixture of Sepiolite and Fly Ash on Carbonation and Chloride Resistance of Modified Cement Mortar," *Construction and Building Materials*, V. 279, Apr., Article No. 122509. doi: 10.1016/j.conbuildmat.2021.122509

Xu, X.; Tang, Z.; Wu, J.; Chen, L.; Li, J.; and Sun, M., 2017, "Preparation and Freeze-Thaw Resistance of Alumina Based Ceramic Insulators for Extremely Cold Areas," *Ceramics International*, V. 43, No. 2, Feb., pp. 2712-2719. doi: 10.1016/j.ceramint.2016.11.090

Xue, W.; Jin, W.; and Yokota, H., 2010, "Influence of Initial Curing Conditions and Exposure Environments on Chloride Migration in Concrete Using Electrochemical Method," *Frontiers of Architecture and Civil Engineering in China*, V. 4, No. 3, Sept., pp. 348-353. doi: 10.1007/s11709-010-0077-3

Zhao, Z.; Grellier, A.; El Karim Bouarroudj, M.; Michel, F.; Bulteel, D.; and Courard, L., 2021, "Substitution of Limestone Filler by Waste Brick Powder in Self-Compacting Mortars: Properties and Durability," *Journal of Building Engineering*, V. 43, Nov., Article No. 102898. doi: 10.1016/j.jobe.2021.102898

Zou, C.; Zhao, J.; and Liang, F., 2008, "Stress-Strain Relationship of Concrete in Freeze-Thaw Environment," *Frontiers of Architecture and Civil Engineering in China*, V. 2, No. 2, June, pp. 184-188. doi: 10.1007/s11709-008-0029-3

ACI MATERIALS JOURNAL TECHNICAL PAPER

Title No. 122-M18

How Does Coarse Aggregate Type Influence Mechanical Properties of High-Strength Concrete?

by Y. El Berdai, Y. Taha, A. M. Safhi, R. Trauchessec, R. Hakkou, and M. Benzaazoua

Research has shown that the type of coarse aggregate (CA) significantly impacts the properties of high-strength concrete (HSC). This paper provides a systematic and comprehensive review of the influence of CA type, strength, and elasticity on compressive strength (CS) and modulus of elasticity (MOE) of HSC. The CS can increase by up to 141% and the MOE gains up to 48% with different CA types, which is explained by the Compressible Packing Model (CPM) and shows the significant impact of CA on the MOE. The equation for the prediction of the MOE presented in the "Report on High-Strength Concrete" by ACI Committee 363 was calibrated using a CA type coefficient based on the data points collected to highlight the influence of CA on the MOE of HSC. Future research could focus on the effect of the adherence and elasticity of CAs.

Keywords: coarse aggregate (CA); compressive strength (CS); high-strength concrete (HSC); modulus of elasticity (MOE); prediction model; systematic review.

INTRODUCTION

In concrete, coarse aggregates (CAs) occupy the largest volume in the range of 35 to 50%, and size in the range of 4 to 32 mm (0.15 to 1.25 in.).[1] Their use reduces the quantity of cementitious materials and the cost of concrete and increases the elasticity and dimensional stability.[2] Natural CAs are derived from rocks; their type depends on the mineralogy, such as limestone and sandstone (sedimentary rocks), basalt and andesite (volcanic rocks), diabase and gabbro (plutonic rocks), granite and quartzite (metamorphic rocks), and gravel.[1] The properties of various CA types highly influence the compressive strength (CS) and the modulus of elasticity (MOE) of normal-strength concrete (NSC). The CS cannot be determined without a prior knowledge of the properties of the CA[3]; this is due to various CA types having differences in mineralogy and geology, and different characteristics such as the shape, texture, porosity, strength, and elasticity. Alexander and Davis[4] assessed the influence of 13 CA types sourced from different quarries, resulting in a relative variation of up to 55% of the CS and up to 40% in the MOE. Kaplan[5] revealed the effect of 13 different types of CA and found that the CS varied up to 30%, which could be attributed to differences in elasticity texture and shape. Tanesi et al.[6] investigated the influence of 11 different CA types and determined that the properties that significantly impact CS and MOE are type, elasticity, texture, and porosity. Góra and Piasta[7] found that the aggregate crushing value of six CA types from 12 different locations influences the MOE more than it influences the CS. de Larrard and Belloc[8] investigated the influence of the five aggregate types on the CS of concrete and found that the adherence between aggregates and the cement paste, which is related to the texture and chemical reactions of aggregates, has a linear relationship with the strength of mortar and dictated the CS.

High-strength concrete (HSC) is a special type of concrete engineered to possess a higher CS than NSC. It is characterized by a 28-day CS greater than 55 MPa (7977 psi)[9] and a slump test value equal to or greater than 200 mm (7.9 in.), with a water-binder ratio (*w*/*b*) less than 0.40.[10] HSC has been used in high-rise buildings since the 1970s[11] and in structures with specific requirements,[12] such as the Île de Ré Bridge in France (28-day CS equal to 68 MPa [9862 psi]) and the Hassan II Mosque in Morocco (28-day CS equal to 70 MPa [10,152 psi]), both constructed in 1988. The mixture proportioning of HSC aims to obtain a minimum porosity[13] by optimizing the packing density,[14,15] reducing the water content using high-range water reducers (HRWRs),[16] producing a compact microstructure using supplementary cementitious materials (SCMs),[17] and selecting a high quality of CA.[18] The influence of the CA type on the mechanical properties of HSC is highly significant, surpassing its impact on NSC. Sengul et al.[19] investigated the use of four different CA types in HSC and NSC. The CS varied up to 19% for HSC (*w*/*b* equal to 0.33) and 1% for NSC (*w*/*b* equal to 0.83), while the MOE varied up to 23% for HSC and 20% for NSC. This was due to the cement paste and the interfacial transition zone (ITZ) type being the weak link in NSC.[20]

RESEARCH SIGNIFICANCE

This systematic and comprehensive review aims to provide an answer to the question: How does the type, strength, and elasticity of CA influence the strength and elasticity of HSC? The proposed answers would contribute to quantifying, understanding, and predicting the impact of CA properties on the mechanical properties of HSC. The developed database could also contribute to providing information on the engineering properties of CAs and the mechanical performances of HSC.

METHODOLOGY

This article used the Preferred Reporting Items for Systematic Reviews and Meta-Analyses (PRISMA) guideline for

ACI Materials Journal, V. 122, No. 3, May 2025.

MS No. M-2024-103.R2, doi: 10.14359/51746716, received January 30, 2025, and reviewed under Institute publication policies.

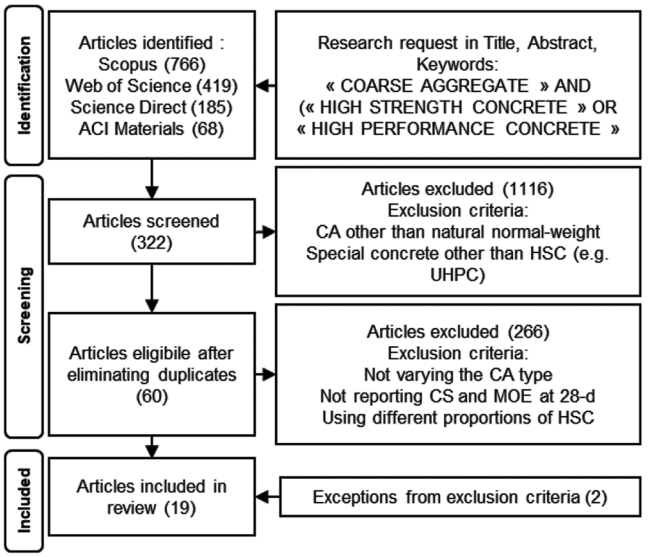

Fig. 1—PRISMA flowsheet used in this systematic review.

reporting systematic reviews, which ensures transparency, accuracy, and completeness.[21] Articles that maintained similar proportions of HSC and cement paste quality were selected, varying only the CA type. To consolidate the research, analyze the data, and identify research gaps, the CS and MOE of CA and HSC were extracted, described, and analyzed. Patterns across articles were identified using relative deviation (Eq. (1)) and examples are presented, then research articles were described and analyzed individually.

$$\text{Relative deviation} = \frac{\text{Maximum} - \text{Minimum}}{\text{Minimum}} \times 100\ (\%) \quad (1)$$

The CA types that did not follow the trend are considered outliers; their features are presented. Three methods were used to answer the research question: a quantitative analysis using the relative deviation, an empirical explanation using the Compressible Packing Model (CPM), and a prediction of the MOE of HSC using the CA type. Based on the outliers noted, articles were discussed, and research gaps were presented.

Selection of articles

Figure 1 presents the PRISMA flowsheet used to identify, screen, exclude, and include articles. The eligibility criterion for inclusion considered the CA type as a qualitative variable in the HSC mixtures. The criteria for exclusions were not varying the CA type, using different mixtures of HSC for different CA types, using alternative CA instead of natural CA, and the study of ultra-high-performance concrete and reactive powder concrete. Scopus, Web of Science, Science Direct databases, and the *ACI Materials Journal* were used to develop the database as of February 2023 and updated in March 2024. The request was (« influence » AND « coarse aggregate » AND (« high-strength concrete » OR « high performance concrete »)) in (Article title, Abstract, Keywords). Many articles were focused on recycled aggregate and ultra-high-performance concrete. This was the

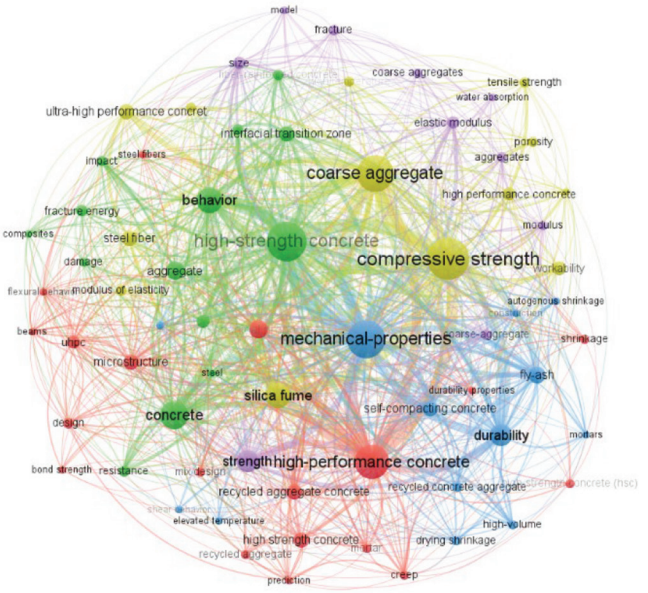

Fig. 2—Visualization map and clusters according to keyword occurrence.

main reason for reducing eligible articles from 1116 to 322. The 322 screened articles were analyzed using VOSviewer, software for creating and analyzing bibliometric networks. The keywords with at least five occurrences were selected; Fig. 2 presents a visualization map featuring four clusters: mechanical properties of high-performance concrete and HSC (green, blue, and red), and CA properties (yellow and purple) (full-color PDF can be accessed at www.concrete.org). These clusters allowed the identification of the main themes of the review and structuring of the analysis accordingly. In the end, a total of 19 articles[19,22-39] that responded to all criteria were selected, including two studies that did not respect the exclusion criteria: Tighiouart et al.[35] because it was written in French, and the study of Sengul et al.[19] that reported the 35-day CS instead of the 28-day CS.

Description of selected articles

The reviewed articles used a wide variety of CA types from different locations, leading to 155 different HSC mixtures using eight categories of CA types. The CA type and the corresponding number of HSC mixtures produced included limestone (42), granite (23), basalt (17), gravel (12), quartzite (11), sandstone (14), andesite (5), and other (31) such as trap rock, anorthosite, charnockite, gneiss, and marble or undetermined type. The CA type is a direct reflection of the mineralogy, density, and water absorption coefficient, which enables the description of its strength, elasticity, and texture.[40] The properties of the parent rock, such as petrography, porosity, and mechanical properties, directly influence the CA type, physical properties (density and porosity), strength, elasticity, and texture.[20] Generally, limestones are considered rough-surfaced and low-strength, granites are smooth and high-strength, and quartzites are very smooth-surfaced.[41] The physio-mechanical properties of the CA types are presented in Table 1, and these CA types are considered of good quality for HSC production.

Table 1—Properties of coarse aggregate used for high-strength concrete

Coarse aggregate type	Specific gravity, t/m^3 (lb/ft^3)	Water absorption, %	Porosity, %	Compressive strength, MPa (psi)	Modulus of elasticity, GPa (× 10^6 psi)
Limestone	2.62 to 2.82 (163.3 to 176.0)	0.4 to 3.8	1 to 7.4	70 to 295 (10,150 to 42,800)	43 to 85 (6.23 to 12.32)
Granite	2.63 to 2.70 (164.2 to 168.6)	0.8 to 1	3.1	96 to 220 (13,900 to 32,000)	28 to 75 (4.06 to 10.87)
Basalt	2.85 to 2.94 (177.9 to 183.5)	0.14 to 2.2	4.2	132 to 322 (19,150 to 46,700)	85 to 101 (12.32 to 14.64)
Gravel	2.55 to 2.65 (159.2 to 165.4)	0.7 to 2.0	—	—	—
Sandstone	2.56 to 2.72 (159.8 to 169.8)	0.6	0.83 to 6.4	52 to 205 (7500 to 29,700)	37 to 58 (5.36 to 8.41)
Quartzite	2.66 to 2.88 (166.1 to 179.8)	0.2 to 0.5	0.44 to 2.7	87 to 323 (12,600 to 46,800)	42 to 110 (6.09 to 15.95)
Andesite	2.52 to 2.91 (157.3 to 181.7)	0.7	—	—	81 (11.74)
Other	2.55 to 2.95 (159.2 to 184.2)	0.14 to 1.79	0.4 to 0.45	78 to 247 (11,300 to 35,800)	22 to 74 (3.19 to 10.74)

The selected articles tested distinct mixtures composed of diverse types of cement, SCMs, admixtures, and *w*/*b*, resulting in varying paste compositions. The used SCMs included silica fume, ultrafine slag powder, fly ash, or a combination of several types. The admixtures included HRWRs in the form of melamine, naphthalene, formaldehyde, and/or polycarboxylate. Slump-retaining, viscosity-modifying, and set-retarding admixtures were also used to obtain the desired consistency of fresh concrete. Several types of cement were used, including ASTM ordinary portland cements Type I (class 42.5 or class 52.5), Type III (early high strength), and high-sulfate-resistance cement. The *w*/*b* reported for HSC varied between 0.20 and 0.35.[25,27]

The extracted data consisted of the CA type and the corresponding CS (103 data points) and MOE (95 data points) at different testing ages, including 28-day (28 days of water curing). The CS ranged from 50 to 130 MPa (7252 to 18,855 psi) and the MOE ranged from 25 to 52 GPa (3.63 to 7.54 × 10^6 psi), while the average CS in each article was greater than 64 MPa (9282 psi).[27] The mechanical properties of HSC are influenced by the testing method, such as the characteristics of the testing machine and the loading rate[42]; each study used similar testing conditions, which reduced the bias.

COMPRESSIVE STRENGTH OF HIGH-STRENGTH CONCRETES

The CS is influenced by the properties of the aggregates, the paste, and the ITZ; it also depends on other testing properties, such as the specimen geometry and size and the loading parameters.[20] The 28-day CS of concrete is tested to ensure the quality control and the quality assurance. It is necessary for construction design and structural applications.[42,43]

Influence of coarse aggregate type on compressive strength

There was a significant variation in the CS of HSC in each article using different CA types. Figure 3 shows a large scatter in the variation of the CS with different CA types (limestone, sandstone, basalt, and so on) for each study. Changing the CA type resulted in an average standard deviation equal to 7.3 MPa (1059 psi); different CA types in each article had a standard deviation in the range of 2 to 28.6 MPa (290 to 4148 psi).[26,28] Kılıç et al.[28] used sandstone, limestone, and basalt to produce concrete with CS equal to 50, 96, and 121 MPa (7252, 13,924, and 17,550 psi), respectively, while Beushausen and Dittmer[26] produced concrete with andesite and granite that had a CS equal to 115 and 117 MPa (16,675 and 16,965 psi), respectively. The variation of the CS between articles is also very significant and is in the range of 2 to 70 MPa (290 to 10,152 psi),[26,28] and the relative deviation varied the CS by 21% on average and up to 141%.[28]

Several CA types were observed to provide a ranking compared to the average CS and other CA types. Basalt CA produced the maximal CS in six out of the seven articles that used it[19,23,25,27,28,33,36] compared to all other CA types, including limestone,[36] sandstone,[19] granite,[23] quartzite,[28] and gravel.[33] Table 1 shows that basalt rocks are very strong (CS between 132 and 322 MPa [19,144 and 46,702 psi]) and very stiff (MOE between 85 and 101 GPa [1.23 and 1.46 × 10^7 psi]). Basalt CAs are generally known to be excellent CA types to produce HSC.[41] Gravels are sourced from natural round gravel found in rivers and produced the lowest CS in all five articles that used it.[25,31,33,34,39] The use of gravel reduced the CS up to 24% compared to other aggregates.[31] The rounded shape and the smooth texture of river gravel was the main factor that explains this. It was found that the rounded shape causes a reduction of 30% of the CS compared to crushed aggregates with the same type,[44] and aggregates with smooth texture reduced the CS compared to aggregates with different surface roughness.[45] Limestone CA was used in 14 out of 19 articles and produced different CS values compared to other CA types. It produced CS values higher than the average, such as in the case of Aïtcin and Mehta[39] where the average was 94 MPa (13,633 psi) and limestone produced 97 MPa (14,068 psi), and CS values lower than the average, such as in the case of Giaccio et al.,[36] where the average was 78 MPa (11,312 psi) and the limestone produced 62 MPa (8992 psi).

On the other hand, the ranking between CA types can change, such as the limestone CA used by Kılıç et al.,[28] which produced a CS of HSC equal to 106 MPa (15,374 psi), higher than the quartzite CA equal to 99 MPa (14,359 psi). In contrast, limestone CA produced in Wu el at.[30] a CS equal to 83 MPa (12,038 psi), lower than CS of quartzite equal to 98 MPa (14,214 psi). Another example is that limestone CA sometimes produced the highest CS[31] or the lowest CS[36] compared to other CA types. The same type of CA produced different CS values due to the geology of the parent rock. Studies were conducted with CAs sourced from diverse geological settings, quarry locations, and mineralogies,

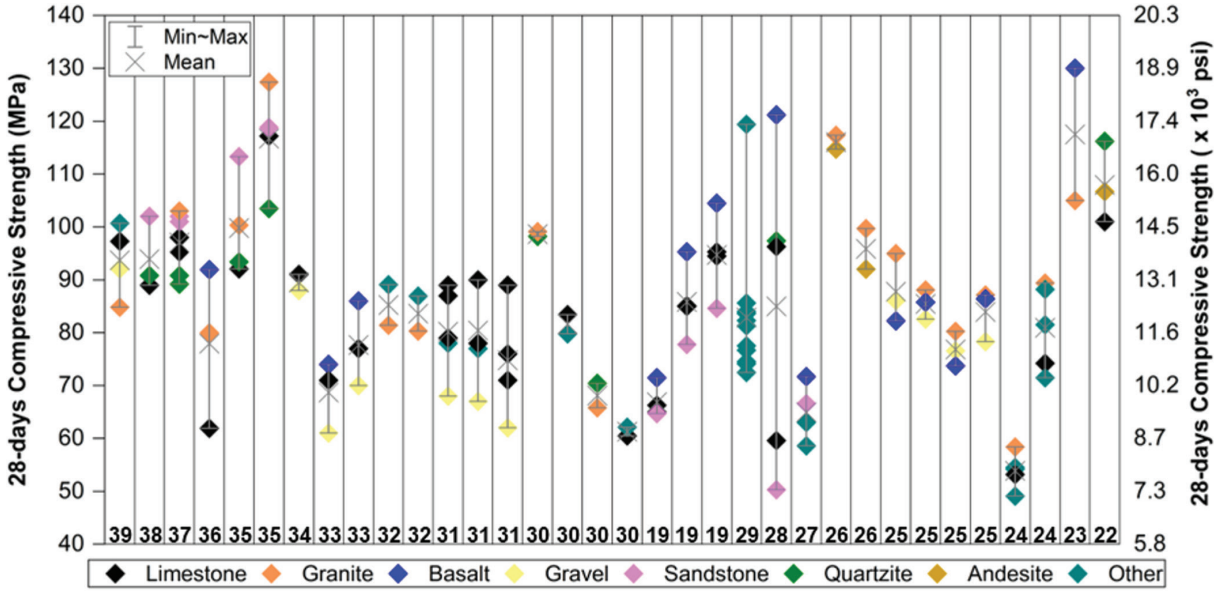

Fig. 3—Variation of CS of HSCs using different CA types.

resulting in different CA type properties, such as dolomitic limestone producing a CS equal to 89 MPa (12,908 psi), higher than calcitic limestone with a CS equal to 79 MPa (11,457 psi).[31] This is due to the intrinsic properties of different CA types (limestone, basalt, and so on), including strength, elasticity, and texture.

de Larrard and Belloc[8] studied the influence of five aggregate types on the CS of concrete. The experimental program consisted of concrete mixtures that were optimized using CPM and used fine and coarse aggregates from five different types: hard limestone (Boulonnais), semi-hard limestone (Arlaut), basalt (Raon-l'Étape), rounded flint (Crotoy), and quartzite (Cherbourg). The authors proposed a quantification of the impact of aggregate type on the CS of concrete using two empirical parameters: bond (a) and ceiling (b), using the relationship between the CS of concrete and the strength of the matrix presented in Eq. (2)

$$f_{c,composite} = \frac{a \times f_{c,matrix} + 1}{b \times f_{c,matrix}} \text{(MPa)} \quad (2)$$

where $f_{c,composite}$ is CS of concrete; and $f_{c,matrix}$ is CS of cement paste matrix.

It was found that the CS of HSC produced with these five aggregates was ranked as follows: basalt ~ flint > hard limestone > quartzite ~ semi-hard limestone. The bond (a) represents the adherence that is related to the texture of CA and the chemical reaction that improves the CS evolution, such as the bond that was higher for limestone (Boulonnais) compared to flint (Crotoy). Limestone has a good adherence because of its rough surface texture and the chemical reaction between cement paste and calcium carbonate, while flint lacks adherence because of the smooth texture. Finally, the ranking of aggregate type was found to depend on the ratio a/b, which is related to the intrinsic strength of parent rock.

Influence of coarse aggregate strength on compressive strength

The relationship between the CS of CA and the CS of HSC is presented in Fig. 4. The variation in the CS of HSC as a function of the CS of CA shows a positive trend overall. The relative deviation of the CS when using a CA with a different strength averages 37% and can be up to 141%.[28] Mousavi and Ranjbar[22] showed that the CS of HSC increased by up to 15% when using limestone with a CS of CA equal to 102 MPa (14,794 psi), andesite with a CS of 161 MPa (23,351 psi), and quartzite with a CS of 323 MPa (46,847 psi) to produce HSC with a CS equal to 101, 107, and 116 MPa, (14,649, 15,519, and 16,824 psi), respectively.

Kılıç et al.[28] found that the CS of sandstone (CS = 52 MPa [7540 psi]) produced an HSC with a CS of 50 MPa (7252 psi), which was considerably lower than the CS of 96 MPa (13,924 psi) produced by limestone (CS = 110 MPa [15,954 psi]). This was due to the low strength of the sandstone CA, which limited the CS of the HSC. In their study, they also tested the CS of basalt (132 MPa [19,145 psi]) and gabbro (247 MPa [35,825 psi]); the CS of the HSC averaged 135 MPa (19,580 psi), which showed that the CS of the HSC was limited by either the strength of the mortar (such as gabbro) or the strength of the CA (such as basalt). This limiting effect was confirmed by Giaccio et al.[36] who reported that the strength of the mortar (91 MPa [13,198 psi]) was equal to or greater than the CS of HSC produced with basalt (91 MPa [13,198 psi]), granite (80 MPa [11,603 psi]), or limestone (62 MPa [8992 psi]).

The CS of HSC increases with the CS of CA up to a limit due to the limiting strength of the mortar or the strength of the CA. This is known as the ceiling effect, where the strength of the CA limits the strength of HSC, according to de Larrard.[14] The ceiling effect quantifies the limiting effect of the aggregate on the strength of HSC; "weaker" aggregates would halt the CS of concrete when the strength of the paste increases.

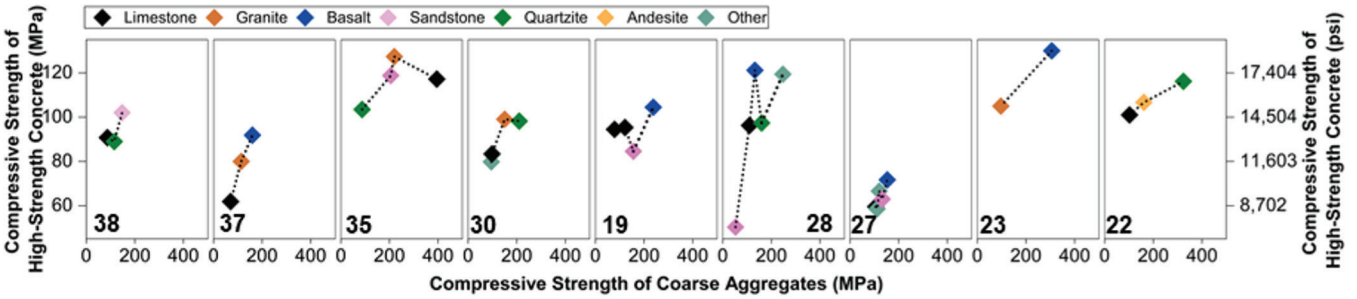

Fig. 4—Trellis plots of evolution of CS of HSC as function of CS of CA.

Sandstone CA is an outlier to this rule[35,38] because it produced concrete with a higher CS than its intrinsic strength. Two exceptions where sandstone produced a lower CS are explained by the irregular shape[19] or to the ceiling effect.[28] Tighiouart et al.,[35] who studied the elasticity of sandstone concretes and CA, suggested that sandstone produced a better elastic compatibility with the matrix, reducing the stress at the interface and leading to a more homogeneous stress repartition in the interface, which is known to improve the CS.[3]

MODULUS OF ELASTICITY OF HIGH-STRENGTH CONCRETES

The elastic properties of HSC are one of the key parameters for the design, construction, and analysis of concrete structures. The most well-known elastic parameter is the MOE, which consists of the short-term deformation of concrete. The value of the MOE is important for designing structures where the deflections are sought to be minimal; selecting the materials to have stiffer concrete becomes essential.[42] The influence of CA type on the MOE of HSC was investigated by 10 articles; the results are presented in the scatter plot in Fig. 5, and the impact of the MOE of CA on the MOE of HSC is presented in Fig. 6. The deviation of the MOE using different types of CA with different MOE is high, varying between 5.0 GPa[23] and 17.0 GPa[35] (7.25×10^5 psi and 2.47×10^6 psi), with a relative deviation varying between 10% and 48%, respectively. The range of the variation of the MOE is more significant than the range of the variation of CS because 1 GPa is equal to 1000 MPa, with 1 MPa equal to 145.04 psi; this change of the MOE has a significant influence on the deformation of structures.

Influence of coarse aggregate type on modulus of elasticity

In Fig. 5, the classification of the MOE of HSC based on the CA type shows that basalt[19,23,27,36] (blue) and quartzite[22,30,38] (green) produced the highest MOE. The performance of limestone varied, producing the highest[35] or lowest[30] MOE depending on the mineralogy and geology of the rock[31]: dolomitic limestone produced an MOE equal to 50 GPa (7.25×10^6 psi), while the MOE of calcitic limestone produced an MOE of 39 GPa (5.66×10^6 psi). The performance of granite was average, but Beushausen and Dittmer[26] found that HSC produced from andesite had an MOE equal to 59 GPa (8.56×10^6 psi) and was superior to the 47 GPa (6.82×10^6 psi) produced from granite. Sandstone produced a significantly lower MOE in the HSC.[19,35,37,38]

Interestingly, the MOE of HSC can vary even when the CS remains the same. This variation is primarily influenced by two factors: the type of CA and the MOE of the CA used. Beushausen and Dittmer[26] produced two HSC using andesite and granite with similar CS but the MOE of the produced HSCs were very different: 59 GPa (8.56×10^6 psi) and 47 GPa (6.82×10^6 psi), respectively. This was also observed in Wu et al.[30] when using quartzite, which produced an HSC with a MOE equal to 48 GPa (6.96×10^6 psi), while granite CA produced only 36 GPa (5.22×10^6 psi). The same trend was observed by Tighiouart et al.,[35] and was more pronounced: sandstone CA produced HSC with an MOE equal to 35 GPa (5.07×10^6 psi), while limestone had an MOE equal to 52 GPa (7.54×10^6 psi). The influence of CA on the MOE of concrete is more important than the influence on the CS of concrete[1]; as revealed here, it is also more pronounced in HSC.

Influence of coarse aggregate elasticity on modulus of elasticity

Figure 6 reveals a clear positive correlation between the MOE of CA and the MOE of HSC. This indicates that as the MOE of the CA increases, the MOE of the HSC also consistently increases. The outlier presented in Baalbaki et al.[38] concerns the MOE of HSC produced using limestone and quartzite, but the difference is not significant. One case where HSC is not very stiff is when using sandstone CA, such as in Baalbaki et al.,[38] where a sandstone HSC with an MOE equal to 31 GPa (4.50×10^6 psi) was significantly lower than the MOE of limestone HSC (MOE equal to 48 GPa [6.96×10^6 psi]).

CAs act as a solid granular inclusion in the composite that restrains the deformations of the paste and makes concrete stiffer.[1] The MOE is affected primarily by the volume fraction and the stiffness of the paste and the aggregates, in addition to the properties of the interface. The prediction of the MOE of an HSC using the MOE of a CA and other properties was proposed by de Larrard and Le Roy[46] and gave a high degree of accuracy with a standard error of 1.6 GPa (2.32×10^5 psi). This model confirms the positive trend between the MOE of CA and the MOE of HSC. The triple-sphere model is presented in Eq. (3) and shows that the properties that influence the MOE of concrete are aggregates and paste volumetric fraction, MOE of both aggregates and paste, and packing density

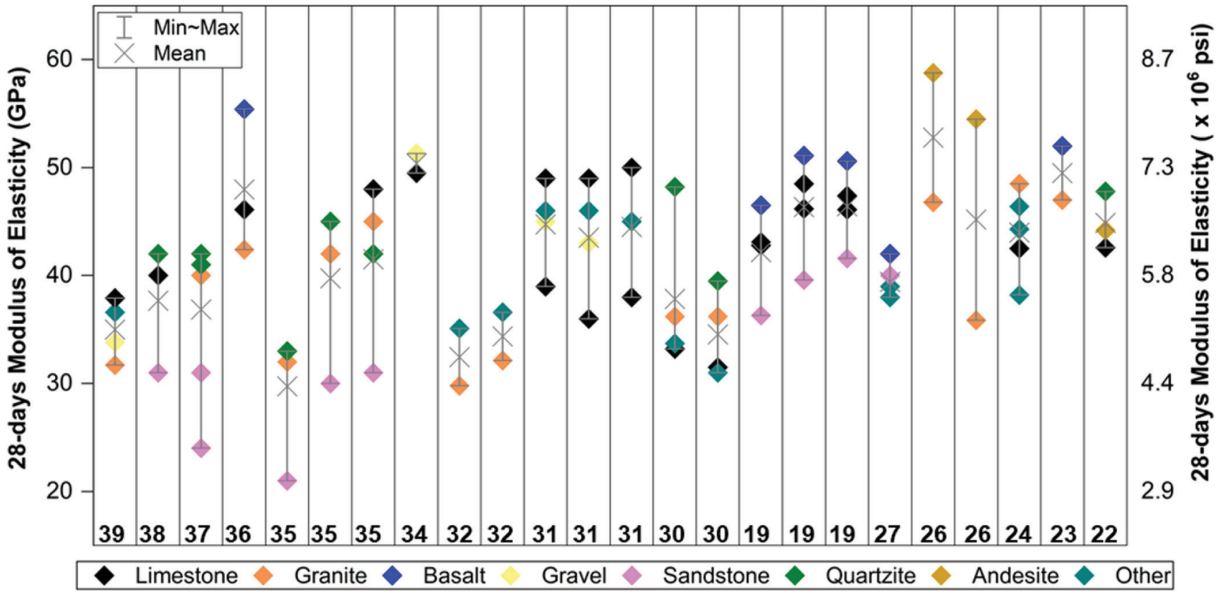

Fig. 5—Variation across articles of MOE of HSCs using different CA types.

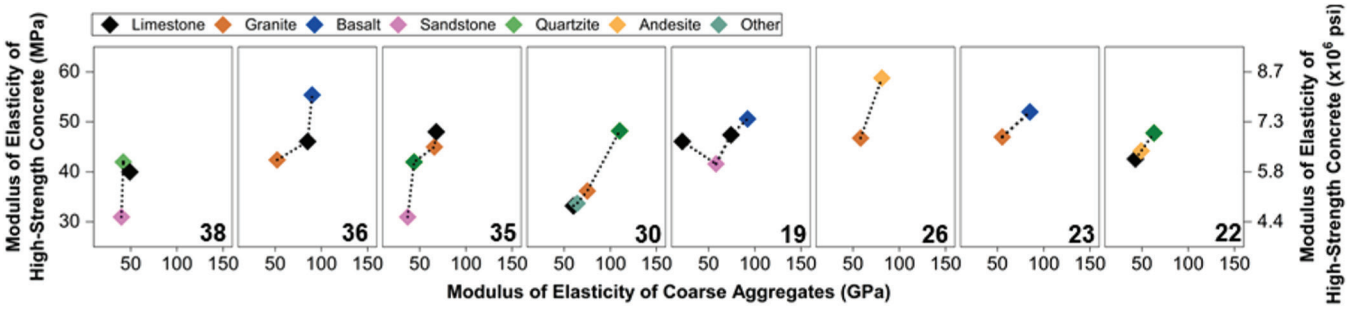

Fig. 6—Trellis plots of variation of MOE of HSCs using different CA types.

$$E_c = \left[1 + 2g\frac{\left(E_g{}^2 - E_m{}^2\right)}{\left(g^* - g\right)E_g{}^2 + 2(2-g)E_gE_m + \left(g^* + g\right)E_m{}^2}\right]E_m \quad \text{(GPa)} \quad (3)$$

where E_c, E_m, and E_a are MOE of concrete, mortar, and aggregates, respectively; g is apparent packing density of aggregates; and g^* is virtual packing density of aggregates.

This model uses homogenization that has two hypotheses, including that concrete is composed of two phases: the paste and aggregate, and aggregates are stiffer than the paste. Packing density refers to how tightly the aggregate particles are packed within concrete, and it is related to the shape and particle size distribution of the aggregate.

PREDICTION OF MODULUS OF ELASTICITY USING ACI 363 EQUATION

Accurately predicting the MOE of HSC is crucial for the design and calculation of structures. However, directly measuring the MOE is often difficult because of testing equipment and methods. Therefore, researchers have developed models that predict the MOE based on the more easily measurable CS. These models, like those proposed in ACI 363R-10[9] and *fib* Model Code 2010,[47] are based on experimental testing data. They are based on the power function of the CS with correction factors that consider the CA type, type of cement, and density of the concrete.[48] Several researchers have proposed coefficients for different CA types[48-50] such as Rashid et al.,[51] who included a parameter of the CA type which helped obtain more accurate predictions. Equation (4) was proposed by ACI 363R-10 for the prediction of the MOE of NSC and HSC, among other equations, for a CS up to 83 MPa (1.20×10^4 psi), which corresponds to an MOE equal to 42 GPa (6.09×10^6 psi). However, the MOE of HSC varies up to 58 GPa (8.41×10^6 psi)[26] with an average of 39.5 GPa (5.73×10^3 psi). There is a need for equations to predict the MOE of HSC more accurately

$$E_c = (40{,}000(f_c')^{0.5} + 10^6)\ \text{(psi)},\ \text{for } 3000\ \text{psi} < f_c' < 12{,}000\ \text{psi}$$

$$E_c = (3320(f_c')^{0.5} + 6900)\ \text{(MPa)},\ \text{for } 21\ \text{MPa} < f_c' < 83\ \text{MPa} \quad (4)$$

where f_c' is average 28-day CS of concrete.

In this review, the authors propose to calibrate the K coefficient in the ACI 363R-10 equation (Eq. (4)) to consider the CA type using Eq. (5)

$$E_c = K \times (40{,}000(f_c')^{0.5} + 10^6)\ \text{(psi)},\ \text{for } 3000\ \text{psi} < f_c' < 12{,}000\ \text{psi}$$

Table 2—Values of *K* coefficient of CA type and variation of predicted modulus of elasticity

Coarse aggregate type	*K* value	Variation, GPa (× 10^5 psi)	
		with *K* coefficient	with *K* = 1.00, ACI 363R-10
Andesite	1.39	5.8 (8.4)	14.7 (21.3)
Basalt	1.33	3.6 (5.2)	12.2 (17.7)
Granite	1.05	6.8 (9.9)	6.6 (9.6)
Gravel	1.20	6.0 (8.7)	7.0 (10.2)
Limestone	1.20	5.1 (7.4)	7.5 (10.9)
Other	1.18	4.6 (6.7)	6.8 (9.9)
Quartzite	1.11	2.5 (3.6)	4.2 (6.1)
Sandstone	0.92	6.4 (9.3)	6.9 (10.0)
	Average variation	5.1 (7.4)	7.4 (10.7)

$$E_c = K \times (3320(f_c')^{0.5} + 6900)\ (\text{MPa}),\quad \text{for } 21\ \text{MPa} < f_c' < 83\ \text{MPa} \tag{5}$$

where *K* is CA coefficient.

A total of 86 data points for 28-day CS and the MOE were extracted from the selected articles.[19,22-24,26,27,30-32,34-39] The 28-day CS of HSC is corrected using the equations of Rashid et al.[51] (Eq. (6) to (8) herein) to represent the testing on Ø150 x 300 mm (Ø6 x 12 in.) cylinders at 28 days of curing (f_c') and the variation calculated with Eq. (9)

$$f_{c,150\times300} = 0.83 \times f_{c,100} \text{ and } f_{c,150\times300} = 0.86 \times f_{c,150} \tag{6}$$

$$f'_{c,150} = 0.96 \times f'_{c,100} - 0.21 \tag{7}$$

$$E_{c,150} = 0.76 \times E_{c,100} + 6.35 \text{ for } 24\ \text{GPa} < E_c < 56\ \text{GPa} \tag{8}$$

where $E_{c,150}$ and $E_{c,100}$ are MOE of concrete for 150 and 100 mm (6 and 4 in.) cubes; $f'_{c,150}$ and $f'_{c,100}$ are CS of concrete for 150 and 100 mm (6 and 4 in.) cubes; and $f'_{c,150x300}$ and $f'_{c,100x200}$ are CS of concrete for Ø150 x 300 mm (Ø6 x 12 in.) and Ø100 x 200 mm (Ø4 x 8 in.) cylinders.

$$\text{Variation} = |\text{MOE}_{\text{predicted}} - \text{MOE}_{\text{exp}}| \tag{9}$$

where $\text{MOE}_{\text{predicted}}$ is predicted MOE; and MOE_{exp} is experimental MOE.

The correction coefficients *K* are presented in Table 2. The prediction equation of the MOE of HSC produces an average variation equal to 5.1 GPa (7.4 × 10^5 psi) when using the CA coefficient compared to 7.4 GPa (1.07 × 10^6 psi) for the ACI 363R-10 equation; it is particularly useful to determine the lower bond value of the MOE of HSC. Figure 7 presents the prediction curves and experimental data.

SUMMARY AND FUTURE PERSPECTIVES

This review systematically investigated the influence of coarse aggregate (CA) type on the mechanical properties of high-strength concrete (HSC). Nineteen research articles were selected based on their rigorous methodology of varying CA type while maintaining consistent paste composition. First, the analysis revealed a significant quantitative impact of CA type on the compressive strength (CS) and modulus of elasticity (MOE) of HSC. Variation in CA type resulted in a relative deviation of the CS of up to 141% and relative deviation of the MOE of up to 48%. Second, key factors influencing the impact of CA on HSC were identified. These include: the type of CA is related to the mineralogy and geology, which influence the variation in properties across different CA types; the intrinsic strength of the CA can limit the maximal CS of HSC; and the elasticity of CA, which is the most crucial factor affecting the MOE of HSC, with variations of up to 17 GPa (2.47 × 10^6 psi) observed at similar CS values. Third, the Compressible Packing Model (CPM) was presented to explain these observations, including the adherence and ceiling effects, in addition to the triple-sphere model that proves the critical role of the MOE of CAs. Finally, the equation proposed in ACI 363R-10[9] for predicting the MOE of HSC can be improved by incorporating a correction factor based on CA type, offering a conservative estimation for structural engineers.

This review highlighted the complex relationship between CA type and the CS of HSC. While basalt consistently delivered high CS and MOE in HSC, gravel performed less favorably. This underlines the importance of strong, stiff, and highly adherent crushed aggregates for HSC; sandstones presented a unique case. Baalbaki et al.[38] indicated that the good adherence and lower MOE of sandstone contributed to better elastic compatibility with the cement paste, potentially improving CS; and Beushausen and Dittmer[26] confirmed this notion because they found that high-strength and high-elasticity andesite CA produced lower CS in HSC compared to granite CA. The scarcity of consistent data highlights the need for further research on the interplay between adherence and elasticity and their combined influence on CS of HSC. Recent advancements in analytical and numerical models for ordinary concrete offer a promising foundation for theoretical investigations into this complex interaction.[52,53] This could help to improve the prediction of the mechanical properties of HSC, leading to more efficient and reliable concrete structures.

AUTHOR BIOS

ACI member **Yahya El Berdai** *is a Doctor at l'Université de Lorraine, Nancy, France. He received his PhD in civil engineering from Mohammed VI Polytechnic University, Ben Guerir, Morocco. His research interests include alternative aggregates, high-performance concrete, and alkali-aggregate reaction.*

Yassine Taha *is an Assistant Professor and HDR at Mohammed VI Polytechnic University. His research interests include environmental engineering, mineralogy, and materials engineering.*

Amine el Mahdi Safhi *is currently an MSCA Research Fellow at Østfold University College, Halden, Norway. He received his joint PhD in civil engineering from the Université de Sherbrooke, Sherbrooke, QC, Canada, and the Institut Mines-Télécom Lille Douai, Douai, France. His research interests include developing sustainable construction materials and circular economy through innovative materials science.*

Romain Trauchessec *is a Research Associate Professor at l'Université de Lorraine. His research interests include structural engineering, materials engineering, and civil engineering, including expertise in cement and civil engineering materials.*

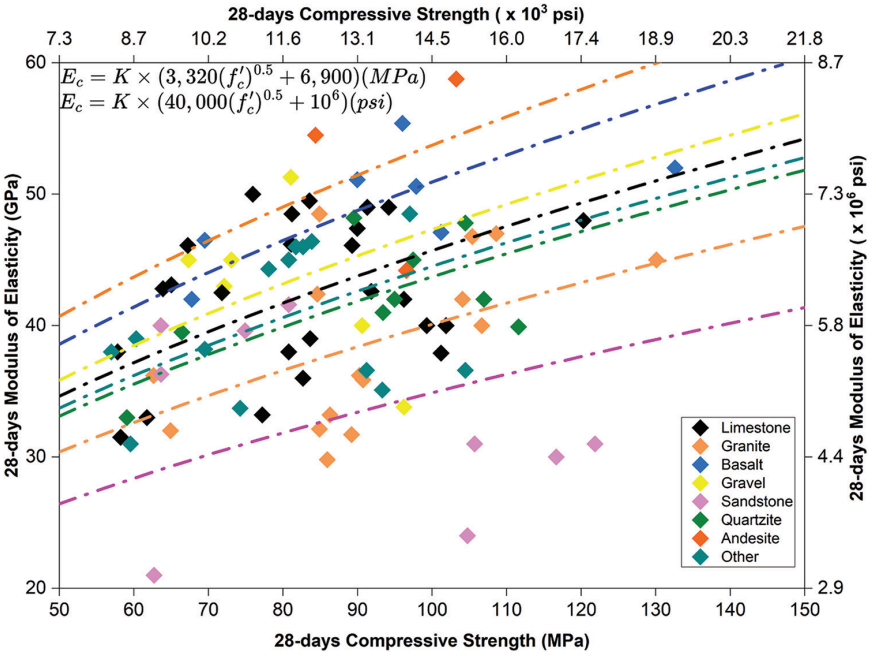

Fig. 7—Prediction curves of 28-day MOE of HSCs as function of 28-day CS of different CA types using calibrated K *coefficient.*

Rachid Hakkou *is a Full Professor at Cadi Ayyad University, Marrakesh, Morocco, and an Affiliated Professor at Mohammed VI Polytechnic University. His research interests include environmental engineering and environmental chemistry.*

Mostafa Benzaazoua *is a Full Professor and the Director of the Geology and Sustainable Mining Institute at Mohammed VI Polytechnic University. His research interests include applied mineralogy and geochemistry, including ore and waste processing and valorizations.*

ACKNOWLEDGMENTS

The authors' work would like to express their gratitude to OCP Group and UM6P for the financial support under specific agreement No. AS66. The authors would like to express their sincere appreciation to A. Lecomte (Rest in Peace) for his significant contribution to this article.

REFERENCES

1. Alexander, M., and Mindess, S., *Aggregates in Concrete*, CRC Press, Boca Raton, FL, 2010, 448 pp.

2. Neville, A. M., *Properties of Concrete*, Longman London, London, UK, 1995.

3. De Brito, J.; Kurda, R.; and Raposeiro da Silva, P., "Can We Truly Predict the Compressive Strength of Concrete without Knowing the Properties of Aggregates?" *Applied Sciences*, V. 8, No. 7, 2018, p. 1095. doi: 10.3390/app8071095

4. Alexander, M. G., and Davis, D. E., "The Influence of Aggregates on the Compressive Strength and Elastic Modulus of Concrete," *Civil Engineering = Siviele Ingenieurswese*, V. 1992, No. 5, 1992, pp. 161-170.

5. Kaplan, M. F., "Flexural and Compressive Strength of Concrete as Affected by the Properties of Coarse Aggregates," *ACI Journal Proceedings*, V. 55, No. 5, May 1959, pp. 1193-1208.

6. Tanesi, J.; Bentz, D.; Jones, S.; Beyene, M.; Kim, H.; Ardani, A.; Arnold, J.; and Stutzman, P., "Influence of Aggregate Properties on Concrete Mechanical Performance," Transportation Research Board Annual Meeting, Washington, DC, Jan. 2017, 20 pp.

7. Góra, J., and Piasta, W., "Impact of Mechanical Resistance of Aggregate on Properties of Concrete," *Case Studies in Construction Materials*, V. 13, 2020, p. e00438. doi: 10.1016/j.cscm.2020.e00438

8. de Larrard, F., and Belloc, A., "The Influence of Aggregate on the Compressive Strength of Normal and High-Strength Concrete," *ACI Materials Journal*, V. 94, No. 5, Sept.-Oct. 1997, pp. 417-426.

9. ACI Committee 363, "Report on High-Strength Concrete (ACI 363R-10)," American Concrete Institute, Farmington Hills, MI, 2010, 65 pp.

10. Marvila, M. T.; de Azevedo, A. R. G.; de Matos, P. R.; Monteiro, S. N.; and Vieira, C. M. F., "Materials for Production of High and Ultra-High Performance Concrete: Review and Perspective of Possible Novel Materials," *Materials*, V. 14, No. 15, 2021, p. 4304. doi: 10.3390/ma14154304

11. Caldarone, M. A., *High-Strength Concrete: A Practical Guide*, CRC Press, Boca Raton, FL, 2008, 252 pp.

12. Malier, Y., *High Performance Concrete: From Material to Structure*, CRC Press, London, UK, 1992, 568 pp.

13. Sohail, M. G.; Wang, B.; Jain, A.; Kahraman, R.; Ozerkan, N. G.; Gencturk, B.; Dawood, M.; and Belarbi, A., "Advancements in Concrete Mix Designs: High-Performance and Ultrahigh-Performance Concretes from 1970 to 2016," *Journal of Materials in Civil Engineering*, ASCE, V. 30, No. 3, 2018, p. 04017310. doi: 10.1061/(ASCE)MT.1943-5533.0002144

14. de Larrard, F. "Structures Granulaires et Formulation des Bétons," Laboratoire Central des Ponts et Chaussées, Paris, France, 2000.

15. Kwan, A. K. H.; Li, L. G.; and Fung, W. W. S., "Wet Packing of Blended Fine and Coarse Aggregate," *Materials and Structures*, V. 45, No. 6, 2012, pp. 817-828. doi: 10.1617/s11527-011-9800-3

16. Aïtcin, P.-C., *High Performance Concrete*, CRC Press, Boca Raton, FL, 2019, 624 pp.

17. Mazloom, M.; Ramezanianpour, A. A.; and Brooks, J. J., "Effect of Silica Fume on Mechanical Properties of High-Strength Concrete," *Cement and Concrete Composites*, ASCE, V. 26, No. 4, 2004, pp. 347-357. doi: 10.1016/S0958-9465(03)00017-9

18. Aïtcin, P.-C., "High-Performance Concrete Demystified," *Concrete International*, V. 15, No. 1, Jan. 1993, pp. 21-26.

19. Sengul, O.; Tasdemir, C.; and Tasdemir, M. A., "Influence of Aggregate Type on Mechanical Behavior of Normal- and High-Strength Concretes," *ACI Materials Journal*, V. 99, No. 6, Nov.-Dec. 2002, pp. 528-533.

20. Mehta, P., and Monteiro, P. J. M., *Concrete: Microstructure, Properties, and Materials*, McGraw Hill Professional, New York, 2005, 683 pp.

21. Page, M. J.; McKenzie, J. E.; Bossuyt, P. M.; Boutron, I.; Hoffmann, T. C.; Mulrow, C. D.; Shamseer, L.; Tetzlaff, J. M.; Akl, E. A.; Brennan, S. E.; Chou, R.; Glanville, J.; Grimshaw, J. M.; Hróbjartsson, A.; Lalu, M. M.; Li, T.; Loder, E. W.; Mayo-Wilson, E.; McDonald, S.; McGuinness, L. A.; Stewart, L. A.; Thomas, J.; Tricco, A. C.; Welch, V. A.; Whiting, P.; and Moher, D., "The PRISMA 2020 Statement: An Updated Guideline For Reporting Systematic Reviews," *International Journal of Surgery*, V. 88, 2021, p. 105906. doi: 10.1016/j.ijsu.2021.105906

22. Mousavi, S. M., and Ranjbar, M. M., "Experimental Study of the Effect of Silica Fume and Coarse Aggregate Type on the Fracture Characteristics of High-Strength Concrete," *Engineering Fracture Mechanics*, V. 258, 2021, p. 108094. doi: 10.1016/j.engfracmech.2021.108094

23. Kristombu Baduge, S.; Mendis, P.; San Nicolas, R.; Rupasinghe, M.; and Portella, J., "Aggregate-Dependent Approach to Formulate and Predict Properties of High-Strength and Very-High-Strength Concrete," *Journal of Materials in Civil Engineering*, ASCE, V. 32, No. 4, 2020, p. 04020053. doi: 10.1061/(ASCE)MT.1943-5533.0003055

24. Vishalakshi, K. P.; Revathi, V.; and Sivamurthy Reddy, S., "Effect of Type of Coarse Aggregate on the Strength Properties and Fracture Energy

of Normal and High Strength Concrete," *Engineering Fracture Mechanics*, V. 194, 2018, pp. 52-60. doi: 10.1016/j.engfracmech.2018.02.029

25. Grabiec, A. M.; Zawal, D.; and Szulc, J., "Influence of Type and Maximum Aggregate Size on Some Properties of High-Strength Concrete Made of Pozzolana Cement in Respect of Binder and Carbon Dioxide Intensity Indexes," *Construction and Building Materials*, V. 98, 2015, pp. 17-24. doi: 10.1016/j.conbuildmat.2015.08.108

26. Beushausen, H., and Dittmer, T., "The Influence of Aggregate Type on the Strength and Elastic Modulus of High Strength Concrete," *Construction and Building Materials*, V. 74, 2015, pp. 132-139. doi: 10.1016/j.conbuildmat.2014.08.055

27. Uysal, M., "The Influence of Coarse Aggregate Type on Mechanical Properties of Fly Ash Additive Self-Compacting Concrete," *Construction and Building Materials*, V. 37, 2012, pp. 533-540. doi: 10.1016/j.conbuildmat.2012.07.085

28. Kılıç, A.; Atiş, C. D.; Teymen, A.; Karahan, O.; Özcan, F.; Bilim, C.; and Özdemir, M., "The Influence of Aggregate Type on the Strength and Abrasion Resistance of High Strength Concrete," *Cement and Concrete Composites*, V. 30, No. 4, 2008, pp. 290-296. doi: 10.1016/j.cemconcomp.2007.05.011

29. Al-Oraimi, S. K.; Taha, R.; and Hassan, H. F., "The Effect of the Mineralogy of Coarse Aggregate on the Mechanical Properties of High-Strength Concrete," *Construction and Building Materials*, V. 20, No. 7, 2006, pp. 499-503. doi: 10.1016/j.conbuildmat.2004.12.005

30. Wu, K.-R.; Chen, B.; Yao, W.; and Zhang, D., "Effect of Coarse Aggregate Type on Mechanical Properties of High-Performance Concrete," *Cement and Concrete Research*, V. 31, No. 10, 2001, pp. 1421-1425. doi: 10.1016/S0008-8846(01)00588-9

31. Cetin, A., and Carrasquillo, R. L., "High-Performance Concrete: Influence of Coarse Aggregates on Mechanical Properties," *ACI Materials Journal*, V. 95, No. 3, May-June 1998, pp. 252-261.

32. Penttala, V., and Komonen, J., "Effects of Aggregates and Microfillers on the Flexural Properties of Concrete," *Magazine of Concrete Research*, V. 49, No. 179, 1997, pp. 81-97. doi: 10.1680/macr.1997.49.179.81

33. Özturan, T., and Çeçen, C., "Effect of Coarse Aggregate Type on Mechanical Properties of Concretes With Different Strengths," *Cement and Concrete Research*, V. 27, No. 2, 1997, pp. 165-170. doi: 10.1016/S0008-8846(97)00006-9

34. Zhou, F. P.; Lydon, F. D.; and Barr, B. I. G., "Effect of Coarse Aggregate on Elastic Modulus and Compressive Strength of High Performance Concrete," *Cement and Concrete Research*, V. 25, No. 1, 1995, pp. 177-186. doi: 10.1016/0008-8846(94)00125-I

35. Tighiouart, B.; Benmokrane, B.; and Baalbaki, W., "Caractéristiques mécaniques et élastiques de bétons à haute performance confectionnés avec différents types de gros granulats," *Materials and Structures*, V. 27, No. 4, 1994, pp. 211-221. doi: 10.1007/BF02473035

36. Giaccio, G.; Rocco, C.; and Violini, D., "High-Strength Concretes Incorporating Different Coarse Aggregates," *ACI Materials Journal*, V. 89, No. 3, May-June 1992, pp. 242-246.

37. Baalbaki, W.; Aitcin, P.-C.; and Ballivy, G., "On Predicting Modulus of Elasticity in High-Strength Concrete," *ACI Materials Journal*, V. 89, No. 5, Sept.-Oct. 1992, pp. 517-520.

38. Baalbaki, W.; Benmokrane, B.; and Chaallal, O., "Influence of Coarse Aggregate on Elastic Properties of High-Performance Concrete," *ACI Materials Journal*, V. 88, No. 5, Sept.-Oct. 1991, pp. 499-503.

39. Aïtcin, P. C., and Mehta, P. K., "Effect of Coarse Aggregate Characteristics on Mechanical Properties of High-Strength Concrete," *ACI Materials Journal*, V. 87, No. 2, Mar.-Apr. 1990, pp. 103-107.

40. Bentz, D. P.; Arnold, J.; Jones, S. Z.; Stutzman, P. E.; Boisclair, M.; Rothfeld, P.; Tanesi, J.; Kim, H.; Munoz, J.; and Beyene, M., *Influence of Aggregate Characteristics on Concrete Performance*, US Department of Commerce, National Institute of Standards and Technology, Gaithersburg, MD, 2017, 97 pp.

41. Aydin, S.; Yazici, H.; and Yardimci, M. Y., "Effect of Aggregate Type on Mechanical Properties of Reactive Powder Concrete," *ACI Materials Journal*, V. 107, No. 5, Sept.-Oct. 2010, pp. 441-449.

42. Lamond, J. F., and Pielert, J. H., *Significance of Tests and Properties of Concrete and Concrete-Making Materials*, STP 169D, ASTM International, West Conshohocken, PA, 2006, 661 pp.

43. Li, Z., *Advanced Concrete Technology*, John Wiley & Sons, Inc., New York, Jan. 2011, 521 pp.

44. Guinea, G. V.; El-Sayed, K.; Rocco, C. G.; Elices, M.; and Planas, J., "The Effect of the Bond Between the Matrix and the Aggregates on the Cracking Mechanism and Fracture Parameters of Concrete," *Cement and Concrete Research*, V. 32, No. 12, 2002, pp. 1961-1970. doi: 10.1016/S0008-8846(02)00902-X

45. Hong, L.; Gu, X.; and Lin, F., "Influence of Aggregate Surface Roughness on Mechanical Properties of Interface and Concrete," *Construction and Building Materials*, V. 65, 2014, pp. 338-349. doi: 10.1016/j.conbuildmat.2014.04.131

46. de Larrard, F., and Le Roy, R., "Relation entre formulation et quelques propriétés mécaniques des bétons à hautes performances," *Materials and Structures*, V. 25, No. 8, 1992, pp. 464-475. doi: 10.1007/BF02472636

47. *fib*, "*fib* Model Code for Concrete Structures 2010," International Federation for Structural Concrete, Lausanne, Switzerland, 2013, 434 pp.

48. Noguchi, T.; Tomosawa, F.; Nemati, K.; Chiaia, B. M.; and Fantilli, A. P., "A Practical Equation for Elastic Modulus of Concrete," *ACI Structural Journal*, V. 106, No. 5, Sept.-Oct. 2009, pp. 690-696.

49. Tibbetts, C. M.; Perry, M. C.; Ferraro, C. C.; and Hamilton, H. R. T., "Aggregate Correction Factors for Concrete Elastic Modulus Prediction," *ACI Structural Journal*, V. 115, No. 4, July-Aug. 2018, pp. 931-940. doi: 10.14359/51701914

50. Iravani, S., "Mechanical Properties of High-Performance Concrete," *ACI Materials Journal*, V. 93, No. 5, Sept.-Oct. 1996, pp. 416-426.

51. Rashid, M. A.; Mansur, M. A.; and Paramasivam, P., "Correlations between Mechanical Properties of High-Strength Concrete," *Journal of Materials in Civil Engineering*, ASCE, V. 14, No. 3, 2002, pp. 230-238. doi: 10.1061/(ASCE)0899-1561(2002)14:3(230)

52. Maruyama, I., and Sugimoto, S. "Critical Influence of Aggregate Types on the Compressive Strength of Concrete," 2024. doi: 10.21203/rs.3.rs-3949961/v1

53. Krishnya, S.; Elakneswaran, Y.; and Yoda, Y., "Proposing a Three-Phase Model for Predicting the Mechanical Properties of Mortar and Concrete," *Materials Today Communications*, V. 29, 2021, p. 102858. doi: 10.1016/j.mtcomm.2021.102858

ACI Faculty Network

Why Join the Faculty Network?

The Faculty Network is a support group for educators interested in ACI and the concrete industry. Members receive notifications about classroom resources, fellowships and scholarships, funding for research, online learning, and calls for papers and presenters.

Free 1-Year Educator Membership

ACI offers complimentary membership to teaching professionals who have not been an ACI member within the past 5 years.

Free Desk Copies

Faculty Network members can request a complimentary print or PDF copy of:

- ACI CODE-318 Building Code Requirements for Structural Concrete and Commentary (includes a free subscription to ACI 318 PLUS)
- ACI CODE-323-24 Low-Carbon Concrete—Code Requirements and Commentary
- ACI CODE-530 Building Code Requirements and Specification for Masonry Structures and Companion Commentaries
- ACI CODE-562 Assessment, Repair, and Rehabilitation of Existing Concrete Structures—Code and Commentary
- MNL-3(20) Guide to the Code for Assessment, Repair, and Rehabilitation of Existing Concrete Structures
- MNL-5(19) Contractor's Guide to Quality Concrete Construction, 4th Edition
- MNL-17(21) ACI Reinforced Concrete Design Handbook (available digitally with ACI 318 PLUS subscription)
- MNL-66(20) ACI Detailing Manual (available digitally with ACI 318 PLUS subscription)

Networking

ACI hosts a Faculty Network Reception twice a year during the ACI Concrete Conventions, giving an opportunity to exchange ideas and network.

aci 318PLUS+ Faculty Network members receive a complimentary annual subscription that provides users with convenient digital interactive access to ACI CODE-318-25, ACI CODE-318-19, the ACI Detailing Manual, and the numerous design examples in the ACI Reinforced Concrete Design Handbook. The platform allows professors to create custom user notes that can be distributed to the students to view alongside the Code. Student members are provided 1-year access to ACI 318 PLUS when they purchase their printed copy of ACI 318-25 or ACI 318-19 at the student price of $105 (plus shipping).

aci Professors' Workshop
Materials | Pavements | Structures
Sponsor: aci Foundation

The Professors' Workshop is designed to provide instructors in civil engineering, architecture, architectural engineering, materials science, and construction management programs the tools to engage students in the latest developments in concrete design, construction, and materials.

aci Foundation
Building the Future

The Concrete Research Council (CRC) seeks concrete research projects that further the knowledge and sustainability of concrete materials, construction, and structures in coordination with ACI Committees. Annual Request for Proposals (RFP) are received annually between August 1 and December 1.

aci
American Concrete Institute
Always advancing

ADVANCE YOUR CLASSROOM WITH ACI

JOIN OR RENEW TODAY! concrete.org/educatorsandresearchers

ACI MATERIALS JOURNAL TECHNICAL PAPER

Title No. 122-M19

Study of Optimized Mechanical Properties in Sustainable Geopolymer Mortar with Tire Waste

by Rondinele A. R. Ferreira, Cristiane Pires, Leonardo S. Gratão, and Leila A. C. Motta

The rapid growth of population, consumption, and economy stimulates the extraction of natural resources at an accelerated rate, directly impacting the environment by generating waste and CO_2 emissions, primarily in the civil construction industry. This research investigates the use of untreated tire waste rubber as a replacement for fine aggregate (sand) in geopolymer mortar, in response to environmental concerns from the civil construction industry. The study uses a central composite design (CCD) and response surface methodology (RSM) to optimize the modulus of rupture (MOR), modulus of elasticity (MOE), and toughness. With a global desirability of 0.73, the optimized values for these variables were 2.85 MPa, 676.3 MPa, and 0.331 kJ/m^2, respectively, with experimental errors below 10%. The results suggest that tire waste rubber can effectively replace fine aggregate in geopolymer mortar, potentially reducing environmental impact.

Keywords: central composite design (CCD); ecological composites; geopolymer mortar; metakaolin; tire rubber (TR).

INTRODUCTION

The rapid growth of urbanization, fueled by the rise in global population, has necessitated significant advancements in the construction industry, which in turn has brought about environmental challenges. Presently, there is a strong emphasis on seeking sustainable alternatives in material production to mitigate impacts and reduce CO_2 emissions within the construction industry.[1]

The process of cement production is widely recognized as one of the primary sources of pollution due to its greenhouse gas emissions, contributing to 5 to 8% of global CO_2 emissions,[2] with 667 kg of carbon dioxide still emitted per ton of cement.[3] Consequently, research has been focused on finding an alternative to cement. In this context, geopolymers have emerged as a highly promising solution,[4] given their ability to incorporate industrial by-products that contain aluminosilicate as the main component.[5]

Geopolymers are alkali-activated binders that are notable in civil construction due to their mechanical and thermal properties, low density, and impermeability. Their applications encompass concrete, mortar, coatings, bricks, and paving blocks. They are produced with aluminum and silica-based materials, such as fly ash and slag, and are activated by alkalis such as Na_2SiO_3 and NaOH. The formation process involves alumination and polycondensation reactions to yield aluminates and silicates.[1,5,6] Still, there are other combinations of alkaline solutions, such as potassium silicate and potassium hydroxide, that result in geopolymers with high compressive strength and low porosity.[7] Solid activators such as sodium silicate, calcium hydroxide, lithium hydroxide, and potassium carbonate can replace liquid alkaline solutions.[8] Using waste-derived activators such as rice husk ash (RHA)-derived sodium silicate can significantly reduce the environmental impact of geopolymers while maintaining comparable mechanical properties.[9] Industrial by-products such as disposed cleaning solutions from the aluminum industry can be used as effective activators, particularly for high-calcium precursors like blast-furnace slag.[10] According to the literature, the optimal combination of alkaline solutions for geopolymers involves using sodium silicate and sodium hydroxide in a specific ratio, with 2.5 being the most effective for achieving high compressive and tensile strength.[7]

The use of industrial by-products such as fly ash and metakaolin decreases costs and gas emissions associated with the production of portland cement.[4,5] The incorporation of waste materials, such as tire rubber (TR), into construction materials is essential for the recycling and preservation of natural resources, and is advocated as a strategy to lessen the environmental impact of improper rubber disposal.[5]

Used rubber tires, due to their non-biodegradable nature, pose serious environmental problems, generating substantial waste from the automotive industry.[4] The improper disposal of these tires leads to soil and air pollution due to the leaching of toxins and the emission of toxic chemicals and heavy metals.[6] The process of crushing and incorporating rubber particles into geopolymers presents a sustainable solution, contributing to environmental preservation and reducing the demand for natural resources in civil construction.[5,6] This is crucial, as the exploitation of natural aggregates can lead to alterations in river courses and a reduction in riverbed stability.[4]

TR can effectively replace traditional aggregates in concrete, offering benefits such as improved flexural and tensile strength, better workability, and enhanced durability. Incorporating TR into concrete generally reduces its compressive strength (especially when replacing coarse aggregates); however, rubberized concrete often shows improved flexural and tensile strength (enhancing its post-cracking behavior and energy absorption capacity). The inclusion of rubber particles decreases the modulus of elasticity (MOE) and increases the deformability of concrete,

ACI Materials Journal, V. 122, No. 3, May 2025.
MS No. M-2024-156.R2, doi: 10.14359/51746717, received February 26, 2025, and reviewed under Institute publication policies.

leading to higher lateral strain at crushing.[11-13] Rubberized concrete exhibits better water absorption and permeability characteristics (which can enhance its durability), and the addition of rubber particles generally improves the workability of concrete mixtures (making them easier to handle and place).[14,15] Waste TR granules contain significant amounts of carbon, zinc, magnesium, and calcium (which influence their interaction with the cement matrix), and rubber particles exhibit stable structures under thermal analysis (indicating their suitability for use in concrete under various temperature conditions).[16]

The construction sector consumes approximately 30% of the extracted natural resources, corresponding to 220 million tons of natural aggregates per year for concrete production, thus exhausting natural reserves in several locations. The commercial availability of TR waste as a substitute for sand in construction materials is gaining attention due to the diminishing availability of natural sand and the environmental issues associated with waste tire disposal, with approximately 3 billion tires commercially transacted and disposed of each year globally. The synthesis and use of TR for commercial use, particularly in large-scale construction, is a multifaceted topic encompassing the production of synthetic rubbers, recycling of waste TR, and the incorporation of rubber into construction materials. The addition of ground tire rubber (GTR) into asphalt has been performed for a very long time to improve the matrix's behavior under different conditions, and recent review articles provide a general overview of the available extensive literature on the subject.[17,18] The addition of rubber particles in concrete formulations is mainly to improve the durability of the matrix (as the particles are elastic and can easily deform under stress).[19,20] Early studies indicate that the effect of the GTR content (5 to 50%) on the mechanical properties (shear, triaxial, and so on) of different types of sand and their particle size distribution[21] achieves optimum performance with approximately 10% GTR content. GTR has also been used as a low-cost solution to stabilize soil for various geotechnical applications, modifying properties such as compression, creep, shear, permeability, and drainage (hydraulic properties).[22]

Additionally, TR is used in commercial products for construction applications, such as jogging paths, playgrounds, and tennis courts, along with other products related to the maintenance and operation of infrastructure, such as traffic-related products and highway crash barriers.[23] Studies have demonstrated that the incorporation of rubber in geopolymers can enhance cracking resistance, impact resistance, durability, energy absorption capacity under load, as well as thermal and acoustic properties.[24-26]

Central composite design (CCD) is a valuable statistical technique for optimizing processes, products, and formulations, facilitating the development of efficient methods for waste use. It enables the evaluation of the effects of independent variables on a response of interest and is characterized by a three-level experimental design, interaction effect analysis, time and cost savings, and robust statistical analysis.[27-29] CCD is an experimental design technique that employs a matrix of central and extreme points, as well as axial points, to investigate the relationship between independent variables and a dependent variable. Some of the key characteristics of CCD include three types of factors: fixed factors (+1 and –1), central factors (0), and axial factors ($+\alpha$, $-\alpha$), allowing for the evaluation of the linear effect of independent variables, nonlinear effects, and interactions. CCD can be configured with different alpha (α) values, depending on the objective of the experiment and the number of independent variables. The most common values for α are 1, 1.414, 1.68, and 2, which ensure varying levels of rotation and orthogonality of the matrix. CCD can be used to investigate the influence of up to k independent variables, where k is the number of columns in the experimental matrix, and the number of central points can also be adjusted to balance the precision of the experiment with resource efficiency.[30,31]

RESEARCH SIGNIFICANCE

This research holds significant value as it delves into the exploration and quantification of the potential of untreated coarse and fine waste rubber from tires, acting as substitutes for fine aggregate (sand) in geopolymer mortar samples across various curing periods. The study strategically used a CCD in tandem with the response surface methodology (RSM) technique and a desirability function. This was done to optimize crucial response variables, specifically the modulus of rupture (MOR), MOE, and toughness (T). The optimization process facilitated the accurate determination of the optimal content, particle size of waste TR, and curing durations for this specific type of metakaolin-based geopolymer mortar. Therefore, the importance of this research is underscored by its potential to transform the application of waste materials in the construction sector, thereby fostering sustainability and enhancing cost efficiency within the industry.

MATERIALS AND METHODS

Characteristics of materials

The metakaolin and its chemical composition were carried out according to Table 1. The material has an average particle diameter of 12.4 μm, exhibiting greater reactivity than the ground clinkers of national portland cement,[32,33] and a density of 2650 kg/m^3. The enhancement of the specific surface area of metakaolin contributes to an increase in the compressive strength of geopolymer paste.[34] The refinement of metakaolin was carried out according to the following steps: calcination, where the kaolin was calcined at a temperature of 750°C for 2 hours in rotary kilns and subsequently cooled, avoiding rehydration and the formation of agglomerates; then, the metakaolin was ground in ball mills, with a reduction in its particles and an increase in the surface area, and classified in vibrating screens. This process improved its solubility and reduced its degree of aggregation, leading to a more homogeneous distribution of the aluminate that reacts with the alkaline activator to form the geopolymer.[32,35-37] This process results in a quicker setting time, enhanced compressive strength, and a more uniform microstructure.

Medium river sand has a specific mass, maximum characteristic dimension, and fineness modulus of 2.657 g/cm^3, 2.36 mm, and 2.75, respectively.[38] The coarse and fine TR

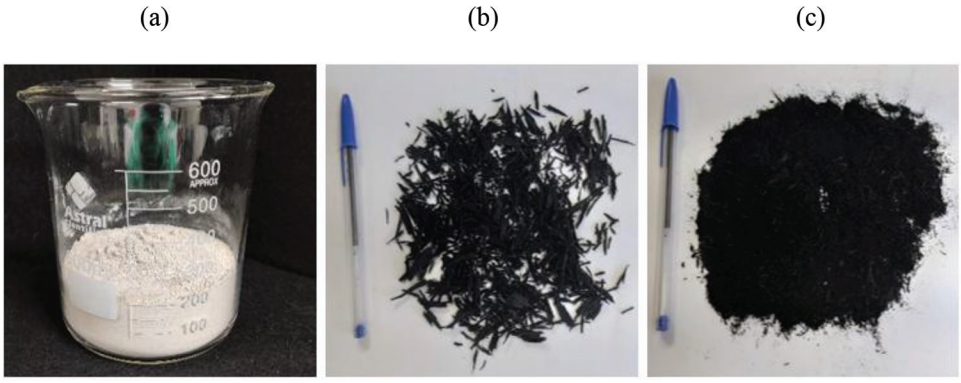

Fig. 1—Materials used in preparation of geopolymeric mortar: (a) metakaolin; and (b) and (c) coarse and fine tire rubber waste, respectively.

Table 1—Concentrations for oxides observed in metakaolin

Oxides	Concentrations, %
SiO_2	51.6
Al_2O_3	40.5
Fe_2O_3	2.8
K_2O	0.2
Na_2O_3	0.1

waste used is derived from the retreading of tires with an elongated shape, with a maximum characteristic dimension of 6.30 and 2.36 mm, respectively.[39] Sodium hydroxide (98.6% purity) and sodium silicate (SiO_2/Na_2O equal to 1.98) were purchased. Figure 1 illustrates metakaolin and the coarse and fine residues of used TR.

Design of experiments (DoE)

The CCD is a statistical approach widely used to formulate regression equations in multivariate nonlinear model contexts, allowing the analysis of variables and their interactions for process optimization. This method is structured by a cubic part, which includes factors with values of +1 and –1, central points, and extreme factors defined by $+\alpha$ and $-\alpha$ (+1.41421 and –1.41421). The CCD configuration is adaptable, depending on the type of α chosen (rotational or orthogonal), the number of independent variables (k), and the number of central points.

The response variables in this study were the MOR, MOE, and T of the geopolymer mortar samples. Comprehensive analyses were conducted using Statistica 7.0 software, with a significance level of 10% (p-value < 0.10) adopted for the analysis of regression parameters.[29,40,41] The minimum and maximum limits for each variable (TR, coarse rubber [CR], and curing time [CT]) were established based on the literature.[42,43]

Thus, Eq. (2) to (4) were generated from the coding of the dependent variables (TR, CR, and CT) and transformation into dimensionless form, considering the following general Eq. (1) in this type of statistical design

$$X_i = \left(\frac{E_i - E(0)}{\frac{E(1) - E(-1)}{2}} \right) \quad (1)$$

where X_i is the coded value assigned to each dependent variable; E_i is the value of the factor in the original scale; $E(0)$ is the central value chosen in the working limits (average between $E(1)$ and $E(-1)$); $E(1)$ is the penultimate highest value for the working limit; and $E(-1)$ is the penultimate lowest value for the working limit.

Table 2 presents the experimental levels of the various independent variables employed for the CCD, according to Eq. (2) to (4)

$$x_{TR} = \left(\frac{\%TR - 10.5}{6.72} \right) \quad (2)$$

$$x_{CR} = \left(\frac{\%CR - 50}{35.36} \right) \quad (3)$$

$$x_{CT} = \left(\frac{CT - 14.5}{9.55} \right) \quad (4)$$

where TR represents the percentage of replacement, by volume, of the fine aggregate (sand) with TR (ranging from 1 to 20%); CR is the percentage (by mass) of coarse rubber waste (the remainder is supplemented by fine rubber waste to total 100%—the variation from 0 to 100% of rubber is a variation of the sum of the percentages of coarse rubber waste and fine rubber waste in the composite); and CT is the curing time, which varies from 1 to 28 days, in accordance with standard civil engineering testing practices.

Regression equations influence input parameters by establishing significant statistical relationships with the response variable, quantifying individual effects through coefficients, identifying interactions between factors, and enabling the optimization of parameter levels. They also facilitate model validation by comparison with empirical data and enable simulations for scenario analysis, supporting informed decision-making.

Production, curing, and mechanical tests of geopolymer mortar samples

The geopolymer was synthesized based on the optimized parameters identified by da Silva Alves et al.,[29] using molar concentration of 12 M for sodium silicate and 15 M for sodium hydroxide, with the mass ratio between the first and second activators being 2.5. In addition, the NaSi/Met ratio (sum of the masses of sodium hydroxide and sodium silicate

Table 2—Experimental levels of different independent variables used for CCD

Parameters	Symbol		Coded levels				
	Decoded	Coded	–1.414	–1	0	1	1.414
Percentage of replacement of fine aggregate by tire rubber, %	TR	x_{TR}	1	3.78	10.5	17.22	20
Percentage (by mass) of coarse rubber waste (remainder is supplemented by fine rubber waste), %	CR	x_{CR}	0	14.64	50	85.36	100
Curing time, days	CT	x_{CT}	1	4.95	14.5	24.05	28

Table 3—Mixture proportioning of mortar

Metakaolin, g	Sand, g	NaOH, g	H_2O for NaOH, g	Na_2SiO_3, g	H_2O for Na_2SiO_3, g	H_2O for workability, g
266.66	533.34	45.42	75.68	113.54	77.52	6.80

Note: Metakaolin-sand ratio: 1:2; fixed proportion of H_2O/metakaolin (*H*/*M*): 0.60; NaOH (15 M); Na_2SiO_3 (12 M).

divided by the mass of metakaolin) has a fixed value of 0.597. The geopolymer mortar was prepared by combining the alkaline activator solution (comprising sodium hydroxide and sodium silicate), metakaolin, sand, and the necessary water to ensure workability of the resulting composite. According to Table 3 (mixture proportioning of mortar), the water-metakaolin ratio was established at 0.60. This ratio encompasses the total mass of water used for preparing the 15 M NaOH and 12 M Na_2SiO_3 solutions, along with the additional water needed for workability, all divided by the mass of metakaolin (Eq. 5).

$$H/M = \frac{\sum(\text{water mass for preparing NaOH and } Na_2SiO_3 \text{ solutions and water for workability})}{\text{Metakaolin mass}} \quad (5)$$

The mass of metakaolin is determined based on a 1:2 metakaolin-sand ratio. The actual water content required for each mixture was calculated using both the water-metakaolin ratio and the metakaolin-sand ratio for each experiment. A total of 18 mixtures (E1 to E18) were prepared, with six specimens produced for each experiment, resulting in a total of 108 specimens.

This mixture was homogenized for 5 minutes at medium speed in an industrial planetary mixer. Six prismatic specimens, each measuring 4 x 4 x 16 cm, were cast, following the guidelines of NBR 13276.[44] The setting time of the mixture was influenced by the ambient curing conditions adopted during the process. Specifically, the geopolymer mortar exhibited a workable consistency suitable for handling, and the initial setting time was approximately 24 hours.[45] These specimens were used to determine the MOR, MOE, and T, according to NBR 13279.[46] The samples were wrapped in plastic film and stored at a room temperature of 25 ± 5°C for the duration of the curing period. In accordance with NBR 13279[46] and RILEM,[47] measurements of the MOR, MOE, and T were conducted using a universal testing machine equipped with a 5 kN load cell.

Characterizations—X-ray diffraction and scanning electron microscopy analysis

X-ray diffraction (XRD) analysis was conducted using lab equipment. The equipment operated at 40 kV and 30 mA with a CuKα radiation source (1.5406 Å), a scanning range of 2θ = 5 to 90 degrees, a scanning speed of 2 deg/min, and a step of 0.02 degrees. Following the flexural strength tests, samples for scanning electron microscopy (SEM) analysis were collected. These samples, approximately 1 cm^3, were placed in an oven at 50 ± 1°C for 24 hours. The SEM analysis was performed using a high-resolution system equipped with a Vega-type imaging module. The geopolymer mortar samples were ground into a powder and subsequently sieved through a 75 μm mesh to obtain a fine powder.

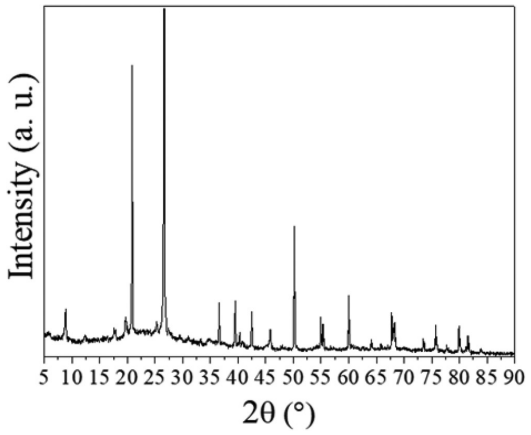

Fig. 2—XRD patterns of metakaolin.

DISCUSSIONS OF RESULTS

Characterization of metakaolin—XRD

The diffractogram of metakaolin revealed an amorphous aluminosilicate halo, exhibiting high reactivity within the 2θ range of 15 and 38 degrees (Fig. 2). Quartz (SiO_2) was identified as the dominant mineral phase, with its characteristic diffraction peaks aligning at 2θ values of 20.62, 26.64, 36.51, 42.37, 50.27, 54.94, 59.97, 67.72, and 73.16 degrees (ICSD-27745).[29,32,48] The diffractogram revealed significant contributions from quartz, alumina, and hematite, which collectively constituted 94.87% of the total elements present. Aluminum oxide (Al_2O_3) exhibited diffraction peaks at 2θ values of 25.33, 35.23, 37.67, and 68.17 degrees (ICSD-68591), while hematite (Fe_2O_3) displayed peaks at 24.16, 50.12, 64.02, and 75.58 degrees (ICSD-56372). Minor peaks at 2θ values of 8.80, 17.67, and 19.64 degrees suggested the

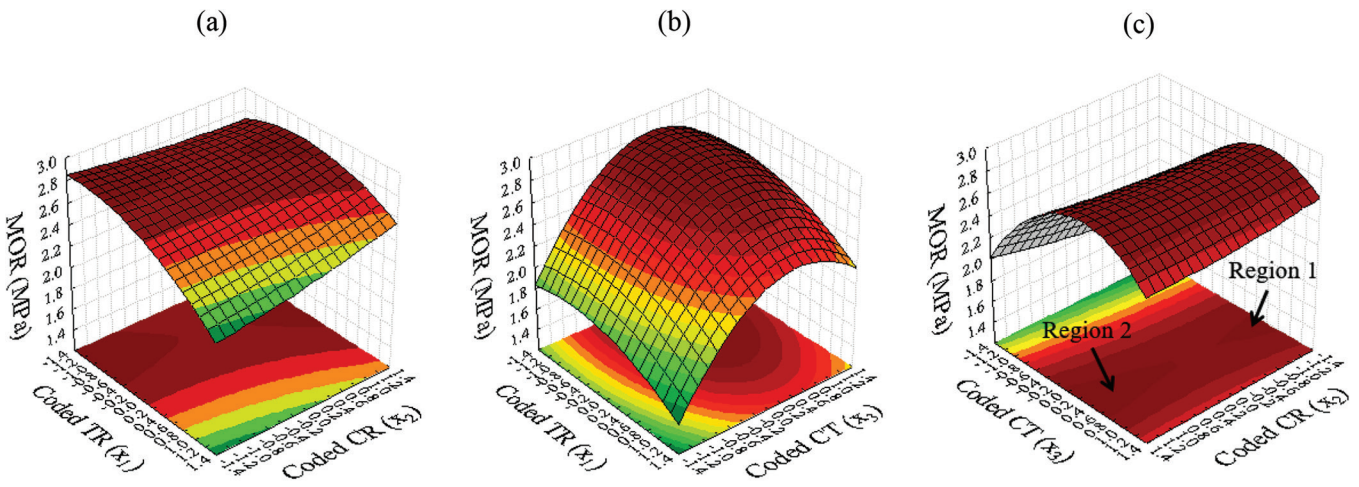

Fig. 3—Response surface for MOR: (a) CT at central level (x_{CT} = 0); (b) CR at central level (x_{CR} = 0); and (c) TR at central level (x_{TR} = 0).

potential presence of kaolinite ($Si_2Al_2O_5(OH)_4$). The oxides of potassium (K_2O) and sodium (Na_2O) exerted minimal influence on the diffractogram.[49]

Design of experiments—statistical analysis

Table 4 shows the values of the response variables (MOR, MOE, and T) from the 18 experiments of the CCD. A multiple regression analysis was carried out with a significance level of 10% (p-value < 0.10).

Modulus of rupture—Equation (6) represents the MOR model, with coded factors

$$MOR = 2.74 - 0.14x_{TR} - 0.1x_{TR}^2 + 0.033x_{CR} + 0.016x_{CR}^2 + 0.25x_{CT} - 0.28x_{CT}^2 + 0.06x_{TR}x_{CR} - 0.01x_{TR}x_{CT} - 0.05x_{CR}x_{CT} \quad (6)$$

Equation (6) yielded a coefficient of determination (R^2) of 0.63. The data variability can be attributed to various external factors that likely varied with each molding process, such as the positioning of coarse and fine TR particles, which exhibited a fibrous aspect. The orientation of the TR fibers directly impacts the MOR. If the fibers are oriented perpendicular to the crack, they can aid in stress resistance by acting as a bridge between the cracks, thereby increasing the MOR value.[50] Conversely, if the fibers are oriented parallel to the crack, they do not contribute to stress resistance and may even reduce the MOR. Given that the positioning of TR within the die is random, its MOR can fluctuate with each molding.

According to Fig. 3(a), the highest MOR value was observed when the percentage of TR (x_{TR}) used was 1% (–1.414 coded) and the percentage of coarse rubber (x_{CR}) was 0% (–1.414 coded), yielding a result of approximately 2.85 MPa. Consequently, the smaller the replacement of fine aggregate (sand) by TR and the corresponding insertion of coarse rubber, the higher the MOR value. When comparing the highest MOR value obtained on the response surface with the best results shown in Table 4 (3.08 and 3.15 MPa for E9 and E12, respectively), it was observed that the most suitable combination among the independent variables was that of E12. This combination resulted in an increase in the replacement of fine aggregate (sand) by TR by 950% (from 1 to 10.50%), an increase in the percentage of coarse rubber, and a corresponding increase in MOR of 10.53% (from 2.85 to 3.15 MPa) at the same curing times of 14.5 days.

Furthermore, upon analyzing Eq. (6), a greater negative contribution of the variable x_{TR} was observed because its linear and quadratic coefficients are greater than the positive coefficients of the variable x_{CR}. According to the analysis of variance, the p-values for the linear (p-value = 0.210561) and quadratic (p-value = 0.469497) variable x_{TR} are closer to 0.10 (p-value < 0.10) than the p-values for the linear (p-value = 0.754282) and quadratic (p-value = 0.906525) variable x_{CR}. This fact confirms what can be observed by analyzing the response surface (Fig. 3(a)). According to Fig. 3(b), a value of 2.85 MPa was observed as the maximum point for the MOR. This value corresponds to a combination of 5.13% (–0.8 coded) for the x_{TR} variable and 19.27 days (+0.5) for the x_{CT} variable.

Analyzing the results observed in Table 4 and the optimal point observed on the response surface, E12 presented the best fits for the MOR response. The percentage of replacement of fine aggregate (sand) by TR increased by approximately 104.68% (from 5.13 to 10.50), as well as the percentage of coarse rubber (50 to 100%), and verified a decrease in curing time from 19.27 to 14.5 days, optimizing the response variable (MOR).

The response surface presented in Fig. 3(c) indicates that the percentage of coarse rubber (x_{CR}) has minimal impact on the MOR response. Two regions of peak points (saddle points) were identified, both corresponding to a curing time (x_{CT}) of 18.32 days (+0.4 coded). These peaks occurred at coarse rubber percentage (x_{CR}) values of 0% (–1.414 coded) and 100% (+1.414 coded), resulting in an MOR value of approximately 2.85 MPa. This MOR value was also consistent with the analyses shown in Fig. 3(a) and (b). The ideal conditions for achieving the highest MOR of 3.15 MPa were found in E12, which involved reducing the curing time by 20.85% (from 18.32 to 14.50 days).

The general analysis of the response surfaces showed that the linear variable percentage of coarse rubber (x_{CR}), as explained earlier, was not significant (p-value = 0.754282).

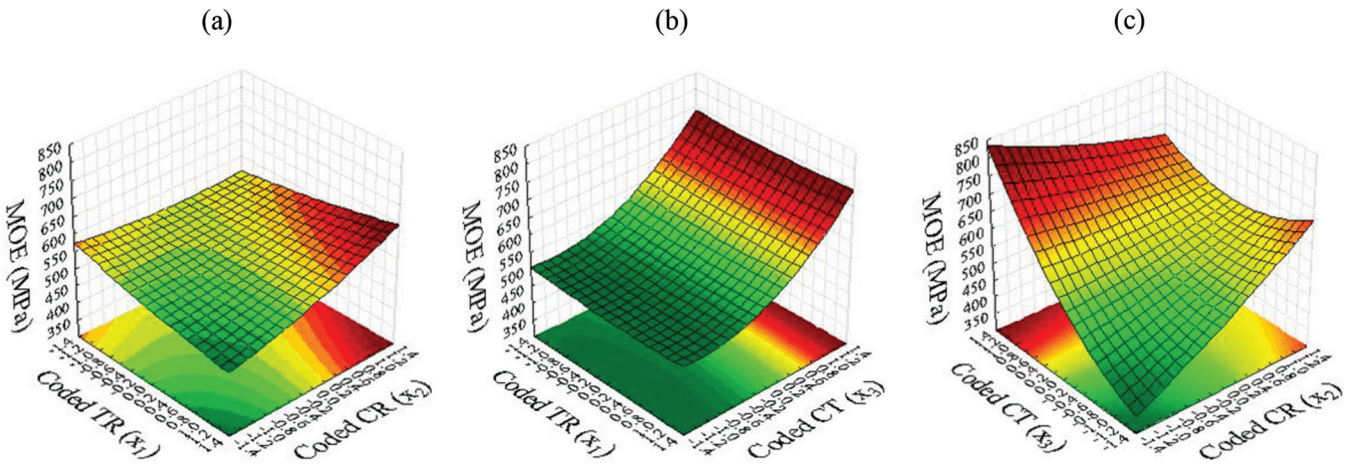

Fig. 4—Response surface for MOE: (a) CT at central level (x_{CT} = 0); (b) CR at central level (x_{CR} = 0); and (c) TR at central level (x_{TR} = 0).

This fact probably occurred due to its high elasticity, causing the rubber particles to deform more than the matrix during compression, leading to the concentration of internal stresses.[24,51-53]

The simultaneous effects of coarse rubber (x_{CR}) and tire rubber (x_{TR}) on the MOR values were contrasting; specifically, coarse rubber had a minimal influence while TR had a negative effect. The addition of TR introduced air into the composite, decreasing its specific mass. Furthermore, the presence of TR and sand created a physical barrier that inhibited the interaction between metakaolin particles and the alkaline activating solution, thereby slowing down the geopolymerization process. This interference resulted in a limited improvement in the mechanical strength of the geopolymeric mortar containing TR.[54-56]

As curing progressed, the geopolymerization process continued, leading to an overall increase in the average strength of the geopolymers. However, during curing, free water in the geopolymer evaporated, creating numerous intergranular pores within the structure. These pores contributed to a decrease in the mechanical strength of the geopolymeric mortar, ultimately lowering the MOR, as shown in Fig. 3(a) and (b).

In their research on geopolymer mortars, Pouhet et al.[57] affirmed that the total pore volume of the geopolymer is directly proportional to the initial volume of water added to the mixture. This relationship allows for the final pore volume and the average diameter of the mesoporosity to be predicted accurately.

Modulus of elasticity—Equation (7), with an R^2 of 0.75, represents the MOE model with coded factors

$$\text{MOE} = 541 - 0.76x_{TR} + 4.35x_{TR}^2 + 26.2x_{CR} + 7.7x_{CR}^2 + 85.5x_{CT} + 36.5x_{CT}^2 + 22.8x_{TR}x_{CR} + 1.9x_{TR}x_{CT} - 61.2x_{CR}x_{CT} \quad (7)$$

According to Fig. 4(a), the peak value of the MOE was noted when the rubber percentage (x_{TR}) used was 20% (+1.414 coded), and the coarse rubber percentage (x_{CR}) was at its maximum of 100% (+1.414 coded). This resulted in an approximate MOE of 650 MPa. It was discerned that the variables x_{TR} and x_{CR} had a subtle influence on the MOE response.

The coefficients for both the linear and quadratic x_{CR} variables were positive, leading to an increase in the MOE values. Moreover, the coefficients of the linear and quadratic x_{CR} variables were 34.34 and 1.77 times larger than those of the linear and quadratic x_{TR} variables, respectively. This indicates that the x_{CR} variable exerted a more substantial influence on the MOE than the x_{TR} variable. Upon examining Fig. 4(b), it was found that only the curing time (x_{CT}) had an impact on the MOE. Additionally, irrespective of the rubber percentage value (x_{TR}), there exists a region of minimum cure times (x_{CT}) ranging from 1 to 6.86 days (−1.414 to −0.8 coded), with an approximate value of 500 MPa. The maximum MOE value was noted when the cure time (x_{CT}) was 28 days (+1.414 coded), regardless of the x_{TR} value, yielding an approximate result of 750 MPa.

In Fig. 4(c), the peak value of the MOE was observed when the percentage of coarse rubber (x_{CR}) used was 0% (–1.414 coded) and the curing time (x_{CT}) was 28 days (+1.414 coded), yielding a result of approximately 830 MPa. Additionally, it was noted that for a percentage of coarse rubber (x_{CR}) of 100% and a curing time (x_{CT}) of 1 day, the MOE value was approximately 668 MPa.

Upon analyzing the experimental values (Table 4) and the points observed on the response surface, it is suggested to adopt the point on the response surface with 1 day of curing, which corresponds to an MOE value of 668 MPa. When sand is replaced by small rubber particles in the composite, there is a decrease in the MOE, which can possibly be explained by the physical and mechanical properties of rubber as compared to sand.[42,53] According to Muhammad et al.,[58] the MOE for TR fiber ranges from 0.0007 to 0.004 GPa, while for sand, it varies between 20 and 100 GPa.

Arunkumar et al.[59] noted a 10.62% increase in the MOE with the addition of 1% fiber from waste derived from the rubber latex industry, after a curing period of 90 days. The fiber had a length of 2 cm and a diameter of 0.3 mm. As the proportion of rubber fiber in geopolymer concrete increased, a decrease in the MOE value was observed. In general, the percentage of rubber (x_{TR}) had minimal influence on the

Table 4—CCD matrix with coded and uncoded values of parameters and obtained reponses at ages to 28 days

	Coded			Decoded			Response variables		
E	x_{TR}	x_{CR}	x_{CT}	TR, %	CR, %	CT, days	MOR, MPa	MOE, MPa	T, kJ/m^2
1	–1	–1	–1	3.78	14.64	4.95	2.2	454.39	0.13
2	–1	–1	1	3.78	14.64	24.05	2.6	744.26	0.11
3	–1	1	–1	3.78	85.36	4.95	2.11	615.07	0.17
4	–1	1	1	3.78	85.36	24.05	2.54	567.21	0.21
5	1	–1	–1	17.22	14.64	4.95	1.73	441.23	0.21
6	1	–1	1	17.22	14.64	24.05	2.31	645.7	0.17
7	1	1	–1	17.22	85.36	4.95	2.10	599.97	0.35
8	1	1	1	17.22	85.36	24.05	2.27	652.81	0.30
9	–1.414	0	0	1	50	14.5	3.08	536.87	0.19
10	1.414	0	0	20	50	14.5	2.62	559.54	0.35
11	0	–1.414	0	10.5	0	14.5	3	496.51	0.26
12	0	1.414	0	10.5	100	14.5	3.15	613.24	0.33
13	0	0	–1.414	10.5	50	1	1.98	426.35	0.22
14	0	0	1.414	10.5	50	28	2.99	798.52	0.18
15	0	0	0	10.5	50	14.5	2.83	451.7	0.29
16	0	0	0	10.5	50	14.5	2.38	482.39	0.26
17	0	0	0	10.5	50	14.5	2.49	559.29	0.22
18	0	0	0	10.5	50	14.5	2.67	672.98	0.24

Note: E is experiments.

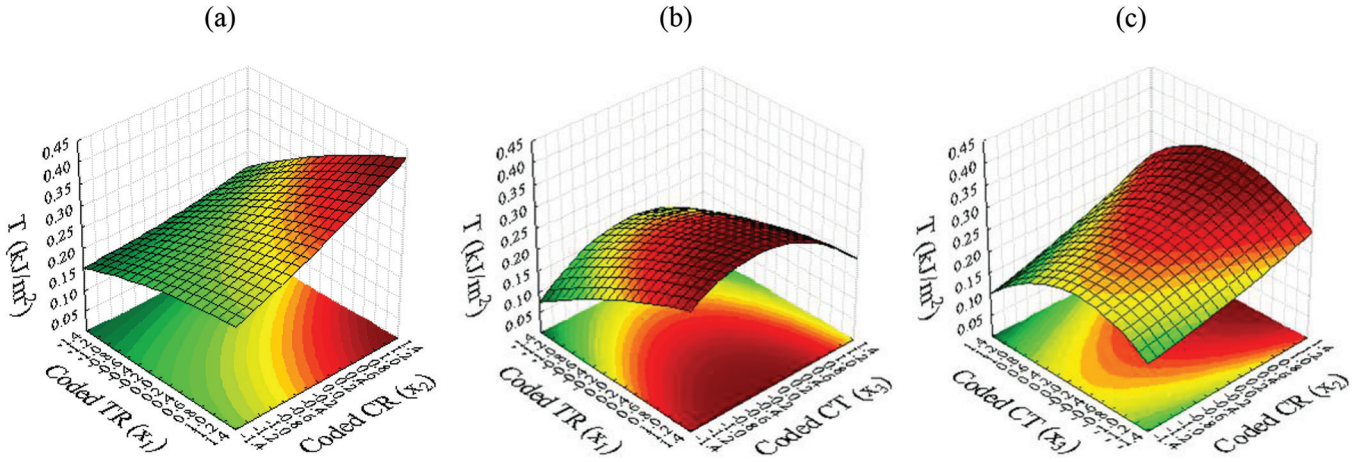

Fig. 5—Response surface for toughness (T): (a) CT at central level (x_{CT} = 0); (b) CR at central level (x_{CR} = 0); and (c) TR at central level (x_{TR} = 0).

MOE. However, the percentage of coarse rubber (x_{CR}) had the most significant impact, particularly in conjunction with the curing time (x_{CT}). This is because the rubber residue increases the content of trapped air.[51] This incorporation is further enhanced by the reduction of rubber particles and the increase in the volume of rubber incorporated into the composite.[60]

Toughness—Equation (8), with an R^2 of 0.89, represents the T model with coded factors

$$T = 0.26 + 0.053x_{TR} - 0.008x_{TR}^2 + 0.042x_{CR} + 0.005x_{CR}^2 - 0.01x_{CT} - 0.043x_{CT}^2 + 0.02x_{TR}x_{CR} - 0.014x_{TR}x_{CT} + 0.06x_{CR}x_{CT} \quad (8)$$

Figure 5 shows the response surfaces for toughness according to the independent variables. The highest T value was observed when the percentage of rubber (x_{TR}) used was 20% (+1.414 coded) and the percentage of coarse rubber (x_{CR}) was 100% (+1.414 coded), resulting in approximately 0.43 kJ/m^2 (Fig. 5(a)). The lowest T value (0.15 kJ/m^2) was obtained at the lowest extremes for both the rubber percentage (x_{TR}) and coarse rubber (x_{CR}) variables. Upon

analyzing the experiments and the point observed on the response surface, E7 demonstrated a superior combination of variables, despite an 18.6% reduction in toughness (from 0.43 to 0.35), a 13.90% reduction in the percentage of rubber (from 20 to 17.22%), and a 14.64% reduction in the percentage of coarse rubber (from 100 to 85.36%). In this experiment, the curing time was reduced by 65.51% (from 14.50 to 5 days). The highest tenacity value, being a maximum point, was observed when the percentage of rubber (x_{TR}) used was 20% (+1.414 coded) and the curing time (x_{CT}) was 10.68 days (–0.4 coded), resulting in approximately 0.33 kJ/m^2 (Fig. 5(b)).

Comparing with the values in Table 4, as well as in the analysis of Fig. 5(a), E7 presented the best relationship between the studied variables. Even with a 13.90% reduction in the percentage of rubber (from 20 to 17.22%), there was a 70.72% increase in the percentage of coarse rubber (from 50 to 85.36%), a 6.69% increase in toughness (from 0.33 to 0.35), and a substantial decrease in the cure time by 53.18% (from 10.68 to 5 days). This behavior was also observed when analyzing the x_{TR} at the central point (10.5% [Fig. 5(c)]).

The increase in toughness with the rising percentage of rubber (x_{TR}) likely occurred due to the low rigidity of the rubber particles, which enhanced the flexibility of the rubber-binder composite and the energy absorption of the mixture.[25] The introduction of fibers (coarse rubbers—x_{CR}) can alter the brittle behavior of the geopolymer to a ductile one. This is explained by the action of the fibers, which increase the resistance to cracking of brittle matrixes, primarily through the bridge mechanism, thereby enhancing energy absorption through post-crack toughness.[2,61] In terms of the significant variable x_{CT}, an increase in the toughness value was observed at early ages, followed by a decrease at later ages. This behavior can be attributed to the increase in resistance with the age of the geopolymers,[62] thereby boosting the composite's capacity to absorb energy.[56]

Desirability function and optimization analysis

Based on the simultaneous optimization of the studied responses, the global desirability (D) was found to be 0.73, with predicted values of 15.25% for TR (x_{TR} = 0.707), 100% for CR (x_{CR} = 1.414), and 21.25 days for CT (x_{CT} = 0.707). The optimized values derived from the combination of variables were 2.72 MPa, 636.2 MPa, and 0.352 kJ/m^2 for MOR, MOE, and T, respectively. The experimental validation of the models for each response variable was carried out using the values obtained from simultaneous optimization (desirability function). According to Table 5, the experimental results validated the statistical models of MOR, MOE, and T, with an experimental error of less than 10%.

Table 5—Validation of models for optimized predicted values

Response	MOR, MPa	MOE, MPa	T, kJ/m^2
Predicted	2.72	636.2	0.352
Experimental	2.85	676.3	0.331
Error, %	4.77	6.30	5.96

Characterization of geopolymer mortars

X-ray diffraction analysis (XRD)—The diffractograms from the 18 geopolymer mortar experiments involving TR waste are included in the Appendix. The main mineral phase observed in the diffractograms of the geopolymer and metakaolin samples is SiO_2 (quartz), with 2θ diffraction peaks coinciding at 20.87, 26.64, 36.36, 41.84, 50.27, 54.94, 59.97, and 67.72 degrees (ICSD-27745). Alumina (Al_2O_3) exhibited 2θ diffraction peaks at 25.44, 35.23, 37.67, and 68.17 degrees (ICSD-68591), and hematite (Fe_2O_3) at 24.16, 49.36, 64.02, and 75.58 degrees (ICSD-56372). Peaks for potassium oxide (K_2O) (23.88, 27.54, and 39.44 degrees—ICSD-6048) and sodium oxide (Na_2O) (45.99 degrees—ICSD-60435) were also observed. The unreacted crystalline phases of metakaolin were present in the geopolymers, as indicated by coinciding peaks.[63,64] Quartz diffraction peaks were observed even after geopolymerization, possibly due to the presence of sand in the geopolymer mortar.[65] These unreacted crystals acted as fillers,[66] potentially filling the voids in the geopolymer microstructure and thereby increasing the density and strength of the matrix. The diffractograms of the 18 experiments showed no significant differences, despite variations in formulations and curing times. The amorphous gel that forms during geopolymerization is essential for the performance of the synthesized geopolymers. It originates from the reaction between metakaolin and alkaline activators, such as NaOH and Na_2SiO_3. When metakaolin is mixed with these solutions, hydroxide ions promote the dissolution of the components, releasing silicon and aluminum. Subsequently, condensation occurs, where these elements reorganize to form a three-dimensional network that results in an amorphous gel. This gel acts as a binder, uniting the metakaolin particles and aggregates, thereby improving the cohesion and structural integrity of the material. Additionally, the gel fills the voids between the particles, reducing porosity and increasing the density and compressive strength of the geopolymer.

The authors suggested that the presence of an amorphous gel phase could play a crucial role in the mechanical properties of geopolymers based on alkali-activated metakaolin, and the presence of the amorphous halo might be overshadowed by the prominent peak of quartz.[67,68] The amorphous gel that forms during geopolymerization is essential for the performance of the synthesized geopolymers. It originates from the reaction between metakaolin and alkaline activators, such as NaOH and Na_2SiO_3. When metakaolin is mixed with these solutions, hydroxide ions promote the dissolution of the components, releasing silicon and aluminum. Subsequently, condensation occurs, where these elements reorganize to form a three-dimensional network that results in an amorphous gel. This gel acts as a binder, uniting the metakaolin particles and aggregates, thereby improving the cohesion and structural integrity of the material. Additionally, the gel fills the voids between the particles, reducing porosity and increasing the density and compressive strength of the geopolymer. The amorphous structure of the gel allows for a uniform stress distribution, contributing to the mechanical strength and hardness of the final product.[69,70] Another

important characteristic of the amorphous gel is its durability. The gel may continue to react with unreacted components over time, resulting in a gradual increase in mechanical strength, making geopolymers even more effective in various applications.[71,72]

Scanning electron microscopy (SEM)—The incorporation of waste TR into geopolymer mortar changed the fracture behavior from brittle to ductile, thereby preventing a complete rupture of the specimen.[61] A force applied to cause rupture separated the TR fibers, which was then followed by an SEM analysis of the fracture surface. The interaction between the matrix and the fiber may have sustained damage during this process.[73] Figure 6 illustrates the adhesion between the geopolymer matrix and the rubber fiber, as well as the formation of cracks caused by rupture.

In the formulation of composites and mortars, the geopolymeric matrix exhibits strong adhesion to aggregates and reinforcements, as supported by numerous studies. Various methods have been employed to enhance compatibility between different types of rubber and matrixes. These include mechanical, chemical, and thermal treatments, as well as the use of alkaline activating solutions.[42,74-77] This is applicable even in the absence of chemical pretreatment of the rubber, suggesting that these solutions can enhance the adhesion between the matrix and the rubber.

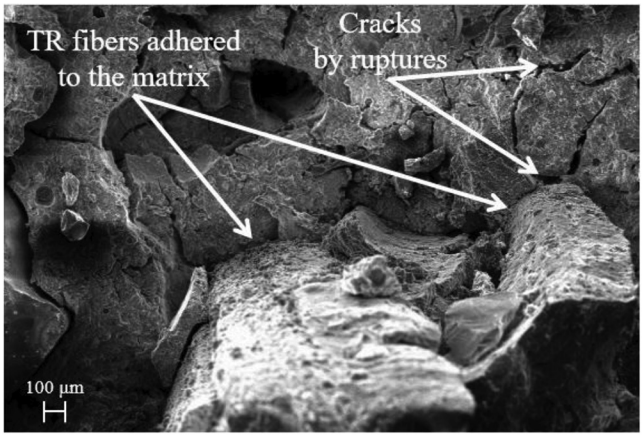

Fig. 6—SEM of ruptured section of experiment 15 (E15): adhesion of geopolymer matrix with tire rubber fibers and crack formation by rupture.

The substitution of fine aggregate with TR in the geopolymeric matrix resulted in an increase in the porosity of the specimens. The porosity was higher with higher levels of substitution by fine rubber (Fig. 7(a)—E6: 85.36% fine rubber), but lower with lower substitutions (Fig. 7(b)—E7: 14.64% fine rubber). The hydrophobic properties of TR particles, particularly when mixed with water, can lead to the presence of air bubbles and an increase in voids within the specimens. This is especially true in instances where the particle sizes are smaller and the volumes of addition are higher.[78] Matrix E6, which contained a higher content of TR in the geopolymer, exhibited fewer cracks. This reduction in cracking is potentially attributable to the higher TR content,[25] despite an increase in the number of voids (porosity). Despite the increase in porosity linked to the higher TR content, the strength parameters of matrix E6—specifically, the MOR at 2.31 MPa, MOE at 645.7 MPa, and T at 0.17 kJ/m^2—demonstrate that the material retains acceptable mechanical performance. The addition of rubber likely enhances stress distribution and ductility, allowing the geopolymer matrix to absorb and dissipate energy effectively without significant crack development. A longer curing period may have positively influenced the geopolymerization process, facilitating the formation of a more robust and cohesive network. This additional time may have allowed for more complete chemical reactions, resulting in a matrix that, while exhibiting increased porosity, maintains solid mechanical properties. Thus, the combination of higher TR content, an appropriate curing duration, and the beneficial properties of the rubber collectively enhance the crack resistance of the geopolymer matrix.

SUMMARY AND CONCLUSIONS

The main research findings are as follows:

- According to X-ray diffraction analysis, the samples from all 18 experiments exhibited no significant differences in chemical composition, with quartz (SiO_2) being the primary mineral phase of metakaolin.
- Samples with higher concentrations of coarse rubber displayed a reduced quantity of pores and a more compact matrix, without significant fissures.

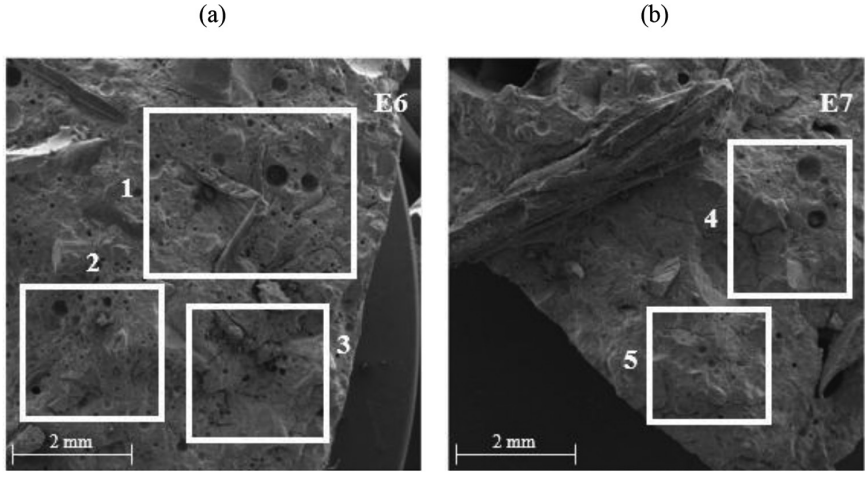

Fig. 7—SEM of ruptured section of experiments E6 and E7: (a) E6 (many pores and few fissures); and (b) E7 (few pores).

- Based on an overall desirability of 0.73, the optimized values of the combination of the tire rubber (TR), coarse rubber (CR), and curing time (CT) variables for the geopolymer composite were 2.72 MPa for modulus of rupture (MOR), 636.2 MPa for modulus of elasticity (MOE), and 0.352 kJ/m^2 for toughness (T).
- The optimized values for MOR, MOE, and T were validated experimentally, showing an error of less than 10%, thus confirming the accuracy of the statistical models used.
- The incorporation of TR can contribute to achieving desirable characteristics, such as reduced density and a more compact matrix. This also highlights the substitution of non-renewable natural resources with high-volume waste materials, which have a significant environmental impact.

AUTHOR BIOS

Rondinele Alberto dos Reis Ferreira *has been working in the area of microstructural characterization and applied statistics since 2012. He received his MS and his PhD in chemical engineering from the Federal University of Uberlândia, Uberlândia, Brazil, in 2012 and 2016, respectively. His research interests include process optimization, microstructural characterization of materials, and development of materials for heterogeneous catalysis.*

Cristiane Pires *is a PhD Student at the Federal University of Uberlândia. She has been working in the area of thermomechanical treatment of fibers and insertion into cementitious matrix composites since 2015. She received her MS in civil engineering from the Federal University of Uberlândia in 2017. Her research interests include process optimization, waste reuse, and microstructural characterization of materials.*

Leonardo Santos Gratão *is a Professor at Faculdade Mais de Ituiutaba, Ituiutaba, Brazil, and a Civil Engineer working in the supervision and monitoring of outsourced works in Ituiutaba, Brazil. He received his BS from the University of Brasília, Brasília, Brazil, in 2009; his postgraduate MBA in project management from Fundação Getulio Vargas (FGV), Rio de Janeiro, Brazil, in 2018; and his master's in civil engineering from the Federal University of Uberlândia in 2021.*

Leila Aparecida de Castro Motta *is an Associate Professor at the Federal University of Uberlândia. She received her BS from the Federal University of Uberlândia in 1994; her master's from the University of São Paulo São Carlos School of Engineering, São Paulo, Brazil, in 1997; and her PhD in civil engineering from the Polytechnic School of the University of São Paulo in 2006. Her research interests include construction materials and components, and the use of waste.*

ACKNOWLEDGMENTS

The authors would like to acknowledge CNPq, CAPES, and FAPEMIG for supporting this work and Metacaulim do Brasil Indústria e Comércio Ltda. for the metakaolin donation.

REFERENCES

1. Öz, A.; Bayrak, B.; Kaplan, G.; and Cüneyt Aydın, A., "Effect of Waste Colemanite and PVA Fibers on GBFS-Metakaolin Based High Early Strength Geopolymer Composites (HESGC): Mechanical, Microstructure and Carbon Footprint Characteristics," *Construction and Building Materials*, V. 377, May 2023, p. 131064. doi: 10.1016/j.conbuildmat.2023.131064

2. Harmal, A.; Khouchani, O.; El-Korchi, T.; Tao, M.; and Walker, H. W., "Bioinspired Brick-and-Mortar Geopolymer Composites with Ultra-High Toughness," *Cement and Concrete Composites*, V. 137, Mar. 2023, p. 104944. doi: 10.1016/j.cemconcomp.2023.104944

3. Guo, Y.; Luo, L.; Liu, T.; Hao, L.; Li, Y.; Liu, P.; and Zhu, T., "A Review of Low-Carbon Technologies and Projects for the Global Cement Industry," *Journal of Environmental Sciences*, V. 136, 2024, pp. 682-697. doi: 10.1016/j.jes.2023.01.021

4. Yeluri, S. C.; Singh, K.; Ramesh Babu, T. S.; and Garikapati, D., "Durability Properties of Rubber Aggregates Based Geopolymer Concrete—A Review," *Materials Today: Proceedings*, V. 93, 2023, pp. 2214-7853. doi: 10.1016/j.matpr.2023.07.264

5. Iqbal, H. W.; Hamcumpai, K.; Nuaklong, P.; Jongvivatsakul, P.; Likitlersuang, S.; Chintanapakdee, C.; and Wijeyewickrema, A. C., "Effect of Graphene Nanoplatelets on Engineering Properties of Fly Ash-Based Geopolymer Concrete Containing Crumb Rubber and Its Optimization Using Response Surface Methodology," *Journal of Building Engineering*, V. 75, Sept. 2023, p. 107024. doi: 10.1016/j.jobe.2023.107024

6. Shanmugam, R.; Sowmiya, S.; Dinesh, V.; Venkatramana, N.; and Naveen, S., "A Study on Eco-Friendly Composite Blocks Incorporating Scrap Tyre Rubber and Steel Slag as Coarse Aggregate with Sisal Fiber," *Materials Today: Proceedings*, 2023. doi: 10.1016/j.matpr.2023.05.234

7. Rocha, T. S.; Dias, D. P.; França, F. C. C.; Guerra, R. R. S.; and Marques, L. R. C. O., "Metakaolin-Based Geopolymer Mortars with Different Alkaline Activators (Na^+ and K^+)," *Construction and Building Materials*, V. 178, July 2018, pp. 453-461. doi: 10.1016/j.conbuildmat.2018.05.172

8. Askarian, M.; Tao, Z.; Samali, B.; Adam, G.; and Shuaibu, R., "Mix Composition and Characterisation of One-Part Geopolymers with Different Activators," *Construction and Building Materials*, V. 225, Nov. 2019, pp. 526-537. doi: 10.1016/j.conbuildmat.2019.07.083

9. Passuello, A.; Rodríguez, E. D.; Hirt, E.; Longhi, M.; Bernal, S. A.; Provis, J. L.; and Kirchheim, A. P., "Evaluation of the Potential Improvement in the Environmental Footprint of Geopolymers Using Waste-Derived Activators," *Journal of Cleaner Production*, V. 166, Nov. 2017, pp. 680-689. doi: 10.1016/j.jclepro.2017.08.007

10. Garcia Lodeiro, I.Cristelo, N.; Palomo, A.; and Fernández-Jiménez, A., "Use of Industrial By-Products as Alkaline Cement Activators," *Construction and Building Materials*, V. 253, Aug. 2020, p. 119000. doi: 10.1016/j.conbuildmat.2020.119000

11. Alaloul, W. S.; Musarat, M. A.; A Tayeh, B.; Sivalingam, S.; Rosli, M. F. B.; Haruna, S.; and Khan, M. I., "Mechanical and Deformation Properties of Rubberized Engineered Cementitious Composite (ECC)," *Case Studies in Construction Materials*, V. 13, Dec. 2020, p. e00385. doi: 10.1016/j.cscm.2020.e00385

12. Bompa, D. V.; Elghazouli, A. Y.; Xu, B.; Stafford, P. J.; and Ruiz-Teran, A. M., "Experimental Assessment and Constitutive Modelling of Rubberised Concrete Materials," *Construction and Building Materials*, V. 137, Apr. 2017, pp. 246-260. doi: 10.1016/j.conbuildmat.2017.01.086

13. Sofi, A., "Effect of Waste Tyre Rubber on Mechanical and Durability Properties of Concrete – A Review," *Ain Shams Engineering Journal*, V. 9, Dec. 2018, pp. 2691-2700. doi: 10.1016/j.asej.2017.08.007

14. Sambucci, M.; Marini, D.; and Valente, M., "Tire Recycled Rubber for More Eco-Sustainable Advanced Cementitious Aggregate," *Recycling*, V. 5, May 2020, p. 11. doi: 10.3390/recycling5020011

15. Aiello, M. A., and Leuzzi, F., "Waste Tyre Rubberized Concrete: Properties at Fresh and Hardened State," Aug.-Sept. 2010, pp. 1696-1704. doi: 10.1016/j.wasman.2010.02.005

16. Jusli, E.; Nor, H. M.; Jaya, R. P.; and Zaiton, H., "Chemical Properties of Waste Tyre Rubber Granules," *Advanced Materials Research*, V. 911, Mar. 2014, pp. 77-81. doi: 10.4028/www.scientific.net/AMR.911.77

17. Li, F.; Zhang, X.; Wang, L.; and Zhai, R., "The Preparation Process, Service Performances and Interaction Mechanisms of Crumb Rubber Modified Asphalt (CRMA) By Wet Process: A Comprehensive Review," *Construction and Building Materials*, V. 354, Nov. 2022, p. 129168. doi: 10.1016/j.conbuildmat.2022.129168

18. Duan, K.; Wang, C.; Liu, J.; Song, L.; Chen, Q.; and Chen, Y., "Research Progress and Performance Evaluation of Crumb-Rubber-Modified Asphalts and Their Mixtures," *Construction and Building Materials*, V. 361, Dec. 2022, p. 129687. doi: 10.1016/j.conbuildmat.2022.129687

19. Bu, C.; Zhu, D.; Lu, X.; Liu, L.; Sun, Y.; Yu, L.; Xiao, T.; and Zhang, W., "Modification of Rubberized Concrete: A Review," *Buildings*, V. 12, June 2022, pp. 999. doi: 10.3390/buildings12070999

20. Li, Y.; Chai, J.; Wang, R.; Zhou, Y.; and Tong, X., "A Review of the Durability-Related Features of Waste Tyre Rubber as a Partial Substitute for Natural Aggregate in Concrete," *Buildings*, V. 12, Nov. 2022, p. 1975. doi: 10.3390/buildings12111975

21. Ding, Y.; Zhang, J.; Chen, X.; Wang, X.; and Jia, Y., "Experimental Investigation on Static and Dynamic Characteristics of Granulated Rubber-Sand Mixtures as a New Railway Subgrade Filler," *Construction and Building Materials*, V. 273, No. 3, 2021, p. 121955. doi: 10.1016/j.conbuildmat.2020.121955

22. Tasalloti, A.; Chiaro, G.; Murali, A.; and Banasiak, L., "Physical and Mechanical Properties of Granulated Rubber Mixed with Granular Soils—A Literature Review," *Sustainability*, V. 13, No. 4, 2021, p. 4309. doi: 10.3390/su13084309

23. Moasas, A. M.; Amin, M. N.; Khan, K.; Ahmad, W.; Al-Hashem, M. N. A.; Deifalla, A. F.; and Ahmad, A., "A Worldwide Development in the Accumulation of Waste Tires and Its Utilization in Concrete as a Sustainable

Construction Material: A Review," *Case Studies in Construction Materials*, V. 17, No. 12, 2022, p. e01677. doi: 10.1016/j.cscm.2022.e01677

24. Gill, P.; Jangra, P.; Roychand, R.; Saberian, M.; and Li, J., "Effects of Various Additives on the Crumb Rubber Integrated Geopolymer Concrete," *Cleaner Materials*, V. 8, No. 6, 2023, p. 100181. doi: 10.1016/j.clema.2023.100181

25. Zhong, H.; AlHuwaidi, A.; Zhang, Y.; and Zhang, M., "Effect of Crumb Rubber on Engineering Properties of Fly Ash-Slag Based Engineered Geopolymer Composites," *Construction and Building Materials*, V. 409, No. 12, 2023, p. 133878. doi: 10.1016/j.conbuildmat.2023.133878

26. Chen, Z.; Ye, H.; and Cai, J., "Recycling of Waste Tire Rubber as Aggregate in Impact-Resistant Engineered Cementitious Composites," *Construction and Building Materials*, V. 359, No. 12, 2022, p. 129477. doi: 10.1016/j.conbuildmat.2022.129477

27. Abdellatief, M.; Mortagi, M.; Elrahman, M. A.; Tahwia, A. M.; Alluqmani, A. E.; and Alanazi, H., "Characterization and Optimization of Fresh and Hardened Properties of Ultra-High Performance Geopolymer Concrete," *Case Studies in Construction Materials*, V. 19, No. 12, 2023, p. e02549. doi: 10.1016/j.cscm.2023.e02549

28. Machado, P. J. C.; Ferreira, R. A. R.; and Motta, L. A. C., "Study of the Effect of Silica Fume and Latex Dosages in Cementitious Composites Reinforced with Cellulose Fibers," *Journal of Building Engineering*, V. 31, 2020, p. 101442.

29. da Silva Alves, L. C.; Ferreira, R. A. R.; Machado, L. B.; and Motta, L. A. C., "Optimization of Metakaolin-Based Geopolymer Reinforced with Sisal Fibers Using Response Surface Methology," *Industrial Crops and Products*, V. 139, 2019, p. 111551. doi: 10.1016/j.indcrop.2019.111551

30. da Costa, D. L.; da Costa, F. P.; Fernandes, J. V.; Pinto, H. C.; Cartaxo, J. M.; Neves, G. A.; Menezes, R. R.; and Rodrigues, A. M., "Multivariate Analysis of a Geopolymeric System Containing Metakaolin and α-Al_2O_3," *Construction and Building Materials*, V. 382, 2023, p. 131302. doi: 10.1016/j.conbuildmat.2023.131302

31. Imanian, M. E., and Biglari, F. R., "Modeling and Prediction of Surface Roughness and Dimensional Accuracy in SLS 3D Printing of PVA/CB Composite Using the Central Composite Design," *Journal of Manufacturing Processes*, V. 75, 2022, pp. 154-169. doi: 10.1016/j.jmapro.2021.12.065

32. Weise, K.; Ukrainczyk, N.; Duncan, A.; and Koenders, E., "Enhanced Metakaolin Reactivity in Blended Cement with Additional Calcium Hydroxide," *Materials*, V. 15, No. 1, 2022, p. 367. doi: 10.3390/ma15010367

33. Helene, P. R. L., and Medeiros, M. H. F., "Estudo da Influência do Metacaulim HP Como Adição de Alta Eficiência em Concretos de Cimento Portland, POLI-USP," Relatório Técnico, São Paulo, 2023.

34. Chub-uppakar, T.; Chompoorant, T.; Thepumong, T.; Sae-Long, W.; Khamplod, A.; Chaiprapat, S., "Influence of Partial Substitution of Metakaolin by Palm Oil Fuel Ash and Alumina Waste Ash on Compressive Strength and Microstructure in Metakaolin-Based Geopolymer Mortar," *Case Studies in Construction Materials*, V. 19, 2023, p. e02519. doi: 10.1016/j.cscm.2023.e02519

35. Maruoka, L. M. A.; Pinheiro, I. F.; Freitas, H. S.; Nobre, F. X.; and Scalvi, L. V. A., "Effect of Thermal Annealing on Kaolin From the Amazon region, Aiming at the Production of Geopolymer," *Journal of Materials Research and Technology*, V. 25, 2023, pp. 2471-2485.

36. Provis, J. L., "Alkali-Activated Materials," *Cement and Concrete Research*, V. 114, 2018, pp. 40-48. doi: 10.1016/j.cemconres.2017.02.009

37. Provis, J. L., "Geopolymers and Other Alkali Activated Materials: Why, How, and What?" *Materials and Structures*, V. 47, 2014, pp. 11-25. doi: 10.1617/s11527-013-0211-5

38. ABNT NBR NM 52, "Fine Aggregate – Determination of the Bulk Specific Gravity and Apparent Specific Gravity," Associação Brasileira de Normas Técnicas, Rio de Janeiro, Brazil, 2009.

39. ABNT NBR 248, "Aggregates – Sieve Analysis of Fine and Coarse Aggregates," Associação Brasileira de Normas Técnicas, Rio de Janeiro, Brazil, 2003.

40. Shi, X.; Zhang, C.; Wang, X.; Zhang, T.; and Wang, Q., "Response Surface Methodology for Multi-Objective Optimization of Fly Ash-GGBS Based Geopolymer Mortar," *Construction and Building Materials*, V. 315, 2022, p. 125644. doi: 10.1016/j.conbuildmat.2021.125644

41. Ferreira, R. A. R.; Meireles, C. S.; Assunção, R. M. N.; Barrozo, M. A. S.; and Soares, R. R., "Optimization of the Oxidative Fast Pyrolysis Process of Sugarcane Straw by TGA and DSC Analyses," *Biomass and Bioenergy*, V. 134, 2020, p. 105456. doi: 10.1016/j.biombioe.2019.105456

42. Liu, J., and Tran, P., "Cement Mortar Containing Crumb Rubber Coated with Geopolymer: From Microstructural Properties to Compressive Strength," *Construction and Building Materials*, V. 383, 2023, p. 131284. doi: 10.1016/j.conbuildmat.2023.131284

43. Azmi, A. A.; Adullah, M. M. A. B.; Ghazali, C. M. R.; Ahmad, R.; Musa, L.; and Rou, L. S., "The Effect of Different Crumb Rubber Loading on the Properties of Fly Ash-Based Geopolymer Concrete," *IOP Conference Series: Materials Science and Engineering*, 2019, p. 12079.

44. ABNT NBR 13276, "Mortars Applied on Walls and Ceiling – Determination of the Consistence Index," Associação Brasileira de Normas Técnicas, Rio de Janeiro, Brazil, 2016.

45. Kim, B., and Lee, S., "Review on Characteristics of Metakaolin-Based Geopolymer and Fast Setting," *Journal of the Korean Ceramic Society*, V. 57, 2020, pp. 368-377. doi: 10.1007/s43207-020-00043-y

46. ABNT NBR 13279, "Mortars Applied on Walls and Ceilings – Determination of the Flexural and the Compressive Strength in the Hardened Stage," Associação Brasileira de Normas Técnicas, Rio de Janeiro, Brazil, 2005.

47. Réunion Internationale des Laboratoires d'Essais et de Recherches sur les Matériaux e les Constructions (RILEM), "Test for Determination of Modulus of Rupture and Limit of Proportionality of Thin Fibre Reinforced Cement Section," *Materials and Structures*, V. 17, Nov. 1984, pp. 441-456.

48. Santos, M. N. G.; Santos, C. M.; Souza, M. T. G.; Vasconcelos, E. A.; Nóbrega, A. C. V.; and Marinho, E. P., "Use of Sodium Metasilicate as Silica Source and Stabilizing Agent in Two-Part Metakaolin-H_2O_2 Geopolymer Foams," *Construction and Building Materials*, V. 391, 2023, p. 131907. doi: 10.1016/j.conbuildmat.2023.131907

49. Yang, F.; Li, Z.; Li, Y.; Han, G.; Fam, H.; Liu, X.; Xu, M.; and Guo, M., "The Effects of Na_2O/K_2O Flux on Ash Fusion Characteristics for High Silicon-Aluminum Coal in Entrained-Flow Bed Gasification," *Energy*, V. 282, Nov. 2023, p. 128603.

50. Luhar, S.; Chaudhary, S.; and Luhar, I., "Development of Rubberized Geopolymer Concrete: Strength and Durability Studies," *Construction and Building Materials*, V. 204, No. 3, 2019, pp. 740-753. doi: 10.1016/j.conbuildmat.2019.01.185

51. Deng, Z.; Yang, Z.; and Pan, X., "Synergetic Effects of Recycled Crumb Rubber and Glass Cullet on the Engineering Properties of Geopolymer Mortar," *Cement and Concrete Composites*, V. 137, No. 3, 2023, p. 104907. doi: 10.1016/j.cemconcomp.2022.104907

52. Ameri, F.; Shoaei, P.; Musaeei, H. R.; Zareei, S. A.; and Cheah, C. B., "Partial Replacement of Copper Slag with Treated Crumb Rubber Aggregates in Alkali-Activated Slag Mortar," *Construction and Building Materials*, V. 256, 2020, pp. 119468.

53. Skripkiūnas, G.; Grinys, A.; and Cernius, B., "Deformation Properties of Concrete with Rubber Waste Additives," *Materials Science*, V. 13, No. 3, 2007, pp. 219-223.

54. Hossein, H. A.; Hamzawy, E. M. A.; El-Bassyouni, G. T.; and Nabawy, B. S., "Mechanical and Physical Properties of Synthetic Sustainable Geopolymer Binders Manufactured Using Rockwool, Granulated Slag, and Silica Fume," *Construction and Building Materials*, V. 367, 2023, p. 130143. doi: 10.1016/j.conbuildmat.2022.130143

55. Negahban, E.; Bagheri, A.; and Sanjayan, J., "Pore Structure Profile of Ambient Temperature-Cured Geopolymer Concrete and Its Effect on Engineering Properties," *Construction and Building Materials*, V. 406, 2023, p. 133311. doi: 10.1016/j.conbuildmat.2023.133311

56. Lizcano, M.; Kim, H. S.; Basu, S.; and Radovic, M., "Mechanical Properties of Sodium and Potassium Activated Metakaolin-Based Geopolymer," *Journal of Materials Science*, V. 47, 2012, pp. 2607-2616. doi: 10.1007/s10853-011-6085-4

57. Pouhet, R.; Cyr, M.; and Bucher, R. "Influence of the Initial Water Content in Flash Calcined Metakaolin-Based Geopolymer," *Construction and Building Materials*, V. 201, 2019, pp. 421-429.

58. Muhammad, S.; Yuan, Q.; Alam, M.; Javed, M. F.; Rehman, M. F.; and Mohamed, A., "Fresh and Hardened Properties of Waste Rubber Tires-Based Concrete: A State Art of Review," *SN Applied Sciences*, V. 5, No. 4, 2023, p. 119.

59. Arunkumar, K.; Muthukannan, M.; and Ganesh, A. C., "Mitigation of Waste Rubber Tire and Waste Wood Ash by the Production of Rubberized Low Calcium Waste Wood Ash Based Geopolymer Concrete and Influence of Waste Rubber Fibre in Setting Properties and Mechanical Behavior," *Environmental Research*, V. 194, No. 3, 2021, p. 110661. doi: 10.1016/j.envres.2020.110661

60. Di Mundo, R.; Petrella, A.; and Notarnicola, M., "Surface and Bulk Hydrophobic Cement Composites by Tire Rubber Addition," *Construction and Building Materials*, V. 172, 2018, pp. 176-184. doi: 10.1016/j.conbuildmat.2018.03.233

61. Obeidy, N. F. A., and Khalil, W. I., "Studying the Possibility of Producing Paving Flags from Geopolymer Concrete Containing Local Wastes," *Engineering and Technology Journal*, V. 41, No. 11, 2023, pp. 1325-1336. doi: 10.30684/etj.2023.141321.1494

62. Duxson, P.; Fernández-Jiménez, A.; Provis, J. L.; Lukey, G. C.; Palomo, A.; and Van Deventer, J. S., "Geopolymer Technology: The Current State of the Art," *Journal of Materials Science*, V. 42, No. 12, 2007, pp. 2917-2933. doi: 10.1007/s10853-006-0637-z

63. Nadi, M.; Allaoui, O.; Majdoubi, H.; Hamdane, H.; Haddaju, Y.; Mandouri, S.; Tamraoui, Y.; Manoun, B.; Hannache, H.; and Oumam, M., "Effect of Natural Graphite Additions on the Microstructural and Mechanical Behavior of Metakaolin Based Geopolymer Materials," *Journal of Building Engineering*, V. 78, No. 12, 2023, p. 107562. doi: 10.1016/j.jobe.2023.107562

64. Shah, V.; Parashar, A.; and Scott, A., "Understanding the Importance of Carbonates on the Performance of Portland Metakaolin Cement," *Construction and Building Materials*, V. 319, No. 2, 2022, pp. 126155.

65. Ates, F.; Park, K. T.; Kim, W. K.; Woo, B. H.; and Kim, H. G., "Effects of Treated Biomass Wood Fly Ash as a Partial Substitute for Fly Ash in a Geopolymer Mortar System," *Construction and Building Materials*, V. 376, No. 6, 2023, p. 131063. doi: 10.1016/j.conbuildmat.2023.131063

66. Jaradat, Y., and Matalkah, F., "Effects of Micro Silica on the Compressive Strength and Absorption Characteristics of Olive Biomass Ash-Based Geopolymer," *Case Studies in Construction Materials*, V. 18, No. 7, 2023, p. e01870. doi: 10.1016/j.cscm.2023.e01870

67. Aziz, A., "Structural and Physico-Mechanical Investigations of New Acidic Geopolymers Based on Natural Moroccan Pozzolan: A Parametric Study," *Silicon*, V. 15, 2023, pp. 1133-1144.

68. dos ReisFerreira, R. A., and Gratão, L. S., and de CastroMotta, L. A., "Evaluation and Optimization of the Replacement of Fine Aggregate by Waste Tire Rubber in Geopolymer Mortar with Metakaolin," *Mechanics of Composite Materials*, V. 59, 2024, pp. 1223-1238. doi: 10.1007/s11029-023-10168-w

69. Castillo, H.; Collado, H.; Droguett, T.; Vesely, M.; Garrido, P.; and Palma, S., "State of the Art of Geopolymers: A Review," *e-Polymers*, V. 22, Jan. 2022, pp. 108-124.

70. Chen, L.; Wang, Z.; Wang, Y.; and Feng, J., "Preparation and Properties of Alkali Activated Metakaolin-Based Geopolymer," *Materials*, V. 9, 2016, pp. 767.

71. Yang, H.; Liu, L.; Yang, W.; Liu, H.; Ahmad, W.; Ahmad, A.; Aslam, F.; and Joyklad, P., "A Comprehensive Overview of Geopolymer Composites: A Bibliometric Analysis and Literature Review," *Case Studies in Construction Materials*, V. 16, No. 6, 2022, p. e00830. doi: 10.1016/j.cscm.2021.e00830

72. Zhang, Z.; Provis, J. L.; Reid, A.; and Wang, H., "Geopolymer Foam Concrete: An Emerging Material for Sustainable Construction," *Construction and Building Materials*, V. 56, No. 4, 2014, pp. 113-127. doi: 10.1016/j.conbuildmat.2014.01.081

73. Mucsi, G.; Szenczi, Á.; and Nagy, S., "Fiber Reinforced Geopolymer from Synergetic Utilization of Fly Ash and Waste Tire," *Journal of Cleaner Production*, V. 178, No. 3, 2018, pp. 429-440. doi: 10.1016/j.jclepro.2018.01.018

74. Zedler, L.; Przybysz-Romatowska, M.; Haponiuk, J.; Wang, S.; and Formela, K., "Modification of Ground Tire Rubber-Promising Approach for Development of Green Composites," *Journal of Composites Science*, V. 4, No. 1, Dec. 2020, pp. 1-11.

75. Formela, K.; Zedler, L.; Kowalkowska-Zedler, D.; Colom, X.; Cañavate, J.; and Saeb, M. R., "Reactive Sintering of Ground Tire Rubber (GTR) Modified by a Trans-Polyoctenamer Rubber and Curing Additives," *Polymers*, V. 12, No. 12, 2020, p. 3018. doi: 10.3390/polym12123018

76. Zedler, L.; Kowalkowska-Zedler, D.; Vahabi, H.; Saeb, M. R.; Colom, X.; Cañavate, J.; Wang, S.; and Formela, K., "Preliminary Investigation on Auto-Thermal Extrusion of Ground Tire Rubber," *Materials*, V. 12, No. 13, 2019, p. 2090. doi: 10.3390/ma12132090

77. Formela, K.; Hejna, A.; Zedler, L.; Colom, X.; and Cañavate, J., "Microwave Treatment in Waste Rubber Recycling – Recent Advances and Limitations," *Express Polymer Letters*, V. 13, No. 6, 2019, pp. 565-588. doi: 10.3144/expresspolymlett.2019.48

78. Mohana, R., and Bharathi, S. M. L., "Sustainable Approach of Promoting Impact Resistant Rubberized Geopolymer by Reducing the Embodied Emission Rate of Climate Changing Substances," *Structures*, V. 57, No. 11, 2023, p. 105241. doi: 10.1016/j.istruc.2023.105241

APPENDIX

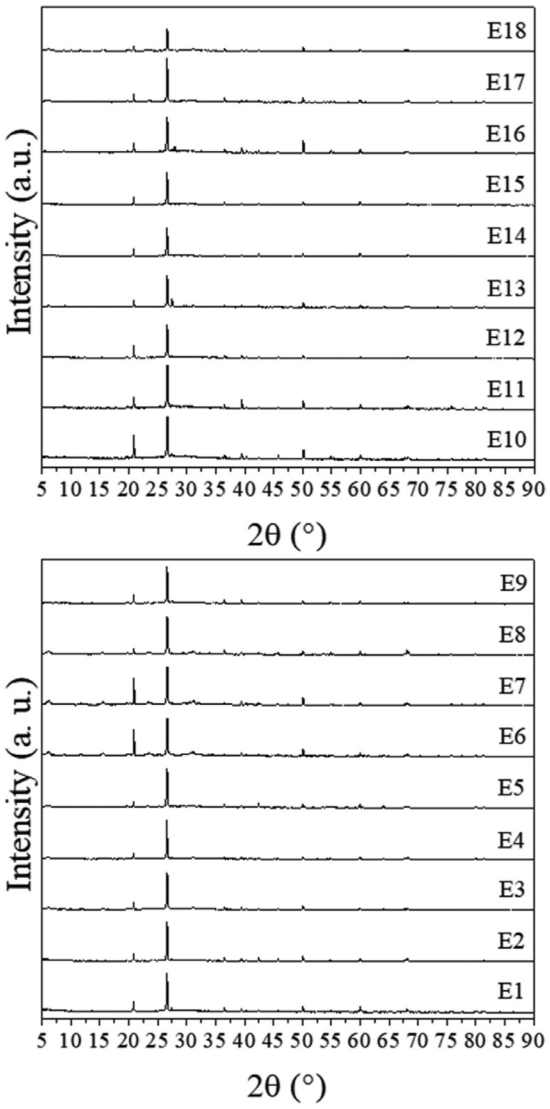

Diffractograms of 18 geopolymer mortar experiments with tire rubber waste.

ACI in Your Classroom

Integrate ACI into your classroom!

To support future leaders, ACI has launched several initiatives to engage students in the Institute's activities and programs – select programs that may be of interest to Educators are:

- **Free student membership –** encourage students to sign up
- **Special student discounts on *ACI 318 Building Code Requirements for Structural Concrete*, *ACI 530 Building Code Requirements and Specification for Masonry Structure*, & *Formwork for Concrete* manual.**
- **Access to *Concrete International* –** free to all ACI student members
- **Access to *ACI Structural Journal* and *ACI Materials Journal* –** free to all ACI student members
- **Free sustainability resources –** free copies of Sustainable Concrete Guides provided to universities for use in the classroom
- **Student competitions –** participate in ACI's written and/or team-based competitions
- **Scholarships and fellowships –** students who win awards are provided up to $15,000 and may be offered internships and paid travel to attend ACI's conventions
- **ACI Award for University Student Activities –** receive local and international recognition for your University's participation in concrete-related activities
- **Free access to the *ACI Collection of Concrete Codes, Specifications, and Practices* –** in conjunction with ACI's chapters, students are provided free access to the online ACI Collection
- **ACI online recorded web sessions and continuing education programs –** online learning tools ideal for use as quizzes or in-class study material

https://www.concrete.org/educatorsandresearchers/aciinyourclassroom.aspx

ARE YOU A RESEARCHER?

SIGN UP FOR ORCID TODAY!

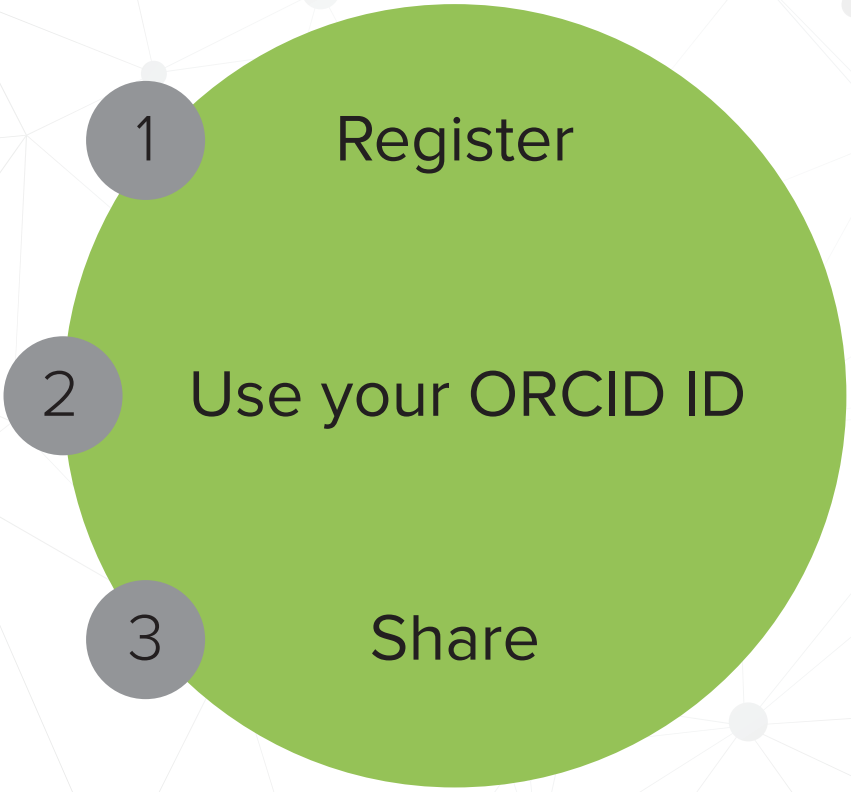

ORCID provides a digital identifier that distinguishes you from every other researcher and, through integration in key research workflows such as manuscript and grant submission, supports automated linkages between you and your professional activities, ensuring that your work is recognized.

ORCID services are FREE and it's as easy as **1-2-3**.

WWW.ORCID.ORG

CALL FOR ACTION

ACI Invites You To...

Share your expertise

Do you have EXPERTISE in any of these areas?

- BIM
- Chimneys
- Circular Concrete Structures Prestressed by Wrapping with Wire and Strand
- Circular Concrete Structures Prestressed with Circumferential Tendons
- Concrete Properties
- Demolition
- Deterioration of Concrete in Hydraulic Structures
- Electronic Data Exchange
- Insulating Concrete Forms, Design, and Construction
- Nuclear Reactors, Concrete Components
- Pedestal Water Towers
- Pipe, Cast-in-Place
- Strengthening of Concrete Members
- Sustainability

Become a Reviewer for the ACI Journals

Then become a REVIEWER for the *ACI Structural Journal* or the *ACI Materials Journal*.

How to become a Reviewer:

1. Go to: **http://mc.manuscriptcentral.com/aci**;
2. Click on "Create Account" in the upper right-hand corner; and
3. Enter your E-mail/Name, Address, User ID and Password, and Area(s) of Expertise.

Update your Manuscript Central user account information

Did you know that the database for MANUSCRIPT CENTRAL, our manuscript submission program, is separate from the ACI membership database?

How to update your user account:

1. Go to **http://mc.manuscriptcentral.com/aci**;
2. Log in with your current User ID & Password; and
3. Update your E-mail/Name, Address, User ID and Password, and Area(s) of Expertise.

QUESTIONS?

E-mail any questions to Journals.Manuscripts@concrete.org.

American Concrete Institute

Always advancing

ACI MATERIALS JOURNAL

The American Concrete Institute (ACI) is a leading authority and resource worldwide for the development and distribution of consensus-based standards and technical resources, educational programs, and certifications for individuals and organizations involved in concrete design, construction, and materials, who share a commitment to pursuing the best use of concrete.

Individuals interested in the activities of ACI are encouraged to explore the ACI website for membership opportunities, committee activities, and a wide variety of concrete resources. As a volunteer member-driven organization, ACI invites partnerships and welcomes all concrete professionals who wish to be part of a respected, connected, social group that provides an opportunity for professional growth, networking, and enjoyment.

American Concrete Institute